NASA CR-122437

MEASUREMENTS FROM SATELLITE PLATFORMS

R-122437) METEOROLOGICAL
IENTS FROM SATELLITE PLATFORMS
Scientific Report, 1970 - 1971 V.E.
Wisconsin Univ.) Feb. 1972 262 p
CSCL 04B G3/20

N72-27646
thru
N72-27652
Unclas
34297

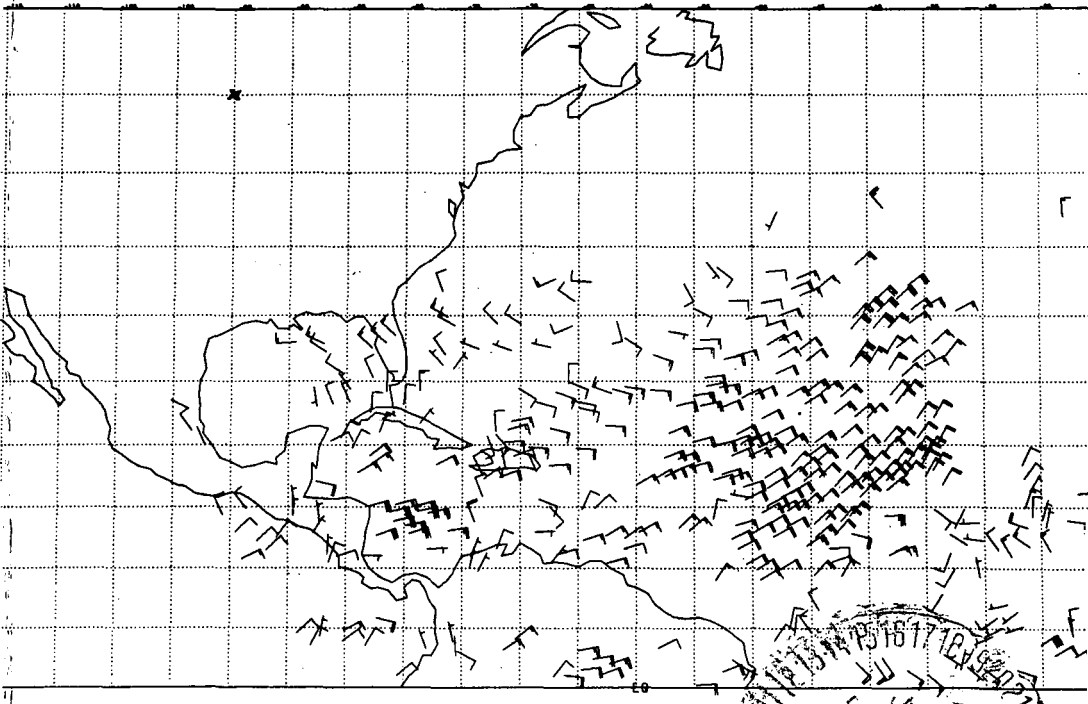

RECEIVED
JUL 1972
NASA STI FACILITY
INPUT BRANCH

Annual Scientific Report on NAS5-11542, 1970-1971
Space Science and Engineering Center
University of Wisconsin—Madison
February 1972

Space Science and Engineering Center
The University of Wisconsin
Madison, Wisconsin

METEOROLOGICAL MEASUREMENTS FROM SATELLITE PLATFORMS

Annual Scientific Report

on

NAS5-11542

1970-1971

The research in this document has been supported in whole or in part by the National Aeronautics and Space Administration.

February 1972

Details of illustrations in
this document may be better
studied on microfiche

PRINCIPAL INVESTIGATOR

Verner E. Suomi

CONTRIBUTIONS BY

Blair C.
Grosh R.
Levanon N.
Oelkers R.
Phillips D.
Sikdar D. N.
Smith E.
Stremler F.

University of Wisconsin

ERRATA

Pages ii and v: The author's name should read R. Oehlkers.

Page 9: Equation (1) should read:

$$\begin{pmatrix} x(t) \\ y(t) \\ z(t) \end{pmatrix} = \begin{pmatrix} \cos(L) & -\sin(L) & 0 \\ \sin(L) & \cos(L) & 0 \\ 0 & 0 & 1 \end{pmatrix} \begin{pmatrix} \cos(2\cdot\pi\cdot(t-t_0)/P_e & \sin(2\cdot\pi\cdot(t-t_0)/P_e & 0 \\ -\sin(2\cdot\pi\cdot(t-t_0)/P_e) & \cos(2\cdot\pi\cdot(t-t_0)/P_e) & 0 \\ 0 & 0 & 1 \end{pmatrix}$$

$$\ldots \begin{pmatrix} 1 & 0 & 0 \\ 0 & \cos(\alpha) & \sin(\alpha) \\ 0 & -\sin(\alpha) & \cos(\alpha) \end{pmatrix} \cdot \begin{pmatrix} h\cdot\cos(2\cdot\pi\cdot(t-t_0)/P_s) \\ h\cdot\sin(2\cdot\pi\cdot(t-t_0)/P_s \\ 0 \end{pmatrix}$$

Page 11: Equation (2) should read:

$$\begin{pmatrix} x' \\ y' \\ z' \end{pmatrix} = \begin{pmatrix} k\cdot\cos((\text{PCLN-LINE})\cdot(\text{RDLN})\cdot\cos((\text{PCEL-ELEMENT})\cdot\text{RDSAM}) \\ k\cdot\cos((\text{PCLN-LINE})\cdot(\text{RDLN})\cdot\sin((\text{PCEL-ELEMENT})\cdot\text{RDSAM}) \\ k\cdot\sin((\text{PCLN-LINE})\cdot\text{RDLN} \end{pmatrix}$$

Page 12: Equation (3) should read:

$$\begin{pmatrix} x'' \\ y'' \\ z'' \end{pmatrix} = \begin{pmatrix} \text{BROT} \end{pmatrix} \cdot \begin{pmatrix} x' \\ y' \\ z' \end{pmatrix}$$

Equation (5) should read:

$$\begin{pmatrix} x \\ y \\ z \end{pmatrix} = \begin{pmatrix} \text{BROT} \end{pmatrix} \cdot \begin{pmatrix} x' \\ y' \\ z' \end{pmatrix} + \begin{pmatrix} \text{BVEC} \end{pmatrix}$$

Pages 15 and 39: The term "1/0" should read "I/O".

Page 16: "A random jitter of $\pm$ 6 ..." should read: "A random jitter of $\pm$ 2 ..." (first paragraph).

Page 19: The last line of the first paragraph should read: "Equations (8)-(11) are needed to define $\bar{b}_{p,q}$, $b\sigma_{p,q}$, $\bar{a}$, and $a\sigma$."

Equation (9) should read:

$$b\sigma_{p,q} = \sum_{j=1}^{32} \sum_{i=1}^{32} (B_{i+p-1,\, j+q-1} - \bar{b}_{p,q})$$

Page 68: A delta should be placed before each caption in the graph in Figure 8.

Page 70: The designations for the dot and triangle in Figure 9 should be reversed.

Page 72: Add to the caption in Figure 11: "Scale on right hand side pertains to 18% contour."

Page 74: The designations for the dot and triangle in Figure 13 should be reversed.

PREFACE

Exploitation and application of the data obtained from meteorological satellites is the ultimate objective of the meteorological satellite program. The techniques and equipments required to process these data into useful information are as much a part of the total meteorological satellite system as are the sensors or the satellite platforms.

The first article in this report describes the initial development of WINDCO, a system intended to convert spin-scan camera signals into cloud displacement field plots from which winds may be inferred by a meteorologist. WINDCO is typical of the final stage in the function chain from sensor to user which makes up a meteorological satellite system. The next two papers investigate the spin-scan camera signals as sources of information from which to measure rainfall amounts. This application of the ATS data was not foreseen when the satellite was built and flown, yet may prove to be of great scientific and economic importance as the techniques are applied operationally. The next two papers report upon work which has refined the design and operation of the balloon-borne radio altimeter. This device will be used as part of a satellite-balloon data collection system in the NIMBUS-F program in 1974. The last paper describes the use of ATS satellite pictures to determine some of the characteristics of tropical cloud clusters.

The individual authors and I wish to thank all the members of the Space Science and Engineering Center who have assisted in this work, and to express our gratitude to the authorities in the National Aeronautics and Space Administration who have encouraged and sponsored our efforts.

Verner E. Suomi
Principal Investigator

PRECEDING PAGE BLANK NOT FILMED

CONTENTS

Page

Technical Articles

1. Phillips,D. and E. Smith: WINDCO: An Interactive System for Obtaining Accurate Cloud Motions from Geostationary Satellite Spin Scan Camera Pictures. 47 1

2. Sikdar, D. N.: ATS-III: Observed Cloud Brightness Field Related to Meso- to Subsynoptic-Scale Rainfall Pattern. 46 53

3. Grosh, R.: Cloud Photographs from Satellites as a Hydrological Tool in Remote Tropical Regions. (Thesis submitted in partial fulfillment of the requirements for a degree of Master of Science in Meteorology) 49 77

4. Stremler,F. G., C. D. Blair and R. A. Oelkers: Design of a Small Radar Altimeter for Balloon Payloads. (Presented at the Third Annual IEEE International Geoscience Electronics Symposium, Washington, D.C., August 27, 1971). 50 125

5. Levanon,N.: Averaged Pulse Shape Measurements of Radar Sea Return at Near-Vertical Incidence. (Research undertaken partially at Department of Environmental Sciences, Tel-Aviv University, Tel-Aviv). 51 140

6. Hasler, S. F.: Properties of Tropical Cloud Clusters Determined from Geostationary Satellite Pictures. 52 166

N72-27647

WINDCO: An Interactive System for Obtaining Accurate Cloud Motions from Geostationary Satellite Spin Scan Camera Pictures

Eric Smith
Dennis Phillips

Abstract:

The measurement of winds to an accuracy of at least 2 knots (1 m/sec) is a major requirement of the Global Atmospheric Research Program (GARP). Such accurate wind measurements will be needed over large regions presently lacking ground or rawinsonde observations. An interactive man-computer system called WINDCO has been developed to measure cloud motion from ATS pictures. This system is capable of providing cloud motion measurement accuracy to better than 2.5 knots (1.2 m/sec) RMS at moderate cost in a real-time environment.

Precise picture alignment has been the crucial barrier for making accurate cloud motion measurements. This problem has been solved with an analytic solution, called ATS Navigation, which is capable of aligning consecutive ATS digital pictures to within one nautical mile.

Cloud motion is measured by tracking clouds over a digital picture sequence by applying two-dimensional cross-correlation analysis. The cloud tracers are selected by a human operator. The Fast Fourier Transform Radix8 method and other programming techniques have been implemented to minimize time and cost.

Three days during the Barbados Oceanographic and Meteorological experiment (BOMEX) in July 1969 were selected for a case study. On each day cloud motion vectors were computed over three time intervals. The repeated measurements of cloud motion vectors indicate that the east-west (u) and north-south (v) components are reproducible within 1.0 knot (0.5 m/sec) and 20 knots (10 m/sec), respectively.

1. Introduction

The photographic coverage of the earth's atmosphere provided by spin scan cameras on board ATS-I and ATS-III satellites has been demonstrated by Suomi (1968) to be a valuable resource for studies of atmospheric phenomena. ATS pictures have enabled man to view the weather in motion, and, in particular, the clouds in motion, especially over the vast unprobed ocean expanses. The inclusion of the time dimension into a view of the atmosphere permits quantification of cloud motion. How cloud motion relates directly to the wind field is not a subject of debate in this article. Studies by Fujita (1969), Hasler (1970), and Hubert (1969) have all indicated that there is a significant relationship between the wind field and cloud motions.

Several techniques have been developed to measure cloud motion by using time-lapsed satellite photographs. However, these techniques have not capitalized on the geometric precision of the raw ATS data. The element position of the spin scan camera is precisely determined as a linear function of time, and the angle of the sweep of the line with respect to the spin axis is controlled by the precision stepping mechanism of the ATS spin scan camera. This information allows precise alignment between consecutive ATS digital pictures. Any technique distorting the basic geometry, such as photographic techniques, degrades the data's precision. The WINDCO system preserves this precision by handling the data in its raw form.

The Global Atmospheric Research Program (GARP) defines, as a major requirement, the capability of determining winds to an accuracy of two knots (1 m/sec). In 1974 the Garp Atlantic Tropical Experiment (GATE) will undertake an investigation of the energetics and dynamics of the atmosphere in the tropical zone of the eastern portion of the Atlantic Ocean. These studies of small and large scale interaction and energy transport in the atmosphere will require that winds be available accurately and consistently over short time intervals. Furthermore, operationally produced winds would significantly improve the accuracy of numerical forecasting. In this article we intend to demonstrate that GARP requirements can be met. The system that has been developed is an interactive man-computer system called WINDCO that could easily be converted to an operational environment. The cost of such a system would be moderate. It has been applied to ATS digital photographs with very promising results.

2. Cloud Tracking

Tracking cloud tracers between two ATS digital photographs is the function of the WINDCO system. The system requires a human operator to select cloud tracers. Cloud field data is input to a computer from which cloud motion vectors are generated. The displacement measurement is accomplished by the application of two-dimensional cross-correlation analysis.

Most of the techniques that have been developed for cloud motion studies depend on the manual measurement of cloud tracer motion. All of these systems are painstakingly slow and highly vulnerable to measurement error. It should be stressed that even small measurement errors will generate very poor results. The ATS photograph is a composite of 2400 by 8192 picture elements as shown in Figure 1. The resolution of the ATS camera at the subsatellite point (SSP) is two nautical miles. A measurement error of one line over a half-hour time interval produces an error in the cloud motion vector of four knots, as illustrated in Figure 2.

The movie loop techniques developed by Fujita, Hasler, and Hubert have shown some promise. In these systems, cloud tracking is accomplished with a time series of ATS photographs displayed repeatedly from a film loop. Each cloud tracer is observed throughout the picture sequence and end point coordinates are marked out by the operator, then measured. The advantage of being able to view the cloud motion enables the operator to integrate the motion before marking coordinates. The disadvantage is that the procedure is slow, vulnerable to measurement error and operator fatigue.

However, this is not to say that the human decision-making process should be eliminated. On the contrary, the human operator should be present to select adequate cloud tracers. His judgment is based upon an understanding of dynamic atmospheric phenomena. He will function as a primary component of the WINDCO system at a TV console using a light pen to signal the computer which clouds to select. In contrast to the manual systems, he is neither required to measure cloud motion nor to align picture frames.

3. Picture Alignment

The crucial barrier to improved cloud motion measurements has been the absence of a precise alignment technique for the earth images. Precision alignment is an absolute requirement for accurate cloud motion measurements. Any misalignment of the earth images causes systematic errors in displacement measurements. Because the spin axis of the ATS satellite is not parallel to the earth spin axis and because of oscillating satellite orbit

Reproduced from best available copy.

Figure 1. ATS-III Picture Showing Line-Element Coordinates

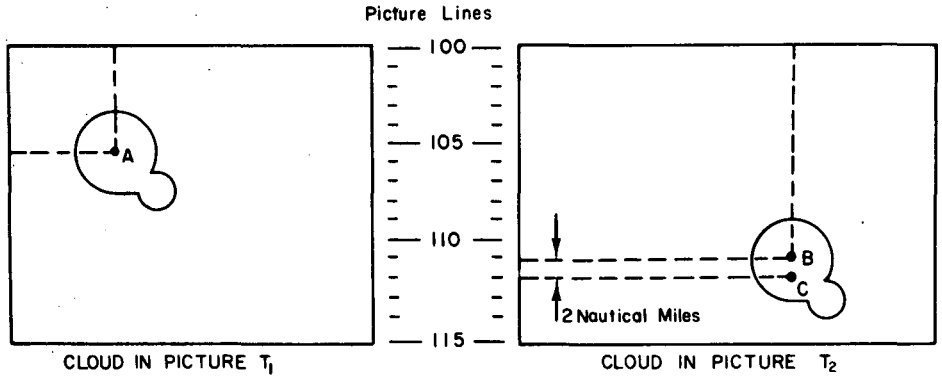

Figure 2. Cloud Motion Measurement Error Caused by Cloud Position Measurement Error

motion, earth images appear to move within the picture frame. The phenomenon of apparent earth motion must be compensated for in the cloud motion vectors. In the WINDCO system, this motion is removed in an analytic fashion by determining a transform function from satellite coordinates to earth coordinates. This process is called ATS navigation.

A major problem with the movie loop techniques is that the pictures are aligned by the eyes lining up geographical reference points or earth limbs on photographic products. This procedure is imprecise, provides no adequate technique to estimate the alignment error, and fails to account for the effects of satellite motion and attitude in the pictures. Changes in aspect during each picture frame cannot be corrected on photographs because the earth moves continuously in each frame because of satellite and orbit effects. Also, any photographic process has inherent problems with film distortion. Furthermore, the eye is not fully dependable as a quantitative alignment device. Small errors in alignment lead to large errors in the cloud motion vectors. Figure 3 illustrates the systematic errors generated by earth image misalignment. The only way to reduce the systematic errors of misalignment is to increase the time interval between picture pairs. However, this decreases the probability of tracking clouds because of changes in the shape or existence of the distinctive features.

The backbone of the WINDCO system is an analytical model which precisely aligns picture frames. By aligning a picture sequence to less than one nautical mile, very accurate cloud motion vectors can be computed. Before discussing ATS navigation, it is useful to trace some of its background. The main problem is to determine the attitude of the ATS satellite. The first ATS navigation system was designed by the ATS team at the Westinghouse Defense and Space Center. This system fits a circle to the limb of the earth. Two such fits are necessary to determine satellite attitude. The Westinghouse report on this subject does not include any mention of the relative alignment errors; however, the absolute errors are fifteen nautical miles. Our tests show that fitting the edge of the earth is difficult and imprecise because of noise and the scattering of the atmosphere at the limb. A second approach, developed by Phillips at the National Environmental Satellite Center and later refined at the Space Science and Engineering Center, utilized landmark detection as the basis for attitude determination. A basic failing of this approach is that each ATS picture is navigated separately. This results in a different attitude determination for each ATS picture from a picture series, and ignores the stability of the satellite's attitude and orbit. Because of the large distance between the satellite and the earth, slight variations in the attitude represent significant errors in earth alignment. To avoid this discontinuity, Phillips replaced the single picture navigation approach with a multi-picture navigation approach which decreased alignment errors to less than satellite resolution.

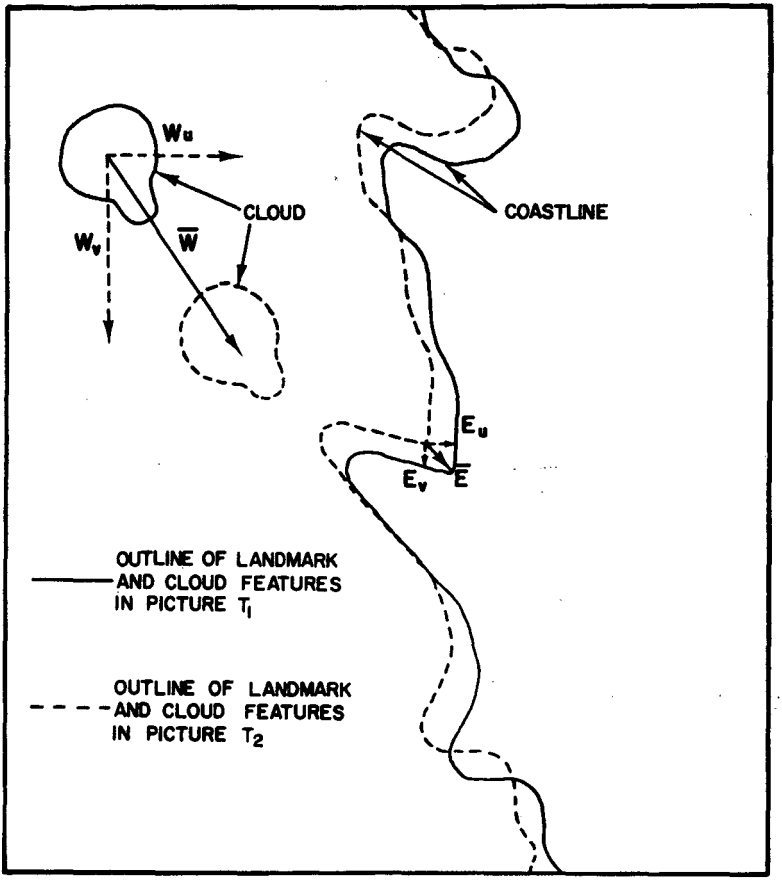

$\overline{W}$ = VECTOR REPRESENTING THE DISPLACEMENT OF A CLOUD OVER TIME INTERVAL $T_1 - T_2$

$\overline{E}$ = VECTOR REPRESENTING THE APPARENT DISPLACEMENT OF A LANDMARK DUE TO PICTURE MISALIGNMENT

$W_u - E_u$ = CORRECTED U COMPONENT

$W_v - E_v$ = CORRECTED V COMPONENT

Figure 3. Cloud Motion Measurement Error Caused by Picture Misalignment

4. ATS Navigation

Cloud motion measurements must be made within an earth frame of reference. Hence, any cloud motion measurements on satellite pictures require a transformation from the satellite's frame of reference to the earth's frame of reference. The procedure of determining this transformation is called ATS navigation. The multi-picture model of ATS navigation is a three-step process:

1. Approximation of the satellite's orbit
2. Derivation of the satellite's attitude
3. Computation of the information needed for centering the earth in an east-west direction in the picture frame.

First, the satellite's orbit is approximated with a circular orbit by using parameters available from NASA. Recognizable landmarks are then measured on a series of ATS pictures to provide inputs for the attitude computation. Aeronautical charts provided by the U. S. Coast and Geodetic Survey are utilized in the identification process. Finally, the information for centering the earth in each frame is derived from the satellite's orbit and attitude and landmark measurements from that particular frame. The final result of this procedure is the ability to transform ATS picture coordinates to earth coordinates and vice versa.

The circular approximation of the satellite's orbit is done with five parameters:

1. Orbital period
2. Satellite height
3. Inclination of the orbit with respect to the equatorial plane
4. Longitude of the satellite's position during an equatorial crossing in the southern direction
5. Time of the equatorial crossing.

Equation (1) gives the position of the satellite in earth coordinates as a function of time.

$$
\begin{bmatrix} x(t) \\ y(t) \\ z(t) \end{bmatrix} = \begin{bmatrix} \cos(L) & -\sin(L) & 0 \\ \sin(L) & \cos(L) & 0 \\ 0 & 0 & 1 \end{bmatrix} \cdot \begin{bmatrix} \cos(2\cdot\pi\cdot(t-t_0)/P_e) & \sin(2\cdot\pi\cdot(t-t_0)/P_e) & 0 \\ -\sin(2\cdot\pi\cdot(t-t_0)/P_e) & \cos(2\cdot\pi\cdot(t-t_0)/P_e) & 0 \\ 0 & 0 & 1 \end{bmatrix} \cdot \ldots
$$

$$
\ldots \begin{bmatrix} 1 & 0 & 0 \\ 0 & \cos(\alpha) & \sin(\alpha) \\ 0 & -\sin(\alpha) & \cos(\alpha) \end{bmatrix} \cdot \begin{bmatrix} h\cdot\cos(2\cdot\pi\cdot(t-t_0)/P_s) \\ h\cdot\sin(2\cdot\pi\cdot(t-t_0)/P_s) \\ 0 \end{bmatrix} \qquad (1)
$$

where

L = Longitude of the satellite's position during an equatorial crossing in the southern direction

t_0 = Time of the equatorial crossing

α = Inclination of the orbital plane with respect to the equatorial plane

h = Height of satellite from the center of the earth

P_s = Orbital period

P_e = Length of a celestial day

Computing the satellite's attitude is a more delicate step in the navigation procedure since actual landmark measurements from ATS pictures are being introduced to the model. In this step, a least squares procedure utilizes the multiple landmark measurements available. Each recognition of a landmark on an ATS picture restricts the attitude of the spin axis to a circular locus on the celestial sphere. This locus is determined as follows. The vector from the satellite to the landmark on the earth intersects the celestial sphere uniquely when extended. The line number of the landmark determines the angle between this point on the celestial sphere and the point where the spin axis would intersect the celestial sphere, if extended. This relationship is illustrated in Figure 4. The intersection of two loci determine the attitude of the spin axis. Use of three or more such loci allows the application of a least squares procedure. Furthermore, the use of three or more loci enables the computation of the line number at which the spin scan camera's axis is perpendicular to the satellite spin axis. The need for such a computation has been documented in the Westinghouse report

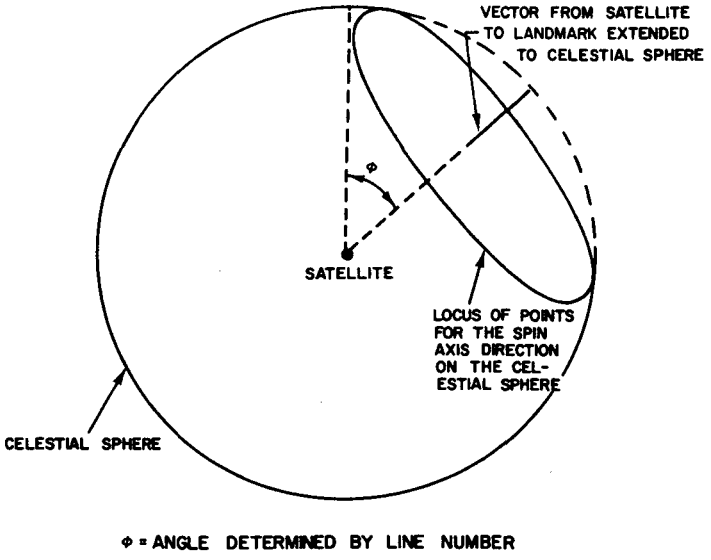

Figure 4. Spin Axis Locus on Celestial Sphere

Investigation of ATS Attitude Anomaly, July 1970. This unknown adds one extra parameter to the least squares calculation. The sum of the squares is minimized by a steepest descent method. One result of this computation is the spin axis direction in earth coordinates at base time t_0, which is usually Greenwich time zero of the day navigated. The other result is the line count at which the spin scan camera's axis is perpendicular to the spin axis of the satellite.

The computation of earth-centering information incorporates the satellite's orbit and attitude along with element numbers of measured landmarks from each picture. For each picture, an angle is computed measuring the subsatellite point shift to the right or left of the picture center element. This angle provides the last parameter necessary to construct a transformation from ATS picture coordinates to earth coordinates and its inverse.

The transformation from ATS picture coordinates to earth surface coordinates is performed in three steps: first, a transformation from the ATS picture coordinate system centered around the satellite; second, a transformation from the satellite-centered coordinate system to an earth-centered coordinate system; finally, a transformation from the earth-centered coordinate system to surface latitude and longitude. The ATS

picture coordinates are the line and element number of the corresponding pictel. The line and element counting system is illustrated in Figure 1. In the satellite coordinate system the z' axis coincides with the spin axis of the satellite, the x' axis is perpendicular to the spin axis and lies in the plane determined by the z' axis and the ray determined by the picture center element (4096) of the current scan. The y' axis is added to make the coordinate system a right-handed orthonormal system, as shown in Figure 5. The earth-centered coordinate system has the x-axis pointing at the intersection of the equator and the Greenwich Meridian, the z-axis directed towards the North Pole and the y-axis completes a right-handed orthonormal coordinate system. The latitude and longitude are geocentric latitude and longitude. Equation (2) transforms ATS picture coordinate (LINE-ELEMENT) to ATS satellite coordinates:

$$x' = k \cdot \cos((PCLN-LINE) \cdot (RDLN) \cdot \cos((PCEL-ELEMENT) \cdot RDSAM)$$

$$y' = k \cdot \cos((PCLN-LINE) \cdot (RDLN) \cdot \sin((PCEL-ELEMENT) \cdot RDSAM) \quad (2)$$

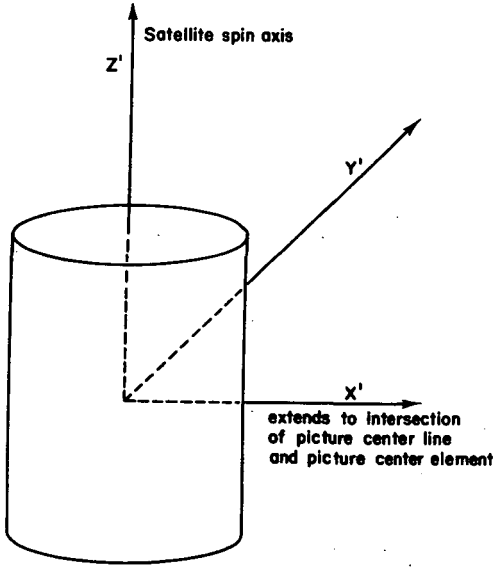

Figure 5. Right-handed Orthonormal Coordinate System Centered at Satellite

where

PCLN = Line at which the spin scan camera is perpendicular to the spin axis

PCEL = 4096

RDLN = Radians per line

RDSAM = Radians per element

The value k is solved for by extending the ray determined by the above vector so that its intersection with the surface of the earth can be determined by Equations (3) and (4). BROT and BVEC are time-dependent.

$$\begin{matrix} x'' \\ y'' \\ z'' \end{matrix} = \text{BROT} \cdot \begin{matrix} x' \\ y' \\ z' \end{matrix} \tag{3}$$

$$\frac{(\text{BVEC}(1) - k \cdot x'')^2 + (\text{BVEC}(2) - k \cdot y'')^2}{a^2} + \frac{(\text{BVEC}(3) - k \cdot z'')^2}{b^2} = 1 \tag{4}$$

where

a = Equatorial radius of the earth

b = Polar radius of the earth

BROT = Rotation matrix

BVEC = Displacement matrix

The transformation from satellite coordinates to earth coordinates is determined by Equation (5).

$$\begin{matrix} x \\ y \\ z \end{matrix} = \text{BROT} \cdot \begin{matrix} x' \\ y' \\ z' \end{matrix} + \text{BVEC} \tag{5}$$

The transformation from earth-centered coordinates to latitude and longitude is done in the customary manner.

The above transformation can be inverted to obtain a transformation from latitude and longitude to ATS picture coordinates. The only difficulty involved in this procedure is that the time parameter is not known for the rotation matrix BROT and displacement vector BVEC. The picture start time is used as a first approximation. The line number then determines the time parameter for the transformation. Achieving an earth frame of reference is crucial to the success of any cloud motion measurements from digital satellite pictures. The ATS navigation system enables one to find the pictel corresponding to the same latitude and longitude on two successive ATS pictures. Hence, a reference point can be set up anywhere on the surface of the earth within satellite view for measuring cloud motion. This technique is used in the WINDCO system. First the cloud motions are measured between two ATS pictures and then the apparent earth motion is subtracted from the cloud motion vectors.

The stability of the earth with respect to the computed frame of reference is used as a criterion of navigation results. If the ATS navigation system assigns the same latitude and longitude to a landmark that is recognized on a series of ATS pictures, this is strong evidence that an accurate earth frame of reference has been achieved. Table 1 presents the ATS-III navigation results of July 26, 27 and 28, 1969. An M following the time column signifies that the four values were measured. A C signifies that the four values were computed. Table 1 shows that on all three days the stability of the landmark used in the navigation is better than satellite resolution. The latitude stability measures how well the satellite's attitude and orbit were approximated. The longitude stability is apparent since only one landmark was used to compute the earth's centering information. In the table, the picture start times are in Greenwich Mean Time. Northern latitudes are positive and west longitudes are negative. Note that the largest discrepancy is .006 degrees latitude on July 26 and again on July 28. This represents a systematic bias of .36 nautical miles in the displacement measurement.

Because of shoal waters and noise contamination of the information in the ATS signal, precise identification of a landmark is not always possible. However, if the misidentified feature can always be recognized on a series of pictures, the navigation system is still able to fit smoothly the motion of the feature, thereby removing the apparent motion of the earth. Misidentification introduces slight rotational errors between consecutive ATS pictures; however, this error is smaller than camera resolution over the time period that we measure cloud motions.

Table 1

ATS Navigation Results from July 26-28, 1969

	Picture	Time		Line	Element	Latitude	Longitude
July 26	12	21	M	639	5930	22.270	-16.630
			C	639.0	5930	22.270	-16.630
Cabo Barbas	12	47	M	639	5926	22.270	-16.630
			C	639.0	5926	22.269	-16.630
on the west	13	13	M	640	5923	22.270	-16.630
			C	639.7	5923	22.267	-16.631
African coast	13	38	M	641	5917	22.270	-16.630
			C	641.0	5917	22.271	-16.630
	14	04	M	643	5913	22.270	-16.630
			C	643.1	5913	22.273	-16.629
	14	30	M	646	5910	22.270	-16.630
			C	645.8	5910	22.273	-16.629
	14	55	M	649	5906	22.270	-16.630
			C	649.0	5906	22.270	-16.630
	16	01	M	660	5893	22.270	-16.630
			C	659.9	5893	22.267	-16.631
July 27	13	15	M	640	5985	22.270	-16.630
			C	640.0	5985	22.271	-16.630
Cabo Barbas	14	06	M	644	5981	22.270	-16.630
			C	644.0	5981	22.270	-16.630
on the west	14	55	M	649	5976	22.270	-16.630
			C	649.0	5976	22.268	-16.630
African coast	15	33	M	653	5973	22.270	-16.630
			C	653.3	5973	22.268	-16.631
	16	24	M	660	5964	22.270	-16.630
			C	660.1	5964	22.272	-16.629
July 28	13	36	M	643	5997	22.270	-16.630
			C	643.1	5997	22.273	-16.629
Cabo Barbas	14	32	M	649	5985	22.270	-16.630
			C	649.4	5985	22.267	-16.631
on the west	14	58	M	653	5982	22.270	-16.630
			C	653.0	5982	22.268	-16.631
African coast	15	24	M	657	5984	22.270	-16.630
			C	656.8	5984	22.271	-16.630
	16	28	M	667	5978	22.270	-16.630
			C	667.0	5978	22.271	-16.630

Continued on next page

Table 1 (continued)

	Picture	Time		Line	Element	Latitude	Longitude
	13	36	M	888	2807	10.920	-65.310
			C	887.9	2807	10.918	-65.310
Isla La Tortuga	14	32	M	894	2801	10.920	-65.310
			C	894.3	2801	10.922	-65.310
off the north-	14	58	M	898	2800	10.920	-65.310
			C	898.0	2800	10.922	-65.310
ern coast of	15	24	M	902	2799	10.920	-65.310
			C	902.2	2799	10.919	-65.310
South America	16	28	M	914	2791	10.920	-65.310
			C	914.0	2791	10.919	-65.310

5. Data Input

The WINDCO system handles a large volume of data. Data segments from two ATS digital pictures need to be available in a random access mode to the computer program. An ATS picture is composed of 2400 line scans, each of which is sampled 8192 times. The radiance resolution of an ATS picture is eight bits. Thus, one ATS digital picture is composed of 19,660,800 pictels, or 157,286,400 bits! This is obviously more data than can fit into even a large computer memory, hence peripheral storage devices are required. The WINDCO system was developed on a UNIVAC-1108 computer which is quite adequate for such large volume data handling. By using a synchronous 1/0 activity, picture segments are transferred to FASTRAND drum from digital tape, independent of the main program activity. Because of the time-sharing environment of the 1108 system, 1/0 processing time is minimized.

A complete digital archive of ATS pictures is not feasible. One digital ATS-I picture fills a complete tape reel; a digital ATS-III color picture fills four tape reels. The ATS spin scan camera is capable of generating approximately fifty pictures a day with picture intervals of less than thirty minutes. To date, many thousands of pictures have been generated by the ATS-I and ATS-III satellites. The need for an alternative approach to digital archiving is apparent. For this reason, ATS pictures are recorded on seven-track analog tape reels. An eighteen-inch reel can hold approximately seventy single-channel ATS pictures. This reduction of raw data by a factor of seventy makes data archiving more compact, but this format is not compatible with the Univac 1108 1/0 units.

An analog-to-digital transcriber is utilized to prepare ATS pictures for computer processing and landmark detection. The design and performance of this system is described in the ATS Analog-to-Digital Transcriber System Operator's Manual, an in-house document from the Space Science and Engineering Center. One unresolved problem has come up during this process. The synchronizing timing information for picture scans is encoded into the scan signals before analog recording. As a result, because of nominal tape head noise introduced during the analog recording process, the scan lines are not perfectly decoded during the digitizing activity. A random jitter of ± 6 pictels is generated in the alignment of digital scans. This jitter degrades the u component measurement of the cloud motion vectors. The quantitative effect of the jitter problem is discussed later.

6. Cloud Tracer Selection

Appropriate cloud tracers are selected by a human operator. The operator makes approximate coordinate measurements of the cloud tracers' location (coarse tuning) providing starting positions for the computer which makes accurate displacement measurements through the use of cross-correlation (fine tuning).

This selection technique controls the amount and quality of the data processed by the WINDCO program. The quality of the results is greatly improved by selecting small tracers. Image grids, fit to the size of the cloud tracers, and centered at the selected coordinates, identify the area of data that must be processed. In this fashion excess data is discarded before the cloud motions are measured. Presently, hard copy photographs are used to detect cloud tracers. A digitizing table is used to measure the rough coordinates. This is not a sophisticated system and has limited real-time application.

A more sophisticated operational system is presently being developed by an engineering team at the Space Science and Engineering Center. This system incorporates a low-resolution analog memory unit interfaced to a TV monitor. Raw data will be viewed on the TV display and with a light pen the operator will indicate the position of clouds he is tracking. The data adjacent to this position are then transmitted to the computer through a high-resolution analog-to-digital converter. Figure 6 illustrates the authors' conception of this system.

The operator locates small clouds which move with the wind. In the tropics independent convective cells are generally expected to move with the mean wind within the layer that they reside. If, however, the cloud has assembled to any great depth, shear stresses in the atmosphere will inhibit the motion of the cloud in terms of the mean flow around it. In

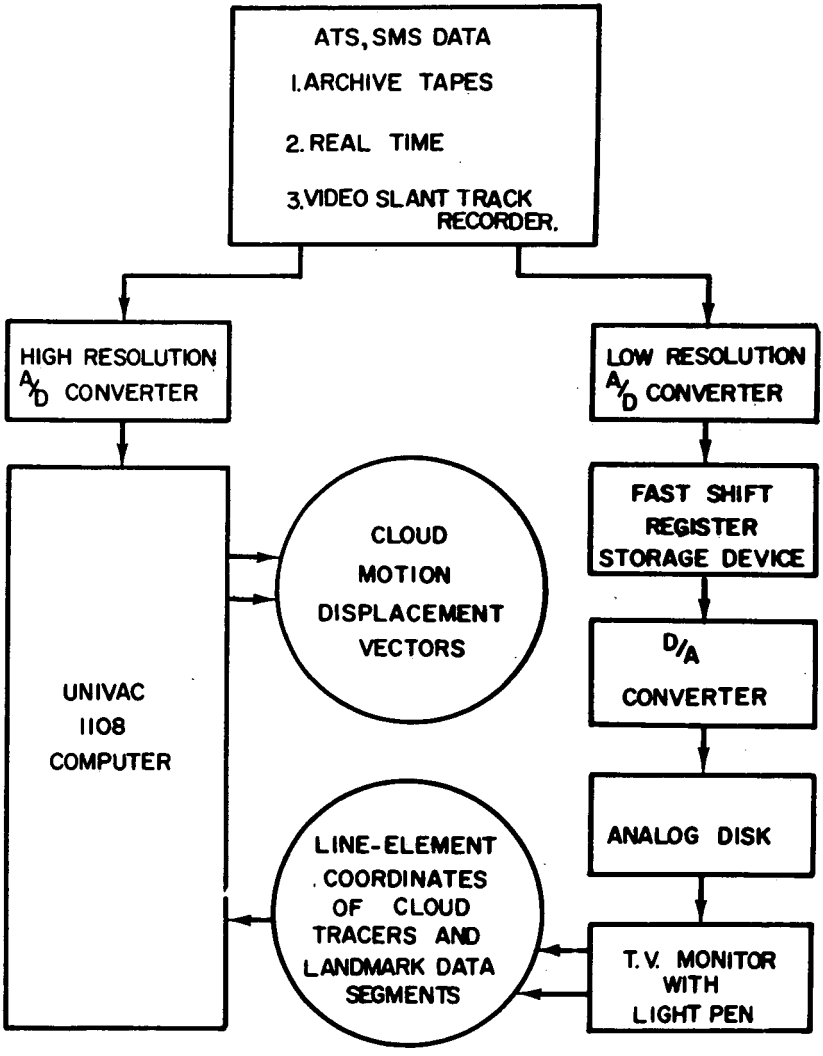

Figure 6. Block Diagram of Operational WINDCO System

general, the best tracers in the 950-750 millibar layer are the convective clouds in their early stages of development. As they continue to develop to the towering cumulus congestus or cumulonimbus stages, their momentum state will differ more and more from the encompassing atmosphere, preventing them from moving freely with the mean flow. Since cirrus clouds may be the only upper air motion indicators available, their utilization as wind tracers must be considered. Tests with uniform cirrus shields have been inconclusive. However, if the cirrus residue is isolated from the full cloud cover, its motion can be measured. But the time interval for tracking these clouds must be as short as possible because of the apparent dissipation of their distinctive features.

7. Cross-Correlation

Two-dimensional cross-correlation analysis is utilized in tracking clouds from picture to picture. A 32-row by 32-column image grid containing a cloud tracer from the first picture is cross-correlated at all the possible lag positions with a 64-row by 64-column image grid from the second picture, thereby generating a 33 by 33 cross-correlation matrix which includes as its center the zero lag position. The cross-correlation array is then searched for its maximum value. The lag coordinate position of the maximum value is expected to measure the line-element shift undergone by the cloud tracer and its surrounding field over the time interval between the two pictures. To increase resolution, a bi-directional quadratic is fit to a neighborhood of the maximum coefficient. This interpolation allows measurements of displacement at nonintegral lag positions.

The displacement with respect to the earth is found by the following procedure. The shift information is transformed to latitude-longitude coordinate end points by using ATS navigation parameters. The u and v components are computed by Equations (6) and (7):

$$u = \frac{(XLON1 - XLON2) \cdot \cos(XLAT) \cdot 60.0}{DELT} \tag{6}$$

$$v = \frac{(XLAT1 - XLAT2) \cdot 60.0}{DELT} \tag{7}$$

where

u = u component

v = v component

XLAT = Average latitude of endpoints

XLAT1 = Latitude of initial endpoint

XLAT2 = Latitude of final endpoint

XLON1 = Longitude of initial endpoint

XLON2 = Longitude of final endpoint

DELT = Time interval between picture pair

Because the direct method of computing cross-correlation coefficients is time-consuming and consequently expensive, Fast Fourier Transform Radix8 method has been implemented. On the Univac 1108, a 33 by 33 cross-correlation matrix is computed in less than two seconds. This method is 4.5 times faster than one using the regular Fast Fourier Transform. We will first describe the computational results desired for a cross-correlation matrix before identifying the techniques used to reduce computational time. Let $(A_{i,j})$, $i = 1,\ldots,32$; $j = 1,\ldots,32$; be an ATS data matrix at time T_1 with the i index corresponding to picture lines and the j index corresponding to picture elements. In the cloud motion studies, groups of three elements were averaged to produce approximately two-nautical mile-square data resolution. Let $(B_{i,j})$, $i = 1,\ldots,64$; $j = 1,\ldots,64$; be a data matrix at time T_2. B is four times larger than A. A cross-correlation coefficient is computed for each lag position that the A matrix can assume with respect to the B matrix. Let row-column lag $(1,1)$ correspond to A fitting into the upper left-hand corner of B. The row and column lag coordinate is increased as A is moved to the right and down as shown in Figure 7. Equations (8)-(11) are needed to define $\bar{b}_{p,q}$, $b\sigma_{p,q}$, $\bar{a}$, and $a\sigma$.

$$\bar{b}_{p,q} = \frac{1}{1024} \sum_{j=1}^{32} \sum_{i=1}^{32} B_{i+p-1,\, j+q-1} \tag{8}$$

$$B\sigma_{p,q} = \sum_{j=1}^{32} \sum_{i=1}^{32} (B_{i+p-1,\, j+q-1} - \bar{b}_{p,q})^2 \tag{9}$$

$$\bar{a} = \frac{1}{1024} \sum_{j=1}^{32} \sum_{i=1}^{32} A_{i,j} \tag{10}$$

$$a\sigma = \sum_{j=1}^{32} \sum_{i=1}^{32} (A_{i,j} - \bar{a})^2 \tag{11}$$

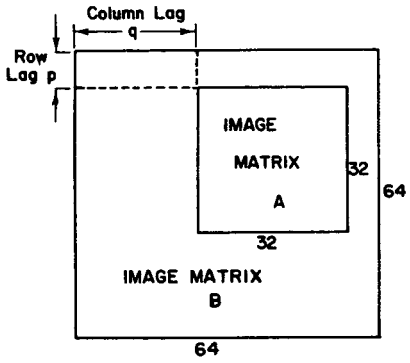

Figure 7. Image Matrix A Superimposed on Image Matrix B

The cross-correlation coefficient $c_{p,q}$ at row lag p and column lag q is defined by Equations (12) and (13).

$$\sqrt{c_{p,q}} = \sum_{j=1}^{32} \sum_{i=1}^{32} \frac{(B_{i+p-1,\,j+q-1} - \bar{b}_{p,q}) \cdot (A_{i,j} - \bar{a})}{\sqrt{b\sigma_{p,q} \cdot a\sigma}} \tag{12}$$

$$c_{p,q} = \sqrt{c_{p,q}} \cdot \left|\sqrt{c_{p,q}}\right| \tag{13}$$

The necessity of taking product sums over entries of the matrices A and B at different lag positions is apparent from Equation (12). These calculations can be completed with fewer operations by first applying a finite Fourier transform to both matrices and then to the product of the two transforms. The computational process becomes more efficient if the matrix representing a finite Fourier transform is factored properly. One technique—the Fast Fourier Transform—reduces the number of complex multiplications and additions proportionate to $N \cdot Ln_2 N$ where N is the number of points to be transformed. Recently, a more efficient method of factoring a finite Fourier transform has been found which decreases the number of complex multiplications performed by a factor of three. This is the Fast Fourier Transform Radix8 method. Also, since the initial data matrices are composed of real numbers, the number of finite Fourier transforms used can be cut in half by proper handling. This gain in computational time reduces the time and cost of obtaining results. Appendix A gives the Fortran subroutines used for the cross-correlation procedure.

In computing $\bar{b}_{p,q}$ and $b\sigma_{p,q}$, sums are taken of elements of multiple sub-arrays contained in the large array B. This summing process can be represented as a matrix product with a vector consisting of elements of B. This matrix has been factored so as to reduce the number of necessary additions by a factor of 172 for the array size used. This efficiency allows the cross-correlation coefficients to be normalized between plus one and minus one with negligible additional cost. A plus one represents a perfect match while a minus one represents a negative image of a perfect match.

Isometric plots of various typical cross-correlation matrices demonstrates the utility of using cross-correlation for measuring cloud displacements. In 70% of the cases (illustrated in Figure 8), the maximum correlation peaks are sharp and easily detected. In approximately 20% of the cases the peaks are not as sharply defined, such as in Figure 9. However, the peaks are detectable. There are cases where the occurrence of the maximum value probably does not represent actual cloud displacement. The surfaces in Figure 10 belong to this category. They occur 7% of the time. Most of these cases could be eliminated with better cloud tracer selection criteria. A fourth type of surface that has multiple nodes is seen in 3% of the cases. Figure 11 shows examples of these. Leese has shown, with a simulated multi-layer cloud experiment, that a relationship between multiple nodes and different cloud motions can be expected. However, our results show that all local maxima do not represent cloud motions. Surface 5 of Figure 11 shows three peaks which come from the spurious alignment of a row of homogeneous clouds. Surface 4 of the same figure contains a ridge which comes from a large cloud bank edge which dominates the correlation computation. Consequently, no attempt was made to translate these multiple nodes into several cloud motions. Furthermore, multi-layer motion could be detected by controlling the selection of cloud tracers with the aid of a dynamic display system.

If the maximum correlation coefficient is detected at the edge of a cross-correlation matrix, a default flag is registered. In this case the absolute maximum of the surface fails to be a local maximum. This is indication that either the selected cloud feature has dissipated or that the feature was inappropriate for the cross-correlation technique.

The possibilities for data input control with spatial and frequency filtering have been maintained as options. Controlling the size of the initial data array to fit the size of the feature of the cloud tracer should eliminate many of the cases with spurious results. Filtering the frequency transform of the data will smooth the cross-correlation surface and may, thereby, allow improved interpolation results.

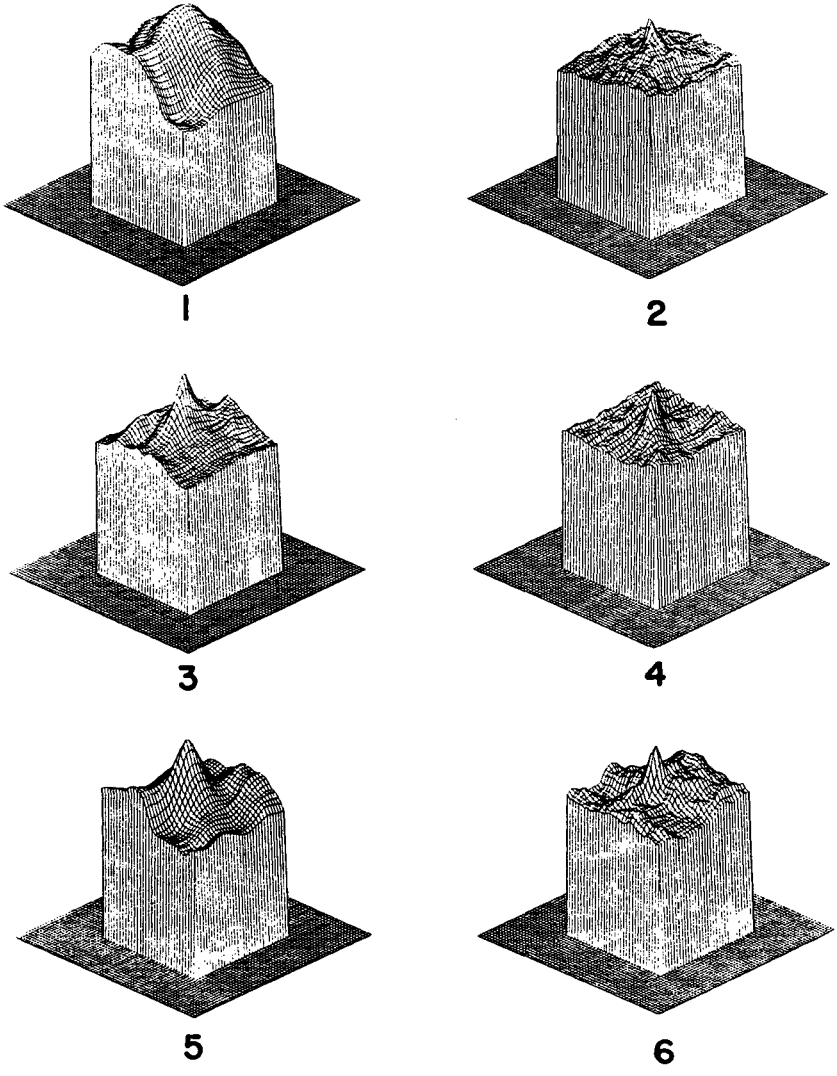

Figure 8. Cross-correlation Matrix Surfaces Containing a Well-defined Peak

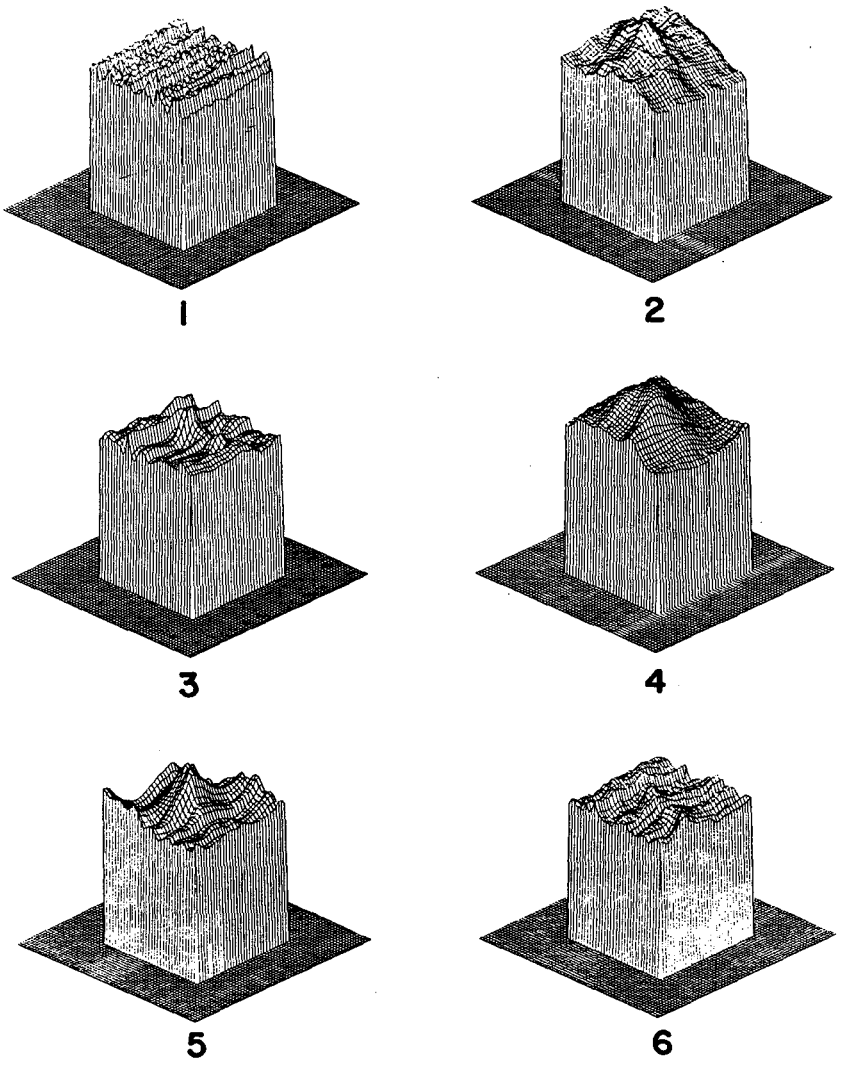

Figure 9. Cross-correlation Matrix Surfaces Containing a Poorly-defined Peak

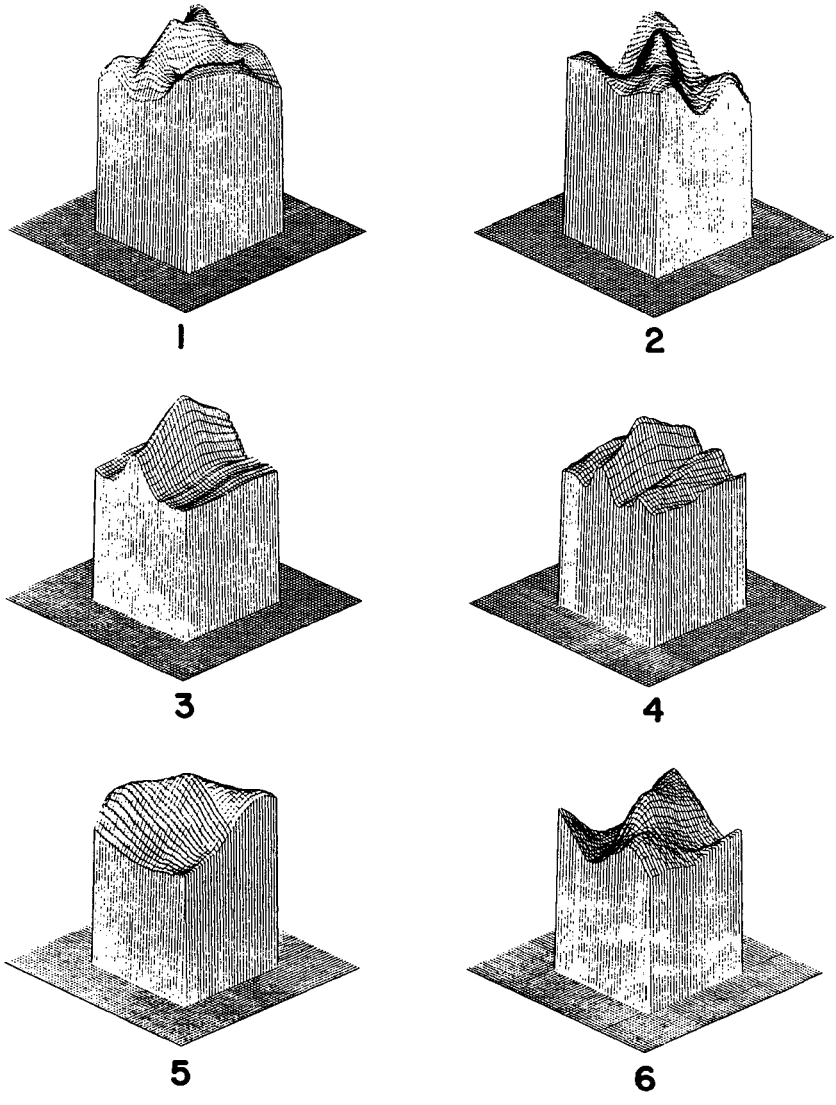

Figure 10. Cross-correlation Matrix Surfaces Containing No Well-defined Singular Peak

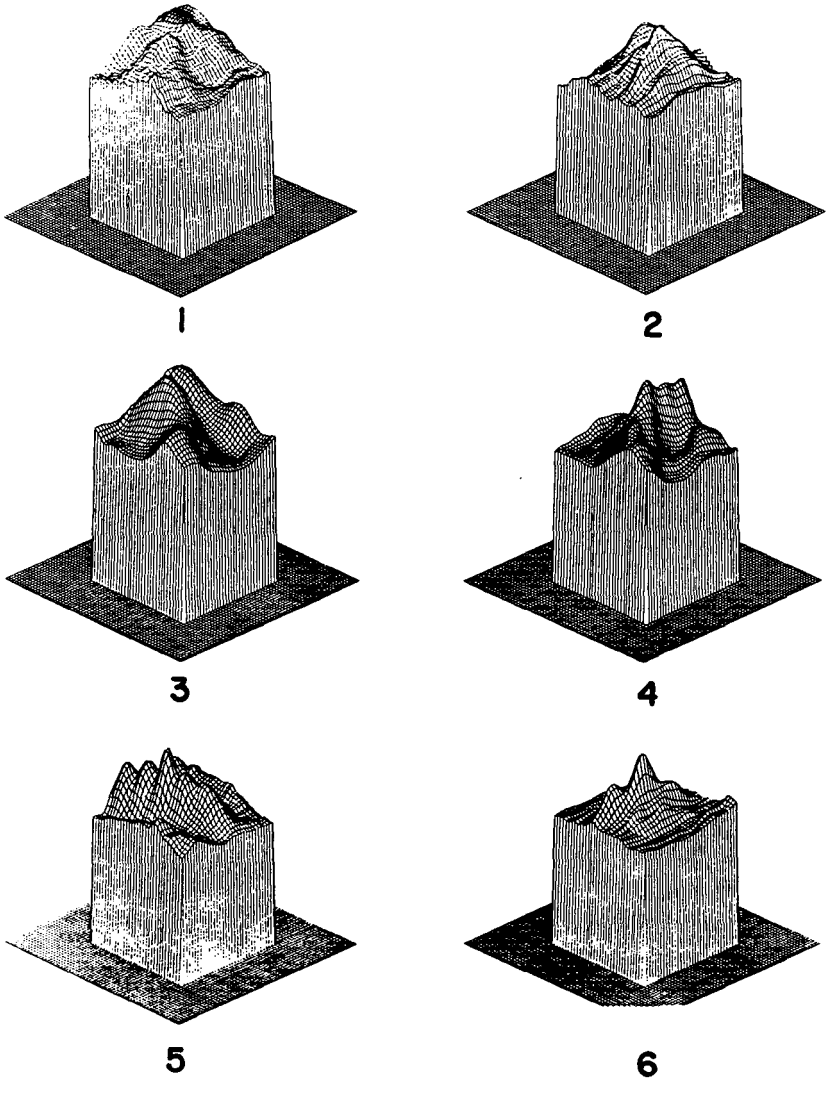

Figure 11. Cross-correlation Matrix Surfaces Containing Multiple Peaks

8. Cloud Motions from July 26-28

The case study used these three days for two reasons. First, cloud motion vectors generated by Hasler's film loop technique were available over the Gulf of Mexico, the Caribbean Sea, and the western Atlantic. Secondly, there was an abundance of ship observations and radiosonde data, collected during the Barbados Oceanographic Meteorological Experiment (BOMEX). This information provided a qualitative comparison for the WINDCO results. On each of the three days, three half-scan ATS pictures were selected. Cloud tracers coordinates were selected from these pictures, over the middle and western Atlantic, north of the equator. The criteria for tracer selection were that the tracer must be visible in all three pictures and that its occurrence could not be near the limb of the earth. The later constraint is necessary because the alignment distortion blows up close to the limb. However, cases were selected which are not to be considered good cloud tracers. Coordinates were taken along frontal systems and storm spirals. Cumulus congestus cells that occurred within developing cloud clusters were selected. Areas containing cirrus cover were also sampled. This variability in cloud type was desired for future studies relating tracking reliability to cloud type. Results classified according to cloud type have not been included.

Cloud motion vectors were generated over each of the three possible time intervals, for each day. These intervals are designated as follows:

1. $T_1 - T_2$

2. $T_2 - T_3$

3. $T_1 - T_3$

where T_1, T_2 and T_3 correspond to the three start times of the ATS pictures. The time interval sizes are listed in Table 2. Measuring the same cloud tracer over three intervals gives a measure for checking the internal consistency of the results. In Figures 12-14 three cloud motion fields are plotted along with cloud motions generated by the film loop technique for that day. Parts A of the figures show the results for the two smaller intervals $T_1 - T_2$ and $T_2 - T_3$. Parts B show the results of the $T_1 - T_3$ interval and the movie loop results which were measured over a three-hour time period. The cloud motion vectors are plotted as wind arrows using the international convection. Approximately 200 vectors were generated from July 26 data° for both July 27 and 28, there were approximately 150 vectors. In general, the agreement between the WINDCO results and the film loop results is good, as can be seen in the figures. A number of the flagrantly bad cases are the defaulted cases previously mentioned.

$T_1 - T_2$

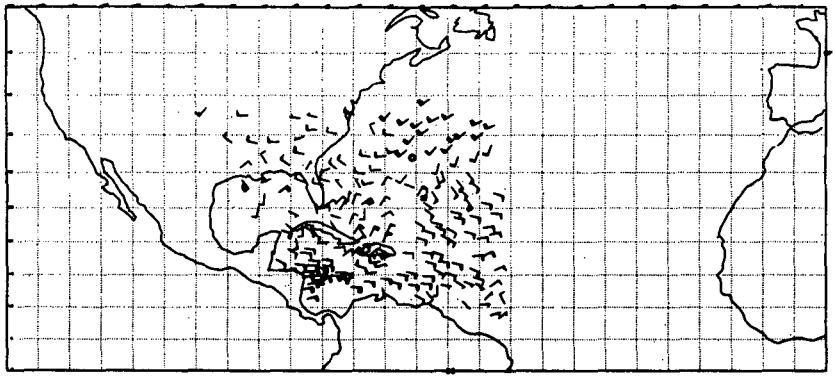

DAY 207 T_1 =13.633 T_2=14.067

$T_2 - T_3$

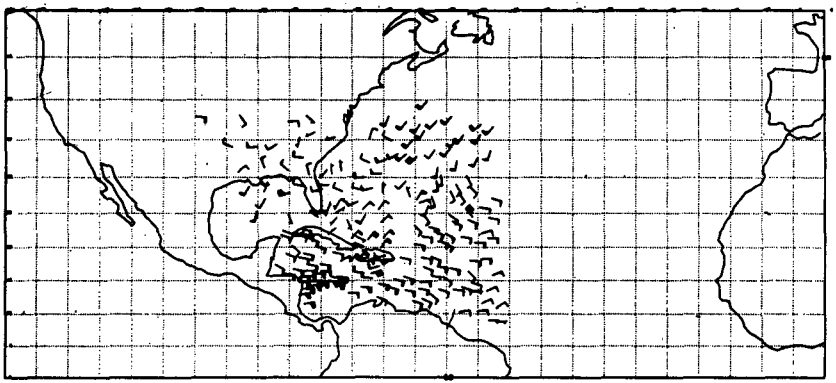

DAY 207 T_2=14.067 T_3 =14.500

Figure 12 (Part A). Cloud Motion Fields from July 26

$T_1 - T_3$

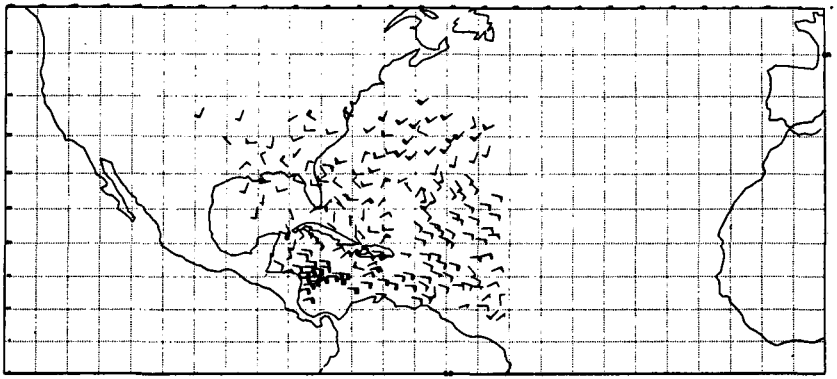

MOVIE LOOP TECHNIQUE (HASLER)

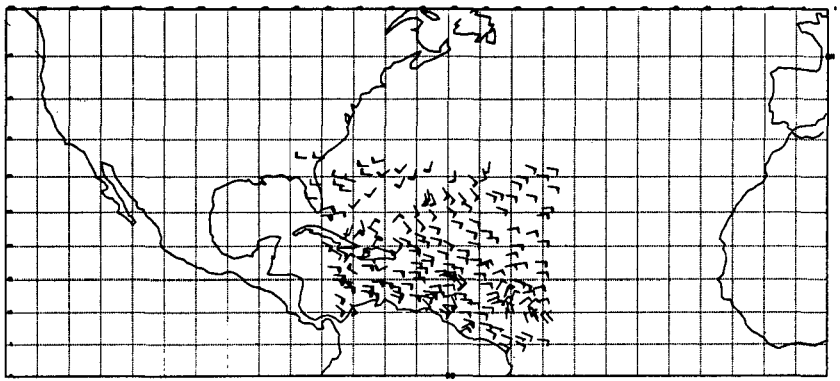

Figure 12 (Part B). Cloud Motion Fields from July 26

$T_1 - T_2$

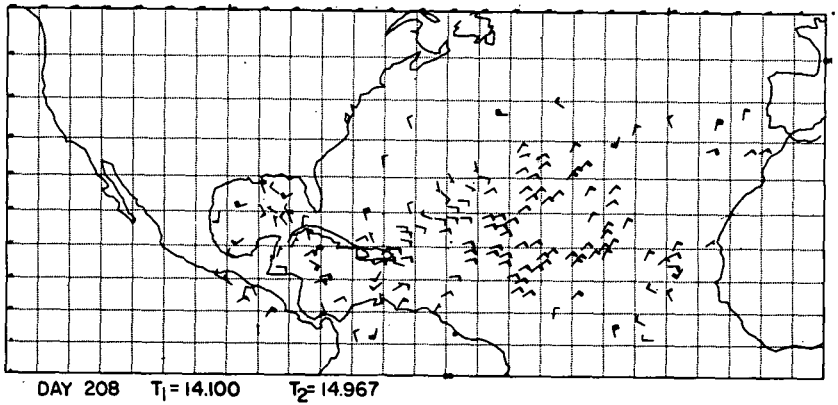

$T_2 - T_3$

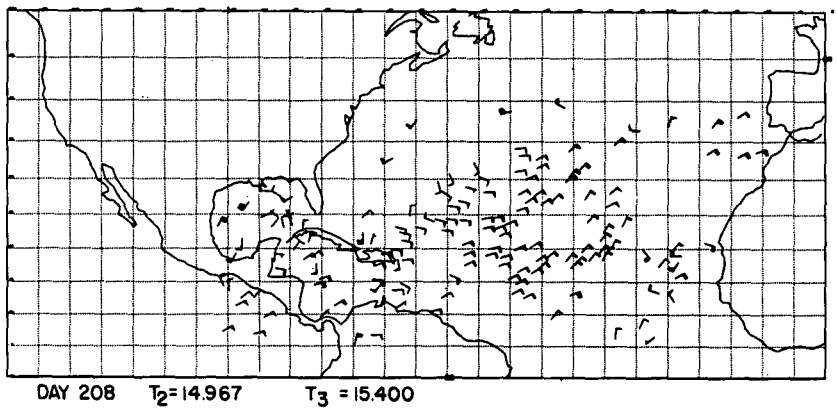

Figure 13 (Part A). Cloud Motion Fields from July 27

$T_1 - T_3$

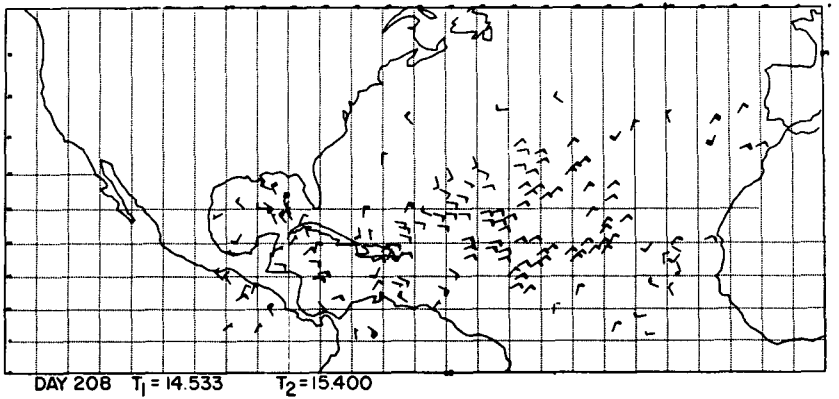

MOVIE LOOP TECHNIQUE (HASLER)

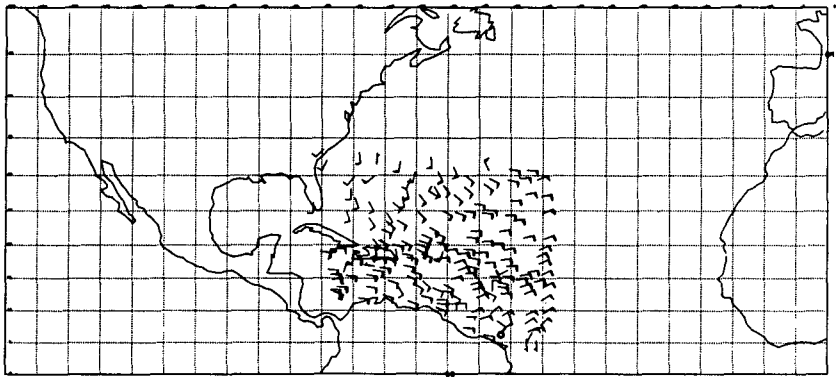

Figure 13 (Part B). Cloud Motion Fields from July 27

$T_1 - T_2$

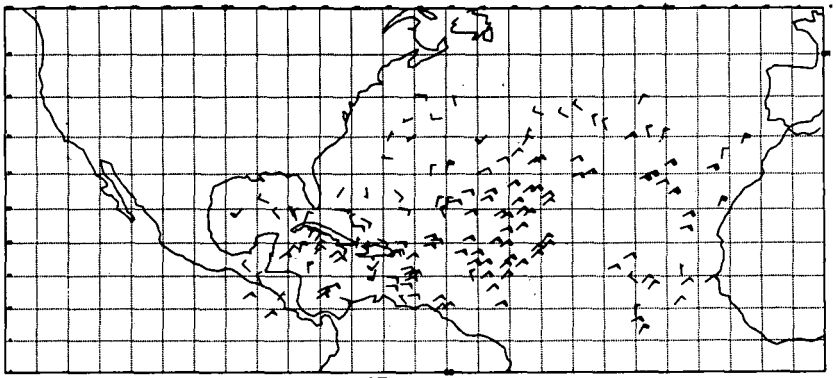

DAY 209 $T_1 = 14.533$ $T_2 = 14.967$

$T_2 - T_3$

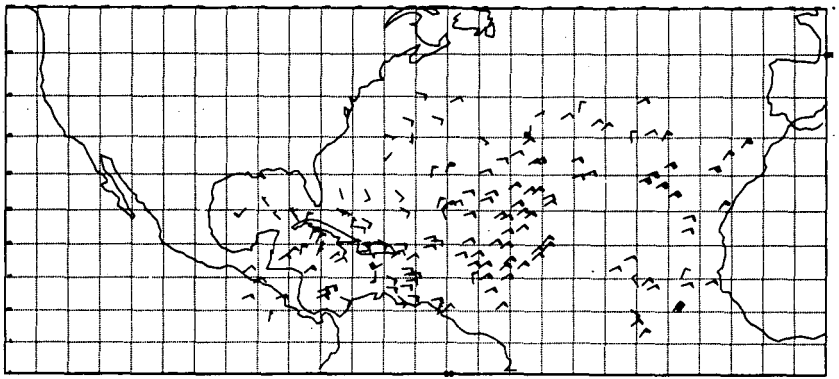

DAY 209 $T_2 = 14.967$ $T_3 = 15.400$

Figure 14 (Part A). Cloud Motion Fields from July 28

$T_1 - T_3$

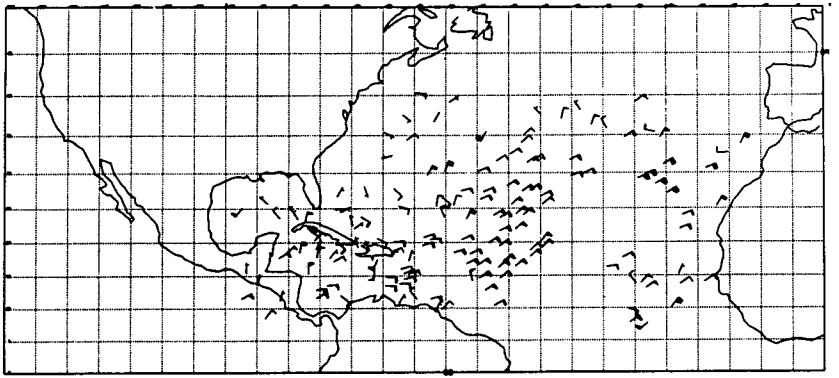

DAY 209 T_1 = 14.533 T_3 = 15.400

MOVIE LOOP TECHNIQUE (HASLER)

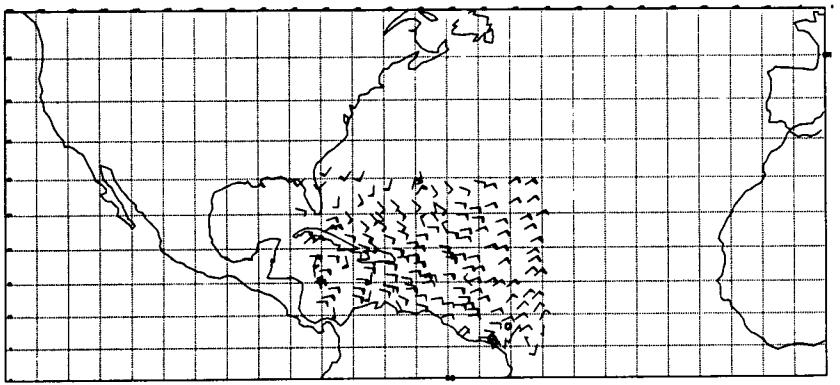

Figure 14 (Part B). Cloud Motion Fields from July 28

Table 2

Picture Pair Time Intervals for July 26-28. Time is given in minutes.

Day	$T_1 - T_2$	$T_2 - T_3$	$T_1 - T_3$
July 26	26	26	52
July 27	49	38	87
July 28	26	26	52

To illustrate the reproducibility of the cloud motions over different time intervals, frequency distributions of the differences between the u and v components (Δu and Δv) over each pairing of cloud motion fields were prepared. The distributions can be seen in Figures 15-20. The top graph in each figure represents the $T_1 - T_2$ and $T_2 - T_3$ comparison; the middle graph represents the $T_1 - T_2$ and $T_1 - T_3$ comparison; the bottom graph represents the $T_2 - T_3$ and $T_1 - T_3$ comparison. The largest deviations are in the comparison of the $T_1 - T_2$ results to the $T_2 - T_3$ results. This is expected since they are the two shortest intervals and therefore any systematic bias or measurement error would be maximized. The measurement error in the system is estimated by the position of the vertical line that goes through the peak of the distribution. The abscissa scale is in knots. The winds are assumed to be constant during the time period under observation. This assumption should be valid in the tropics because of the stability of the trade winds. The spread of the Δu component distribution is larger than the spread of the Δv component distribution. We believe that this is due to the jitter in the scan line synchronizing. This contamination could be removed by improving the digitizing scheme.

It is also apparent that there is a definite oscillation, especially in the u component differences, on July 26 and 28. The $T_1 - T_2$ and $T_2 - T_3$ time intervals on both of these days are twenty-six minutes. On July 27, the two intervals were somewhat larger and the oscillation is not as apparent. This phenomenon is probably due to the ATS camera resolution. Also, the quadratic interpolation scheme used in determining the surface position of the maximum correlation coefficient may not be overcoming the tendency to select integer displacement measures.

The comparisons of the u and v components for all the interval pairings are listed in Table 3. The differences are consistent. The largest v

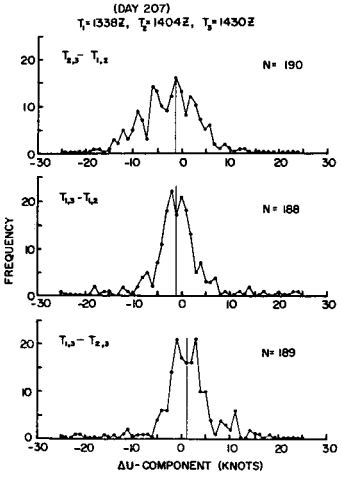

Figure 15. u-component comparisons for 26 July 1969 (Day 207)
T_1 = 1338Z
T_2 = 1404Z
T_3 = 1430Z

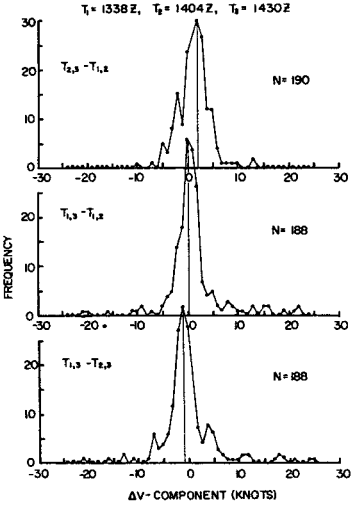

Figure 16. v-component comparisons for 26 July 1969 (Day 207)
T_1 = 1338Z
T_2 = 1404Z
T_3 = 1430Z

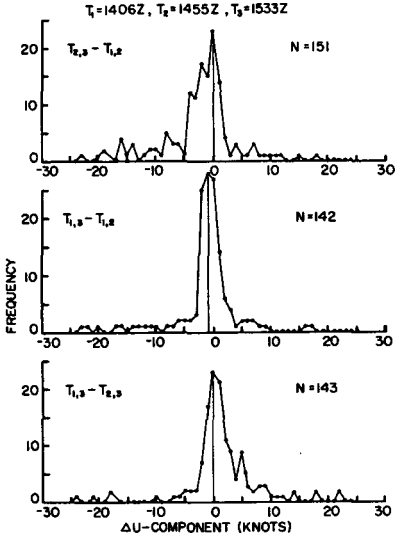

Figure 17. u-component comparison for 27 July 1969 (Day 208)
T_1 = 1406Z
T_2 = 1455Z
T_3 = 1533Z

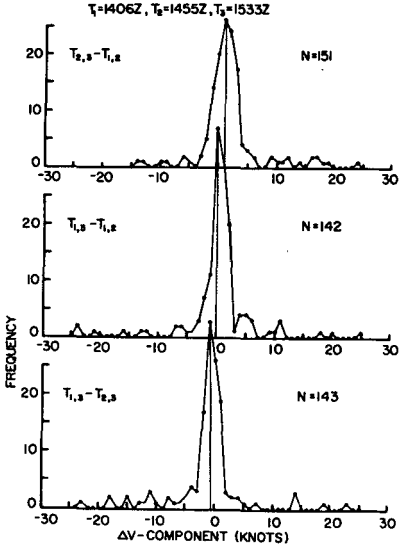

Figure 18. v-component comparisons for 27 July 1969 (Day 208)
T_1 = 1406Z
T_2 = 1455Z
T_3 = 1533Z

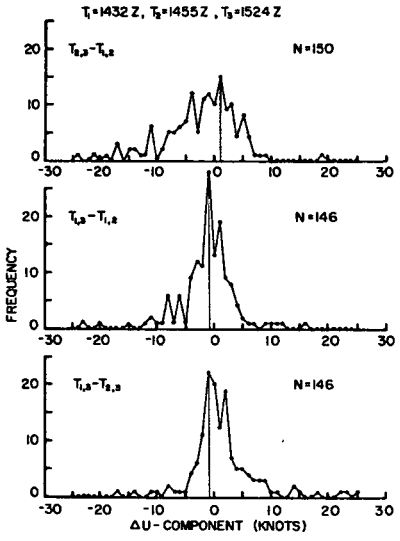

Figure 19. u-component comparisons for 28 July 1969 (Day 209)
T_1 = 1432Z
T_2 = 1455Z
T_3 = 1524Z

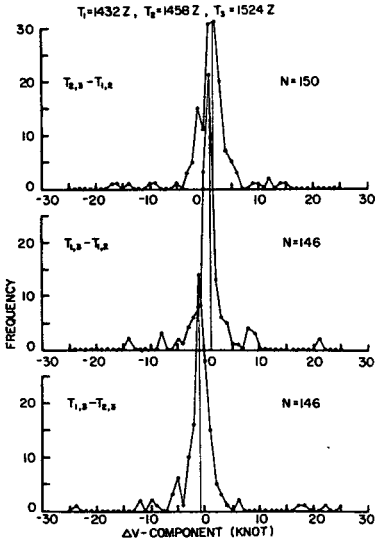

Figure 20. v-component comparisons for 28 July 1969 (Day 209)
T_1 = 1432Z
T_2 = 1458Z
T_3 = 1524Z

Table 3

Comparison of the Differences of the u and v Component for Each Time Interval Pairing. Differences are given in knots.

Day		T_1-T_2 to T_2-T_3	T_1-T_2 to T_1-T_3	T_2-T_3 to T_1-T_3
July 26	u	1	1	1
	v	2	0	1
July 27	u	0	1	0
	v	1	0	.5
July 28	u	1	1	1
	v	2	1.5	1

component discrepancy is two knots, while the largest u component discrepancy is one knot. All of the wind vectors computed, excepting those given a default flag, were used in the comparison. The inclusion of poor cloud tracers accounts for part of the scatter in the distributions.

To determine the effect of changing the navigation landmarks or the navigation period, some of the cloud motion fields were recomputed with different navigation parameters. On July 28, two different tests were made. In the first test the cloud motion using Cabo Barbas as the navigation landmark was compared to the results using Isla La Tortuga as the navigation landmark. There should be some differences in the Δu component because different line centering information is used. However, changing landmarks should not affect the attitude determination. Therefore the Δv component should not be affected. In Figure 21, the two distributions on the right of the figure illustrate the comparison between the two cases of cloud motion fields. The Δu component distribution peaks at 2.5 knots, while the Δv component peaks at 0 knots.

In the second test a navigation was recomputed using Isla La Tortuga; however, the navigation period was shortened to two hours from the recommended three-hour period. The cloud motion field of this case was then compared to the original results which had used the same landmark. The Δu component should not be affected since the equivalent line centering information is used. However, the Δv component should be degraded because the attitude cannot be determined as accurately over the shorter time period. The two middle distributions in Figure 21 illustrate the results.

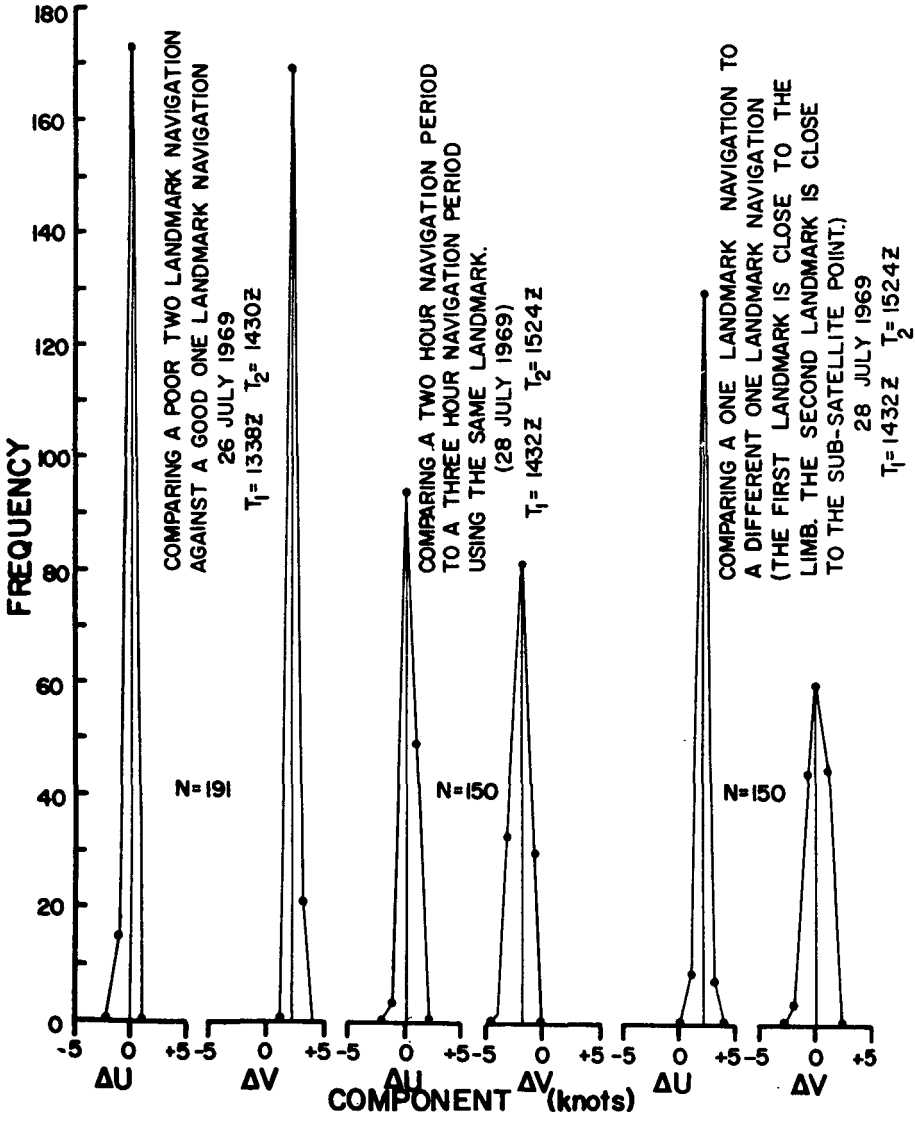

Figure 21. Comparison of Displacement Results as a Function of Changes in the Navigation Inputs

The Δu component peaks at 0 knots while the Δv component peaks at two knots. Finally, to demonstrate that even a poor navigation can produce useful information, a navigation was recomputed on July 26 using two poorly measured landmarks. One point on the west African coast was selected which was partially overcast and difficult to detect. Another point on the eastern tip of Cuba was selected which was difficult to separate from the surrounding ocean due to the low sun angle. In the comparison with the original cloud motion results, the Δu component differed by 0 knots and the Δv component differed by two knots. The two distributions on the left of Figure 21 illustrate these comparisons.

The cloud motion measurements on the three days were reproducible to two knots in the v component and one knot in the u component. This represents a motion vector error of 2.3 knots. The error estimate in the system is based on these figures. More cases are needed to pinpoint exactly the sources of the errors; however, the navigation tests indicate that the significant errors originate during the navigation process. This residual navigation error is the cause of the mean differences in the u and v components. Since it can be identified from examination of the residual distributions, it is possible to remove the systematic effects from all the vectors. Furthermore, the bad data measurements can be rejected if they do not meet reproducibility criterion. Therefore, the error in the system can be further reduced by using a quality control scheme, based on multi-interval measures. A better orbit calculation will further improve the v component accuracy, and the alleviation of the line jitter problem will further improve the u component accuracy. Much of the random error of this system will be reduced by better cloud tracer selection.

9. Time and Cost

On the Univac 1108 computer, a single cloud motion vector is computed in approximately two seconds of CPU time. The time necessary for the cross-correlation calculation is 1.5 sec. The corresponding real time duration is three times greater due to a time-sharing environment. The present cost of a single cloud motion vector including all I/O charges is approximately \$0.20. At this rate, 500 cloud motion vectors can be computed for \$100.00.

The computer charges for an ATS navigation run are insignificant. Navigation parameters for a day of pictures can be generated for less than \$1.00.

10. Conclusions

The view of the weather in motion provided by ATS pictures has been a source of stimulation and motivation for meteorologists. However,

researchers have not fully exploited the high precision of the ATS data. By taking advantage of this precision, the WINDCO system is measuring cloud motions accurate to 2.5 knots (1.2 m/sec). The success of this operation should encourage considering the use of geosynchronous satellite data for the real time operational computation of winds.

References

ATS-I SSEC Data Reducation And Analysis, Applications Technology Satellite Program, 1967: Prepared for NASA by Westinghouse Electric Corporation Defense And Space Center, Baltimore, Maryland.

ATS-III SSEC Data Reduction And Analysis Final Report, Applications Technology Satellite Program, 1967: Prepared for NASA by Westinghouse Electric Corporation Defense And Space Center, Baltimore, Maryland.

BOMEX Bulletin No. 3, 1969: Prepared by the BOMEX Project Office, An Interagency Scientific Planning Group, Rockville, Maryland.

Brigham, E. O., and F. R. Morrow, 1967: The Fast Fourier Transform. IEEE Spectrums, 63-70.

DeDecker, R., 1969: ATS Analog to Digital Transcriber System, Operators Manual. In-house document, Space Science and Engineering Center, Madison, Wisconsin.

Doolittle, R. C., C. L. Bristor, and L. Lauritson, 1970: Mapping of Geostationary Satellite Pictures, An Operational Experiment. ESSA Tech. Memo NESC TM-20, 28 pp.

Fujita, T. T., K. Watanabe, and T. Izawa, 1969: Formation and Structure of Equatorial Anticyclones Caused by Large-Scale Cross-Equatorial Flows Determined by ATS-I Photographs. J. Appl. Meteor., 8, 649-667.

Hasler, A. F., 1971: "Tropical Cloud Clusters Analyzed Using Techniques for Obtaining Wind, Divergence, and Vorticity Fields from Geostationary Satellite Pictures," Ph. D. dissertation, University of Wisconsin.

Hubert, L. F., 1969: "Accuracy of Wind Estimates from Geostationary Satellites," In-house memo, Meteorological Satellite Laboratory, Suitland, Maryland.

Investigation of an ATS Attitude Anomaly, 1970: Prepared for NASA by the Westinghouse Electric Corporation System Support Division, Baltimore, Maryland.

Leese, J. A., C. S. Novak, and B. B. Clark, 1970: An Automated Technique for Obtaining Cloud Motion from Geosynchronous Satellite Data using Cross-Correlation, J. Appl. Meteor., 10, 118-132.

Nimbus IV User's Guide, 1970: Prepared by the NIMBUS Project, Goddard Space Flight Center, NASA.

Phillips, D. R., and E. A. Smith, 1971: Program Document NAVIGATION, In-house document, Space Science and Engineering Center, Madison, Wisconsin.

Shenk, W. E., and E. R. Kreins, 1970: A Comparison Between Observed Winds and Cloud Motions Derived from Satellite Infrared Measurements, J. Appl. Meteor., 9, 702-710.

Singleton, R. C., 1969: An Algorithm for Computing the Mixed Radix Fast Fourier Transform. IEEE Trans. Audio Electroacoustics, AU-17, No. 2, 93-102.

Smith, E. A., and D. R. Phillips, 1971: Program Document WINDCO, In-house document, Space Science and Engineering Center, Madison, Wisconsin.

Suomi, V. E., and D. W. Martin, 1971: On the Requirements of a Boundary Layer Instrumentation System for the GARP Tropical Experiment, Final Report on the Boundary Layer Instrumentation Study, Space Science and Engineering Center, Madison, Wisconsin.

Suomi, V. E., and R. J. Parent, 1967: ATS Spin-Scan Cloud Cloud Camera and Pre-launch Calibration Procedures, in Studies in Atmospheric Energetics Based on Aerospace Probings, Annual Report on WBG-27, Amendment No. 1, 1966, pp. 1-40. Department of Meteorology, University of Wisconsin, Madison.

Suomi, V. E., and R. J. Parent, 1968: A Color View of Planet Earth, Bulletin A. M. S., 49, 74-75.

APPENDIX A

FORTRAN LISTING OF TWO DIMENSIONAL CROSS CORRELATION ANALYSIS SUBROUTINES

```
'FOR,SI ATS*LIB.AUTOCO
C
C      *****
C      AUTOCO COMPUTES AND NORMALIZES THE CORRELATION COEFFICIENTS WITH NECESSAI
C      CALLS TO RCRCSQ AND FFT.
C      *****
C
       SUBROUTINE AUTOCO(X,Y,M,N,M1,N1)
       DIMENSION X(M),Y(M1)
       COMMON/WORK/ZF(12288)
       DIMENSION ZZF(128)
       COMPLEX ZZ(64)
       EQUIVALENCE (ZZ(1),ZZE(1))
       COMPLEX Z(256)
       EQUIVALENCE (ZF(1),Z(1))
       M11=M-M1+1
       N11=N-N1+1
       MN11=M11*N11
       M1N1M=M1*N1-M1
       JJ=-M
       XYFCT=M1*N1
       YFACT=0.0
       DO 1 J=0,M1N1M,M1
       JJ=JJ+M
       DO 1 I=1,M1
       KY=I+J
       KX=I+JJ
       KZ1=KX+KX
       KZ=KZ1-1
       T=Y(KY)
       YFACT=YFACT+T**2
       ZE(KZ)=X(KX)
     1 ZE(KZ1)=T
       IF(M1.EQ.M)GO TO 3
       M1P1=M1+1
       MNMN=M*N-M
       DO 2J=0,MNMN,M
       DO 2 I=M1P1,M
       KX=I+J
       KZ1=KX+KX
       KZ=KZ1-1
       ZE(KZ)=X(KX)
     2 ZE(KZ1)=0.0
     3 CONTINUE
       IF(N1.EQ.N) GO TO 5
       N1P1=N1+1
```

```
      JB=(N1P1-1)*M
      JE=MNMN
      DO 4 J=JB,JE,M
      DO 4 I=1,M1
      KX=I+J
      KZ1=KX+KX
      KZ=KZ1-1
      ZE(KZ)=X(KX)
    4 ZE(KZ1)=0.0
    5 CONTINUE
      IOPT=1
      MNLM=M*N-M
      MNLM1=MNLM+1
      DO 40 I=1,MNLM1,M
   40 CALL FFT(Z(I),Z(I),M,IOPT)
      DO 46 J=1,M
      II=0
      DO 45 I=0,MNLM,M
      K=J+I
      II=II+1
   45 ZZ(II)=Z(K)
      CALL FFT(ZZ,ZZ,N,IOPT)
      II=0
      DO 46 I=0,MNLM,M
      K=I+J
      II=II+1
   46 Z(K)=ZZ(II)
      MD2=M/2
      ND2=N/2
      KK=2*(M*(N+1)+2)
      M2=M+M
      JE=(ND2-1)*M2
      DO 6 I=4,M2,2
      DO 6 J=M2,JE,M2
      K1=I+J
      K=K1-1
      KR1=KK-K1
      KR=KR1-1
      T=ZE(K)
      T1=ZE(K1)
      TR=ZE(KR)
      TR1=ZE(KR1)
      XR=T+TR
      YR=T1+TR1
      YI=TR-T
      XI=T1-TR1
      ZE(K)=XR*YR+XI*YI
      ZE(K1)=YR*XI-XR*YI
      ZE(KR)=ZE(K)
    6 ZE(KR1)=-ZE(K1)
      ND2P1=ND2+1
      DO 7 J=1,ND2P1,ND2
      DO 7 I=2,MD2
      K1=(I+(J-1)*M)*2
      K=K1-1
      KR1=((N+2-I)+(J-1)*M)*2
```

```
      KR=KR1-1
      T=ZE(K)
      T1=ZE(K1)
      TR=ZE(KR)
      TR1=ZE(KR1)
      XR=T+TR
      YR=T1+TR1
      YI=TR-T
      XI=T1-TR1
      ZE(K)=XR*YR+XI*YI
      ZE(K1)=YR*XI-XR*YI
      ZE(KR)=ZE(K)
    7 ZE(KR1)=-ZE(K1)
      DO 8 J=2,ND2
      K1=(1+(J-1)*M)*2
      K=K1-1
      KR1=(1+(N+1-J)*M)*2
      KR=KR1-1
      T=ZE(K)
      T1=ZE(K1)
      TR=ZE(KR)
      TR1=ZE(KR1)
      XR=T+TR
      YR=T1+TR1
      YI=TR-T
      XI=T1-TR1
      ZE(K)=XR*YR+XI*YI
      ZE(K1)=YR*XI-XR*YI
      ZE(KR)=ZE(K)
    8 ZE(KR1)=-ZE(K1)
      YMCT=ZE(2)/XYFCT
      ZE(1)=ZE(1)*ZE(2)*4.0
      ZE(2)=0.0
      K1=(1+ND2*M)*2
      K=K1-1
      ZE(K)=ZE(K)*ZE(K1)*4.0
      ZE(K1)=0.0
      K1=(MD2+1)*2
      K=K1-1
      ZE(K)=ZE(K)*ZE(K1)*4.0
      ZE(K1)=0.0
      K1=(MD2+1+ND2*M)*2
      K=K1-1
      ZE(K)=ZE(K)*ZE(K1)*4.0
      ZE(K1)=0.0
      MN=M*N
      XMN=MN*4
      XFACT=1./XMN
      DO 10 I=1,MN
   10 Z(I)=Z(I)*XFACT
      IOPT=2
      JE=(ND2P1-1)*M+1
      DO 25 J=1,JE,M
   25 CALL FFT(Z(J),Z(J),M,IOPT)
      M2=M*2
```

```
      JE=M2*(ND2-1)
      MN2=M*N*2
      DO 26 J=M2,JE,M2
      DO 26 I=2,M2,2
      K1=I+J
      K=K1-1
      KR1=MN2+I-J
      KR=KR1-1
      ZE(KR)=ZE(K)
   26 ZE(KR1)=-ZE(K1)
      JB=2
      JE=M11*2
      IE=MN2-2*M
      DO 30 J=JB,JE,4
      II=0
      DO 27 I=0,IE,M2
      II=II+2
      K1=I+J
      K=K1-1
      KR1=K1+2
      KR=KR1-1
      KZZ1=II
      KZZ=II-1
      ZZE(KZZ)=ZE(K)-ZE(KR1)
   27 ZZE(KZZ1)=ZE(K1)+ZE(KR)
      CALL FFT(ZZ,ZZ,M,IOPT)
      II=0
      DO 28 I=0,IE,M2
      II=II+2
      K1=I+J
      K=K1-1
      KR1=K1+2
      KR=KR1-1
      KZZ1=II
      KZZ=II-1
      ZE(K)=ZZE(KZZ)
   28 ZE(KR)=ZZE(KZZ1)
   30 CONTINUE
      JB=0
      JE=(N11-1)*M2
      IE=2*M11
      IE1=IE-1
      JJ=-M11
      DO 12 J=JB,JE,M2
      JJ=JJ+M11
      II=0
      DO 12 I=1,IE1,2
      II=II+1
      K1=I+J
      K=II+JJ
   12 ZE(K)=ZE(K1)
      MN112=MN11+MN11
      MN111=MN11+1
      MN1121=MN111+MN11
      CALL RCRCSQ(ZE(MN1121),ZE(MN111),X,M11,N11,M,N)
      JE=(N11-1)*M11
```

```
      DO 20 J=0,JE,M11
      DO 20 I=1,M11
      K1=I+J
      K2=K1+MN11
      K3=K2+MN11
      TEMP=ZE(K3)
      TP=ZE(K1)-YMCT*TEMP
      TPS=TP*TP
      IF(TP.LT.0.0)TPS=-TPS
   20 ZE(K1)=TPS/((ZE(K2)-TEMP**2/XYFCT)*(YFACT-XYFCT*YMCT**2))
      RETURN
      END
*FOR,SI ATS*LIB.FFT
C
C     *****
C     FFT COMPUTES A FINITE FOURIER TRANSFORM BY THE FFT RADIX8 METHOD
C     *****
C
      SUBROUTINE FFT(X1,Y1,N,IOPT)
      COMPLEX X1(N),Y1(N)
      COMPLEX       Y(64),Z(64),EXP(8,8)
      COMPLEX T
      DIMENSION          YR(2,64),ZR(2,64),TEX(2,8,8)
      EQUIVALENCE                (Y(1),YR(1,1)),(Z(1),ZR(1,1))
      EQUIVALENCE (EXP(1,1),TEX(1,1,1))
      DATA SQTW,JCSSN/.70710678,1/
      JENT=1
  700 CONTINUE
      IF(JCSSN.EQ.2)GO TO 5
      JCSSN=2
      TWPFC=3.14159265/32.
      DO 4 I=1,8
      DO 4 J=1,8
      XK=(I-1)*(J-1)
      TEX(1,I,J)=COS(XK*TWPFC)
    4 TEX(2,I,J)=SIN(XK*TWPFC)
    5 CONTINUE
      LCT=-2
      K=N
      IF(JENT.EQ.2)GO TO 6
      DO 7 I=1,N
    7 Y(I)=X1(I)
    6 K=K/2
      LCT=LCT+1
      IF(K.GT.1) GOTO 6
      IF(IOPT.EQ.1)GO TO 9
      IF(JENT.EQ.2)GO TO 9
      DO 8 I=1,N
    8 YR(2,I)=-YR(2,I)
    9 CONTINUE
      N1=N/8
      JLOOP=1
      GO TO 500
  200 DO 202 I=2,8
      II=I*2
```

```
      Y(II)=Y(II)*EXP(5,I)
  202 CONTINUE
      DO 203 I=1,15,2
      I1=I+1
      Z(I)=Y(I)+Y(I1)
  203 Z(I1)=Y(I)-Y(I1)
      KI=0
      DO 205 I=1,2
      KJ=0
      DO 204 J=1,8
      K=KI+J
      K1=I+KJ
      Y(K)=Z(K1)
  204 KJ=KJ+2
  205 KI=KI+8
      GO TO 600
  500 DO 550 I=1,N1
      K1=I
      K2=K1+N1
      K3=K2+N1
      K4=K3+N1
      K5=K4+N1
      K6=K5+N1
      K7=K6+N1
      K8=K7+N1
      IHD=1
      GO TO 551
  510 TR=YR(1,K7)
      YR(1,K7)=-YR(2,K7)
      YR(2,K7)=TR
      TR=YR(1,K8)
      YR(1,K8)=-YR(2,K8)
      YR(2,K8)=TR
      T=Y(K1)
      Y(K1)=T+Y(K3)
      Y(K3)=T-Y(K3)
      T=Y(K2)
      Y(K2)=T+Y(K4)
      Y(K4)=T-Y(K4)
      T=Y(K5)
      Y(K5)=T+Y(K7)
      Y(K7)=T-Y(K7)
      T=Y(K6)
      Y(K6)=T+Y(K8)
      Y(K8)=T-Y(K8)
      T=Y(K2)
      Y(K2)=Y(K5)
      Y(K5)=T
      T=Y(K4)
      Y(K4)=Y(K7)
      Y(K7)=T
      TR=YR(1,K6)*SQTW
      TRR=YR(2,K6)*SQTW
      YR(1,K6)=TR-TRR
      YR(2,K6)=TR+TRR
      TR=YR(1,K8)*SQTW
```

```
      TRR=-YR(2,K8)*SQTW
      YR(1,K8)=TRR-TR
      YR(2,K8)=TRR+TR
      TR=YR(1,K7)
      YR(1,K7)=-YR(2,K7)
      YR(2,K7)=TR
      IHD=2
      GO TO 551
  520 CONTINUE
      GO TO 550
  551 T=Y(K1)
      Y(K1)=T+Y(K5)
      Y(K5)=T-Y(K5)
      T=Y(K2)
      Y(K2)=T+Y(K6)
      Y(K6)=T-Y(K6)
      T=Y(K3)
      Y(K3)=T+Y(K7)
      Y(K7)=T-Y(K7)
      T=Y(K4)
      Y(K4)=T+Y(K8)
      Y(K8)=T-Y(K8)
      GO TO (510,520),IHD
  550 CONTINUE
      GO TO (600,200,300,400),LCT
  400 IF(JLOOP.EQ.2) GO TO 600
      JLOOP=2
      DO 401 I=1,64
  401 Z(I)=Y(I)
      KJ=0
      DO 402 J=1,8
      K1=1+KJ
      Y(K1)=Z(J)
      Y(J)=Z(K1)
  402 KJ=KJ+8
      KI=8
      DO 405 I=2,8
      KJ=8
      DO 404 J=2,8
      K1=I+KJ
      K2=J+KI
      IJ=I*J
      Y(K1)=Z(K2)*EXP(I,J)
  404 KJ=KJ+8
  405 KI=KI+8
      GO TO 500
  600 IF(IOPT.EQ.1) GO TO 611
      DO 610 I=1,N
  610 YR(2,I)=-YR(2,I)
  611 DO 612 I=1,N
  612 Y1(I)=Y(I)
      RETURN
  300 KI=4
      DO 302 I=2,8
      JJ=2
```

```
      DO 301 J=3,7,2
      K=KI+JJ
      Y(K)=Y(K)*EXP(I,J)
  301 JJ=JJ+1
  302 KI=KI+4
      DO 303 I=0,28,4
      K1=I+1
      K2=I+2
      K3=I+3
      K4=I+4
      Z(K1)=Y(K1)+Y(K3)
      Z(K3)=Y(K1)-Y(K3)
      Z(K2)=Y(K2)+Y(K4)
      Z(K4)=Y(K2)-Y(K4)
      TR=ZR(1,K4)
      ZR(1,K4)=-ZR(2,K4)
      ZR(2,K4)=TR
      T=Z(K1)
      Z(K1)=T+Z(K2)
      Z(K2)=T-Z(K2)
      T=Z(K3)
      Z(K3)=T+Z(K4)
      Z(K4)=T-Z(K4)
      T=Z(K2)
      Z(K2)=Z(K3)
  303 Z(K3)=T
      KI=0
      DO 311 I=1,4
      KJ=0
      DO 310 J=1,8
      K=KI+J
      K1=KJ+I
      Y(K)=Z(K1)
  310 KJ=KJ+4
  311 KI=KI+8
      GO TO 600
      ENTRY FFTR(R,Y1,N,MI,IOPT)
      DIMENSION R(MI)
      JENT=2
      DO 701 I=1,MI
  701 Y(I)=R(I)
      IF(MI.EQ.N) GO TO 700
      M1=MI+1
      DO 705 I=M1,N
  705 Y(I)=0.
      GO TO 700
      END
*FOR,SI ATS*LIB.RCRCSQ
C
C     *****
C     RCRCSQ COMPUTES NORMALIZING FACTORS FOR CROSS CORRELATION COEFFICIENTS
C     FROM THE T2 ARRAY
C     *****
C
      SUBROUTINE RCRCSQ(A,AA,B,J1,K1,M,N)
      DIMENSION A(J1),AA(J1),B(M)
```

```
      J11=J1-1
      K11=K1-1
      J=M-J11
      K=N-K11
      MNMN=M*N-M
      J1K1=J1*K1
      AA(J1K1)=0.0
      A(J1K1)=0.0
      IIB=(K1-1)*M
      IIE=MNMN
      DO 10 I=J1,M
      DO 5 II=IIB,IIE,M
      T=B(I+II)
      AA(J1K1)=AA(J1K1)+T**2
    5 A(J1K1)=A(J1K1)+T
   10 CONTINUE
      KM=K*M
      KKA=0
      KKE=(K11-1)*M
      DO 20 KK=0,KKE,M
      KKA=KKA+J1
      AA(KKA)=0.0
      A(KKA)=0.0
      KKK=KK+KM
      DO 15 I=J1,M
      T=B(I+KK)
      TT=B(I+KKK)
      AA(KKA)=AA(KKA)+(T-TT)*(T+TT)
   15 A(KKA)=A(KKA)+T-TT
   20 CONTINUE
      KA=J1*(K1-1)
      IB=M*(K1-1)
      DO 30 JJ=1,J11
      KKA=KA+JJ
      AA(KKA)=0.0
      A(KKA)=0.0
      JJJ=JJ+J
      DO 25 I=IB,MNMN,M
      T=B(JJ+I)
      TT=B(JJJ+I)
      AA(KKA)=AA(KKA)+(T-TT)*(T+TT)
   25 A(KKA)=A(KKA)+T-TT
   30 CONTINUE
      KE=(K11-1)*M
      KA=-J1
      DO 40 KK=0,KE,M
      KA=KA+J1
      KKK=KK+KM
      DO 35 JJ=1,J11
      JJJ=JJ+J
      KKA=KA+JJ
      T=B(JJ+KK)
      TT=B(JJJ+KKK)
      S=B(JJ+KKK)
      SS=B(JJJ+KK)
```

```
      AA(KKA)=(T-S)*(T+S)+(TT-SS)*(TT+SS)
   35 A(KKA)=T-S+TT-SS
   40 CONTINUE
      IKE=(K1-1)*J1
      DO 50 I=1,J11
      II=J1-I
      III=II+1
      DO 45 IK=0,IKE,J1
      KA=II+IK
      KKA=III+IK
      AA(KA)=AA(KA)+AA(KKA)
   45 A(KA)=A(KA)+A(KKA)
   50 CONTINUE
      IE=(K11-1)*J1
      DO 60 I=0,IE,J1
      II=IE-I
      IIA=II+J1
      DO 55 IJ=1,J1
      IJA=II+IJ
      AA(IJA)=AA(IJA)+AA(IIA+IJ)
   55 A(IJA)=A(IJA)+A(IIA+IJ)
   60 CONTINUE
      RETURN
      END
```

PRECEDING PAGE BLANK NOT FILMED

N72-27648

ATS-III Observed Cloud Brightness Field Related to Meso- to Subsynoptic-Scale Rainfall Pattern

D. N. Sikdar
Space Science and Engineering Center
The University of Wisconsin
Madison, Wisconsin

Abstract:

The geosynchronous satellite (ATS-III) time-lapse cloud brightness data have been analyzed with a view to correlating the time variations of cirrus shield area to rainfall rate in mid-latitude storm complexes. While inadequate rainfall sampling precludes point-to-point comparison, an excellent correlation is obtained with the time-change of radar echo areas in the cloud complex. Also presented are preliminary results on excellent correspondence between subsynoptic-scale cloud brightness anomaly patterns and the precipitation patterns in mid-latitude frontal zones.

1. Introduction

In the past decade there has been a growing interest in the use of meteorological satellite data to illucidate the pattern and processes of meteorological events for ultimate use in the long-range weather prediction model. Two University of Wisconsin experiments, spin-scan cameras on board the ATS-I and ATS-III satellites, have further stimulated efforts toward that goal. ATS (Applications Technology Satellite) time-lapse information has been used in the remote sensing of the dynamics and energetics of convective systems across a wide range of space and time scales (Sikdar and Suomi, 1971; Sikdar et al., 1970). Precipitation plays a significant role in storm energetics, through interaction with the airflow, yet on many occasions, because of its meso-scale nature, it escapes detection by the generally sparse network of raingauge stations. The use of satellites

in determining rainfall on a large scale therefore has obvious advantages over rainfall measurements made at points on the earth's surface.

In the recent past, a number of investigators have had some success in relating rainfall to data obtained from earth-orbiting satellites (Gerrish, 1970; Barrett, 1970; Rainbird, 1969). The primary objective of this study is to investigate the degree of correspondence between ATS-observed cloud features and characteristics on a meso-to-subsynoptic scale, and rainfall patterns. It is hypothesized that cloud particles in the cirrus canopy come from the penetrating towers and are distributed laterally by the upper wind field. This lateral spread is related to the divergence at the upper level (Sikdar, 1969) which in turn is related to the number of active cumulonimbi entering the shield and to their updraft velocity. Rainfall rate in a thunderstorm complex has a unique relation to the vertical motion field; therefore, it should have a good correspondence with the cirrus shield area change. This conjecture will be examined in the two meso-scale analyses presented in this paper.

The area and the data source for this case study are the same as those already presented by Sikdar et al. (1970) except for the subsynoptic-scale analysis. The presentation has been divided into two sections: 1) comparisons of the meso-scale rainfall pattern with cirrus shield area expansion atop deep convective systems; 2) the comparison of subsynoptic scale isohyet patterns with cloud brightness anomaly patterns.

2. ATS-Observed Convective Cloud Features and the Synoptic Situation in the Study Area

Figure 1a is a section of ATS-III cloud photographs at 234450 GMT on 19 April 1968. The most spectacular feature in this picture is the presence of cirrus outflow from convective towers in the dry environment marked by a clear space. A careful examination of the cloud complexes on high quality photographs reveals the presence of bright spots, probably resulting from towers penetrating the cirrus shield. The majority of those bright spots are aligned north-south along the 97° W meridian with a second such front along the 94° W meridian.

Figure 1b presents radar echoes located in the region of confluence between moist air streaming northward from the Gulf of Mexico and dry air moving from the west. The region of storm development was characterized by a high-level jet overrunning the axis of low-level moisture inflow, a typical synoptic situation favoring severe storm development (Fawbush, et al., 1951; Fawbush and Miller, 1953).

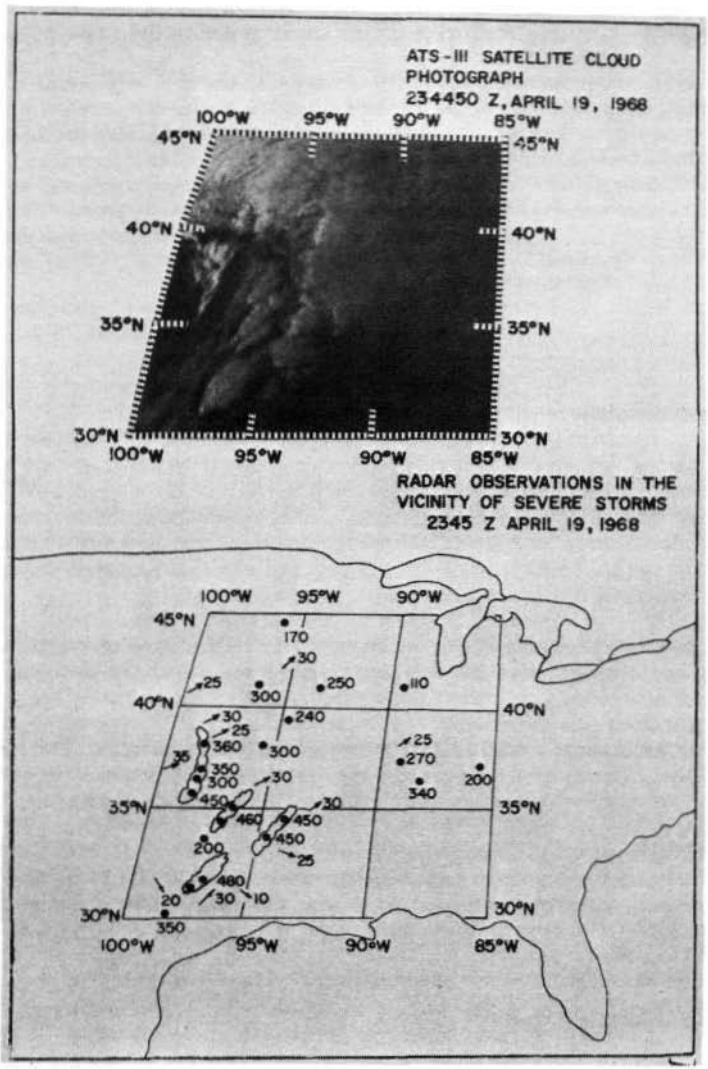

Figure 1(a) A section of ATS-III cloud photograph on 19 April 1968 showing the area of severe storm clouds at 234450 GMT.

(b) Radar echoes at 2345 GMT in the vicinity of severe storm on 19 April 1968.

Figure 2 is another example exhibiting similar meso-scale cloud characteristics on 23 April 1968. Thunderstorm activity became pronounced between 1900 and 2200 GMT and continued late into the night of 23 April.

In regard to subsynoptic-scale analysis, the reader is referred to cloud features east of longitude 94° W in Figure 1. A massive cirrus canopy emerging from a few scattered thunderstorm complexes extends north-south, with the cirrus outflow aligned SW to NE. In contrast to the meso-scale regime along the 97° W meridian, hardly any clear space around any individual thunderstorm complex can be identified in this region. This renders isolation of an individual complex difficult, although a relative cloud brightness gradient is noticed in the area 92° W - 94° W, 37° N - 40° N and 92° W - 95° W, 33° N - 37° N.

3. Data Processing

a. Meso-scale

The grid matrix of ATS-III cloud photos consists of 8196 digital elements and 2018 west-to-east scan lines. Within this grid we have information ranging from 0 to 255 digital counts. Meso-scale convective systems, while difficult to analyze on photographic images because of the photographic image's limited dynamic range, can easily be treated on brightness-normalized digital contour displays.

Satellite picture normalization involves two important steps: 1) navigation, and 2) brightness correction for sun-satellite-cloud geometry. Some complications in cloud brightness normalization are obvious, for the cloud brightness depends on many variables, including solar zenith angle, satellite viewing angle, the location of the cloud with respect to the sun and satellite, and camera response characteristics. The most important of them is the dependence on solar zenith angle, if one neglects attenuation and scattering by the atmosphere and assumes uniform performance of camera and recording systems. Although clouds in general are not Lambertian reflectors (Ruff et al., 1967), over limited geometries on the scale of resolution of the ATS camera thick cirrus shields emerging from cumulonimbus towers do tend to behave as such reflectors (Martin and Suomi, 1971). Accordingly, for deep convection regimes in satellite photos, our major interest in this paper, we have normalized cloud brightness for cosine angle change only.

Sample photographs of computer processed normalized iso-contour brightness displays of cloud systems in Figures 1 and 2 are shown in Figures 3 and 4. For correlating rainfall rate with the cirrus shield area-change, hourly precipitation charts were prepared for meso-systems having lifetimes much

longer than two hours. The raingauges that received rainfall from a particular cloud system were identified by superimposing a number of brightness contour displays, made twenty-eight minutes apart, on the precipitation charts and also by considering radar echo displacements during the hour. The areas of high cloud-brightness (approximately the uppermost 20% of the ATS total-brightness range in the grid) were assumed to be the core region and the primary sources of precipitation.

Hourly precipitation data were analyzed and, in addition, a number of radar images were enlarged for comparison with near-simultaneous ATS data. Radar selection was governed by the availability of good quality radar

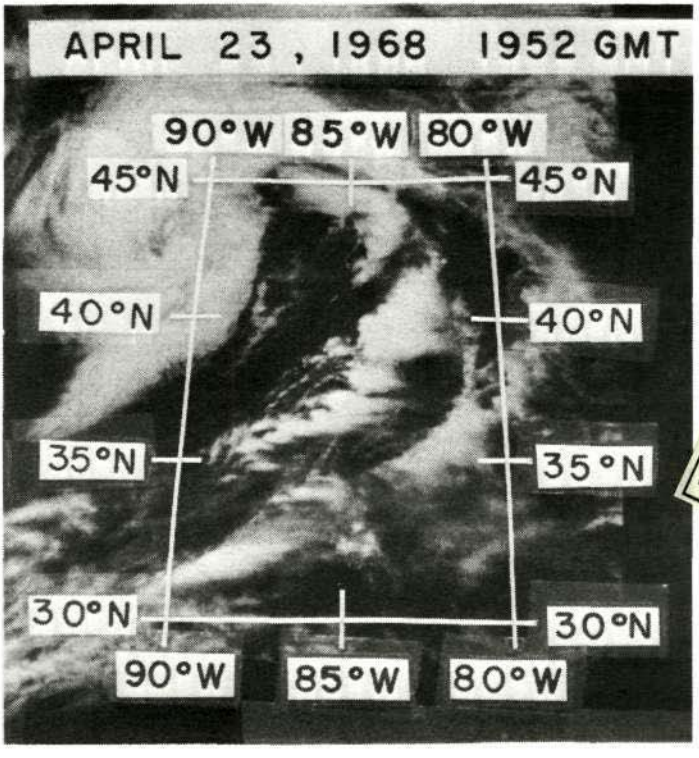

Reproduced from best available copy.

Figure 2. Same as in Figure 1a but for 23 April 1968 at 1830 GMT.

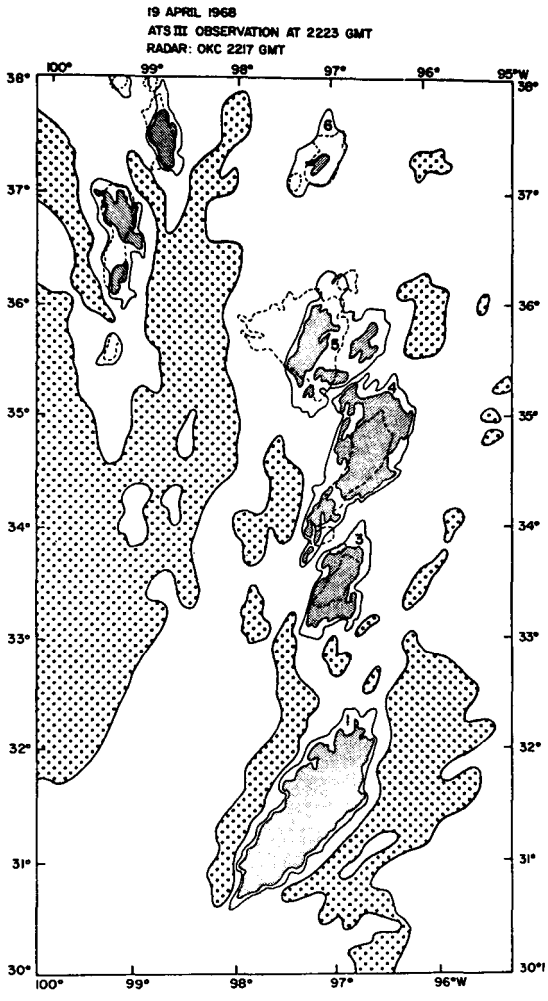

Figure 3(a). ATS-III observations at 2223 and 2251 GMT on which are superimposed radar observations from OKC at 2217 and 2251 GMT, respectively. Clear areas are stippled. Thin cloud outlines represent upper 40% of the total brightness range in the picture while the shaded areas are 30%. Radar echoes are outlined by broken lines.

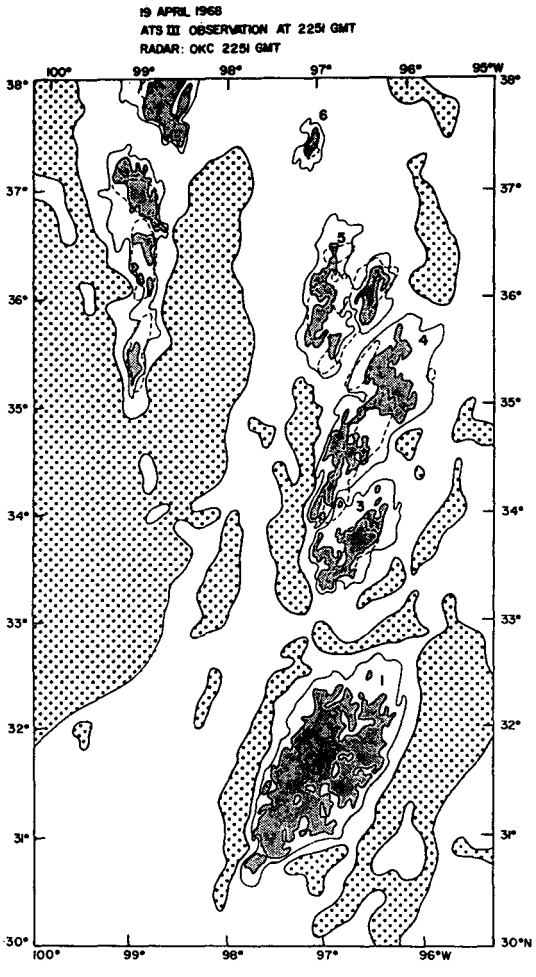

Figure 3(b). See Figure 3(a).

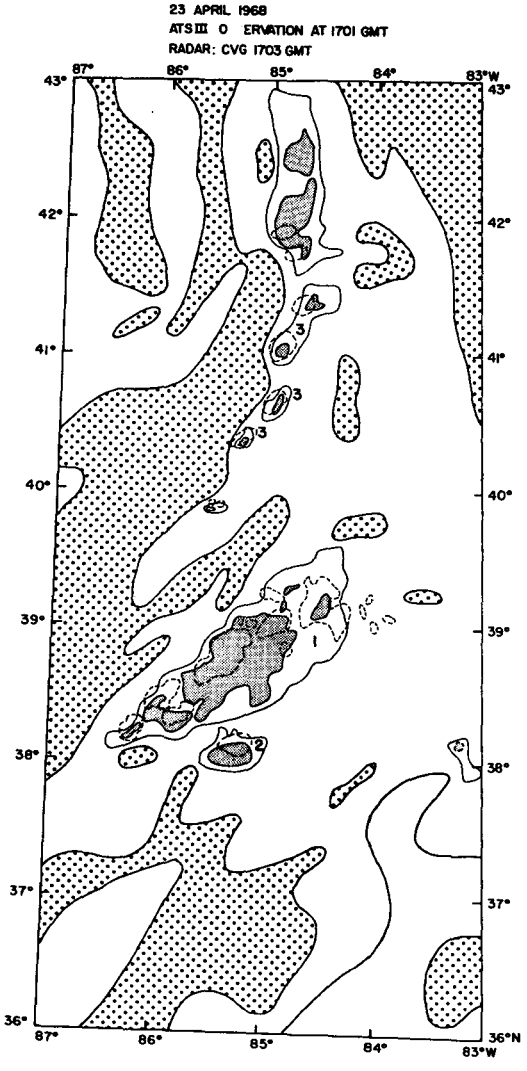

Figure 4(a). Same as in Figure 3 but for 23 April 1968. Thin cloud lines represent 36% while the shaded areas are 22%.

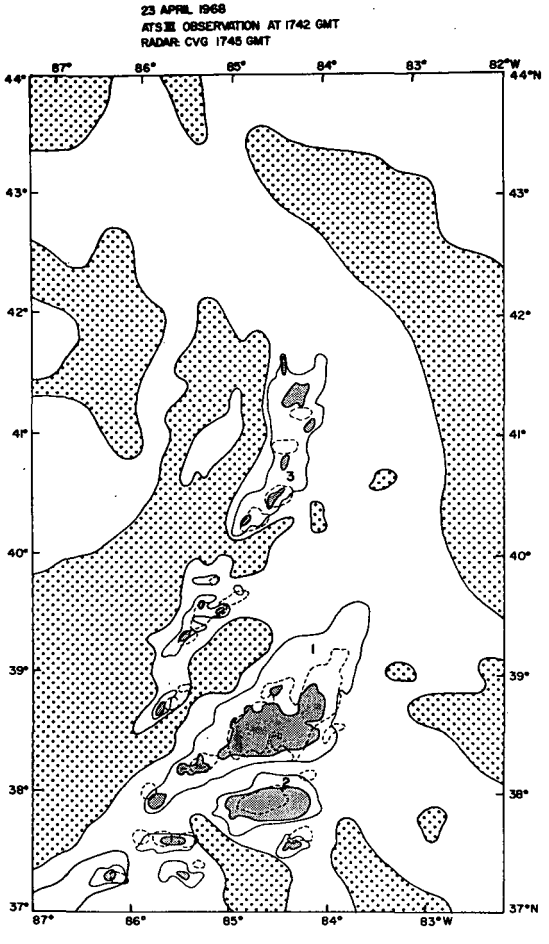

Figure 4(b). See Figure 4(a).

pictures corresponding to the ATS digital tapes analyzed. Direct comparisons of ATS data with radar images were not possible because of projection differences. Therefore ATS data were converted to a gnomonic projection, with the nearest radar site as the origin, and were displayed as contour maps of digital brightness on approximately the same scale as the enlarged radar pictures. Lack of point-to-point correspondence in the modified projections may be attributed to error sources such as distortion in the original ATS and radar data, measurement errors in determining the scale, enlargement inaccuracy, uncertainty in finding the exact location of radar sites on the ATS brightness displays and time differences between radar and satellite images. Time variations of normalized radar echo-areas were then compared with the cirrus shield-area expansion at intervals of twenty-eight minutes. In matching the radar echoes with the brightness contour display, all radar echoes in cloud complexes were included in the upper 40% of the ATS-III brightness range on 19 April, and the upper 36% on 23 April. This difference in cut-off level may be due to differences in geographic locations of the storm systems and also to differences in storm intensity. Figure 5 is

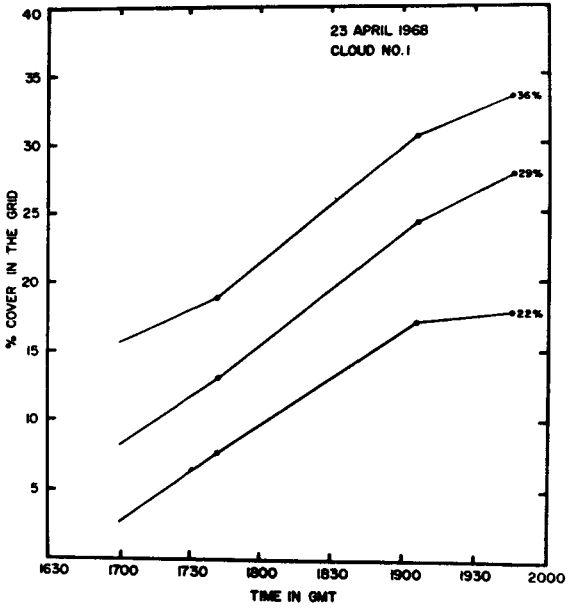

Figure 5. Time variations of percent cover in the grid of brightness contour of upper 36, 29, and 22% of total brightness range.

an example showing time variations of percent area of three contour levels (upper 22%, 29% and 36% of the total brightness range in the grid) on 23 April 1968. The purpose of this diagram is to show a uniform quasi-linear growth rate in all contour levels except in the last period when variation hardly exceeded a few percent in the 22% contour area. This departure may be related to precipitation release in the core area after 1900 GMT, a fact actually observed beneath the cloud systems.

b. Subsynoptic scale

Navigated and brightness-normalized tapes were processed for the area 91° W - 96° W and 33° N - 41° N, as shown in Figure 10. Each data point represents an average brightness of a small matrix of 10 scan lines × 33 elements (size approximately 1/2° latitude × 1/2° longitude). Brightness anomaly charts ($B_a = B_{i,j} - \bar{B}_j$, $i = 1, 113$, $j = 1, 3$, where i = number of small grid boxes; j = number of pictures used) were constructed in Eulerian coordinate for pictures at 2156, 2223 and 2251 GMT, and isocontours were drawn. Hourly precipitation charts were made for the same area, ending at 2200, 2300 and 2400, and the patterns of isohyets drawn. Although inadequate rainfall sampling prohibits one-to-one comparison, it was felt that some useful information could be derived on the feasibility of estimating rainfall patterns from the ATS time-lapse information, especially for areas of ill-defined convective cloud regimes. To increase confidence in the objectivity of the technique, radar echoes from Kansas City and Little Rock, properly normalized for the ATS scale, are superimposed on the brightness anomaly displays.

4. Results

a. Correlation between cirrus shield area change and rainfall rate

Figure 6 is a map of hourly precipitation ending at 2300 GMT upon which is superimposed the cloud brightness contour at 2223 GMT outlining the upper 40% of the total brightness range in the picture. Inadequacy of raingauge density for meso-scale analysis is apparent from this diagram. Hourly rainfall data from various raingauges in the path of the cloud complex during the hour, using the technique outlined in Section 3, are given in Table 1. The plots of these hourly rainfall averages and cirrus shield areas as a function of time for clouds number 1, 3 and 5 on 19 April 1968 and for 1 on 23 April 1968, are presented in Figure 7. Selection of clouds was governed by the spatial rainfall sampling. Despite poor sampling in the complex, the trends in Figure 7 indicate a definite positive correspondence between the outflow-area and the average rainfall amount. In the case of cloud number 1 on 23 April 1968, most of the precipitation appears to have

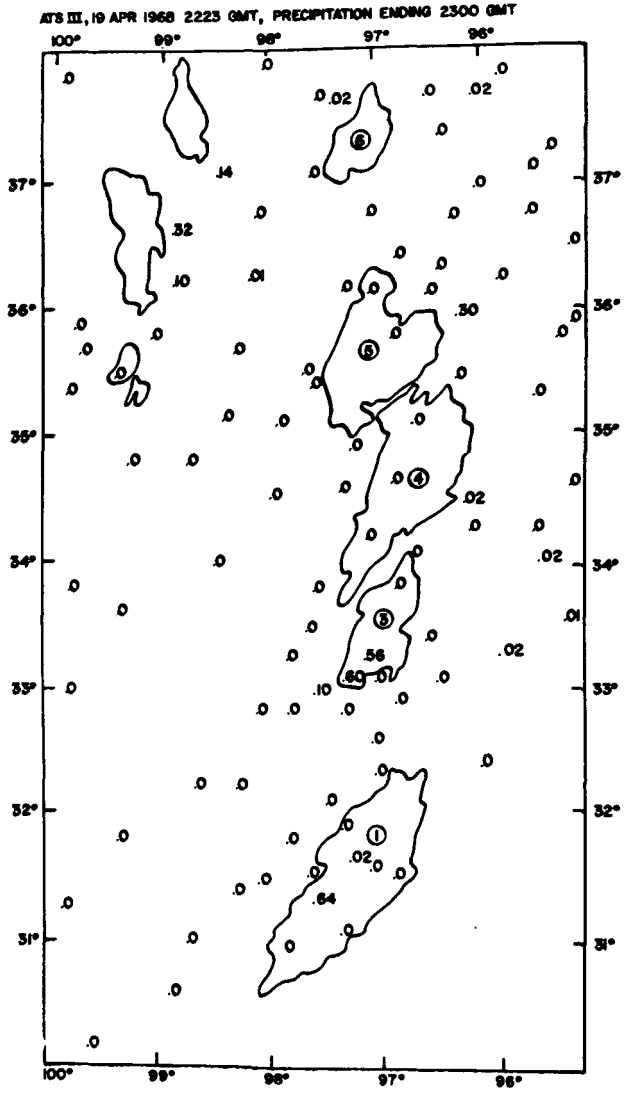

Figure 6. Hourly precipitation (inches) chart ending at 2300 GMT superimposed on which is the upper 40% brightness contour at 2223 GMT. Cloud numbers are circled.

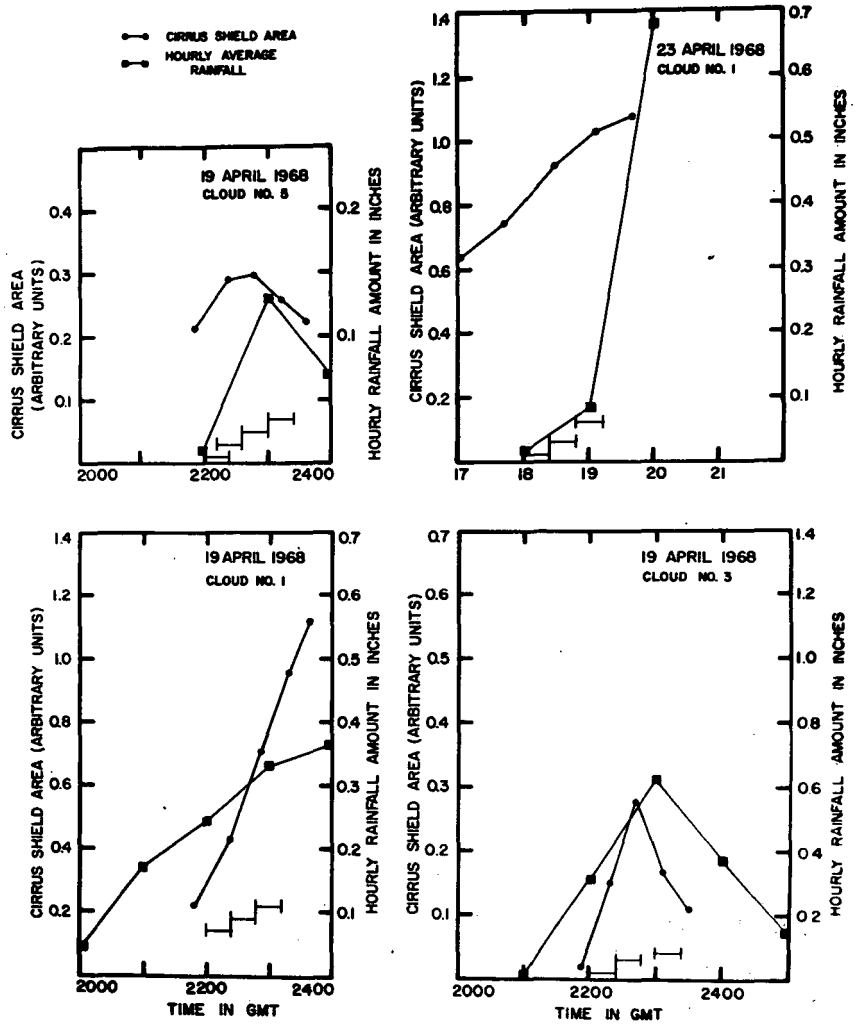

Figure 7. Time variation of cirrus shield area and cumulative hourly precipitation on the 19th and 23rd in storm complexes investigated.

Table 1

Raingauge Locations and Hourly Rainfall Amount

Time GMT	Reporting stations	Latitude north	Longitude west	Hourly rainfall in inches	Average rainfall
Cloud number 1			Date: 19 April 1968		
2000-	Briggs	30° 53'	97° 55'	0.42	
2100	Moline	31° 23'	98° 19'	0.07	0.17
	Whitney Dam	31° 52'	97° 22'	0.01	
2100-	Coryell City	31° 33'	97° 37'	0.66	
2200	Evant	31° 29'	98° 04'	0.04	0.24
	Moline	31° 23'	98° 19'	0.03	
2200-	Waco WBAP	31° 37'	97° 15'	0.02	
2300	Flat	31° 19'	97° 38'	0.64	0.33
2300-	Rusil	31° 29'	96° 53'	0.39	
2400	Waco Dam	31° 35'	97° 06'	0.42	0.36
	Waco WBAP	31° 37'	97° 13'	0.28	
Cloud number 3					
2100-	Weatherferd	32° 46'	97° 49'	0.11	
2200	Reno	32° 57'	97° 35'	0.5	0.30
2200-	Justin	33° 02'	97° 19'	0.6	
2300	Denton	33° 13'	97° 08'	0.56	0.58
2300-	Gordonvelle	33° 48'	96° 51'	0.64	
2400	Ardmore Water-works	34° 10'	97° 08'	0.1	0.37
Cloud number 5					
2100- 2200	Okema	35° 26'	96° 18'	0.01	0.01
2200-	Heyburn Dam	35° 57'	96° 17'	0.30	
2300	Lehigh	34° 28'	96° 13'	0.02	0.16
2300- 2400	Heyburn Dam	35° 57'	96° 17'	0.07	0.07

Table 1 — continued next page

Table 1 (cont.)

Time GMT	Reporting stations	Latitude north	Longitude west	Hourly rainfall in inches	Average rainfall
Cloud number 1			Date: April 1968		
1800-1900	Versailles waterworks Indiana	39° 05'	85° 15'	0.18	0.18
1900-2000	London Sewage plant, Ohio	39° 53'	83° 27'	0.90	
	Springfield New Water-works, Ohio	39° 59'	83° 49'	0.89	
	Lebanon Hwy Dept., Ohio	39° 26'	84° 12'	0.84	0.68
	Xenia treatment plant	39° 42'	83° 54'	0.75	
	Covington WB Airport, Kentucky	39° 04'	84° 40'	0.22	

occurred in the late evening when no usable satellite observations were available because of darkness. However, for studying a point-to-point correspondence both in space and time, one needs detailed simultaneous aircraft and surface data on both variables. Unfortunately such simultaneous quantitative measurements were not available to us, except from a few close-by radar stations which photographed the PPI scope.

Before we discuss radar echoes related to cirrus shield expansion, it is worthwhile to plot the time change of the cirrus shield area against the rainfall amount obtained from Figure 7 (Figure 8). The data intervals picked up from Figure 7 for comparison are indicated at the bottom of each inset. Although there is some scatter in the data points in Figure 8, a general agreement between the two variables is apparent. Most interesting in this data set is cloud number 1 on 19 April 1968 which showed significant outgrowth but produced comparatively little precipitation. Lack of meteorological data incloud and in the immediate environment at the time of storm-growth precludes any definite explanation for this phenomenon. It is, however, possible that a major part of the water vapor entering into the storm passed on to the ice phase due to a strong updraft and thus escaped

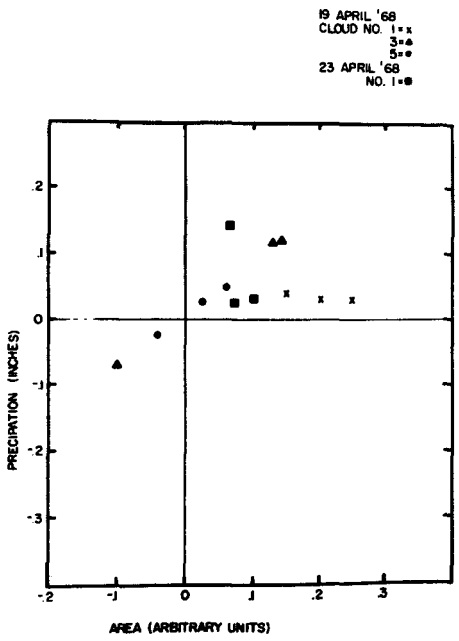

Figure 8. Correlation between the cirrus shield area change and the change in the hourly precipitation amount as derived from Figure 7.

precipitation, and also that a part of the precipitation in the downdraft might have evaporated in the dry environment before reaching the ground. These two effects together can account for such a phenomenon. In fact, the upper air soundings in the synoptic scale environment prior to the occurrence of the storm do suggest a dry condition in the inflow layer with a strong inversion at about 915 mb. Unfortunately, no suitable time sequence of radar observations was available to verify the time-change in precipitation area beneath this cloud.

To examine the degree of correspondence more closely, we have used time variations of the radar echo area in respective cloud complexes (Figure 3, 4). We have assumed that the radar echo area change is a measure of change in vertical motion field and therefore a change in rainfall rate during the life cycle of the complex. No normalization of the radar echo areas was

attempted except for matching the ATS scale, for we were mainly concerned with the relative changes in the echo-area in twenty-eight minutes. In this time interval, the clouds had hardly moved more than 10 n. m. - 15 n. m. Radar photos from Oklahoma City were employed for the case studies on 19 April and from Cincinnati and Detroit for 23 April. We limited our comparison to within 100 n. m. except for cloud number 3 on 19 April, which was around 125 n.m. from the OKC radar site. In making comparisons, only those severe storm clouds that could be identified as individual complexes were selected. In Figures 3 and 4, radar echoes have been superimposed on near-simultaneous satellite pictures. A comparison of solid radar echo area and the area of bright portions of the ATS images (the uppermost 36% to 40% of the total brightness range in the picture) in general yielded a good correspondence except for a few small scattered echoes which had no cloud counterpart above the selected brightness cut-off level. However, most of these small echoes corresponded to the brightness cut-off level at the upper 50% - 60% of the total range in the pictures.

Figure 9 presents the plot of the radar echo area-change against cirrus shield area-change. A good correlation is apparent in this data sample. Although this data sample is too small, it appears that an echo area change of one corresponds to a cirrus area change of three.

b. Correlation between subsynoptic-scale rainfall pattern and ATS cloud brightness anomaly pattern

Presented in Figure 10 are brightness anomaly charts at 2156, 2223 and 2251, and hourly rainfall distribution in the same area ending at 2200, 2300 and 0000 GMT (20 April 1968) east of 96° W (Figure 1). A time change in the brightness anomaly field observed in this figure may be attributed to decreasing mean brightness values (Table 2) as the disturbance moved eastward through the fixed grid box which resulted in a greater clear area caused by advected dry air from the west. A higher convective activity during the same period resulted in an increase in percent cover of high brightness values (e.g. the area contoured by the upper 18% in Figure 11 increased with time). The increased convective activity and greater precipitation intensity and extent are borne out clearly in the time section. Although space averaging suppressed a few meso-scale rainfall areas in the brightness anomaly chart, a striking agreement was found between the subsynoptic scale brightness anomaly field at 2156, 2256 GMT and the hourly rainfall pattern ending at 2200 and 2300 GMT, respectively. To substantiate objectivity in drawing isohyet patterns on the hourly rainfall charts, near simultaneous radar echoes from Kansas City and Little Rock have been superimposed on the brightness anomaly displays (Figure 12). A striking similarity between the isohyet pattern and the radar echo distribution is revealed in this diagram.

Table 2

Time Variation of Mean Brightness

Time (GMT)	Mean brightness ($\bar{B}$) (digital number)
2156	183.6
2223	177.4
2251	166.0

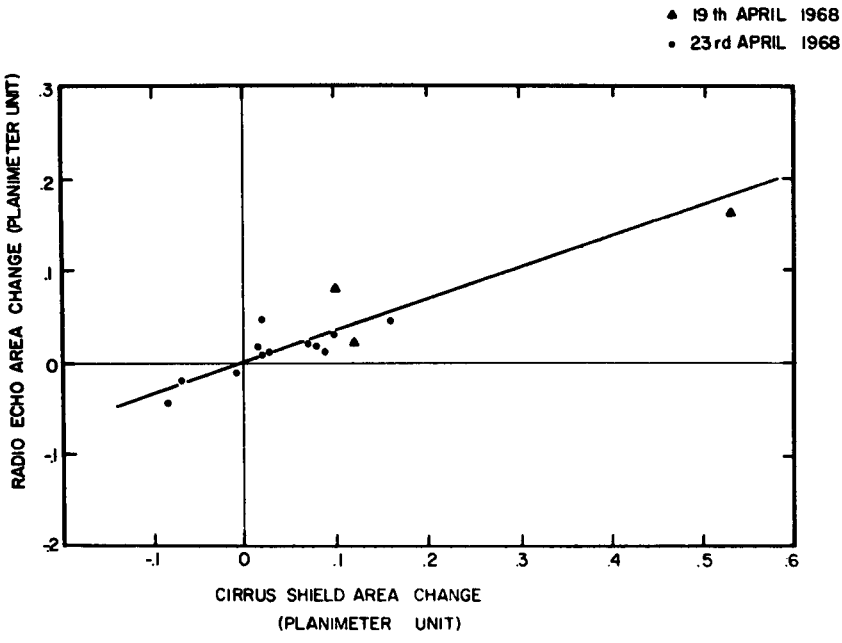

Figure 9. Time variation of cirrus shield area against that of radar echo area in various storm complexes.

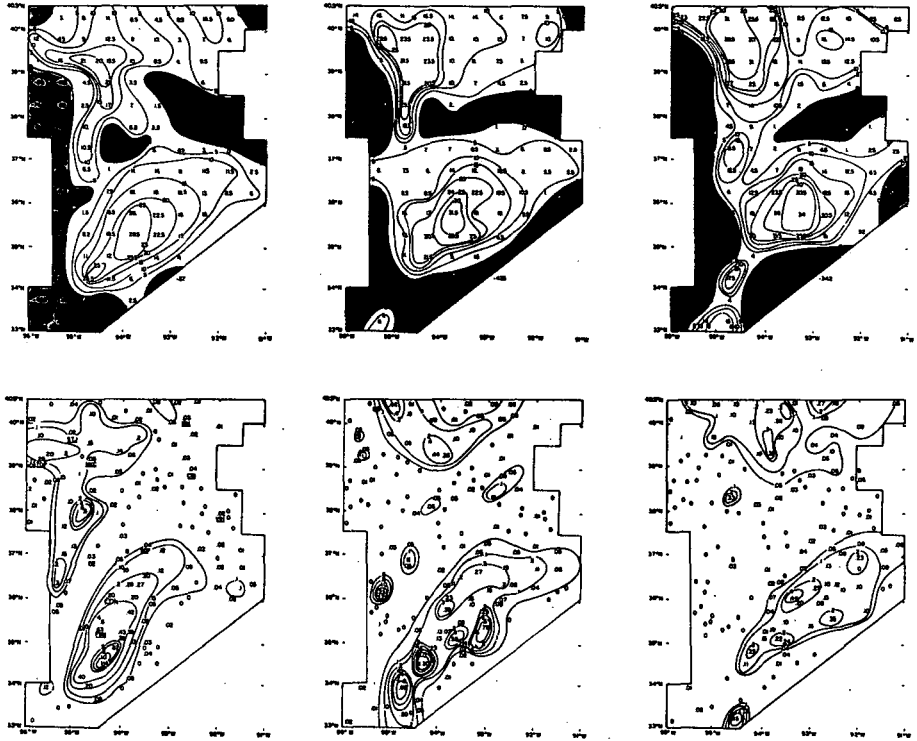

Figure 10. Upper diagrams are ATS observed subsynoptic scale brightness anomaly field (negative anomaly fields are shaded) at 2156, 2223 and 2251 on the 19th, while bottom diagrams show hourly rainfall charts ending at 2200, 2300, and 2400 GMT in the same area.

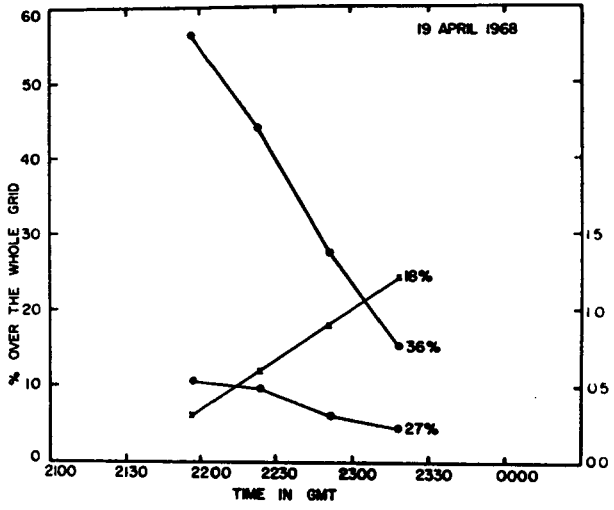

Figure 11. Time variation of area enclosed by 18%, 27%, 36% contour (percent of total) in the area as in Figure 10.

In summary, there is an excellent correlation between the positive brightness anomaly area, radar echo area and the precipitation pattern. For more quantitative information on the correspondence, measurements on brightness anomaly area were taken from the average of two charts at 2156 and 2223 GMT (Figure 10) and corresponding rainfall area from the precipitation chart ending at 2300 hr. GMT (Figure 10) and plotted in Figure 13. Cumulative hourly precipitation of less than 0.2 inches has been ignored in this plot. Table 3 presents the correlation between rain area and brightness anomaly area as read out from Figure 13.

5. Concluding Remarks

Although the data sample presented in this research is small, it has shown clearly a good correspondence between rainfall rate and time change of cirrus shield area atop active deep convection in mid-latitude frontal zones. Also seen from the superimposition of normalized ATS brightness isocontours on properly scaled radar photographs is a good agreement between the occurrence of rain at the ground and the absolute brightness of cloud

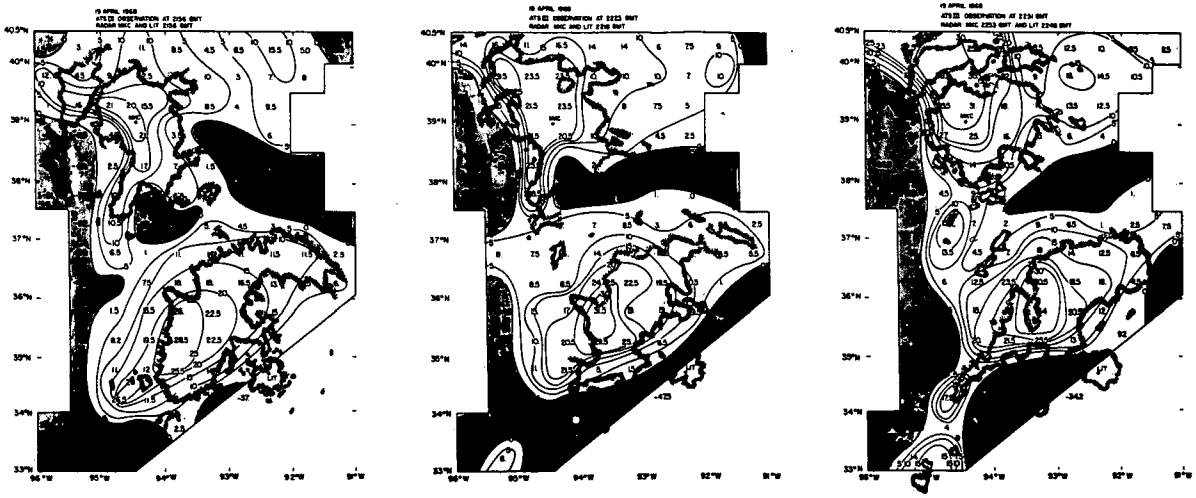

Figure 12. Superimposition of near simultaneous radar echoes from Kansas City and Little Rock on the brightness anomaly fields in Figure 10.

Table 3

Correlation Between Rain Area and Brightness Anomaly Area as Read From Figure 13

Brightness anomaly area (arbitrary unit)	Rain area (arbitrary unit)	Cumulative hourly rainfall (in inches)
310	63	0.2
250	47	0.3
200	36	0.4
160	29	0.5
125	22	0.6
90	16	0.7
50	11	0.8
45	7	0.9
30	3	1.0

1 arbitrary unit = $\frac{1}{4}$ (deg)^2 approximately.

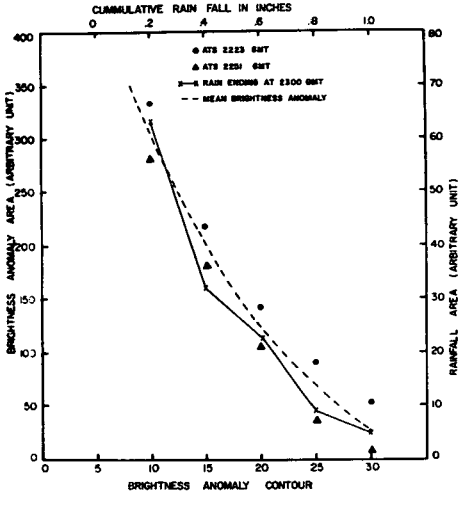

Figure 13. Plots of brightness anomaly area and cumulative hourly rainfall area against brightness anomaly contour and isohyets of rainfall, respectively, as derived from Figure 10.

masses. High absolute brightness of a cloud mass, however, may not be a sufficient criterion for assessing the intensity and stage of activity of cumulonimbus cells beneath it.

Furthermore, in the subsynoptic disturbance regime where extensive thick cirrus canopy and low clouds preclude visual isolation of individual complexes, brightness anomaly patterns are very helpful. Areas of a positive brightness anomaly pattern seem to agree well with isohyet patterns on the hourly rainfall chart. However, for a more useful time sequence, such charts should be constructed in Lagrangian coordinate rather than in Eulerian systems so that the mean brightness can be weighted over the moving cloud systems only.

It may be reasonably concluded from this research that remote sensing of intensity, extent and frequency of meso-to-subsynoptic scale convective precipitation is possible from a geostationary altitude. Further study in this area should be fruitful from the viewpoint of synoptic meteorology and climatology.

Acknowledgments

The research reported in this paper was supported by the National Aeronautics and Space Administration under contract number NAS-5-11542. The author is thankful to Dr. D. W. Martin for reviewing the manuscript and to Professor V. E. Suomi for constant encouragement and valuable discussion during the course of this work. Thanks are due to many individuals at the Space Science and Engineering Center for contributing in many ways in this research program.

References

Barrett, E. C., 1970: The Estimation of Monthly Rainfall from Satellite. Mon. W. Rev., 98, 4, 322-327.

Fawbush, E. J., R. C. Miller, and L. G. Starrett, 1951: An Empirical Method of Forecasting Tornado Development. Bull. Amer. Meteor. Soc., 32, 1-9.

Fawbush, E. J., and R. C. Miller, 1953: The Tornado Situation of 17 March 1951. Bull. Amer. Meteor. Soc., 34, 139-145.

Gerrish, H. P., 1970: Satellite and Radar Analysis of Meso-Scale Features in the Tropics, Semi-annual report, ECOM-0205-20, U. S. Army Electronics Command, Fort Mammouth, New Jersey.

Martin, D. W., and V. E. Suomi, 1971: A Satellite Study of Cloud Clusters Over the Tropical North Atlantic Ocean, Final report on STAG contract E-127-69-(N), NOAA.

Rainbird, A. F., 1969: Some Potential Applications of Meteorological Satellites in Flood Forecasting, Hydrological Forecasting, WMO publication, No. 228, TP. 122, 73-80.

Ruff, I., R. Koffler, S. Fritz, J. S. Winston, and P. K. Rao, 1967: Angular Distribution of Solar Radiation Reflected from Clouds as Determined by TIROS Radiometer Measurements, ESSA Tech. Report NESC-38, U. S. Dept. of Commerce, Washington, D. C.

Sikdar, D. N., 1969: Convective Heat Transport over the Tropical Mid-Pacific as Estimated from a Geosynchronous Satellite Altitude. Ph. D. thesis, Dept. of Meteorology, The University of Wisconsin, Madison.

Sikdar, D. N., and V. E. Suomi and C. E. Anderson, 1970: Convective Transport of Mass and Energy in Severe Storms over the USA—An Estimate from a Geostationary Altitude. Tellus 22, 5, 521-532.

Sikdar, D. N. and V. E. Suomi, 1971: Time Variation of Tropical Energetics as Viewed from a Geostationary Altitude. Jour. Atmos. Sci. 28, 2, 170-180.

49

N72-27649

Cloud Photographs from Satellites as a Hydrological Tool in Remote Tropical Regions

by Ronald C. Grosh

1. Introduction

The use of meteorological satellites, which are able to view large areas of the earth, to determine hydrological parameters has obvious advantages over measurements made at points on the surface. Objective techniques to evaluate rainfall and runoff derived from satellite data would be useful to agriculture, hydrology, and meteorology.

Several investigators have reported on the relation of rainfall to data obtained from satellites:

Gerrish (1970) related estimated cloud cover values for thirty nautical mile squares, exclusive of cirrus, to rainfall amount up to twenty-four hours after the satellite pass.

Barrett (1970) used cloud type, as well as cover, to get monthly rainfall estimates.

Rainbird (1969) related average infrared radiation intensity to average rainfall in a basin for the twenty-four-hour period following the satellite pass. He found a general trend toward lower radiation temperature values with increasing rainfall. However, there was a good deal of scatter in the data, and the lowest radiation intensities were found to occur during light rain in the decaying phase of a storm. This lag in the radiation minimum was also found by Rodok (1966) in the analysis of data for individual station rainfall. The expanded cirrus shield is the cause of this.

Lethridge (1967), using temperatures derived from infrared measurements from Tiros-IV to determine precipitation probabilities for short periods after the satellite pass, found that a stronger relationship was obtained if the brightness of reflected sunlight was used for a predictor as well.

In the present study, we attempted to find a relationship between brightness measurements obtained from the high resolution camera of the Applied Technology Satellite and rainfall and runoff measured on the ground. Tall, thick cumulonimbus clouds, from which one would be most likely to expect rain (Spillane, 1962), should reflect more sunlight back toward a satellite than should other clouds. Thick clouds should reflect more light than the underlying land viewed through broken clouds, and tall cumulonimbi should reflect light that suffers less atmospheric attenuation. The volume of runoff from a storm should depend in some way upon the storm's horizontal area. For this reason, the area covered by bright patches in satellite photographs should be related to runoff.

1.1 Data

Surinam was chosen as a site for this experiment for three reasons:

(i) rain is abundant during June and July;

(ii) it was in the center of the ATS-III picture and therefore navigation was simplified; and

(iii) it is a country with relatively inaccessible areas and it would be able to benefit from the practical results of such research.

The data were to be collected during June and July, the end of the major Surinam rainy season. Because the satellite data had to be recorded on magnetic tape, only a short period of data gathering was available. Surinam's high frequency of rainfall made it an ideal data source for economic tape use. Some Surinam stations average 628 showers a year. Furthermore, the Surinam Hydrometeorological Service was extremely cooperative in collecting data in remote areas.

1.2 Geography

Surinam (4° N 56° W) is located on the northern coast of South America (see Fig. 1). Most of the country is covered with hilly rainforest. Separating the wet coastal lowlands from the rainforest is a narrow zone in which savannas are frequently found (see Fig. 1).

Surinam has a small internal market for goods produced within the country. Therefore, exports are very important to its economy.

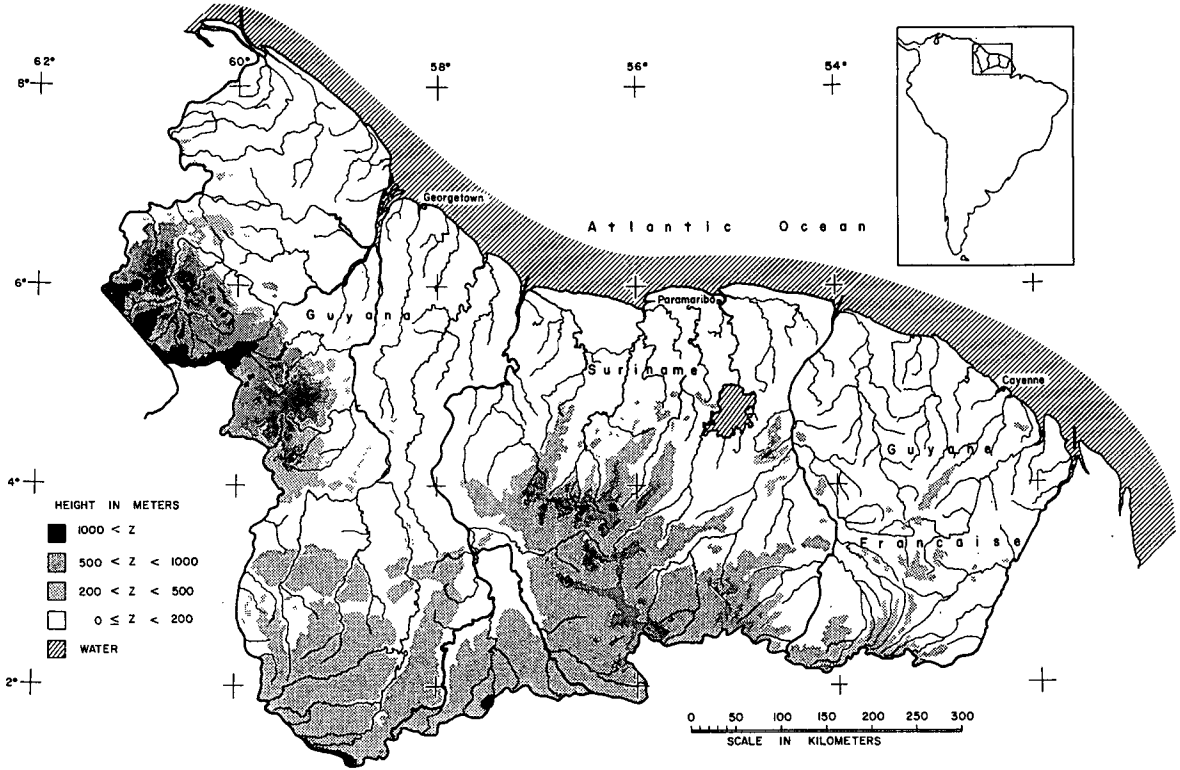

FIGURE 1 TOPOGRAPHIC MAP OF THE GUIANAS

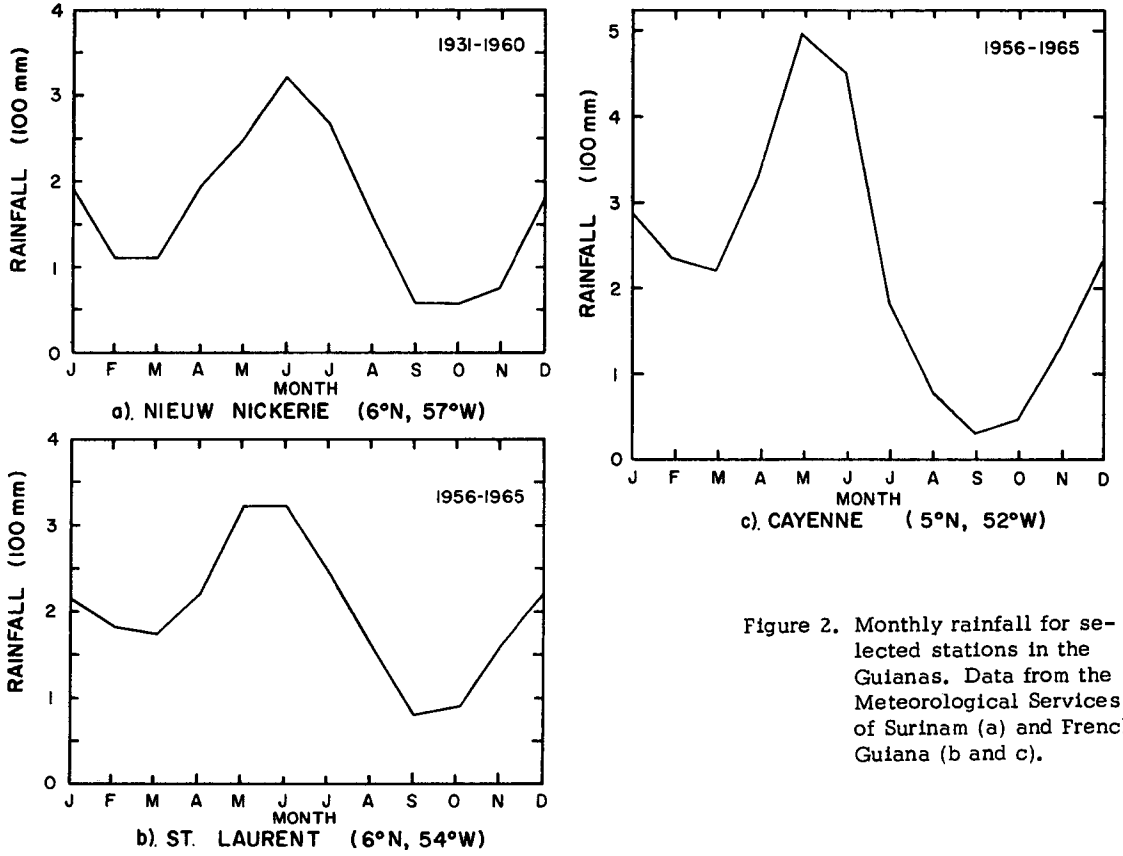

Figure 2. Monthly rainfall for selected stations in the Guianas. Data from the Meteorological Services of Surinam (a) and French Guiana (b and c).

Aluminum accounts for 80% of Surinam's exports. Surinam is thus among the world's largest sources of aluminum. Much of the bauxite is processed in Surinam before it is exported. Aluminum refining requires electricity to remove impurities, and hydroelectric generators supply the needed electricity. To help meet the great electrical requirements, a sixty-million dollar dam has been built at Afobaka (5° N 55° W), and this dam has created the lake at Brokopondo (5° N 55° W).

Agriculture accounts for 12% of Surinam's exports, and 75% of the country's agricultural produce is rice. This makes the prosperity of much of the agriculture of the country highly dependent upon rainfall.

Because roads are scarce in the interior, the predominant modes of transportation are by small boats on the many rivers, or by airplanes. Most communities are therefore along rivers. Thus, every segment of the population is intimately connected to the rainfall climate.

1.3 Climate

1.3.1 Microscale climate

Surinam and the other Guianas receive large amounts of rain. Located close to the equator, the weather depends mainly upon the position and the activity of the intertropical convergence zone. As a result, the climatology of Surinam shows a long and a short rainy season (see Fig. 2a). The long one lasts from the second half of April through July when the ITCZ moves from Brazil northward into the Atlantic, roughly following the sun. This movement can be seen in the location of the maximum monthly total rainfall measured at various stations of the Guiana Coast (see Fig. 2). As the ITCZ moves northward we find Cayenne (5.5° N 52° W) starting with a rainfall peak in May, Saint Laurent (6° N 54° W) with a peak in both May and June, and finally Nieuw Nickerie (6° N 57° W) with a peak in June.

The short rainy season is in December and January when the ITCZ moves back to the south. Toward the end of both rainy seasons, periods favorable to the development of severe thunderstorms (locally known as sibiboesies) occur. During February, March, and the first half of April, the northeast trade winds bring on a relatively dry period. In September, October, and November, the southeast trades blow in dry air from the Guiana highlands. A long distinct dry period occurs, during which the warmest temperatures of the year are observed. Readings range from 35° C at the coast up to 40° C in the interior.

Due to the strong convergence that takes place during a large part of the year, one can find many areas where more than three meters annual rain-

fall occurs (see Fig. 3). Here, as is the case in many tropical locations, rainfall is the most significant meteorological factor, showing great day to day and seasonal variations.

1.3.2 Mesoscale climate

1.3.2.a—Coastal rainfall characteristics: Near the coast a strong sea breeze regime is found (see Fig. 4) with the rainfall maximum occurring in the afternoon hours.

A variance spectrum was run for rainfall sums for two-hour intervals at Zorg en Hoop (6° N 55° W) during the long rainy season of 1968 (see Fig. 5). It is interesting to note the great amount of variance at periods of about one day, indicating the importance of solar-forced convection. This points out the importance of real time data for forecasts applicable to this area.

A variance spectrum was run with daily rainfall data to take a more detailed look at the peak from two to five days (see Fig. 5). Figure 6 shows a peak at four to five days, a periodicity also found in the meridional wind component in the tropical Pacific (Wallace and Chang, 1969), and in rainfall spectra for India (Ananthakrishnan and Kesavamurthy, 1970).

1.3.2.b—Interior rainfall characteristics: Farther inland one finds the nocturnal precipitation maximum commonly found in tropical air masses (see Fig. 4). One also notes (Fig. 3) a distinct increase in the total precipitation in the interior. This is probably attributable to rising topography in the interior.

A variance spectrum was run for daily wet season rainfall values at Sipaliwini (2° N 56° W). This spectrum is distinctly different from the coastal spectrum (see Fig. 7). Longer period disturbances have most of the variance. This agrees with stream flow data from the area. Figure 8 shows a typical river flow rate time series measured in the interior. These data show peaks three to four times a month in agreement with rainfall spectra from this region.

2. Ground Truth

2.1 Rain gauge network

The rainfall data were collected at thirty-two sites located throughout Surinam, but with a definite bias toward concentration near the population centers on the coast (see Fig. 9). Rainfall amounts recorded during daytime

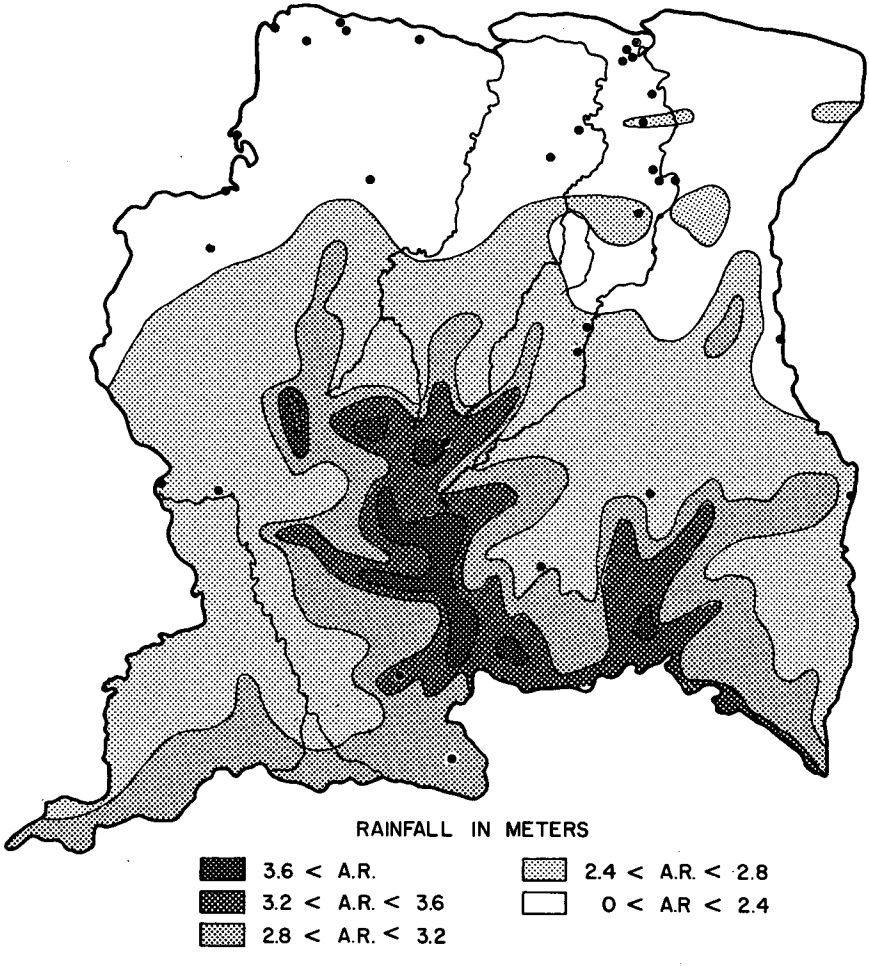

Figure 3. Surinam Annual Rainfall

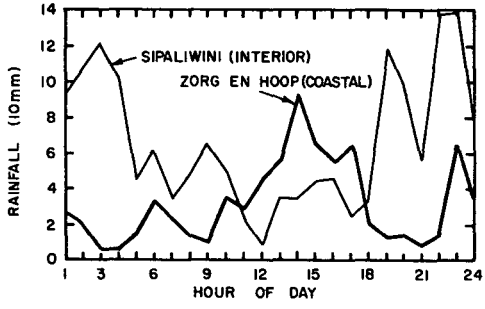

Figure 4. Diurnal Rainfall Variation at the Coast and in the Interior. Data compliments of Surinam Meteorological Service.

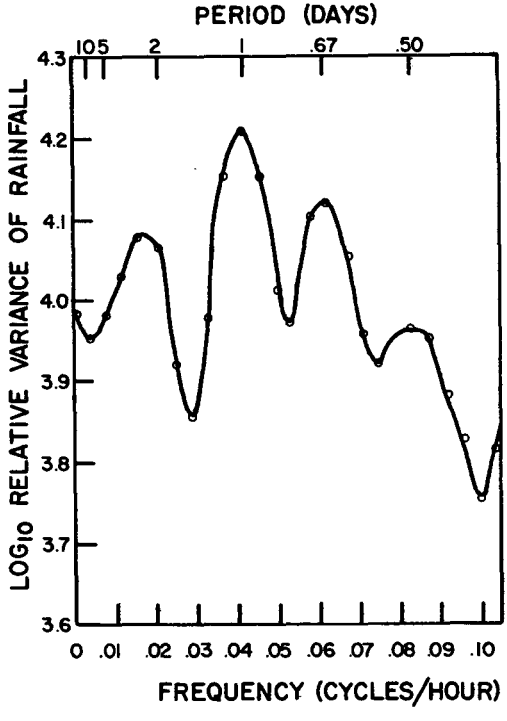

Figure 5. Detailed Rainfall Variance Spectrum for Zorg En Hoop (6° N 55° W). Data compliments of Surinam Meteorological Service.

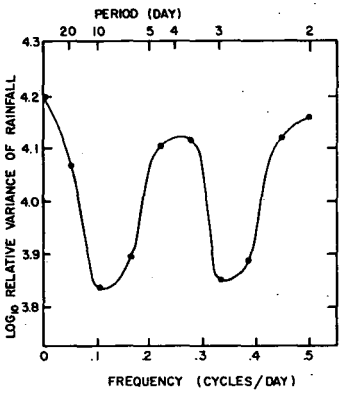

Figure 6. Zorg en Hoop (6° N, 55° W) Rainfall Variance Spectrum. Data compliments of Surinam Meteorological Service.

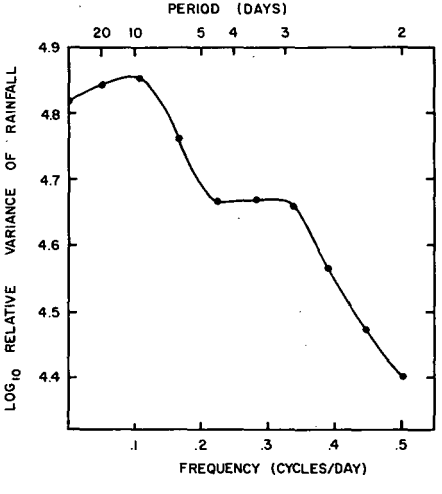

Figure 7. Sipaliwini (2° N, 56° W) Rainfall Variance Spectrum.

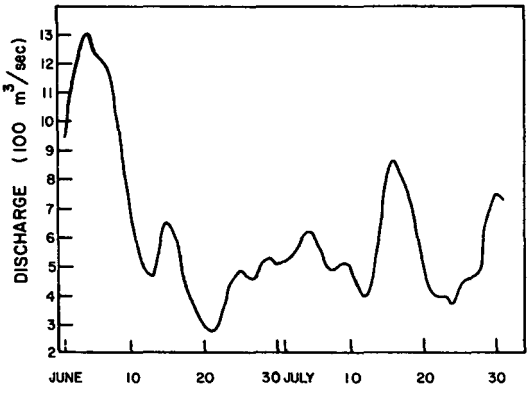

Figure 8. Stream Flow at Coeroeni (3.5° N, 57.5° W).

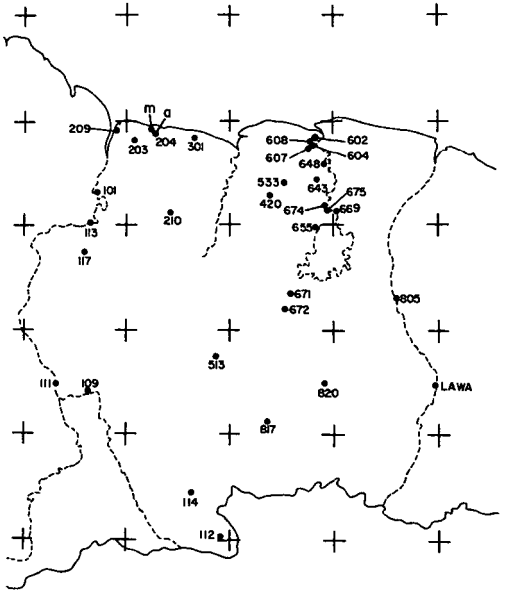

Figure 9. Rain Gauge Network

were given along with the time period during which they fell. The time at which rainfall commenced and terminated was recorded; this allowed the calculation of average rainfall rates for each shower.

2.2 Streamflow

Stream discharge data was obtained from the Surinam Hydrological Service for the fourteen basins shown in Figure 10. Data were obtained from most stations from June through July 1970.

3. Satellite Information

The ATS data used in this study came from two sources. Real time data was recorded on tape at the Space Science and Engineering Center ATS data facility at the University of Wisconsin during seven days in June 1970. The correlation attempted between brightness and rainfall rate was made using only this type of satellite data.

The stream flow relation was derived using satellite data from the ATS archive tapes at the University of Wisconsin as well as from the real time tapes. These tapes could be played back over the equipment at the ATS data facility of SSEC to yield the pictures to be analyzed.

3.1 Instrumentation

The satellite pictures were specially processed to have two distinct features. They were level enhanced and contoured. (For details on these procedures and the equipment used in them, see Appendix A.)

3.2 Level enhancement

Low brightness features, such as landmarks and coast lines needed for navigation, were given high contrast. All brighter objects were given disproportionately little contrast on the film. They therefore appeared relatively grey on the pictures. This was done to avoid confusion between contours and the brighter parts of cumulonimbus clouds.

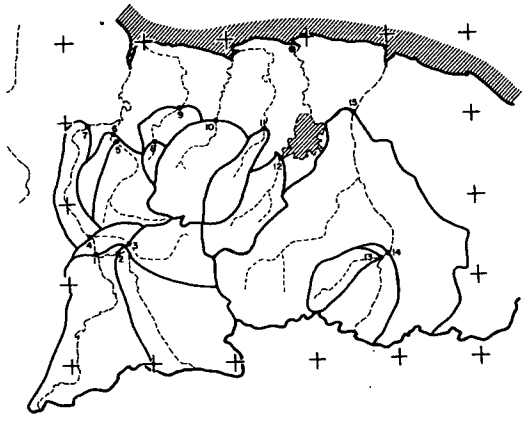

Figure 10. Stream Gauge Network

Table 1

Stream Gauge Network

Number	Name
1	Coeroeni
2	Meeteiland
3	Lucie
4	Ben. Luciemonding
5	Champion
6	Avanavero
7	Mataway
8	Blanche Marie
9	Stondansie
10	Maskitakreek
11	Dramhosso
12	Pokigron
13	Oelemarie
14	Litanie
15	Langatabbetje

3.3 Contouring

The second feature needed was an objective way to quantitatively determine the brightness of the cloud element being viewed. The contour generator described in Appendix A delineated the boundaries of clouds with brightness which exceeded predetermined value. If the pulse entering the contour generator from the data tape exceeded the brightness level at which the contour generator was set, it completely saturated the output going onto the film (see Fig. 11). On negatives this produced an easily distinguished black ring around that part of the cloud where the brightness exceeded the contour level setting. In practice this contour frequently was the size of a picture element (approximately four kilometers). Because the smaller storm systems were of this size or smaller, such small cumulonimbi appeared to be black spots.

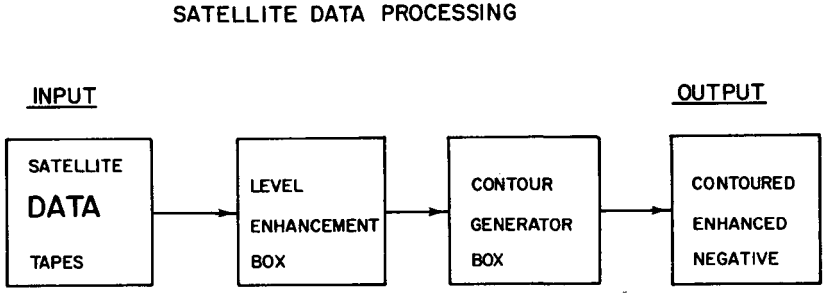

Figure 11. Enhancement and Contouring Schematic.

3.4 Brightness maps

Slides were made from negatives that had been enhanced, as described above, and contoured at various brightness levels characterized by predetermined output voltage. These slides were projected onto a large map (scale 1:2,500,000). This allowed for the accurate alignment of landmarks on the slide and on the map. Such landmarks were the orographic clouds over the northern Andes mountains near Lake Maracaibo and other large topographic features such as the Amazon River. Once this navigation was achieved, a small base map was superimposed over Surinam, and the contour for that negative was traced onto it. By superimposing negatives

exposed at other brightness contour settings on the same base map, a complete contour map of the brightness field was obtained for the picture (see Fig. 12).

From such contour maps it was possible to determine: (i) the brightness of the cloud cells over a rain gauge station located on the map; and (ii) the area enclosed by a certain brightness contour (the area of a cell) located over a particular river basin.

The numerical values of the contour brightness settings were divided by the cosine of the solar zenith angle to account for changes in intensity of cloud brightness caused by changes in the solar zenith angle and not from changes in the clouds themselves. Adjustments were also made in the computed transmission to account for the slant path length which depended on the solar zenith angle.

4. Method

4.1 Correlation of rainfall rate and brightness

4.1.a—Rainfall rate: The maximum in the brightness field closest to a rain gauge was used as a measure of the brightness. It was assumed that a cloud core such as this would be the main source of rain. In view of the uncertainty in the navigation, more refined methods seemed questionable. Only rainfall rates were used when the total rainfall exceeded 2mm; this arbitrary value was used as a criterion that a core had passed over the gauge.

4.1.b—Data adjustment: It was felt that more appropriate estimates of the rainfall rate than the average rate obtained from the raw data could be obtained by assuming that all the rainfall fell from the brightest core of the clouds. Rough estimates of the cloud core velocity were made by averaging the core displacements from one picture to the next for a whole day. Then the diameter of the core in question was measured from the map. Dividing the diameter by the velocity gave a new estimate of the rainfall duration. If this estimate was shorter than the original duration in the raw data, it was used to calculate a new higher rainfall rate for the station involved.

The use of a velocity averaged over a number of pictures gave a stable velocity to use for these calculations. Measurements of cloud core displacements varied from picture to picture during the same day. Navigational uncertainty doubtlessly played a role in some of the variations. Therefore, error bounds were computed for rainfall rates based on the minimum and maximum velocities calculated during a day.

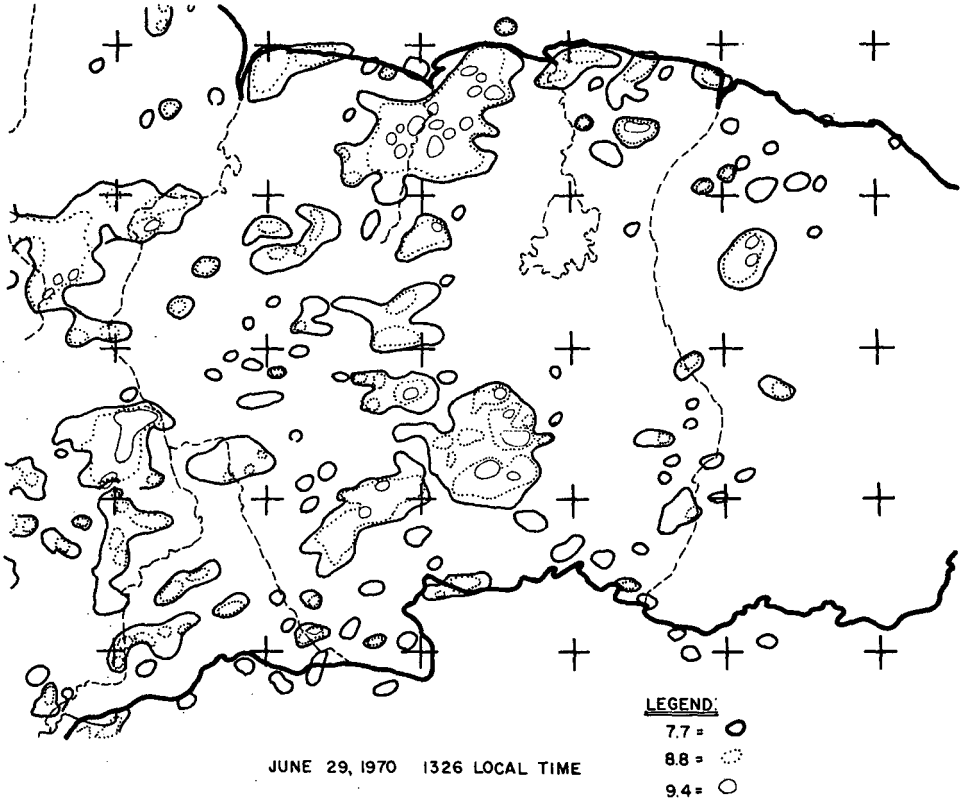

Figure 12. Example of Brightness Contour Map.

The error bounds in brightness result from having originally used half-volt intervals for the satellite contour voltages ($\pm$ .25 volts error bounds). In the final corrected form the typical error bounds were about $\pm$ .3 volts.

4.2 Correlation of runoff and area contained within the nine-volt video contour

4.2.a—Streamflow: The stream discharge data were given as time series of daily values for each river basin. When the stream discharge vs. time was plotted on semi-log graph paper, the recession of each peak in a series of peaks may be extrapolated by a straight line if the individual peaks are distinct enough. When the extrapolated recession of streamflow is replotted on cartesian graph paper, the volume of runoff may be calculated (see Figs. 13 and 14). The extrapolated recession of a peak is extended under the following peak. A "reasonable" background level (according to the criterion of Linsley et al., 1958) is drawn under the following peak. The area on the graph so enclosed is the volume of the runoff. According to Linsley (p. 205), rivers with a length of 260 miles and a river length to basin centroid of 130 miles should show a peak discharge in about fifty hours or less. Typically, one finds the most rain falling as the peak builds to a climax (see Fig. 15) for basins of this size. Because the choice of background in the runoff calculation is somewhat arbitrary, an error of about 10% may have resulted. Actual flow measurements typically have an error of 5%. The combined total error is thus about 11%.

4.2.b—Data adjustment: The area enclosed by the nine-volt video signal contour defines the precipitation area which is used here for the independent variable. (The nine-volt video contour was chosen for reasons discussed in section 5.2.) Pictures used to obtain the areas contained within the nine-volt video contour were required to have been taken no more than three days, and preferably around two days, before a stream flow peak. Pictures used were taken at about 1:30 to 2:30 pm local time. This is about the time the afternoon rain starts (see Fig. 4). Only one picture from one day was used to obtain the areas.

If afternoon pictures from more than one day were available during the time a peak was developing, the one with the largest area inside the nine-volt video contour was used in the correlation. In some cases (basin 3) only one picture was available during the build-up phases, and its contour area had to be used. Such data gave poorer results in the correlation than other cases where a more complete choice was available.

The error in the calculation of the areas enclosed by the nine-volt video contour is about 10%. The error arises from the graphical nature of the

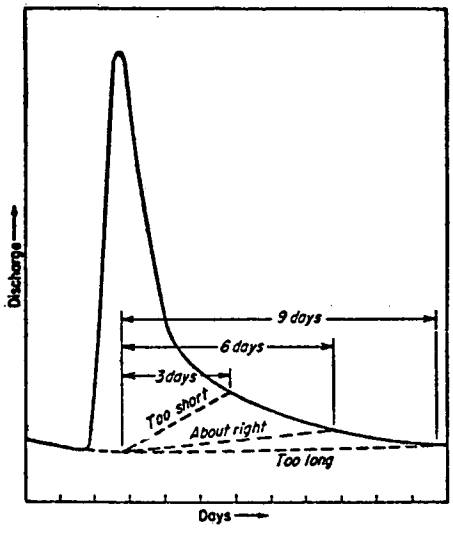

Figure 13. Selection of the Time Base for the Surface-Runoff Hydrograph. Source: Linsley, et al., 1958.

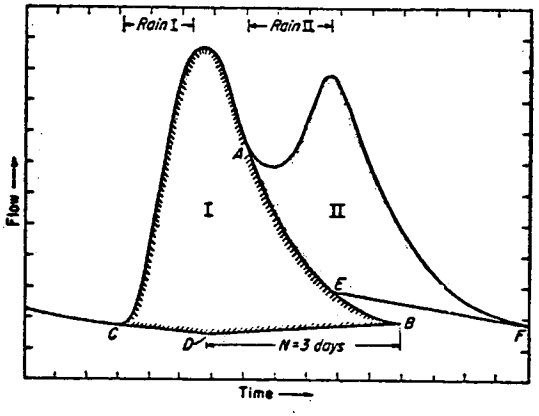

Figure 14. Separation of Complex Hydrographs, Using Recession Curves. Source: Linsley, et al., 1958.

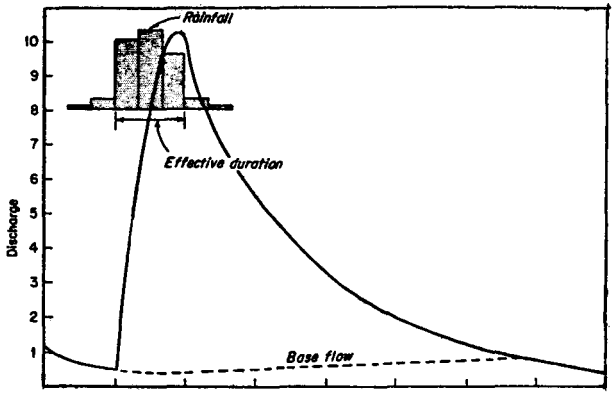

Figure 15. Relation of Time of Rainfall to Hydrograph Peak. Adapted from Linsley, et al., 1958.

calculations, as well as from slight differences of the actual contour settings for the pictures from nine volts.

5. Results

5.1 Video signal voltage brightness vs. rainfall rate

It is assumed that video signal voltage measured by the satellite depends on the solar radiance which reaches the satellite camera. The solar irradiance is assumed to be reflected off a cloud and then reaches the satellite. The higher the cloud top reflecting surface is, the smaller the optical thickness of the atmosphere to the cloud top, and the less the irradiance will be attenuated. In addition, the higher the sun is in the sky, the greater will be the irradiance striking cloud tops and then passing back to the satellite. The cloud albedo, A, is assumed to be independent of the solar zenith angle, a fair assumption for thick cumulonimbi (Shettle and Weinman, 1970). The video signal voltage from the satellite is

$$V = \mu_0 B_0 A e^{-P(1 + \frac{1}{\mu_0})\frac{\tau}{700}} \qquad (1)$$

where V is the measured output voltage of the satellite camera system, P is the pressure at the reflecting cloud top, τ is the optical thickness from the top of the atmosphere to the cloud top, μ_0 is the cosine of the solar zenith angle, and B_0 is the solar irradiance in the spectral interval over which the ATS camera responds.

If one assumes that the rainfall rate is a function of the height of the cloud top, the rainfall rate may be approximated by

$$R = R_0\left(1 - \left(\frac{P - 50}{650}\right)^{\frac{1}{10}}\right) \qquad (2)$$

where R is the rainfall rate, and R_0 is the greatest rainfall rate possible. The world record for thirty minutes, according to Fletcher and Sartor (1951), was $R_0 = 3.75$ mm/min. Equation (2) assumes that a cloud top must be higher than the 700 mb level in order to produce any rain, and that as the cloud top rises from this altitude, the rate of rainfall increases slowly at first. The rainfall rate begins to increase rapidly around 400 mb, a level where the temperature typically is about -20° C. The maximum rate of rainfall is assumed to be reached when the cloud top is at 50 mb.

Figure 16 shows Equation (2) along with several observed points. The observations show values of rainfall rate at, or near, the surface, and the pressure at corresponding cloud top heights. Both the rainfall rates and cloud height pressures (shown in Fig. 16) are usually inferred from radar measurements (Donaldson, 1958; Browning, 1968; Joss, 1970). Donaldson's rainfall rates at points 1 and 3 in the figure have been averaged over a period of about a half-hour to be consistent with our normalization to the half-hour world record. The heights of the tops are the maximum that occurred during the half-hour period (see Donaldson's echo "B" and "C", Fig. 6, p. 48). Cloud heights as seen on radar typically are underestimates of the visual cloud top height by several thousand feet. For this reason, 2,000 feet have been added to the heights. These points give a rough justification for the use of Equation (2). The power of one-tenth was chosen because the curve would then lie to the left of points designated 1 and 2. These points probably were overestimates of the rainfall rate since they were not measured exactly at the ground. The heights for points with large rates of rainfall may be underestimates since the tropical tropopause is normally at lower pressure than the mid-latitude tropopause where these radar measurements were made. Error bounds of $\pm$ 2,000 feet were seen as appropriate for the cloud height estimations. Donaldson indicates his rainfall estimates may be wrong by a factor of 6. Browning's rainfall was measured at the surface and 95% of Joss's values are within 26% of his mean.

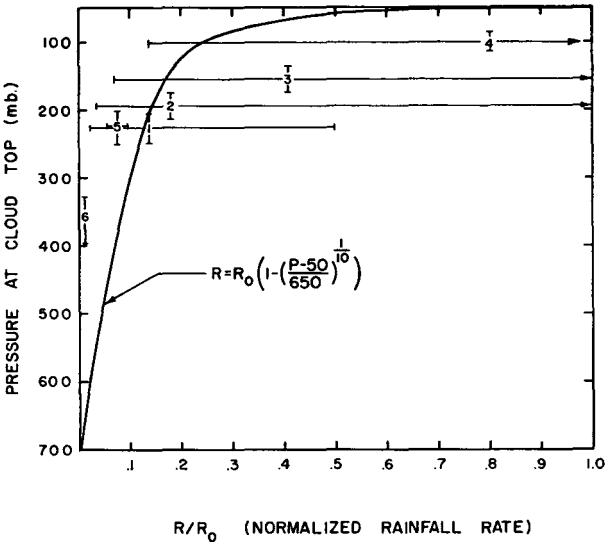

Key:	Points	Author	Comments
	1-4	Donaldson	No. 4 is pre-tornado cloud
	5	Joss	Measured in Switzerland
	6	Browning	Snow

Figure 16. Relationship of Rainfall Rate to Pressure of Cloud Top.

Figure 17 shows the results of matching the point rainfall rates observed in Surinam with the brightness of nearby bright storm cores. The brightness has been corrected with regard to solar zenith angle and path length through the atmosphere, such that the values plotted would be equivalent to the brightness measured by the satellite at noon on a day when the satellite and the sun were exactly over Surinam ($\mu_0 = 1$).

The rate of rainfall from a particular storm changes very rapidly with distance away from the storm center (see Fig. 18). Huff (1970) found that the correlation coefficient of rainfall rates measured over periods of one to ten minutes dropped to be less than or equal to about .8 between two points if they were separated by about a mile or more (see Fig. 19). Thus the small sampling area of a rain gauge is very likely to be missed by the center

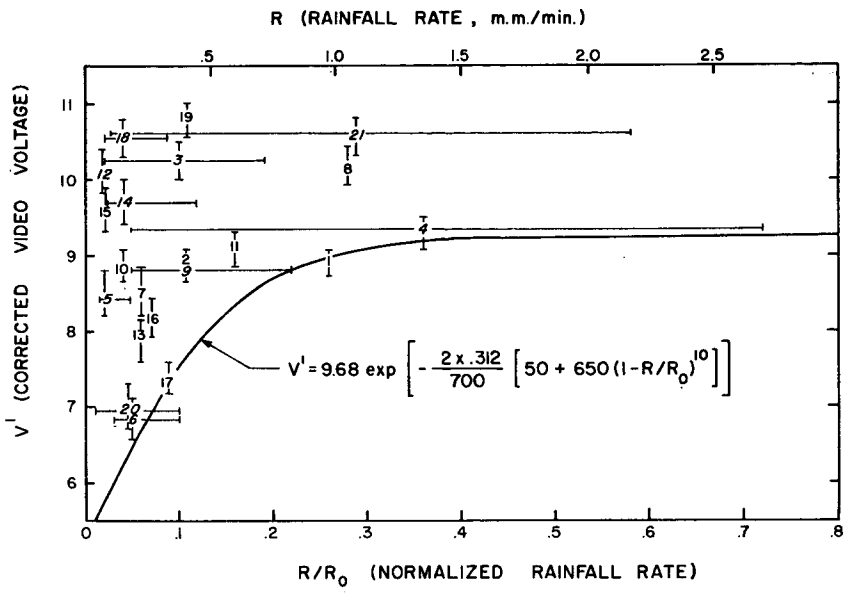

Key: Script signifies that cloud velocity was used in the calculation of R.

Figure 17. Corrected Brightness vs. Normalized Rainfall Rate.

of an individual bright cloud. In these cases the rainfall rate calculated for the gauge will be too low. Thus the lowest points in Figure 17 probably provide the best estimate of the relationship between rainfall rate and cloud brightness inasmuch as they presumably correspond to a superimposition of the storm center over the rain gauge.

A curve based on our theory was fit to the lowest points. Combining Equations (1) and (2) gives

$$\ln \frac{V}{\mu_0} = \ln B_0 A - (1 + \frac{1}{\mu_0}) \frac{\tau}{700} [50 + 650(1 - \frac{R}{R_0})^{10}] \qquad (3)$$

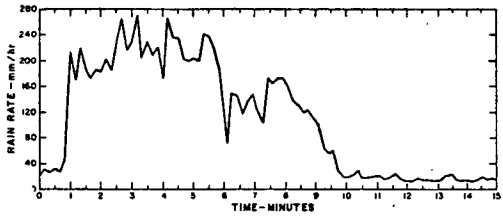

Figure 18. Example of Instantaneous Rainfall Rate Gradient. Source: Semplak, 1971.

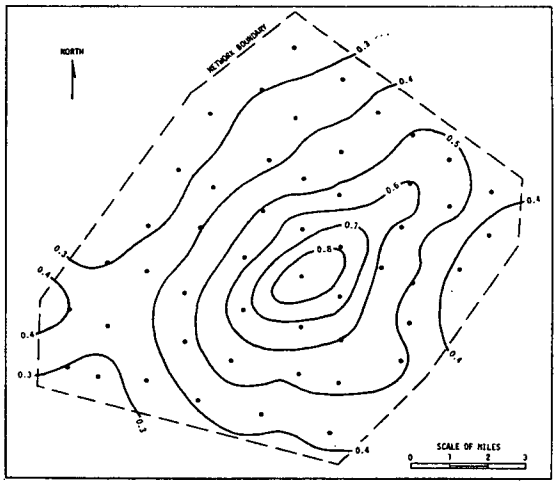

Figure 19. Average Correlation Pattern of Rainfall Rate. Adapted from Huff, 1970.

Table 2

Key to Figure 17

Point Number	Station	Time (Local)	Day
1	604	1319-1331	6/12/70
2	607	1330-1345	"
3	602	1340-1423	"
4	608	1320-1415	"
5	210	1325-1355	"
6	113	1427-1445	6/29/70
7	204a	1415-1430	"
8	602	1404-1412	"
9	301	1342-1500	"
10	602	1330-1348	"
11	209	1300-1315	"
12	513	1230-1315	"
13	113	1154-1220	"
14	817	1102-1215	"
15	608	1408-1436	"
16	117	1320-1335	7/2/70
17	210	1220-1230	7/30/70
18	101	1230-1315	"
19	113	1319-1328	"
20	420	1200-1400	"
21	204m	1200-1730	"

where V and R are given from points 1 and 17 in Figure 17. Plotting $\ln(\frac{V}{\mu_0})$ versus the quantities on the right side of Equation (3) allows evaluation of the y intercept ($\ln B_0 A = 2.27$) and the slope ($\tau = .312$). This value of the optical thickness is about twice the value ($\tau = .170$) given by interpolation of Elterman's (1965) values which were derived from measurements made in the clear air of the southwest United States. The present enhanced derived turbidity of tropical air is consistent with measurements conducted during BOMEX (Gille, 1970).

Extrapolation of this curve in Figure 17 indicates that a zero rainfall rate occurs if brightness falls below about 5.2 volts. On the other hand, the nine-volt contour should include rainfall rates exceeding 1.0 mm/min.

5.2 Stream flow vs. area of contour

Howell (1967) has indicated that in the Afobaka region, little stream flow results from light rain. Most of the runoff comes from less frequent intense storms. It was therefore important to choose a high brightness level to use in the stream flow study. The nine-volt video contour was chosen because the regions which it encircled would be subjected to high rainfall rates. These areas would give significant runoff in a short period.

The correctness of this decision seems to be borne out by the calculations below (see Table 3). At present we may note that there seems to be a fairly clear relation between the area inside the nine-volt video contour and the volume of runoff (see Fig. 20).

Table 3

Values of K

Basin Number	Date of Stream Flow Peak	V_{run} ($10^7 m^3$)	V_{rain} ($10^7 m^3$)	$K = V_{run}/V_{rain}$
1	6/29	2.6	17.0	.15
3	7/1	6.5	9.7	.67*
3	6/14	6.0	5.5	1.09*
5	7/3	11.0	55.0	.20
6	7/3	7.3	27.5	.27
9	6/30	1.0	7.8	.13
11	6/29	.3	9.7	.03
12	6/29	.3	8.6	.03

$\frac{\Sigma K_i}{N} = .14$ Standard deviation = .04

*Not used in average K since data point has questionable validity.

Hydrologists (when working with individual storms) have found that the maximum mean depth of rainfall decreases as the rainfall is averaged over larger surface areas. When such values are plotted for a particular time duration, the result is a depth-area-duration (d-A-t) curve (see Fig. 21).

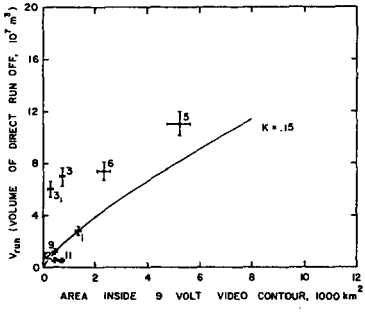

Figure 20. Nine-Volt Video Contour Area vs. Runoff Volume.

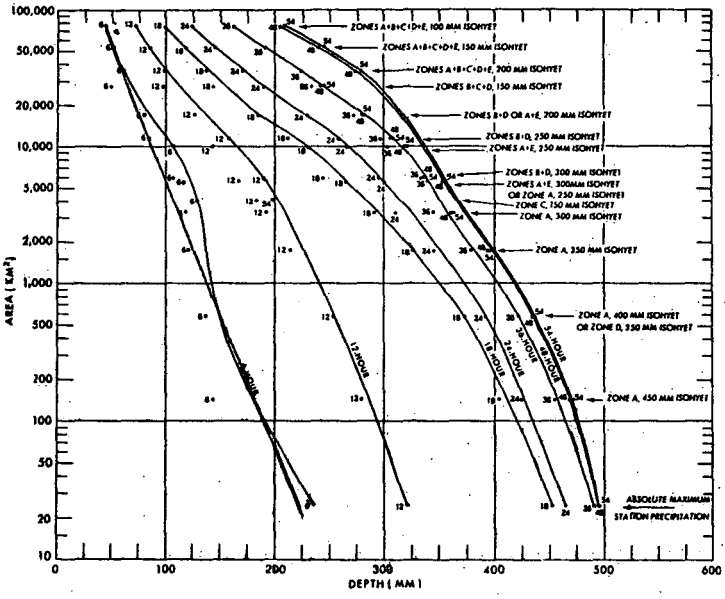

Figure 21. Maximum Depth-Area Curves for Various Durations, Storm of May 16-18, 1953. Source: WMO 1969b.

Alexander (1969) claims that over a wide range of areas d-A-t curves will be straight lines if plotted on semi-log graph paper. Thus, if d is the average depth for area A of the storm, d_0 the mean depth of A_0, the area of the whole storm, then $d = d_0 + c_1 \log_{10} \frac{A_0}{A}$ where c_1 is the slope of the curve. Such a model could be applied to groups of storms.

The volume of rainfall is

$$V_{rain} = Ad \tag{4a}$$

The volume of runoff is

$$V_{run} = KV_{rain} \tag{4b}$$

where K, the runoff coefficient, is always less than one. The value of K depends on the characteristics of the river basin, as well as on the amount of rain, the soil moisture, and the season (WMO, 1969a). Substituting for d we find $V_{rain} = A(d_0 + c_1 \log_{10} \frac{A_0}{A})$. Referring to Figure 21 for the storm of May 16-18, 1953 in the southern United States, one can obtain estimates of d for some given area A of other storms. A logarithmic curve was fit to the six-hour d-A-t curve to yield estimates of d. This was done using the nine-volt video contour areas for A. Rainfall volumes obtained by this method allow us to check the validity of using the nine-volt contour to define the storm boundary. Such rainfall volumes should always be greater than the corresponding runoff volume. Table 1 shows this to be the case with but one exception. Only one value of K was greater than one. The crudeness of the graphical techniques used in the calculation of the runoff and nine-volt video contour area may well be responsible for this. However, it is more likely that the nine-volt video contour may have been a poor estimate here, since there was only one value for the June 14 peak to choose from. A small area will result in V_{rain} being too small. In addition, the possibility of significant storms developing which are not on the photo being used is always present. Particularly, night rain may be expected. Still, it is satisfying to note that the average K (in Equation (4b)) $= .14 \pm .04$ is very similar to the $K = .15 \pm .05$ suggested by Richards (1955) for heavy forests.

5.3 Communication experiment

Brightness maps with only one contour can be produced very quickly. Their usefulness as a forecast tool has been shown above. They can be used

to locate areas of intense rainfall, and give a good indication of runoff volumes to be expected in the next day or two. It is therefore desirable to transmit such predictions to those who will be most immediately affected by the stream flow due to intense rainfall. A method for transmitting such charts or other graphical meteorological data over long distances by amateur radio and office equipment in real time was developed to provide a simple communications link for such data transmission. A demonstration of the test transmission and the equipment involved are described in Appendix B.

Summary

This research demonstrated the following items:

1) An empirical relation was found between the brightness of clouds measured by a geosynchronous satellite and the maximum measured rainfall rate measured by rain gauges under the clouds.

2) There is a good indication that the area inside a high brightness contour on the picture can be related to stream runoff from the basin covered by the area bounded by the contour.

3) Graphical meteorological data can be transmitted conveniently by amateur radio and office equipment in near real time to inform hydrologists and meteorologists about conditions which affect their areas.

References

Alexander, G. N., 1967, "Mathematical models of area rainfall," Hydrological Forecasting, World Meteorological Organization Publication No. 228, TP. 122, pp. 81-100.

Ananthakrishnan, R., and Kesavamurthy, R. N., 1970, "Fluctuations in the pressure and wind fields over India during the summer and winter monsoon seasons," Proceedings of the Symposium on Tropical Meteorology, University of Hawaii, Honolulu, Hawaii.

Barrett, E. C., 1970, "The estimation of monthly rainfall from satellite," Monthly Weather Review 98(4), pp. 322-327.

Browning, K. A., and Wexler, R., 1968, "The determination of kinematic properties of a wind field using Doppler radar," Journal of Applied Meteorology, February, 1968, pp. 105-113.

Donaldson, Ralph J. Jr., 1957, "Analysis of severe convective storms observed by radar," Journal of Meteorology, Vol. 15, February 1958, pp. 44-50.

Elterman, L., 1964, "Atmospheric attenuation model, 1964, in the ultraviolet, the visible, and the infrared windows of altitudes of 50 kilometers," Environmental Research Paper No. 46, Air Force Cambridge Research Center.

Fletcher, R. D., and Sartos, D., 1951, Air Weather Service Technical Report No. 105-181, 1951.

Gerrish, H. P., 1970, "Satellite and radar analysis of mesoscale features in the tropics," Semiannual Report, ECOM-0205-20, United States Army Electronics Command, Fort Monmouth, New Jersey.

Gille, John, Chairman, 1970, Summary of findings of the workshop on BOMEX radiation and particulate investigations, October 21-23, 1970.

Howell, W. E., associates inc., 1967, Rain stimulation for the Brokopondo watershed Suriname, Lexington, Massachusetts, p. 17.

Huff, F. A., 1970, "Spatial distribution of rainfall rates," Water Resources Research, Vol. 6, No. 1.

Joss, J., and Waldvogel, A., 1970, "A method to improve the accuracy of radar measured amounts of precipitation," Paper presented at the Fourteenth Radar Meteorology Conference, Nov. 17-20, 1970, Tucson, Arizona.

Lethridge, M., 1967, "Precipitation probabilities and satellite data," Monthly Weather Review 95(7), pp. 487-490.

Linsley, R. K., Kohler, M. A., and Paulhus, J., 1958, Hydrology for Engineers, McGraw-Hill Book Company, New York.

Radok, U., 1966, "An appraisal of Tiros III radiation data for Southeast Asia," Atmospheric Research Paper No. 102, Colorado State University.

Rainbird, A. F., 1969, "Some potential applications of meteorological satellites in flood forecasting," Hydrological Forecasting, World Meteorological Organization Publication No. 228, TP. 122, pp. 73-80.

Richards, B. D., 1955, Flood Estimation and Control, Chapman and Hall Ltd., London, p. 59.

Semplak, R. A., 1971, "A rare event of intense rainfall," Monthly Weather Review 99(2), pp. 155-157.

Shettle, E. P., and Weinman, J. A., 1970, "The transfer of solar irradiance through inhomogeneous turbid atmospheres evaluated by Eddington's approximation," Journal of the Atmospheric Sciences, Vol. 27, No. 7, pp. 1048-1055.

Spillance, K. T., and Tamaguchi, V., 1962, "Mechanisms of rain producing systems in southern Australia," Australian Meteorology Magazine, 38, p. 2.

Wallace, J. M., and Chang, C. P., 1969, "Spectrum analysis of large-scale wave disturbances in the tropical lower troposphere," Journal of the Atmospheric Sciences, Vol. 26, No. 5, Part 2, pp. 1010-1025.

World Meteorological Organization, 1969a, Estimation of Maximum Floods, No. 233, TP. 129.

_____, 1969b, Manual for Depth-Area-Duration Analysis of Storm Precipitation, No. 237, TP. 129.

Appendix A

ATS-III Data Enhancement System

T. W. Schwalenberg

Introduction

The purpose of this paper is to describe that portion of the University of Wisconsin ATS Data Facility, located at the Space Science and Engineering Center, which provides the capability to produce enhanced pictures. Operationally, the Video Enhancer allows the user to choose three regions of input levels and to adjust the proportion of the film's density range which each of these regions will occupy on the finished picture.

ATS Data Facility

At the University of Wisconsin Space Science and Engineering Center an operational data facility exists solely for the purpose of producing ATS

pictures, digital tapes, film loops, and related products. This ATS Data Facility has the complete library of analog ATS tapes produced at the Mojave, Rosman and—more recently—the Wallops ground stations. Most of these tapes were recorded using the Westinghouse synchronizing system, the digital core and the FR-1900. (Reference: ATS Technical Data Report, Section 8.1.3 SK-1600B/FR-1900 Analog Recording Subsystem.) The facility also has the original SK-1600 tapes. In addition to this archive library, the facility also has a telephone line to NESS (Suitland) over which lower resolution, real time, ATS-I and ATS-III data are regularly received.

The basic ATS Data Facility is shown in Figure A-1.

Enhancement System

The actual voltage levels coming from the "Transcriber System" and fed to the "Precision Display" is zero to plus ten volts maximum. This means that deep space is represented by zero volts and the highest radiance cloud possible is represented by ten volts, with all other radiances falling in between. Without enhancement, the zero- to ten-volt signal results in a certain optical density range on the finished negative. Exactly what portion of the gamma curve of the film is used is determined by two calibrated operational adjustments within the precision display.

One adjustment, the "intensity control," sets the "fogging" density (film density for zero volts inputs) on the film. The other adjustment, the "attenuation factor," sets the optical density change from the fogging density, as the input voltage increases from zero to plus ten volts. These two adjustments are settable to 0.1%, and, operationally, their effect is repeatable to this tolerance. Their purpose is to allow the precision display to make optimum and consistent use of the film's dynamic range (gray scale). Once the Intensity and Attenuation Factor is set, the film density range is determined for the input voltage range of zero to plus ten volts.

On the data input end of the facility, the video contains linear radiance information. On a zero- to ten-volt scale, ocean for instance, is from zero to about 0.25 volt (except in the vicinity of the sun glint). Land usually is from .25 volts to 1.25 volts. Thin and/or low level clouds take up most of the mid range; and high level and/or dense clouds get into the seven- to nine-volt range. Only the cores of the very deepest large storms get into the nine- to ten-volt range. When a normal picture is produced, all this information is normally compressed into the limited gray scale of the film. However, using the enhancement system, it is possible to modify this relationship and to choose various ranges of video and expand them to cover a larger portion of the film gray scale.

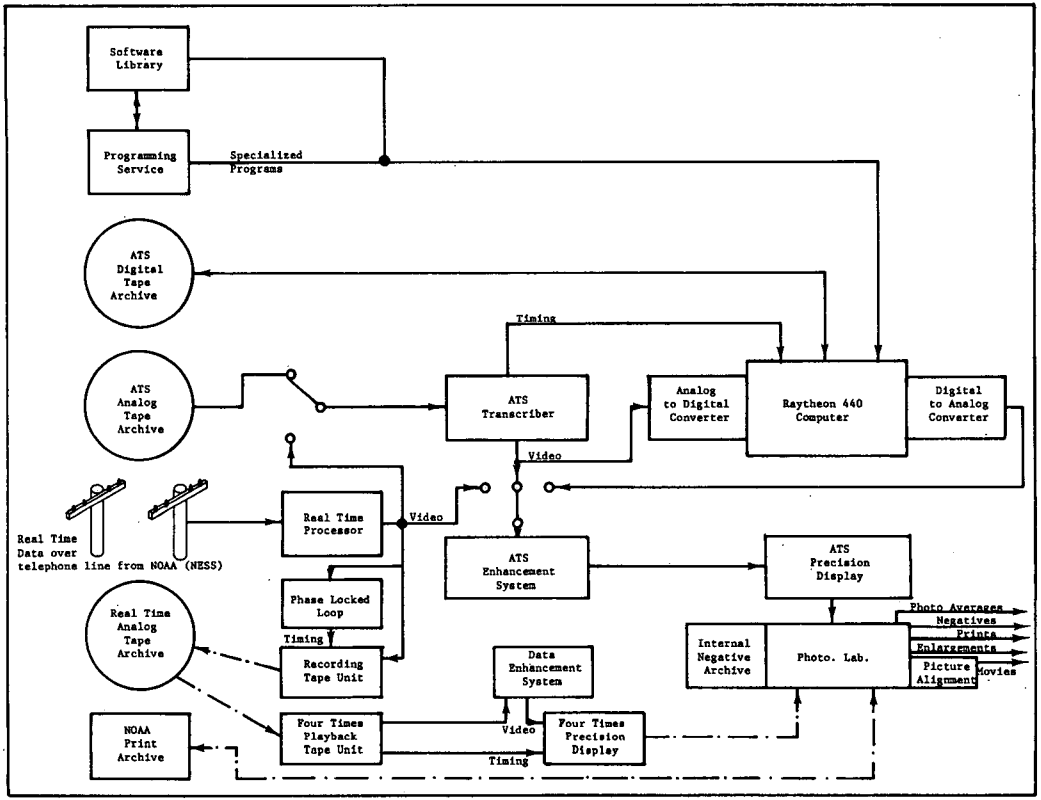
Software Library
Programming Service
Specialized Programs
ATS Digital Tape Archive
ATS Analog Tape Archive
Timing
ATS Transcriber
Analog to Digital Converter
Raytheon 440 Computer
Digital to Analog Converter
Video
Real Time Data over telephone line from NOAA (NESS)
Real Time Processor
Video
ATS Enhancement System
ATS Precision Display
Photo Averages
Negatives
Prints
Enlargements
Movies
Picture Alignment
Phase Locked Loop
Timing
Real Time Analog Tape Archive
Recording Tape Unit
Data Enhancement System
Internal Negative Archive
Photo. Lab.
NOAA Print Archive
Four Times Playback Tape Unit
Video
Timing
Four Times Precision Display

Fig. A-1

The enhancement system consists of two types of enhancement: level enhancement and contour enhancement. The "level enhancer" provides five independent adjustments which allow the user to choose up to three regions of video input and determine how much of the film density range each region will cover. Looking at it in a slightly different way, the operator can specify the "gain" of an amplifier, independently in each of three input voltage ranges. In Figure 2, G1, G2, and G3 represent these gains and BP1 and BP2 stand for the breakpoints which specify the three regions. These five variables are controlled by the user to produce various effects. For instance, if G1 is made quite large over the range of zero to 1.25 volts, land information will be expanded to take up a large amount of the film gray scale and consequently more land detail will be noticeable in the picture. Of course, the gray scale range of the film is not altered, so that if one region is expanded, another must be compressed.

The "contour enhancer" was added in an attempt to quantify images. In effect, what the contour enhancement system does is to instantaneously superimpose on the video a high-level, short-duration pulse whenever the video equals a predetermined voltage. This reference voltage can be adjusted over the entire zero- to ten-volt range via a calibrated control, with repeatability to 0.1%. The effect on the picture is to put white dots wherever the video level is the same as the set reference level. In effect, the picture is contoured for this one level. Also a picture may be re-run a number of times with the reference level changed for each picture, and the resultant set of pictures would give an indication of radiance distributions.

To date, contour enhancement has been used in conjunction with a project to determine rain distribution in northern South America. In this case the principal investigators contoured the clouds to show the density texture at high radiances and found a correlation between rain and clouds with sharp well-defined "cores" (areas of significantly higher densities within clouds). In order to achieve the desired contouring for this project, it was necessary to combine both level enhancement and contour enhancement, as shown in Figure 3. Figure 4 shows the actual settings and resultant transfer functions achieved. In this application, level enhancement was used to do a number of things. First, it compressed the entire picture so that the high-level pulses from the contour enhancement would be discernable when superimposed over the white clouds. Second, it further compressed most of the mid-range radiances where no clouds of interest would be found. And, third, it expanded the low and extreme high ranges in order to accent the land (which would be used for reference) and to bring out the texture of the high radiance clouds. The overall effect was to produce a rather dark picture with good land features along with textured gray clouds with white dot contours indicating which areas of these clouds were above a given brightness level.

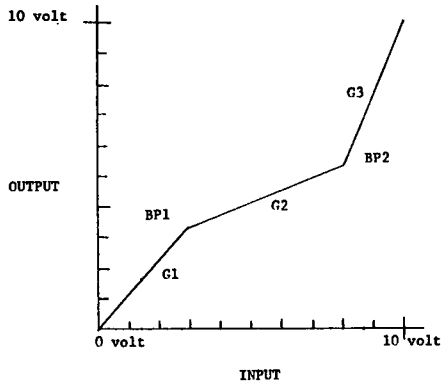

Figure A-2. General Response of ATS Level Enhancer

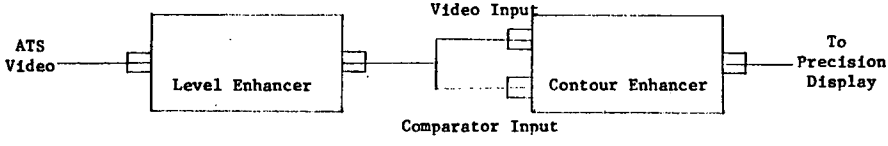

Figure A-3. Combination of Level Enhancer and Contour Enhancer

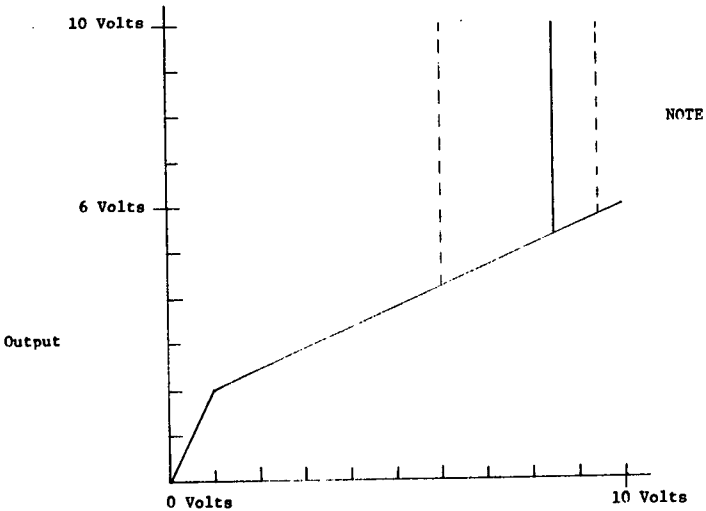

NOTE: Contour levels of 6 volts to 9 volts, in half volt increments, were used to produce a set of pictures.

Level Enhancer Settings		Contour Enhancer Settings	
G1= 862	BPL= 137	6.0v= 374	8.0v= 441
G2= 706	BP2= 950	6.5v= 393	8.5v= 463
G3= 950		7.0v= 410	9.0v= 477
		7.5v= 422	9.5v= 495

Figure A-4. Rain distribution transfer function resulting from combining the Level Enhancer and the Contour Enhancer.

Conclusion

This paper attempted to give a brief overview of the enhancement capability of the ATS data facility located at the University of Wisconsin Space Science and Engineering Center. Additional technical information about the facility can be obtained for the asking as well as the products and results of the above-described project.

Video Enhancer

Introduction

The video enhancer was developed to enable the linear response of the ATS data to be modified in order to enhance the "meteorology" contained in the photographic product made from this data. Basically, the video enhancer has a linear piecewise transfer function, with virtually independent control over the gain of three linear regions and the location of the two breakpoints which determine these three linear regions.

Operationally, the video enhancer allows the user to choose three regions of input levels and to adjust the proportion of the film's density range each of these regions will occupy on the finished picture.

Specifications

Input voltage:	0 to +10 V
Input impedance:	. 10 k ohms
Bandwidth:	12 KHz
Output voltage:	0 to +10 V (short circuit protected)
Output drive capability:	15 ma maximum
Power:	115 Vac, 60 Hz, 50 ma

System Operation

The video enhancer has been designed to work with a 0 to +10 volt video range. To use this unit, it is installed in the video data stream at some

convenient point where the video levels correspond to the 0 to +10 volt range. Once installed, the appropriate enhancement function is determined and set in via the five controls.

The enhancement function to be used is determined accordingly to meteorolgocal requirements and is defined in terms of breakpoints and gain settings, which in turn are tied to input and output voltages. Setting up the video enhancer consists of determining which control settings produce the desired enhancement function.

The quickest way to set up the video enhancer is to apply a 0 to +10 volt, periodic sawtooth signal to the input and compare the output to the input on a scope. If the sawtooth is used to drive the horizontal sweep of the scope, and the external horizontal sweep gain is adjusted to give exactly 10 cm of sweep for the 0 to +10 volts of the sawtooth, and if the video enhancer output is applied to the vertical input, the scope will display the transfer function. Once the scope is set up, the control settings for various enhancement functions can be very quickly ascertained. Figure A-5 shows an even easier setup if the scope used has an external "sweep" signal available.

Because the video enhancer is implemented with operational amplifiers the control settings should be very stable and very repeatable over long time periods, especially if the unit is operated in the temperature controlled environment of the laboratory.

Theory of Operation

From the system point of view, the video enhancer consists of two amplifiers whose gain is a function of the video level. Each amplifier has one gain for video inputs below a specific level and another gain for inputs above this level. The outputs of these two amplifiers are summed to give the required piecewise linear response. Figure A-6 shows the schematic of the video enhancer. The video signal first enters a buffer consisting of a non-inventing unity gain operational amplifier circuit with complementary power-drive capability. The buffer drives the two amplifiers whose gain is level dependent.

The high level suppressor is a basic inverting operational amplifier circuit with a higher gain for low levels than for high levels. The low level gain is the ratio of the 27K resistor to the series combination of the 2K resistor and the setting of the 100K potentiometer. This potentiometer is labeled G1 (gain 1) and determines the gain for the first region of the piecewise linear response of the video enhancer. See Figure A-7. The gain of G1 ranges from : $\frac{27K}{2K} = 13.5$ to $\frac{27K}{102K} = 0.26$. When the output level of

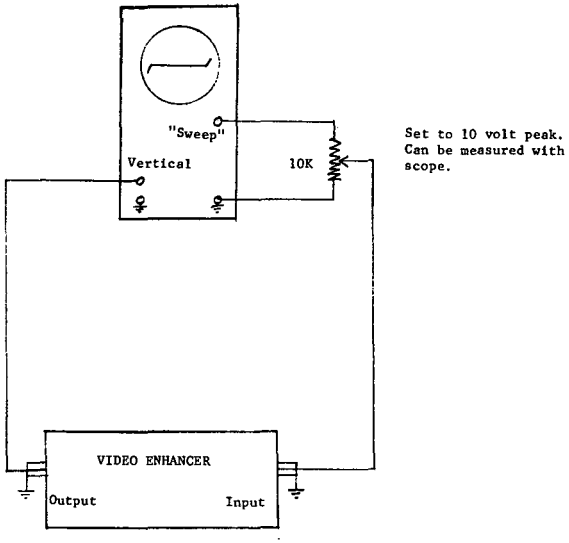

Figure A-5

the high level suppressor reaches the voltage determined by the setting of the 1K potentiometer labeled BP1 (breakpoint 1) the 25K potentiometer labeled G2 (gain 2) is switched in parallel with the 27K resistor. This has the effect of lowering the operational amplifiers' feedback resistance and thereby decreases its overall gain. The gain after BP1 is determined by the setting of G2 and is given by $\frac{27K//G2}{2K + G1}$. The 1K potentiometer allows the adjustment of BP1 over the range from 0 to +10 volts.

The low level suppressor is a basic non-inventing operational amplifier circuit whose low level gain is very small $\frac{18K}{1M} = 0.018$ and whose high level gain depends on the value of the 100K potentiometer labeled G3 (gain 3). G3 ranges from $\frac{18K}{102K} = .17$, to $\frac{18K}{3K} = 9.0$. The exact input level at which the gain changes is determined by the setting of the 1K potentiometer labeled BP2 (breakpoint 2). BP2 can be adjusted from 0 to +10 volts.

The output stage is a basic inverting operational amplifier stage wired as a summer with a gain of 1 for both inputs, and with its output limited to

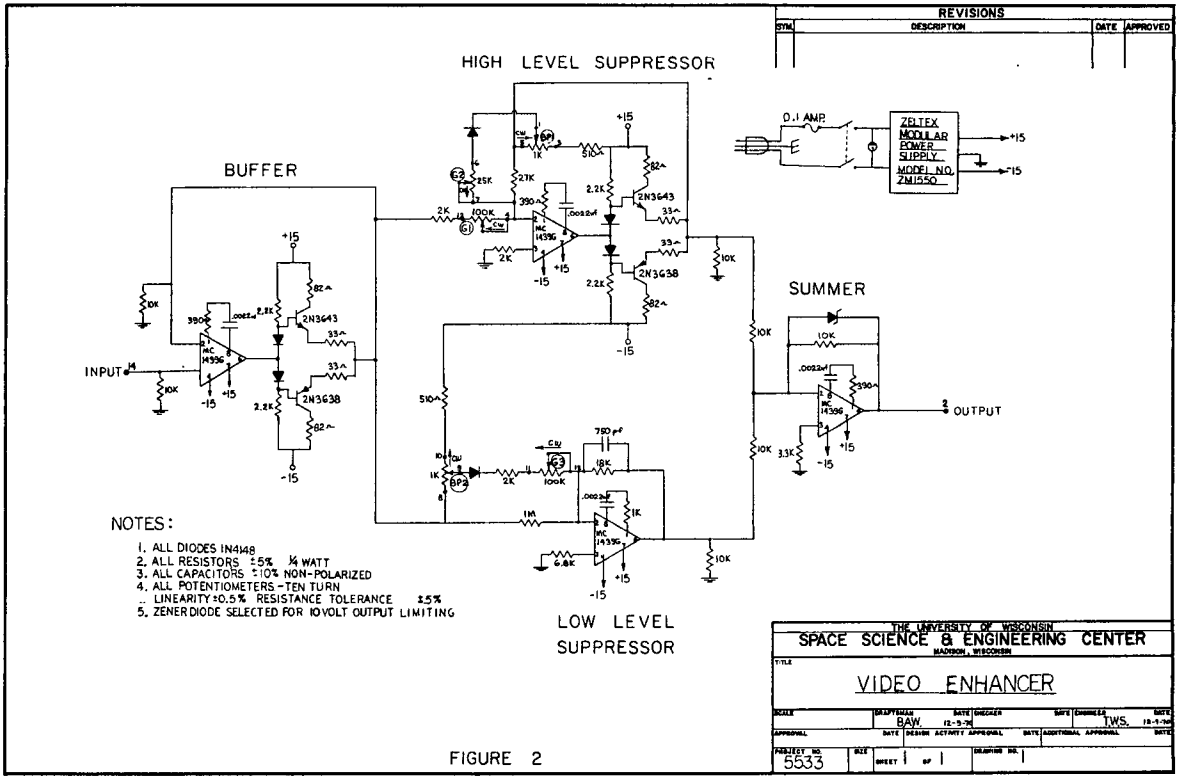

FIGURE 2

Fig. A-6. Video Enhancer

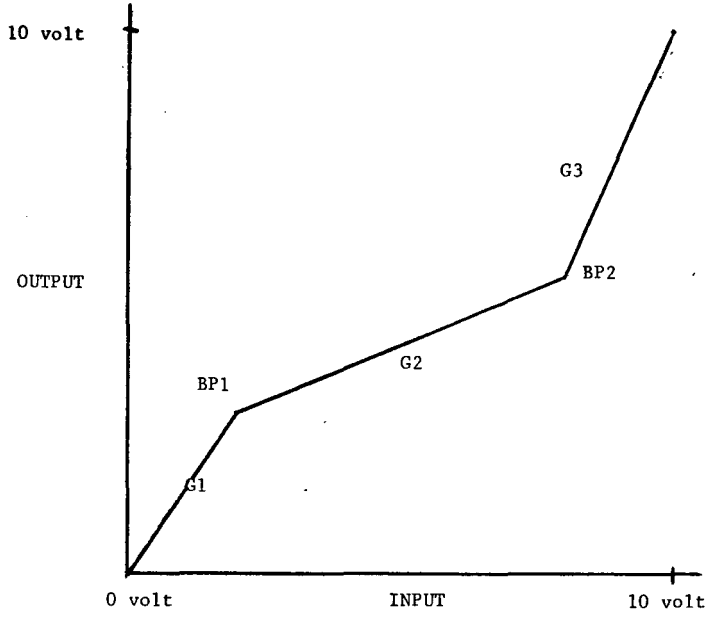

Figure A-7

+10 volts. Thus the basic piecewise linear response of Figure A-7 is implemented.

ATS Contour Enhancer

Introduction

At the University of Wisconsin Space Science and Engineering Center, an operational data facility exists solely for the purpose of producing ATS pictures, digital tapes, film loops and related products. This paper describes the "contour enhancer" which provides the contour enhancement capability of this facility.

C3

Specifications

Input Level:	0 to +10 volts
Input Impedance:	100K
Frequency Response:	D. C. to 10 KHz
Output Level:	0 to +10 volts
Output Drive Capability:	15 ma maximum

Theory of Operation

The "contour enhancer" compares the input video level to an adjustable reference, and superimposes a high level narrow pulse of the video whenever they are equal. The reference level is adjustable, with the external control labeled "contour level set," over the entire range of 0 to +10 volts. The control is a ten turn potentiometer with a calibrated dial settable to 0.1%. Overall linearity is about 1%, so that the dial is calibrated in reference voltage directly. A more precise setting can be accomplished by using a scope and sawtooth generator.

The contour enhancer is usually used in conjunction with the level enhancer as shown in Figure A-8. The main purpose of the level enhancer is to darken the picture so that the superimposed high level pulses will be clearly visible. This is especially important if storm clouds are being contoured.

In actual operation, the video to be contoured is applied to both the comparator input and the level enhancer; and the output of the level enhancer is applied to the video input. The comparator is an operational amplifier operated open loop. The operational amplifier output remains at high level saturation whenever the video is less than the reference set in and remains at low level saturation whenever the video is greater than the reference set in. As the video changes from higher than the reference to lower than the reference, or vice versa, the comparator output level very quickly changes from one saturation state to another. The speed of transition is a function of the slow rate of the operational amplifier and not the rate of change of the video signal because of the extremely high open loop gain of the operational amplifier.

The output of the comparator is differentiated with an RC differentiator having a time constant of $0.1 \times 10^{-6} \times 20 \times 10^{3}$ = smsec. to give a positive expodential pulse at the time the video level goes from greater than the reference to less than the reference, and a negative expodential pulse at

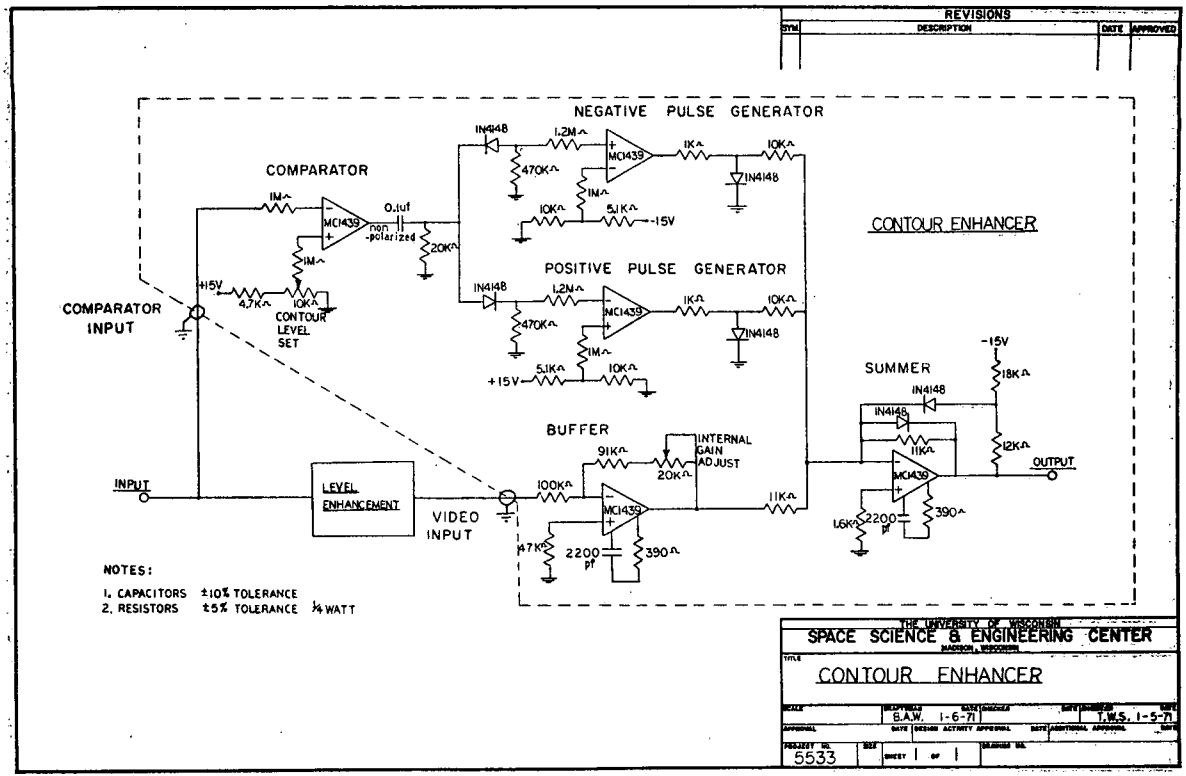

Fig. A-8. Contour Enhancer

the time the video level goes from less than the reference to greater than the reference. The positive expodential pulse is directed to the "positive pulse generator" and the negative expodential pulse is directed to the "negative pulse generator" by steering diodes.

The positive and negative pulse generators are operational amplifiers operated open loop as comparators, with the reference voltage set at about 67% of the peak height of the expodential pulses. The output of both pulse generators is a square 0 to -14 volts pulse of about 2msec. duration. Note that the output pulses from both pulse generators are of the same polarity even though the input expodential pulses are of opposite polarities.

The "buffer" (see Fig. A-8) has a gain internally set to 1 and its purpose is to accept the video from the "video input" through a relatively high impedance and present it to the "summer" through a relatively low impedance. In the summer, the video and the pulses are added to produce the required contoured video.

APPENDIX B

A Demonstration of the Intercontinental Exchange of Graphic Data Utilizing Telecopiers and Radio Telephony

J. A. Weinman
R. C. Grosh
R. Calheiros
C. W. van Scherpenzeel

Introduction

The time scale which frequently characterizes meteorological phenomena in the tropics may be of the order of a day or less. It is occasionally desirable to send graphical meteorological data in real time to those who are directly affected by tropical weather. Unfortunately, rapid communications channels are not always available for this purpose. The test described below demonstrates the feasibility of exchanging graphic data between widely separated locations by means of amateur radio equipment and telecopiers.

Instrumental Considerations:

The recent development of the telecopier X-400 by the Xerox Corporation* renders it feasible to transmit documents by means of communications systems used for voice transmission, viz. telephones or amateur radio. The telecopier X-400, shown in Figure B-1, is a portable machine measuring 16.5 × 50.5 × 40.5 cm, and it weights 11.3 kg. The telecopier was easily transported as hand luggage between Madison (USA) and Bauru (Brazil) by airplane and various automobiles and buses. The telecopier operates on 110v. 60Hz and it draws .5 amps.

The 21.6 × 28.0 cm picture produced by the telecopier consists of a raster of 19.7 lines/cm. burned black or grey into specially treated paper. The picture resolution is comparable to that of a U. S. television picture. The telecopier produces pictures with six shades of grey. This contrast is comparable to that which is found in newspaper pictures. Telecopy pictures can be transmitted in about 5 minutes. Each telecopier can send and receive graphical data; two-way communication is therefore feasible.

The telecopier signal is a frequency-modulated audio frequency carrier. The picture may therefore be transmitted over voice quality radio transmitting equipment. The audio signal level from the telecopier is very high; care must therefore be exercised not to damage linear amplifiers and other transmitting equipment. The telecopier signal should not be transmitted with equipment rated only for intermittent voice operation.

The transmitting stations which participated in this test were:

Call letters:	W9YT	PY20Y
Operator:	Scott Ellington	Guilheame Ferraz
Location:	Madison, Wisconsin USA	Bauru, S.P. Brazil
Transmitter:	Drake T-4XB	Collins 32 S-3
Amplifier:	Linear, grounded grid	National N CL-200
Output power:	1 kw.	1 kw (2kw., p.e.p.)
Antenna:	Five element Yagi	Mosley TA-33
Mast height:	26 m	30 m

Any single sideband receiver with a nominal 3 kHz bandwidth appears to be sufficient to receive telecopy pictures. Although care should be

*Xerox Corporation, Xerox Square, Rochester, New York, USA.

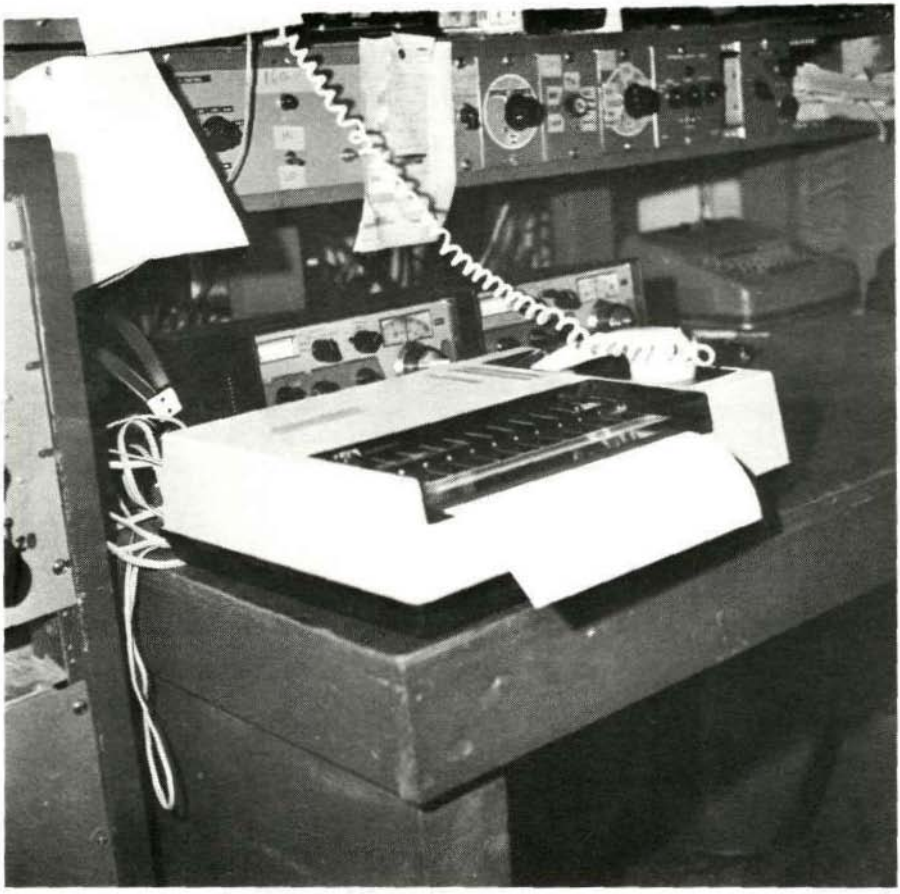

Fig. B-1. Telecopies X-40 connected to the transmitter of W9YT.

Reproduced from best available copy.

taken to tune the receiver, a small frequency error (less than 200 Hz) does not seem to degrade the picture quality. Strong signals are necessary for clear pictures because interference from other stations appears to be the greatest source of picture degradation.

Results

Figure B-2 shows the results of our first transmission, from Madison to Bauru, conducted on August 27, 1970. The transmission was conducted at 21 MHz, signal strength was 5-8 to 5-9, and propagation conditions were normal. (We also sent graphic data from Bauru to Madison during these tests.)

It is instructive to compare the picture of South America as viewed by ATS-III, which was transmitted from Madison, with the picture of the east coast of Brazil received by the APT receiving equipment at Bauru. The dashed lines mark the area which was observed by the ESSA-8 satellite. The lower picture shows the telecopy of this ATS-III picture received in Bauru. Both APT and ATS-III pictures show the stationary front over Sao Paulo and Guanabara. The coastal clouds over Espirito Santo and eastern Bahia are visible, and the cloud-free region over Minas Gerais and western Bahia is also evident on all pictures. Note that the original pictures were of better quality than the third generation copies shown in these figures.

Because the telecopier grey scale response is somewhat limited, and because the density of a photograph is not a linear function of brightness, it is desirable on occasion to transmit maps which present the voltage output of the satellite camera signal. An isodensitracer circuit* was therefore constructed; this circuit yields a bright output signal when the input signal exceeds a predetermined voltage.

Figure B-3 shows a detailed view of Surinam obtained on September 13, 1970. The ATS-III satellite produces pictures with spatial resolution between 3 and 12 km. which clearly show the location of mesoscale phenomena such as cumulus congestus clouds. Isophots corresponding to satellite camera signal voltages exceeding 6.5 volts are shown in this figure. It is noteworthy that Paramaribo was subjected to 15 mm. of rainfall during the afternoon when the picture was taken. (The crosses represent intersection of 1° increments in latitude and longitude.)

---

*A detailed description of the isodensitracer circuit will be found in the M.S. thesis of R. C. Grosh.

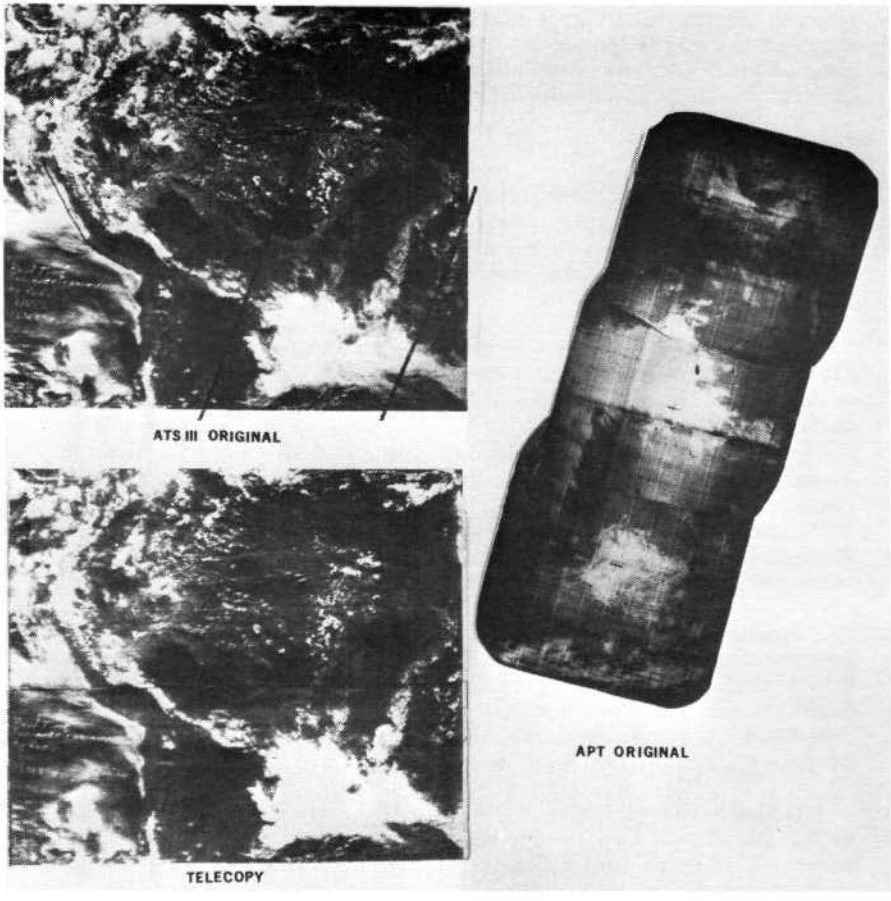

Fig. B-2. Comparison of pictures of South America on Aug. 27, 1970, viewed by the ATS-III satellite. This picture, transmitted from Madison, Wisconsin, is compared with the picture obtained from the telecopier connected to the receiver of PY20Y in Bauru. The picture obtained from the APT is also shown for comparison. The dashed lines bound the area observed from the ESSA satellite.

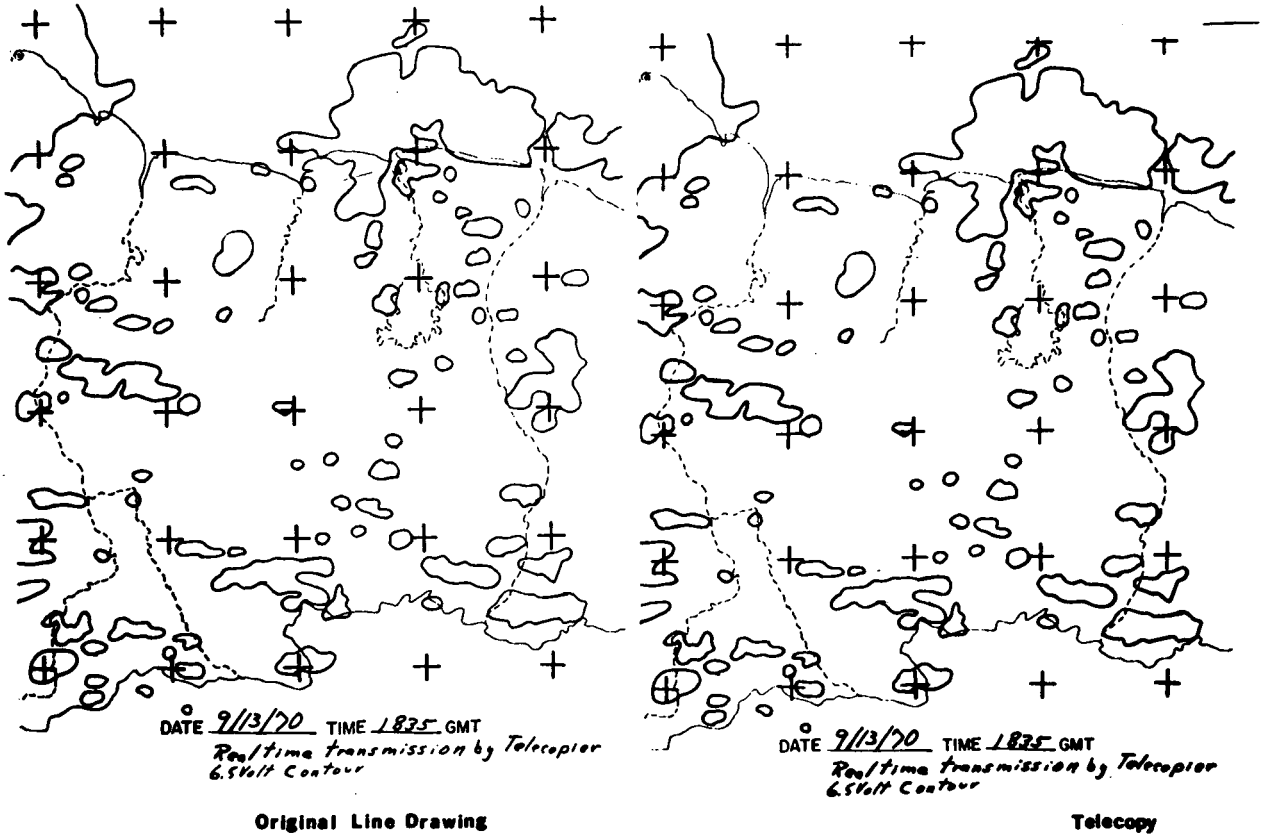

Fig. B-3. Close-up view of Surinam on Sep. 13, 1970 derived from an ATS-III picture. The isophots delineate regions covered by clouds whose brightness produced a signal greater than 6.5 volts.

Figure B-3 shows the original map and the copy received in Paramaribo by means of the telecopier and the receiver of PZIAK operated by Mr. Ed Deira. The transmission was conducted at 21 MHz, signal strength was 5-8 to 5-9, and propagation conditions were reasonable. This test demonstrates that line drawings, such as weather maps, may be transmitted by radio with good clarity.

The telecopy pictures were received in Bauru and Paramaribo a few hours after they were taken by the ATS-III satellite. If such picture transmission would be conducted regularly, the delay could be reduced to one hour.

Conclusion

We have demonstrated that it is technically feasible to exchange graphical scientific data between widely separated locations by means of conventional amateur radio and office copying equipment. The pictures compare favorably with pictures transmitted by currently available methods. It should be noted that pictures may be sent in either direction. We believe that the relatively modest cost and simplicity of the apparatus required to process these pictures should enable scientists separated by great distances to exchange data in real time.

Acknowledgments

We would like to express our thanks to Messrs. Scott Ellington, Art Boyars, and Stan Burns of the University of Wisconsin Badger Amateur Radio Society, Mr. G. Ferraz of Bauru, Brazil, and Mr. Ed Deira of Paramaribo, Surinam, who established the necessary radio links. We also wish to acknowledge the assistance of Messrs. Terry Schwalenberg and Dave Cadle of the University of Wisconsin Space Science and Engineering Center, whose efforts made it possible for us to obtain the ATS-III pictures.

The telecopiers were provided by Mr. H. Johnson of the Xerox Corporation; we hereby express our gratitude for his cooperation in this venture.

Funds for this experiment were provided by Fundacão de Amparo a Pesquisa do Estado de São Paulo, the United States National Science Foundation and National Aeronautics and Space Administration and the Graduate School of the University of Wisconsin. We would like to thank these agencies for their support.

N72-27650

Design of a Small Radar Altimeter for Balloon Payloads

Ferrel G. Stremler
Charles D. Blair
Robert A. Oehlkers

Abstract:

The radar altimeter design described here is intended primarily for high-altitude balloon flights. It permits one to make geometric altitude measurements up to 35 km over water and 13 km over land to an accuracy of 0.03%. Minimum altitude for operation is 2 km although this can readily be extended down another kilometer by readjustment of circuit parameters. Range ambiguity is equal to the minimum range of the device.

The complete altimeter, excluding power source, weighs less than 100 grams. It is designed to operate at temperatures down to -55°C and to be nonhazardous to aircraft. A schematic diagram of an altimeter which operates at 400 MHz is shown. Test results using this design are given. Units similar to the one described here have been flown on several standard neoprene balloons and on superpressure balloons.

I. Introduction

A direct measurement of geometric height is a recent practical possibility in balloon instrumentation. Normally temperature, pressure and humidity measurements are sufficient to obtain vertical profiles, particularly when samples are taken frequently and the altitude is low. With increasing emphasis on improved accuracy at higher altitudes and the remote operation of sensor packages, however, the possibilities of absolute measurements of altitude become quite attractive.

The motivation for the development of a small radar altimeter is to enable one to make an independent accurate measurement of geometric altitude with very reasonable weight, cost, and power requirements. The idea of such a device was conceived by Prof. Verner E. Suomi and developed by Dr. Nadav Levanon at the University of Wisconsin. Both the theory and a description of a prototype design were described in 1970.* The presentation here describes some results of further design and development work at the University of Wisconsin to produce repeatedly a very small, light-weight, inexpensive altimeter.

Various types of radio or, more specifically, radar altimeters have been designed and built for aircraft, rocket, and satellite applications. In contrast, the use of such a device on a balloon poses some very different and often very stringent requirements. The radar must be self-contained and accurate, with no special operator requirements. It should not present a hazard to aircraft which may use common airspace. It should be able to operate over wide temperature ranges without sacrificing accuracy. It should operate reliably up to high altitudes and yet consume very meager amounts of power. And above all, it should be cheap and not weigh more than a few grams!

Obviously some compromises must be made. This paper describes an attempt to meet as many of the above demands as possible in the prototype design of an altimeter for high-altitude balloon flights. To keep the design simple, a pulse-type radar is used which seeks and determines its own repetition rate, eliminating elaborate timing circuits. The basic design strategy is to make this device operate at a repetition rate determined by the altitude of the balloon.

II. Principle of Operation

The radio altimeter described here is a pulse-radar system in which the elapsed time period between transmitted pulses is a measure of altitude. A single RF superregenerative stage serves as both the transmitter and the receiver. This stage is an oscillatory circuit held from oscillating by a negative quench voltage. When a positive quench pulse is applied, oscillations are allowed to grow. A pulse of radio frequency (RF) energy results whose envelope area depends on the RF input signal present when the quench pulse is applied. The frequency of oscillation is carefully controlled in these units by coupling to strip lines etched on a teflon circuit board.

---

*N. Levanon, "Balloon-Borne Radio Altimeter," IEEE Trans. on Geoscience Electronics, GE-8, 1, Jan. 1970, 19-30.

As the pulse period approaches the delay time of a previously transmitted pulse returning from the ground, the envelope of the superregenerative circuit output reaches a peak. If the RF superregenerative stage is gated on a little too early or a little too late, the envelope area decreases, as illustrated in Figure 1. A correct operating repetition period T is:

$$T = \frac{2h}{c} + \tau \qquad (1)$$

where h is the altitude, c is the velocity of light, and τ represents the fixed delays in the altimeter circuitry.

The overall operation illustrated in Figure 1 suggests that an error signal could be derived to drive the repetition rate to the correct value. The remainder of the altimeter circuitry is needed to generate this error signal, both in magnitude and sense; to filter it; and to adjust the repetition rate accordingly to keep this error signal small. A block diagram of the complete radio altimeter is shown in Figure 2. The voltage-controlled oscillator (VCO) determines the repetition rate of the transmitted pulses. A sinusoidal voltage at a preset frequency, f_p, is added to the derived error signal to vary the repetition rate about the correct value. Variations at this frequency in the superregenerative detector output are amplified and then multiplied by the sinusoidal voltage to derive a slowly-varying error voltage for controlling the repetition rate. An integrator is used to average the error voltage. Typical values are 200 Hz for f_p and a one-second time constant in the integrator. The closed-loop response shows a close resemblance to the familiar phase-lock loop. * A second-order system is one commonly used for such systems and has been used here.

For short transmitted pulses, the shape of the returned pulse is an integrated version of the transmitted pulse in cases of scattered reflections and an attenuated replica of the transmitted pulse in cases of specular reflection, as shown in Figure 3. In both cases, there is a relatively well-defined break point in the returned pulse at the point corresponding to the trailing edge of the transmitted pulse. Taking advantage of this fact, the altimeter is made to scan from longer to shorter repetition periods and locks on the trailing edge. Shaping of the transmitted pulse waveform aids in making a more uniform return (i. e., one which is not so dependent on the characteristics of the terrain). This has been incorporated so that the representation of the pulse as a rectangular waveform in Figure 3 is for convenience only.

---

*F. M. Gardner, Phaselock Techniques, John Wiley & Sons, New York, 1966.

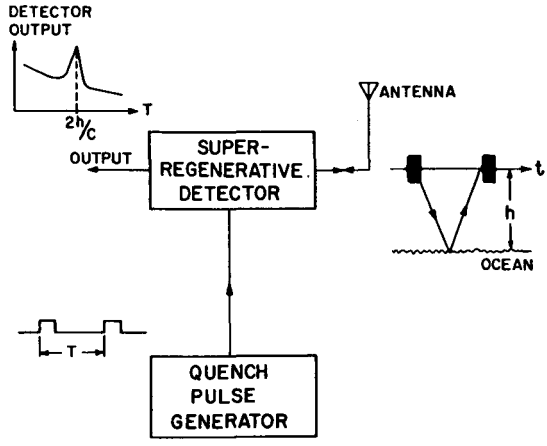

Figure 1. Principle of Superregenerative Altimeter Operation.

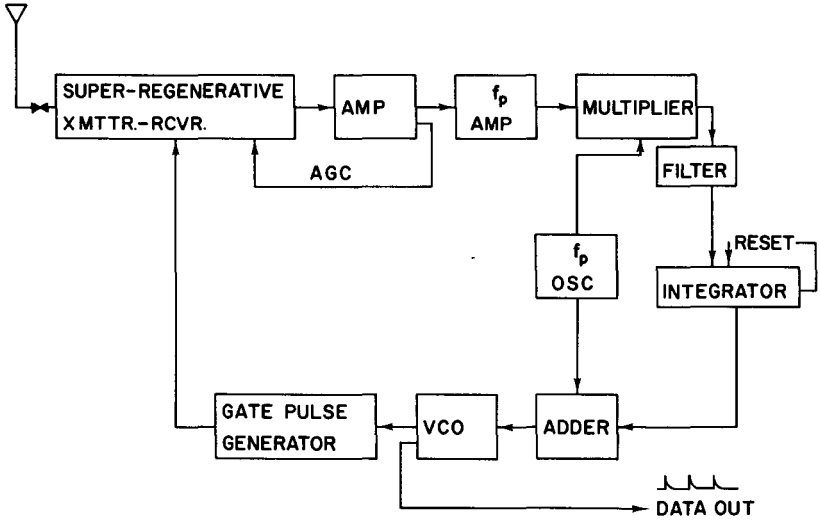

Figure 2. Block Diagram of the Altimeter.

III. Range Ambiguities

The idea of transmitting a pulse as soon as a previous one is received is an efficient means of operation for a radar altimeter. A major drawback of the method, however, is the presence of the range ambiguities which can result. Under certain conditions this is not too serious for balloon flights as long as some other means for coarse altitude readings is available.

The range ambiguity problem arises whenever the altimeter transmits another pulse before the previous one is received. This subharmonic mode of operation can occur at any altitude above twice the minimum altitude of operation. In other words, the range ambiguity of the device is equal to the minimum altitude of operation. This is not a major drawback on high-altitude balloon flights, but becomes quite serious for low-altitude operation. For high-altitude operation, the minimum range has been set at about 2 km.

Allowing for this subharmonic mode of operation, the relations between the geometric altitude, h, and the pulse repetition period, T, of Eq. (1) is extended to:

$$h = \frac{c}{2}(nT - \tau) \qquad (2)$$

where n is the subharmonic mode number. The range of the number n can be restricted by presetting the range of the VCO if the approximate altitude is known in advance. A preferable method is to use a baroswitch or other device to give a crude altitude reading.

Subharmonic operation is desirable to a certain extent, particularly at high altitudes, because the quench pulse frequency remains high yielding more pulses per unit time. Therefore there is a greater average transmitted power and better signal-to-noise ratio. Range ambiguities are equal to the minimum altitude and can be resolved by pressure readings or by extrapolation of the balloon ascent data. On the other hand, changes in the subharmonic mode number directly affect the gain of the phase-lock loop, and this alters the bandwidth and damping factor of the control system. The result is that subharmonic operation is desirable if the variability of the subharmonic mode number is kept low; otherwise it introduces as many problems as it solves. Figure 4 illustrates some test results of altimeter loop behavior with increasing subharmonic number.

The maximum altitude of operation is influenced by transmitter power, antenna gain, choice of operating frequency, terrain, etc. The estimated upper limit for altimeters currently being used is 35 km - 40 km over water and 12 km - 15 km over land using five-element yagi antennas at 403 MHz. These differences in maximum altitude capability are directly proportional to the reflectivity coefficients for the terrain.

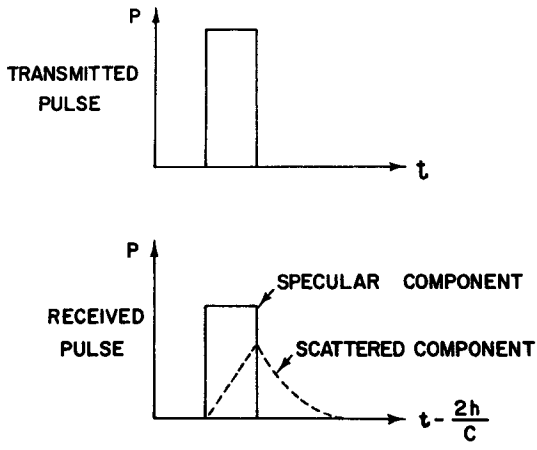

Figure 3. Simplified Transmitted and Received Pulse Envelope Shapes.

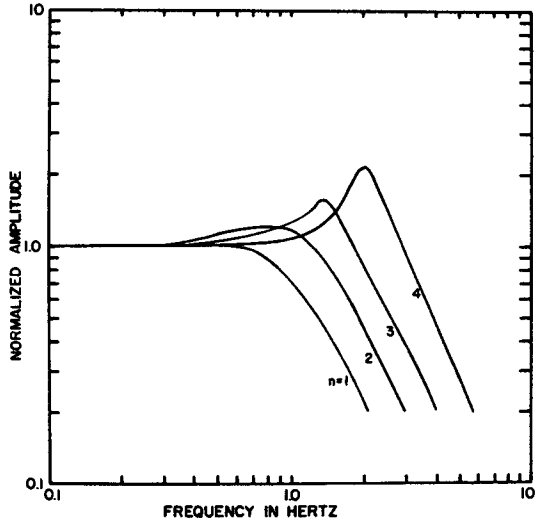

Figure 4. Closed-loop Response Tests for Varying Subharmonic Number.

IV. Output Data

The best means of extracting the altitude data is counting the pulse repetition rate. For short-range balloon flights, such as radiosonde flights, this is relatively easy since the ground station is within receiving range of the altimeter, allowing direct reception of the altimeter signals. The range can be extended considerably on radiosonde flights by modulating the radiosonde transmitter with the VCO pulses.

For longer balloon flights it is more efficient to reduce the data before transmission to the ground station. One way is to sample the voltage at the input to the VCO and use the analog information for the telemetry signal. However, this requires a very linear, temperature-stable VCO characteristic and it is difficult to maintain accurate calibration. An alternative to this is to count the VCO frequency over a given time interval and send the count to the ground station. Currently this is being done by gating the VCO on for 4.7 seconds, using a fourteen-stage counter to count down, and then reading out the last nine digits. The counter is permitted to overflow to provide expanded range accuracy in a given range interval.

V. Circuit Design

A typical circuit design for an operating radio altimeter is described here. An effort was made to design the altimeter with maximum accuracy and reproducibility while attempting to keep weight, cost, and aircraft hazards to a minimum. Design of the unit makes maximum use of the availability of low-cost self-compensated operational amplifiers. While this does not always yield the lowest power consumption—this altimeter design requires one watt of average power at $\pm$ 12 volts—it does enable one to obtain a very repeatable system performance and convenient circuit changes for different experiments and also aids in keeping adjustments to a minimum. The complete unit, except for the antenna, can be constructed on two small printed-circuit boards requiring less than $100 in parts. Use of military-grade components assures dependable operation to -55°C. A schematic diagram of the design chosen is shown in Figure 5.

The RF circuitry of the altimeter is shown in the diagram in Figure 5. It is constructed on a 1/32" teflon circuit board and the remainder of the circuitry is placed on a 1/64" fiberglass epony board. A single transistor, the 2N5108, serves as the superregenerative transmitter-receiver. The RF stage is stabilized by coupling to a quarter-wave microstrip resonator cut to the correct operating frequency.

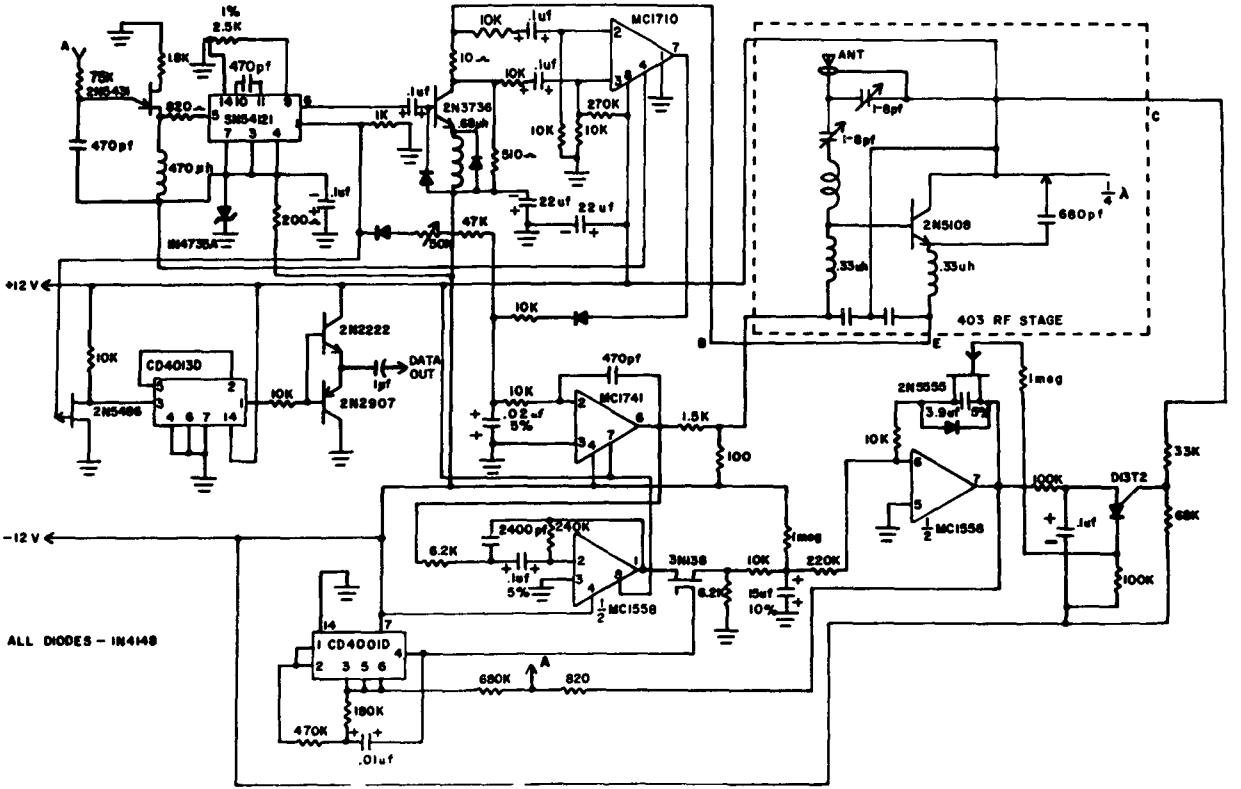

Figure 5. A Schematic Diagram of a 400 MHz Radio Altimeter.

The envelope of the transmitted waveform is developed across a ten-ohm resistor. The pulse-shaping network, a transistor switch in series with an inductance, forces the RF stage to produce a pulse 200 nanoseconds wide and with a peak at its trailing edge. As discussed earlier, this ensures that the altimeter locks to the trailing edge of the returned pulse under varying terrain conditions. Because the variations in pulse width result in the 200 Hz error-signal information, the signal is clipped using a high-speed comparator and then filtered at 200 Hz. The resultant 200 Hz error signal is synchronously detected using an FET chopper, filtered, and integrated. A portion of the 200 Hz generated by the CD4001D is added to the error signal before it is used to drive the VCO (the 2N5431). The VCO controls the timing of the precision quench pulse generator (the SN54121) which in turn controls the gating of the transmitter.

During the locked condition, the VCO repetition period must satisfy Eq. (2). When not locked to a returned signal, the integrator senses a small d. c. offset voltage applied to its input and develops a linearly-increasing voltage at its output. This causes the VCO period to change so that the altimeter performs a search operation. The integrator and the search is reset using a programmable unjunction and an FET. The offset voltage used for the search operation is kept small enough to avoid disturbing the locking behavior of the phase-lock loop.

A photograph of the electronics for the radio altimeter is shown in Figure 6. A ground plane is used on one side of the RF circuit board to prevent interference problems and to serve as the ground plane for the microstrip resonator. A five-element yagi antenna is used for both the transmitting and receiving operations. A photograph of the complete altimeter, excluding power source and thermal packaging, is shown in Figure 7. This complete unit weighs less than 100 grams.

Tests have shown that the new altimeter model has enough sensitivity to lock on specular components in ground clutter, e. g., metal roofs of buildings, etc., beyond the minimum range of the unit. A very convenient and inexpensive test is to point the altimeter at the horizon from the top of a tall building. Minimum signal to maintain lock is 3μv at the antenna terminals.

VI. Recent Test Results

A prototype model of the design described here was flown on a GHOST superpressure balloon by the National Center for Atmospheric Research. The balloon was launched from Christchurch, New Zealand in October 1970 and the data records of the first two days are shown in Figure 8. Power was supplied by a Clevite thin-film CdS solar panel and was sufficient to operate the

Reproduced from best available copy.

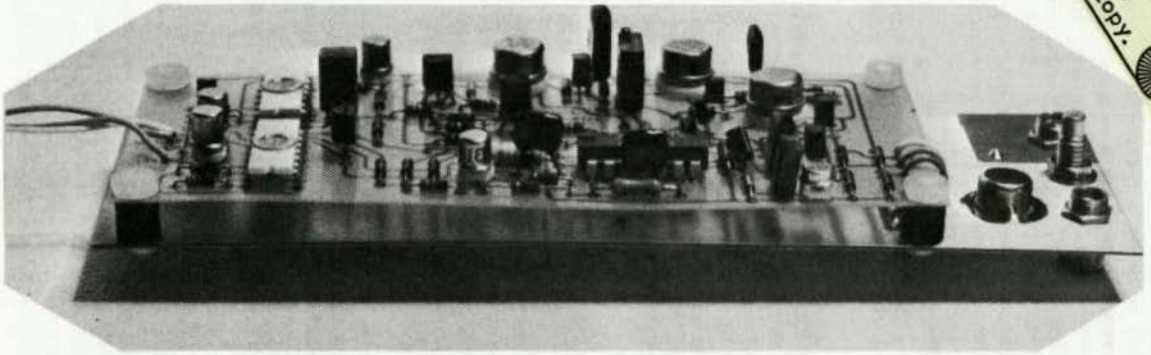

Figure 6. The Radio Altimeter Electronics.

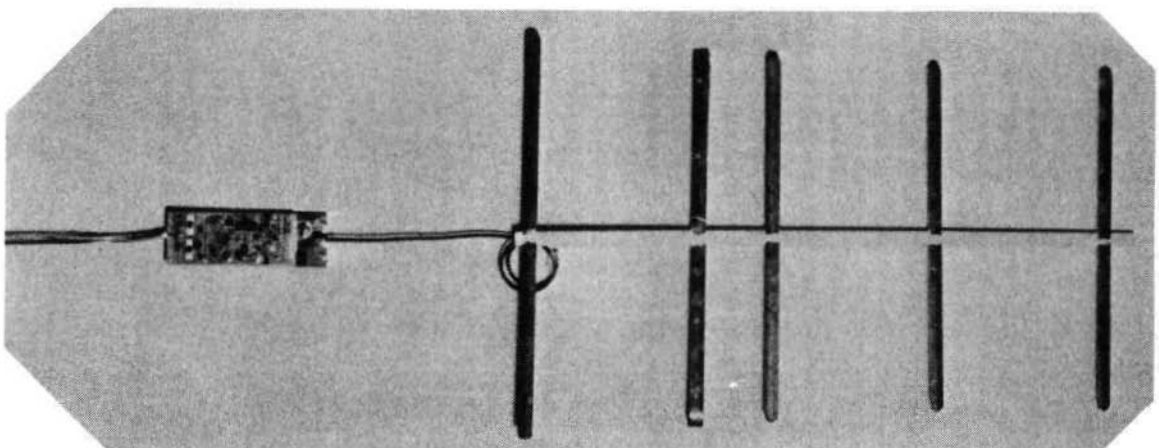

Figure 7. The Radio Altimeter Readied for Flight (without thermal packaging).

altimeter from 20° solar angle. The data shows a gradual decline in balloon altitude together with some short-term fluctuations. The range of the VCO was restricted on this flight to avoid any possibilities of ambiguities. However, the balloon lost enough altitude by the third day that the altimeter would no longer lock.

In an effort to assess the random fluctuations that one could expect in altimeter readings and to determine the maximum usable altitude over land, an altimeter of the design described here was launched from Madison, Wisconsin on July 15, 1971. This altimeter was suspended from a standard 1200 gram neoprene balloon together with a 1680 MHz radiosonde. A string about fifty meters in length separated the balloon from its payload to minimize pendulum effects. Power was supplied by water-activated batteries. The VCO frequency was divided by two in a buffer stage and then this signal was superimposed on the radiosonde modulation. Because this frequency was about two decades higher than those normally used in the radiosonde modulation, it was a rather simple matter to extract this frequency on the ground by filtering. This was applied to a counter with a one-second gate time and printed every two seconds.

Altitude data obtained from the July 15, 1971 flight is shown in Figure 9 and plotted at intervals of one minute from the time of launch. Good performance was exhibited up to about 13 km. The altimeter continued to lock for short periods of time and then lost lock again up to 21 km. Heights calculated from the temperature and pressure data obtained from the radiosonde agreed well with the data shown in Figure 9.

A two-minute segment of the data on the July 15, 1971 flight around 10 km is shown in Figure 10 to illustrate the precision of the altimeter. This data is plotted at two-second intervals (i.e., at the rate that the printer operated) and the differences between successive altitude readings are shown in Figure 11. The rms altitude fluctuations from the mean ascent rate of the balloon are only 1.47 meters for this two-minute segment of data. These results show significant improvements over the data obtained using previous altimeters.* An uncertainty in making comparisons with the previous data, however, is that all of the previous flights were over water. It has been assumed that performance on over-land flights would be poorer for a given altitude as a result of the lower reflectivity coefficient of land. However, the effects of pulse shape also enter. The development of the altimeter concept has progressed to the point where more studies should be devoted to the return-pulse-shape problem. An investigation of the returned pulse as a function of terrain and altitude will be pursued in the next phase of this work.

---

*N. Levanon, ibid.

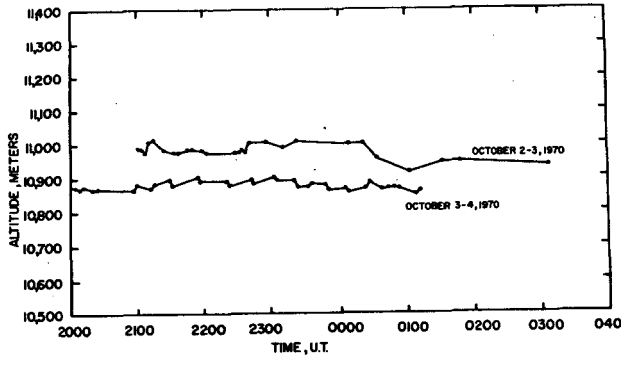

Figure 8. Radio Altimeter Test Data from a GHOST Superpressure Balloon Flight.

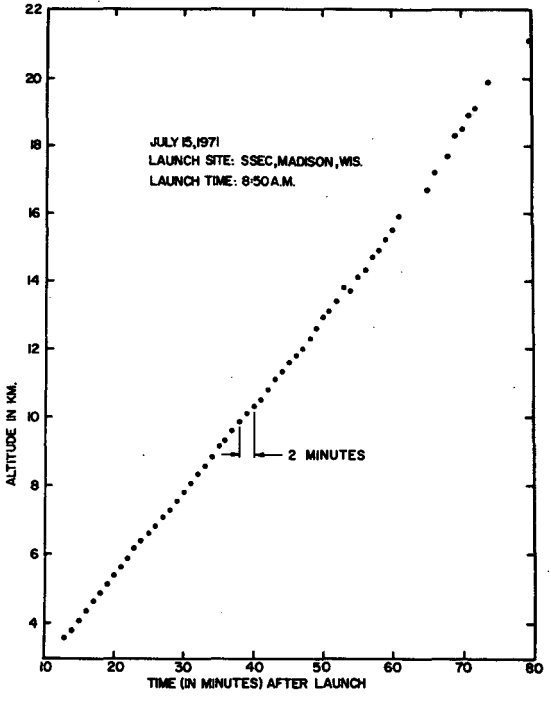

Figure 9. Recorded Altimeter Height Readings during the Ascent of July 15, 1971, Madison, Wisconsin.

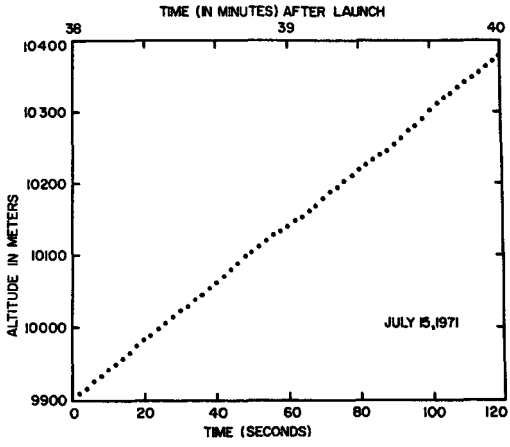

Figure 10. An Expanded Data Record at 10 km during the Ascent of July 15, 1971, Madison, Wisconwin.

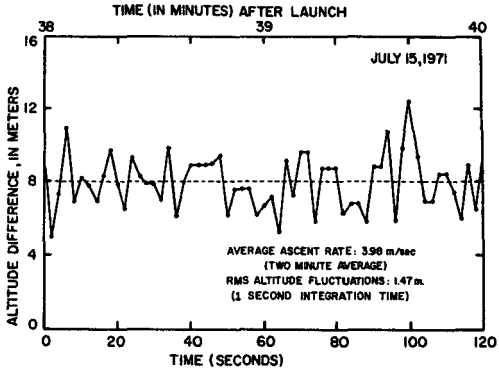

Figure 11. Altitude-Differences for the Data of Figure 10.

VII. Summary and Extensions

The use of recent integrated-circuit developments and careful control of RF pulse shaping have improved the performance of the balloon-borne radio altimeter. Application of feedback techniques has reduced the necessary adjustments and use of solid-state devices and thin circuit boards has reduced its weight and density.

An area for further improvement is the reduction of the power required without sacrificing the performance and without increasing the cost. Presently the parts costs are about $100 in small quantities for the altimeter design described here. The low-power integrated-circuit devices which are becoming available are generally quite expensive.

Future work on the altimeter will include a study of the returned pulse shapes since this is the key to its accuracy. Another area currently under investigation is an absolute altitude calibration of the altimeter. To date any attempt at this has ended up being a calibration of the wrong device! A third area for further work is in the development of altimeters for low-level experiments. To retain the high relative accuracy and to make the altimeter delay (τ) small, requires the use of very fast rise times. Fast rise times in turn require high carrier frequencies. The 1680 MHz allocation has been investigated but is not high enough to offer much improvement. A current possibility is at 4 GHz as the new solid-state devices become available for that frequency.

Acknowledgment

The authors wish to thank electrical engineering students Farrokh Albuyeh and David Platt for their antenna design work. The help of James Maynard and of William Jasperson and Prof. Frank Sechrist of the Department of Meteorology in the flight tests and reduction of radiosonde data are sincerely appreciated. Thanks are due also to Ernest Lichfield of the National Center for Atmospheric Research for the launching of the superpressure balloon from New Zealand.

[redacted]

N72-27651

Averaged Pulse Shape Measurements of Radar Sea Return at Near-Vertical Incidence

Nadav Levanon

Abstract:

This work presents some average pulse shape measurements of radar sea returns at near-vertical incidence. The measurements were made at a 75 cm wavelength, from light aircraft, flying at altitudes of 2 km to 2.3 km, over various water surfaces.

Greater knowledge of the return shapes could help the design of high-accuracy radar altimeters. It could also contribute to several areas of remote sensing.

Both specular and scattered reflections were observed in all the returns, with clear distinction between the two components. Dominance by either the specular or the scattered component was observed, the former being more frequent.

Real-time averaging was obtained by utilizing a sampling technique. This enabled a reduction of the system bandwidth to several hertzs, allowing the use of low peak power RF pulses (1 W), and low-speed chart recorders.

Twenty-one recorded average returns are given, along with an interpretation of the recordings, and a description of the measuring system.

Introduction

Despite many theoretical and experimental works on radar terrain return, there seems to be no easily available answer to the question: What is the shape of a radar pulse return at near-vertical incidence? Some important

works by Moore [1, 2], Edison [3], and Brown [4], give experimental results on earth terrain returns, and Evans [5] measured returns from planetary bodies.

The limited number of experimental results is emphasized by the variety of terrain, such as desert, vegetation, snow, urban areas, lakes and oceans. It is further emphasized by the variety of conditions in which each terrain could be found, e. g., wetness of land, roughness of sea, etc.

An answer to this question could contribute in at least two important areas. First, it could help to improve the design of high accuracy radar altimeters. Altitude accuracies on the order of 10^{-6} and better are required in such areas as satellite geodesy [6], oceanography [7] and meteorology. Second, an answer could yield information on some terrain characteristics such as roughness, sea state, and moisture.

This work presents some measurements of the average shape of radar pulse sea return, at a 75 cm wavelength. These were selected from some 700 returns recorded during six flights over Lake Michigan, Lake Winnebago (Wisconsin), and the eastern Mediterranean near the shore of Israel. Each recorded return is the average (by sampling) of approximately 10^6 received returns. This large amount of data partly compensates for the limitations of the present system and permits some qualitative interpretation.

The main objective of this paper is to present the recorded shapes of averaged sea near-vertical returns. To the author's best knowledge, such measured waveforms have not been reported before.

Two secondary purposes are: a) To support the view that a near-vertical return is a composite of specular and scattered returns; and b) To demonstrate the feasibility of a low-power, low-cost, return shape measuring system, which utilizes sampling techniques for real-time averaging.

Simplified Theoretical Discussion

In the following discussion, the transmitted pulse is assumed to have a rectangular shape.

Specular Reflection

The specular reflection is a mirror-like coherent reflection in which the shape of the returning pulse is an attenuated version of the transmitted one. As is known from optics, in order to obtain the maximum intensity of the

specular component, the mirror should cover the first Fresnel zone. From the height of our flights (2 km - 2.3 km) and the wavelength (75 cm), we get a first Fresnel zone with a diameter of about 60 meters. Such a large mirror perpendicular to the incident radiation is expected to be found only directly beneath the radar.

Moore and Williams [1] give the following equation for the mean received power:

$$P_R(t) = \frac{P_T G^2(0, \phi) \lambda^2 K}{(4\pi)^2 (2h)^2} \qquad (1)$$

where

$P_R(t)$ = the mean received power at time t ($t = 0$ is the arrival time of the first return)

P_T = the transmitted power

h = the altitude

$G(0, \phi)$ = the antenna gain, straight down

λ = the wavelength of the carrier radiation

K = the reflection coefficient, including an indication of what part of the required mirror was actually existing.

For a given geometry and sea state, the mean received power is, therefore, a constant. On a phasor diagram, the above statement and the coherency assumption results in the vector representing the specular field to be of fixed length and angle.

Scattered Reflection

The scattered reflection is a noncoherent reflection from many scatterers on the surface. The first return is a reflection of the leading edge from the radar subpoint. The illuminated area then grows, until the trailing edge is reflected from the subpoint, while the leading edge is reflected from a circle whose radius is approximately $(ch\,\tau)^{\frac{1}{2}}$, where τ is the length of the transmitted pulse, and c is the velocity of light. At this time, if the antenna beam-width is not limiting, the returned power reaches its peak. Moore and Williams [1] have shown that the mean power envelope of the received

pulse is a convolution integral of the transmitted pulse with a function representing the effects of the incidence angle on the average scattering cross section—σ^0 of the ocean, the radar antenna pattern, and the additional attenuation due to a longer path toward a side reflection. They have also shown that if the transmitted pulse duration is considerably shorter than the delay, and the antenna pattern and the ground reflection pattern are assumed constant over the participating angles, then the envelope of the leading edge of the return is given by:

$$P_R(t) = \frac{P_T G^2 \sigma^0 \lambda c t}{4(4\pi)^2 h^3}, \qquad 0 < t < \tau \tag{2}$$

In other words, under these assumptions, the convolution integral is replaced by a regular integral, and a transmitted rectangular pulse is reflected back as a linear ramp, for the duration of one transmitted pulse. Then, for $t > \tau$, those assumptions become less accurate, and the convolution integral will cause a slow decay of the received signal which constitutes the trailing edge.

The scattered field is a random variable. Most authors assume Rayleigh probability density for the field intensity, and an equal probable phase between $-\pi$ and $+\pi$. Less information is available on the power spectrum in cases of near-vertical return. The power spectrum is related, partly, to the sea state, the size and geometry of the illuminated area, and the movement of the radar set. Nathanson [8] has accumulated results of several authors on the relation between surface wind velocity and sea clutter bandwidth at low grazing angles. His summary is that the half-power width of the sea clutter, Δf (Hz), is related to the wind velocity, v (knots), and the wavelength, λ (m), by the linear relation

$$\Delta f = 0.24v/\lambda \tag{3}$$

At our wavelength (0.75m) and at a wind velocity of 10 knots, Δf will equal 3 Hz. The power spectrum broadening as a result of the airborne radar set movement may be calculated [2] as a function of the aircraft height and velocity, and $\sigma^0(\theta)$. Crude calculations will show that the half-power width due to this contribution will also be on the order of a few hertz. The above discussion led us to conclude that on the phasor diagram the vector representing the scattered field has a Rayleigh probability density, its mean power increasing linearly, its phase equiprobable between $-\pi$ and $+\pi$, and its power spectrum a few hertz wide. The last two statements mean that, on the average, the vector will cross any particular angle several times per second.

Composite Reflection

Both the specular and the scattered reflection always exist. However, their proportions change with sea state. The average shape of each one by itself appears in Figure 1. There, P_{SP} is the constant power of the specular return, and P_{SC} is the average power of the scattered reflection at the peak of the envelope, i.e. at $t = \tau$. Note that the logarithmic power scale distorts the linear ramp.

The power envelope of the composite reflection is the sum of the two envelopes. In Figure 2, four theoretical cases appear in which the ratio P_{SP}/P_{SC} equals 100, 10, 1 and 0.1, respectively. The logarithmic power scale emphasizes the significant transition in the shape of the return around the ratio $P_{SP}/P_{SC} = 1$.

When $P_{SP} > P_{SC}$, the envelope resembles the rectangular shape of the transmitted pulse. More precisely, it rises from P_{SP} at $t = 0$ to $P_{SP} + P_{SC}$ at $t = \tau$. However, at that moment, the envelope does not drop to zero, instead it drops to P_{SC}, and from then on follows the envelope of the scattered reflection.

When $P_{SP} < P_{SC}$, the leading edge becomes more complicated. At $t = 0$ there is a sharp rise to the level P_{SP}. During $0 < t < \tau$ the power rises (linearly) until at $t = \tau$ it reaches the level $P_{SP} + P_{SC}$. The drop at that moment, due to the disappearance of the specular reflection, is less noticed. Again, for $t > \tau$ there remains the long trailing edge of the scattered reflection.

The return envelopes appearing in Figure 2 do not include fading. They are each the result of averaging many returns, during a period much longer than the autocorrelation time constant. For shorter averaging periods, fading is noticed. When $t > \tau$ the fading range is that of the scattered reflection. When $t < \tau$ the fading range depends on the relative intensities of the two components. If $P_{SP} > P_{SC}$, the specular component, which was assumed to be free of fading, dominates the return, and the range of fading is relatively small. Again, the case where $P_{SP} < P_{SC}$ is more complicated. During the rise of the scattered average envelope, there is a moment when the average scattered field equals the specular field (e.g. when $P_{SP} = 0.1\ P_{SC}$, this will occur at $t = 0.1\tau$). On the phasor diagram [9] this situation will be described by the sum of a vector of fixed length and direction, and a vector of the same length (on the average) with random direction, which happens to cross any particular angle several times per second. Clearly, when the two vectors happen to be out of phase the chances for a large dip in the envelope are relatively high. In other words, the interference between the specular and the scattered fields will cause fading of the composite return to

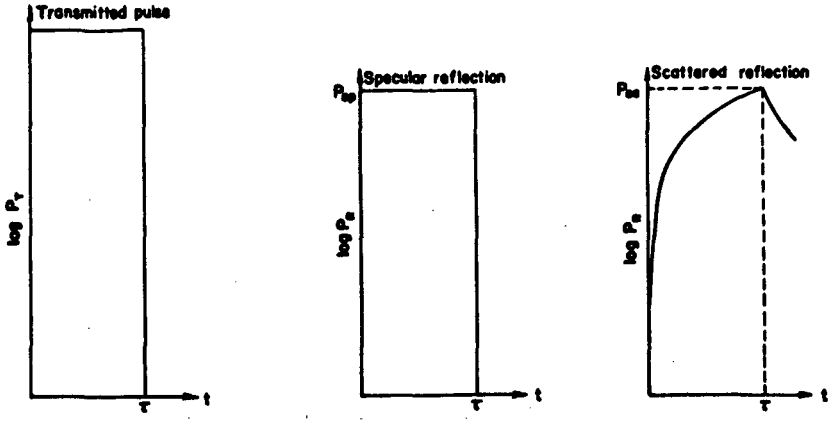

Figure 1. Specular and scattered theoretical average reflections of a rectangular transmitted pulse.

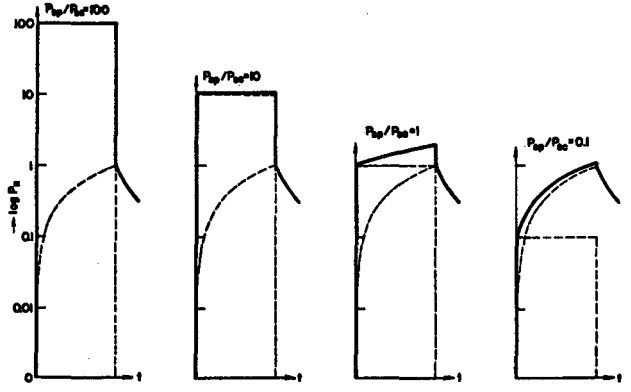

Figure 2. Composite theoretical returns resulted by four different ratios between the specular and the scattered components.

be larger than the fading range of the scattered field alone. The logarithmic power scale will emphasize the nulls rather than the peaks. The time when such nulls are most likely is given by

$$t_{null} = \tau P_{SP}/P_{SC} . \quad (4)$$

The mathematical justification for the above discussion is given in Appendix I.

The Measuring System

The measuring system was a modified radio altimeter used for balloon-borne applications [10]. The recording of each complete return usually requires high bandwidth. Since we are interested in the average return, the system bandwidth could be reduced by applying real time averaging. This was done by utilizing sampling technique. With such a technique there is no need for the complete shape of each single return; rather, each return is sampled once, at a discrete point. Each sample is taken on a different return at progressively later and later points (Figure 3). These samples reconstruct the shape of the return on a much slower time base, hence require a narrower bandwidth.

A simplified block diagram of the system is given in Figure 4. This is a pulse radar system where the pulse repetition rate is varied by a VCO following a sawtooth function. A receiving window exists before each transmitted pulse. As the pulse period approaches the delay time of the returning pulse, the receiving window samples the return. After the repetition frequency is filtered out and a correction is inserted to compensate for the increasing density of samples, the output of the receiver is recorded on a chart recorder to yield the shape of the returned pulse.

The transmitter, receiver, gates and delay blocks of Figure 4 are all combined in a single superregenerative stage. Such a stage when quenched into oscillations shows a receiving sensitivity at the beginning of the oscillation growth, which upon reaching saturation, becomes the transmitted pulse. The superregenerative stage is inherently a logarithmic receiver, with a wide dynamic range.

Another deviation from the simplified block diagram is a small sinusoidal perturbation superimposed on the linear voltage ramp fed to the VCO. That perturbation is synchronously detected from the return signal, producing the derivative of the shape, rather than the pulse shape itself. An integrator is then added before the shape is recorded on the chart recorder. This scheme has some advantages, including a 3 dB improvement in signal-to-noise ratio.

(A) FAST WAVEFORM BEING OBSERVED

(B) VOLTAGE SAMPLES FROM (A) PLOTTED ON SLOWER TIME BASE

Figure 3. The principle of sampling technique.

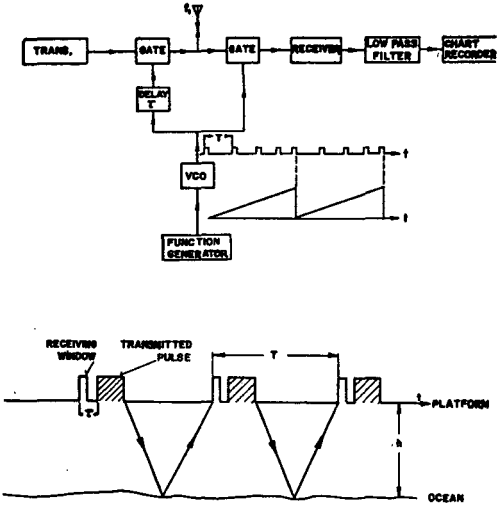

Figure 4. The measuring system principle of operation and block diagram.

However, it adds some limitations which will be discussed later. The compensation for the linear increase in samples density is a fixed bias fed to the input of the integrator.

The general system parameters are summarized in Table I. The system is very simple and light. It was flown on board small aircraft (Cessna 172 and Cherokee 6). If telemetry were used to separate the radar section from the recording section, the former could be carried aloft by a small meteorological balloon.

Table I

Measuring System Parameters

Altitude	2 km - 2.3 km
Radio frequency	403 MHz
Peak RF power	1 W
Pulse width	0.2 μs - 0.6 μs (controlled)
Pulse repetition frequency	30 KHz - 100 KHz
Perturbation frequency	200 Hz
Antenna	2 elements Yagi
Polarization	Linear
Dynamic range	60 dB
Baseline level (approximate)	- 95 dBm
Scanning rate	0.2μs/s - 0.5 μs/s (controlled)
Radar system input power	2W
Radar weight	1 lb.

The System Limitations

Several limitations of the system should be mentioned before an attempt is made to analyze the results.

a. Antenna beamwidth and direction—The two-element Yagi antenna used in all flights has a relatively wide beam, and should start affecting the return significantly only late in the trailing edge. Yet, if the beam is tilted, either by misplacing it with respect to the aircraft body, or by tilting of the aircraft itself, the effect on the return will be twofold: the specular component will be partly attenuated, and the peak of the scattered component will be delayed. A tilt of 15 degrees at an altitude of 2.3 km can cause this delay to be 0.5 μs.

b. Baseline—The stage prior to the recorder is an integrator. Hence, the baseline is an integral of random noise and has fluctuations as well as accumulated random dc level. In addition, a fixed bias is fed at the input of the integrator to compensate for the linearly increasing density of samples. If over-compensation or under-compensation occurs, the baseline will have an undesirable slope.

c. Transmitted pulse—The transmitted pulse is not perfectly rectangular. A typical transmitted pulse has a rise time (10% to 90%) of 130 ns, and fall time of 45 ns.

d. Power scale—While the horizontal time scale could be maintained and calibrated accurately, the vertical power scale is only relative, and its accuracy is ± 15%. As a crude reference, the absolute level of the baseline is approximately - 95 dBm.

e. Harmonic operation—Scanning of the delay range is accompanied by an increase in the pulse repetition frequency, since each receiving window is followed by a transmitted pulse. When this is added to the fact that the delay of the received leading edge is not much longer than the length of the received trailing edge, it becomes clear that when the receiving window scans the leading edge of the prior pulse reflected from the ocean, it also scans the trailing edge of the reflection of the pulse preceding this prior one.

f. Receiving window width—The width of the receiving window is determined mainly by the amplitude of the sinusoidal perturbation superimposed on the voltage ramp fed to the VCO. It is also affected by the superregenerative stage rate of oscillation growth. The period during the beginning of the oscillation build-up which is sensitive to the received signal is not easily defined. However, it is considerably shorter than the chosen perturbation width. The perturbation width cannot be reduced without limit. The detected

perturbation is the system's actual input signal. Reducing its width would reduce the signal-to-noise ratio. Calculated on the basis of the perturbation amplitudes, the effective receiving window widths were: 100 ns in flight numbers 1 and 2, and 20 ns in flight numbers 3 to 6.

Measured Returns

Returns recorded during six flights are given in this section. The flight details are summarized in Table II.

Figures 5 and 6 were both recorded during flight number 3. The specular reflection was predominant during this flight, which explains the rectangular shape of the pulse. The transition from specular to scattered reflection, at $t = \tau$, is clearly visible. To remove a possible doubt, the flat top of the pulse could not have been the result of saturation in the measuring system. The dynamic range of the system was wider than the range occupied by the sea return. This was tested in the laboratory with simulated returns. Figures 7 to 11 were all recorded during flight 5. During this flight, the scattered component was the predominant one. All the returns are characterized by the sharp, fade-free, rise time of the specular component. It is followed by the logarithmic rise (due to the logarithmic scale) of the scattered component which is more susceptible to fading. The point where the scattered component takes over is preceded, in most cases, by a relatively deep null. This is the null discussed in the theoretical section on composite reflection. In Figures 7 to 11, the return peaks appear about 0.5 μs later than the theory suggests. This may indicate that the antenna beam was tilted during this flight. This possibility is supported by the relatively weak specular component observed in this flight.

Figures 12 to 14 are returns recorded during flight number 6 which took place several hours after flight number 5 over the same path. The instrument used for recording returns 12 to 14 was the same as the one used for returns 7 to 11 (transistorized RF stage). The only difference was a slight change in the antenna position, and a calmer sea. This time, the specular reflection was dominant. Similar dominance by the specular reflection is observed in Figure 15, which was also recorded during flight number 6 with, however, the vacuum tube RF stage.

Figures 16 and 17 were recorded during flight number 4. Figure 16 is a sequence of four consecutive sea returns emphasizing the repeatability gained by averaging. Since the baseline during these recordings was not flat, a baseline recorded in the absence of a return is given for reference. For comparison, a return recorded over the city of Tel-Aviv, during the same flight, is given in Figure 17.

Table II

Flight Details

Flight number	Date	Local time	Aircraft	Barometric altitude (ft)	Flight path	Sea state	Max. ave ht. (m)	RF stage
1	10/23/69	10:30-13:00	Cessna 172	6700	Lake Winnebago	calm	0.1	vacuum tube
2	11/19/69	12:00-15:00	"	7200	Lake Michigan off Milwaukee	slight	1.2	"
3	6/28/70	12:00-13:10	Cherokee 6	7400	Mediterranean off Tel-Aviv	smooth	0.5	"
4	7/27/70	10:15-11:30	"	"	"	slight	1.0	"
5	8/17/70	10:45-12:10	"	"	"	moderate	1.5	transistor
6	8/17/70	15:10-16:30	"	"	"	slight	1.2	transistor and vacuum tube

Figures 18 and 19 are returns recorded during flight number 2 over Wisconsin. Figure 18 is a land return recorded several kilometers west of Milwaukee. The specular component is again the dominant one. Figure 19 is a return from Lake Michigan, several kilometers east of Milwaukee. The vertical scale is the same in both recordings, but the lake return is attenuated by 6 dB. The lake return seems to be dominated by scattered reflection; however, the narrow time scale prevents clear distinction.

Figures 20 to 23 were recorded during flight number 1. The first two were over Lake Winnebago, and the last two are land returns recorded several

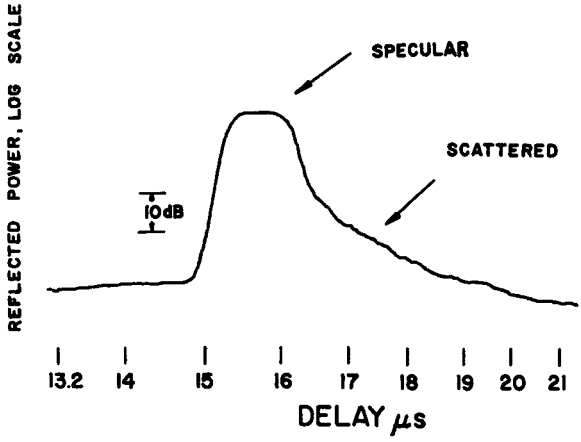

Figure 5. Recorded sea return (flight number 3)

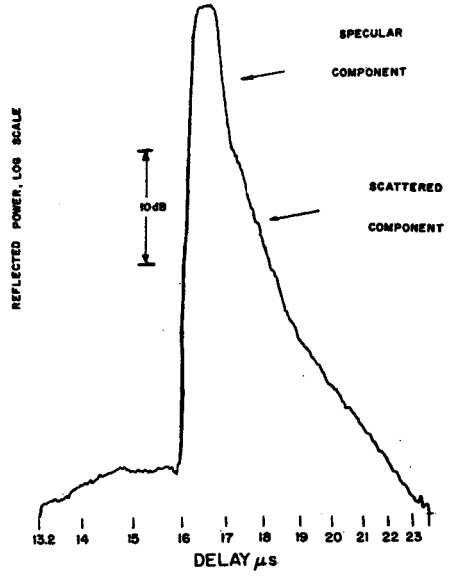

Figure 6. Recorded sea return (flight number 3).

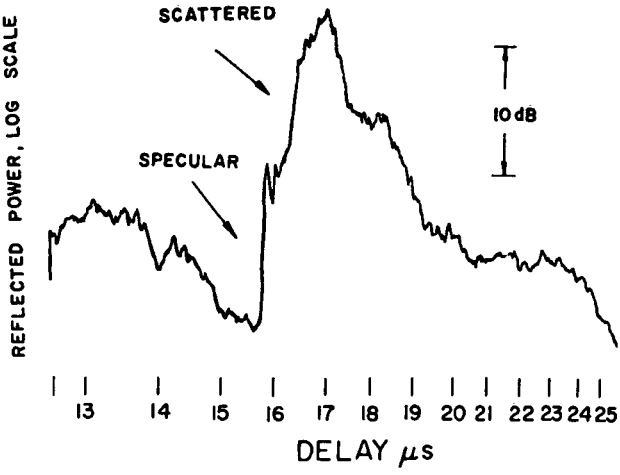

Figure 7. Recorded sea return (flight number 5).

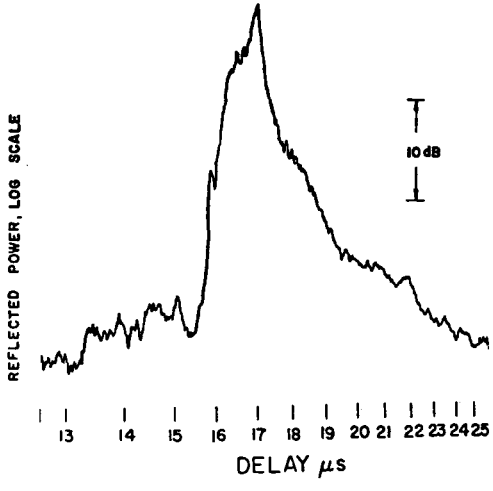

Figure 8. Recorded sea return (flight number 5).

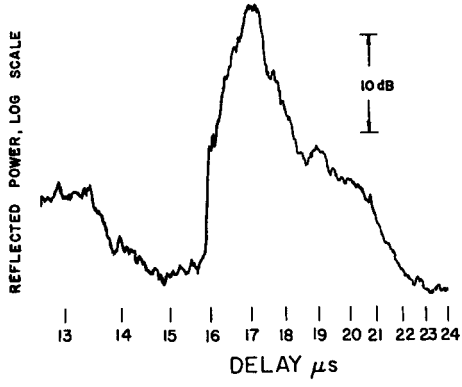

Figure 9. Recorded sea return (flight number 5).

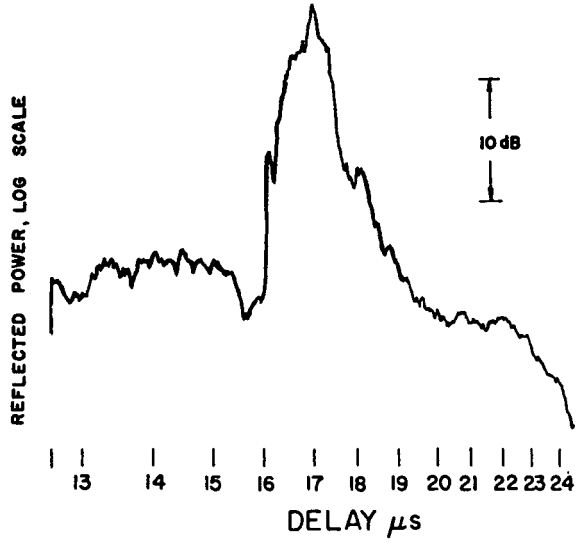

Figure 10. Recorded sea return (flight number 5).

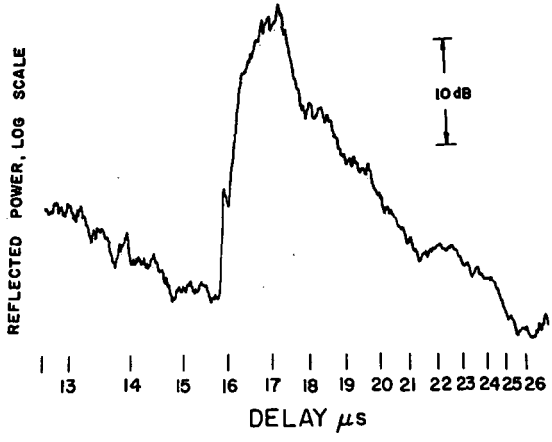

Figure 11. Recorded sea return (flight number 5).

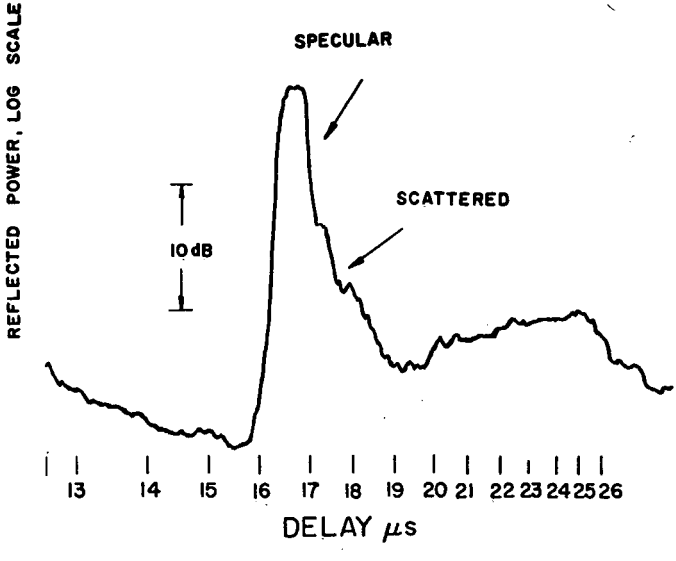

Figure 12. Recorded sea return (flight number 6).

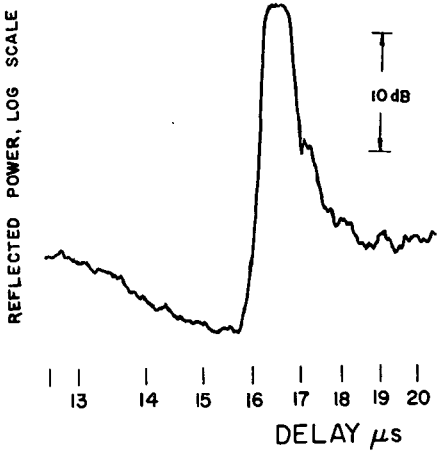

Figure 13. Recorded sea return (flight number 6).

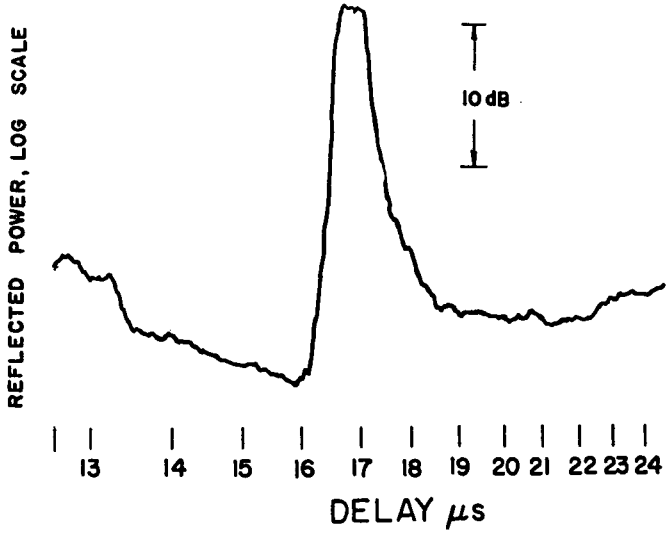

Figure 14. Recorded sea return (flight number 6).

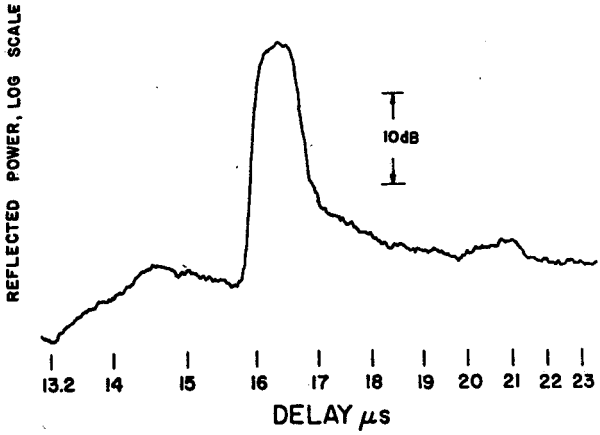

Figure 15. Recorded sea return (flight number 6).

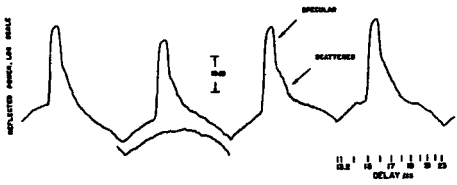

Figure 16. Sequence of four sea returns with a reference baseline (flight number 4).

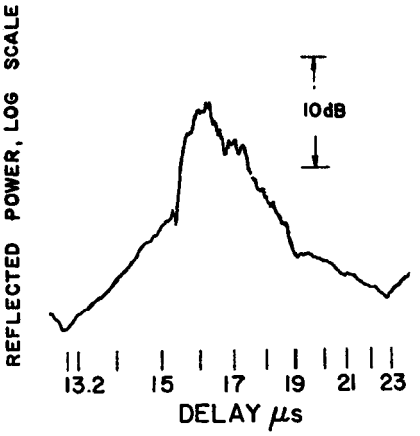

Figure 17. A return recorded above the city of Tel-Aviv (flight number 4).

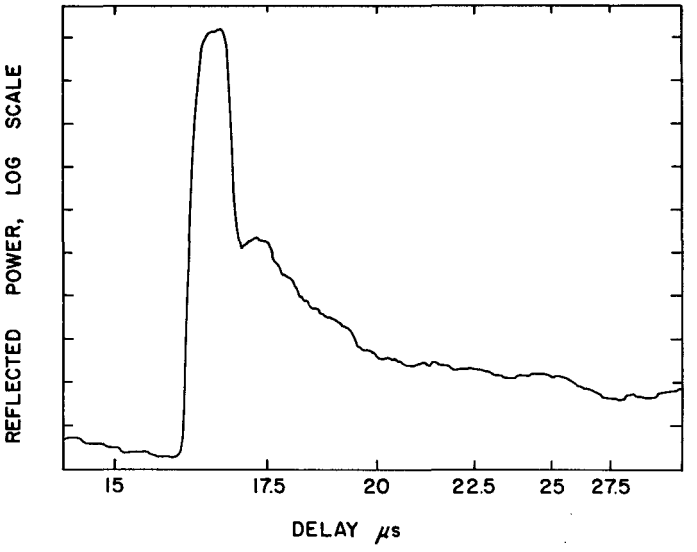

Figure 18. Recorded land return (flight number 2).

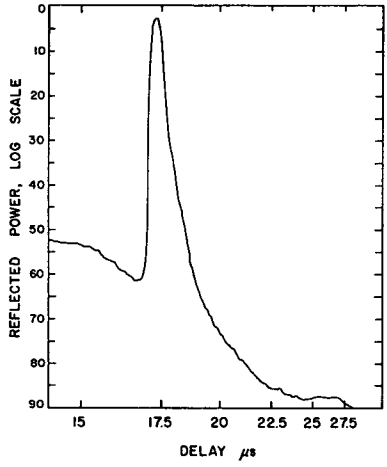

Figure 19. Recorded lake return (flight number 2).

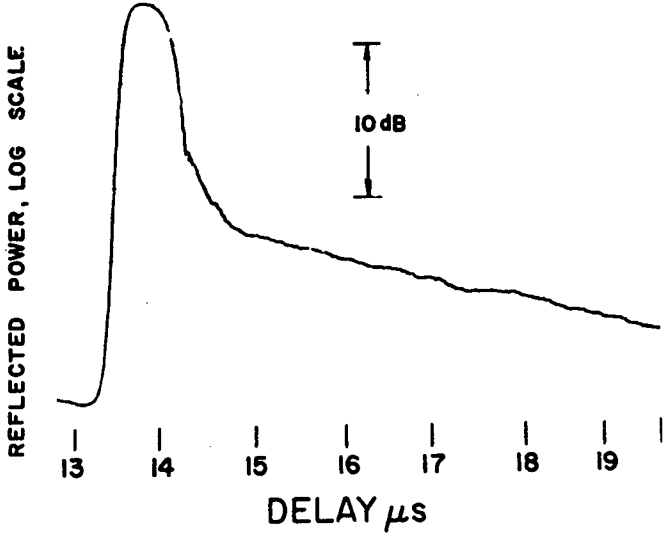

Figure 20. Recorded lake return (flight number 1).

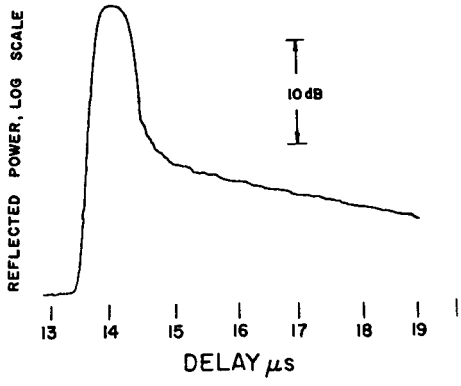

Figure 21. Recorded lake return (flight number 1).

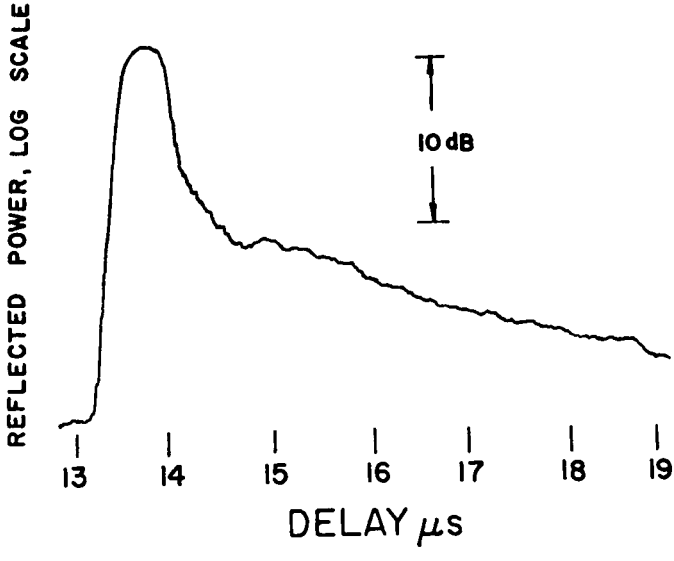

Figure 22. Recorded land return (flight number 1).

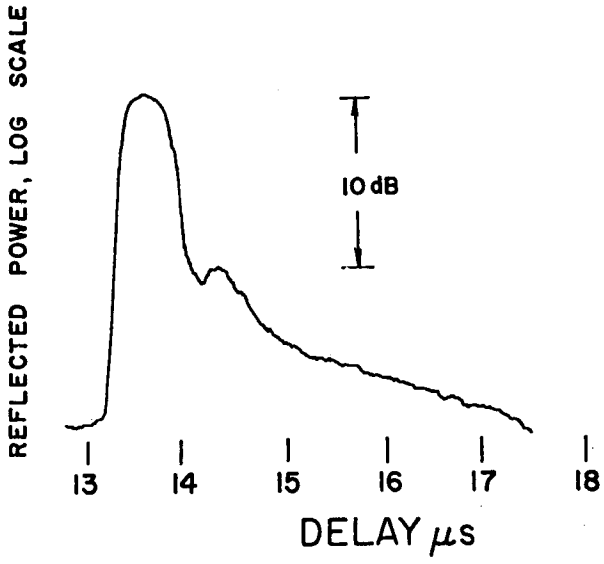

Figure 23. Recorded land return (flight number 1).

kilometers south of Fond du Lac, Wisconsin. All four returns are dominated by specular reflection. The land returns differ from the lake returns by their weaker specular component, and by stronger fading of the trailing edge. Lake Winnebago is the smallest water surface from which returns described in this work were recorded. This may raise the legitimate question of whether the whole return was reflected from the water surface. To remove this doubt, it should be pointed out that Lake Winnebago is 45 km long and 6 km to 16 km wide. From an altitude of 2 km, only echoes arriving 10 μs after the leading edge of the received pulse could be contributions from the shore, and our time scale did not extend that far. It should be noted that in this flight, and only in this one, the time scale is not accurate, and its highest value could be off by 2 μs.

It should also be repeated here that the effective width of the receiving window during flights number 1 and 2 was approximately 100 ns, which is five times wider than during the other flights. This wider window could be partly responsible for the roundness of the returns in Figures 20 to 23.

Summary and Conclusions

The measuring system described here suffers from several limitations. The two most severe ones are the uncertainty in antenna beamwidth and direction, and the uncertainty in the recordings base-line position.

Yet, the results obtained—real time recordings of average shapes of pulse radar near-vertical returns—are new and interesting, and warrant presentation as they are.

Furthermore, the twenty-one recorded waveforms given in this paper are typical representatives of some 700 returns, recorded during six different flights. Each recorded return is the average (by sampling) of approximately 10^6 received returns. This large amount of data partly compensates for the limitations of the present measuring system, and justifies some qualitative interpretation.

The presented interpretation is based on the overall shape of the returns, and on sharp transitions, sometimes even accompanied by a notch, between what were referred to as the specular and scattered components. The distinct difference between the two components with respect to amplitude and fading, and the well-defined boundary between them, give support to the view that the two components are affected by reflections with different characteristics.

The summarized interpretation is that at a 75 cm wavelength and from altitudes of 2 km - 2.3 km, sea and lake returns were always a composite of specular and scattered reflections, with a varying proportion of the two

components. The ratio of the two determines the overall shape of the returned pulse. Returns dominated by specular reflection were quite different in shape from those dominated by scattered reflection. In both cases it is always possible to distinguish between the specular and the scattered contribution.

Despite the system limitations, it is believed that the results demonstrate the feasibility of a low-power, low-cost, return shape measuring system, which utilizes sampling techniques for real-time averaging. With some improvements, such a system could be used to extend the measurements to a wider scale of sea states, a larger variety of terrains, different altitudes, and shorter wavelengths.

Appendix I

The Ratio of Specular and Scattered Fields Which is Most Likely to Yield Nulls

The probability density of a Rayleigh distributed scattered field plus specular field is the same as that of sine waves plus noise [11], and is given as

$$p(v) = \psi^{-1/2} \exp[-(v^2 + a^2)/2\psi]\, I_0(va/\psi) \qquad (5)$$

where

v = envelope field

ψ = mean square field

a = sine wave peak field

$I_0(\ )$ = modified Bessel function

We are looking for the ratio ψ/a^2 which yields the highest probability of small v. We will find this ratio by requiring

$$\lim_{v \to 0} \partial p/\partial\psi = 0 . \qquad (6)$$

The derivative of (5) is

$$\partial p/\partial \psi = [(v^2 + a^2 - \psi)(1/2) I_0(va/\psi) - va\, I_1(va/\psi)]$$

$$\psi^{-5/2} \exp[-(v^2 + a^2)/2\psi] \tag{7}$$

using:

$$\lim_{x \to 0} I_0(x) = 1 \tag{8}$$

and

$$\lim_{x \to 0} I_1(x) = 0 \tag{9}$$

we get

$$\lim_{v \to 0} \partial p/\partial \psi = (a^2 - \psi)(1/2)\psi^{-5/2} \exp(-a^2/2\psi) \tag{10}$$

(6) and (10) will give

$$a^2 = \psi \tag{11}$$

which means that the highest probability for nulls exists when the specular field equals the scattered field.

Acknowledgment

I wish to thank Profs. V. E. Suomi and F. G. Stremler for their encouragement and help which enabled this work. Thanks go also to C. D. Blair and A. Slonim for their fine work on the instrumentation.

This research was supported by NASA under contract NAS5-11542.

References

1. Moore, R. K., and C. S. Williams, Jr., "Radar terrain return at near-vertical incidence," Proc. IRE, vol. 45, pp. 228-238, February 1957.

2. Moore, R. K., "Ground echo," in Radar Handbook, M. I. Skolnik, ed. New York: McGraw-Hill, 1970, ch. 25.

3. Edison, A. R., R. K. Moore, and B. D. Warner, "Radar terrain return measured at near-vertical incidence," IRE Trans. Antennas and Propagation, vol. AP-8, May 1960, pp. 246-254.

4. Brown, W. E., Jr., "Radar studies of the earth," Proc. IEEE, vol. 57, April 1969, pp. 612-620.

5. Evans, J. V., and T. Hagfors, "Study of radio echos from the moon at 23 centimeters wavelength," J. Geophys. Res., vol. 71, October 1966, pp. 4871-4889.

6. "Space geodesy altimeter study," Final report on NASA contract NASW-1709, Raytheon Company, October 1968.

7. "August study in solid-earth and ocean physics," Report to NASA of a study at Williamstown, Mass., August 1969.

8. Nathanson, F. E., Radar Design Principles, New York: McGraw-Hill, 1969, pp. 241-246.

9. Beard, C. I., I. Katz, and L. M. Spetner, "Phenomenological vector model of microwave reflection from the ocean," IRE Trans. Antennas and Propagation, vol. AP-4, April 1956, pp. 162-167.

10. Levanon, N., "Balloon-borne radio altimeter," IEEE Trans. Geoscience Electronics, vol. GE-8, January 1970, pp. 19-30.

11. Rice, S. O., "Mathematical analysis of random noise," Bell Sys. Tech. J., vol. 23, 1945, pp. 282-332, 1944; and vol. 24, pp. 46-156.

N72-27652

PROPERTIES OF TROPICAL CLOUD CLUSTERS DETERMINED FROM GEOSTATIONARY SATELLITE PICTURES

Arthur Frederick Hasler

ABSTRACT

This thesis treats the use of geostationary satellite pictures for observations concerning tropical convective ensembles or cloud clusters. The synoptic-scale wind, divergence and vorticity fields in the vicinity of cloud clusters can be observed.

A "close-up" time-lapse movie technique was developed by which cloud trajectories were measured from a geostationary satellite with 1.5 meters/second (m/s) accuracy at better than synoptic-scale resolution for low clouds over tropical oceans. For 120 low cloud trajectories 68% of the speeds were within 2.5 m/s of the 950 mb rawinsonde winds. High clouds were not abundant enough to provide synoptic-scale resolution everywhere.

An objective "polygon" technique was developed to measure the divergence and vorticity of the synoptic-scale cloud trajectory field. The divergence technique uses the area change of a polygon which has a cloud at each of its vertices while the vorticity measuring technique approximates the line integral $\oint \frac{\vec{V} \cdot \vec{ds}}{A}$ around the polygon.

The random error for divergence and vorticity measurements at the

---

Thesis submitted in partial fulfillment of the requirements for the degree of Doctor of Philosophy (Meteorology).

$10° \times 10°$ scale was 1×10^{-6} sec^{-1} at the one sigma level while the systematic error could be as high as 3×10^{-6} sec^{-1} in cases with very poor picture alignment. Planimeter and polygon measurements of the cirrus shield expansion were used to estimate the high level divergence.

The average bulk properties of nineteen cloud clusters were found to be: low level divergence -7×10^{-6} sec^{-1}, low level vorticity 7×10^{-6} sec^{-1}, high level divergence 6×10^{-5} sec^{-1}. The high level divergence was highly correlated to the low level convergence. A simple two-level model was constructed which estimated the sub-cloud layer convergence to be 15% to 25% of the total mass flow. Convergence and positive vorticity, 5° to the east of the cloud cluster on the previous day, was found to be a necessary but not sufficient condition for the formation of cloud clusters on the following day.

CONTENTS

		Page
1.	Introduction	169
2.	Techniques	171
	2.1 Can Precise Measurements of Cloud Trajectories be Made?	171
	2.1.1 Close-up Time Lapse Movie Technique	173
	2.1.2 Error Analysis	173
	2.1.3 Comparison with Cloud Trajectories Measured by Other Techniques	173
	2.2 Do the Cloud Trajectory Measurements Give Accurate Estimates of the Low-level Wind Field at Synoptic-scale Resolution?	174
	2.2.1 Comparison with Rawinsonde Estimates of Wind Velocity	174
	2.2.2 Cloud Trajectories as Wind Estimates	174
	2.2.3 Spatial Density	178
	2.3 Can the Divergence and Vorticity of the Satellite Derived Wind Field be Measured Accurately?	179
	2.3.1 Polygon Technique for Measuring Divergence and Vorticity	179
	2.3.2 Error Analysis	179

3. Results 180
3.1 Can the Satellite Data be Used to Describe the Synoptic-Scale Field? 180
3.2 Can the Satellite Data be Used to Measure the Bulk Properties of the Cloud Cluster? 184
3.2.1 Low-Level Divergence and Vorticity of the Cloud Cluster 185
3.2.2 High-level Divergence Estimates from Measurements of the Cirrus Shield Expansion 187
3.2.3 Subcloud Layer Mass Divergence 187
3.2.4 The Variability of the Above 187
3.2.5 Relationships Among the Bulk Properties 187
3.3 Can the Satellite Data be Used to Parameterize the Bulk Effects of the Cloud Cluster on the Synoptic-Scale Field? 191

4. Conclusion 192

Appendix A. Techniques 194

Appendix B. Comparison with Other Data 212

Appendix C. Analysis of Tropical Cloud Clusters 220

Appendix D. A "Blink" Measuring Technique for Quantitative Measurement of Cloud Motion from ATS-I Spin-Scan Camera Pictures 228

Appendix E. Data Illustrations 248

Acknowledgments 268

References 269

1. INTRODUCTION

The following question is one of the most important to be answered in seeking a better understanding of the general circulation of the atmosphere: What is the interaction between the synoptic-scale motions and the convective-scale motions in tropical convective ensembles or cloud clusters? Since a complete detailed physical understanding of the interaction processes appears hopelessly complex at this time, it has been suggested that a parameterization of the convective-scale motions in terms of synoptic-scale quantities would be the most fruitful approach. For this reason we will ignore the internal structure of the cloud cluster for the most part and concentrate on the next larger scale.

The problem can be separated into three parts: a) a description of the synoptic-scale field; b) a description and measurement of the bulk properties of cloud clusters; and c) the use of the bulk cloud cluster properties to parameterize the effects of convection on the synoptic-scale fields in terms of synoptic-scale quantities. An outline of the problem, the meaning of these terms and scales, and a field program called the GARP Atlantic Tropical Experiment (GATE) to obtain better observations have been discussed in detail in a series of documents[1] published by the Joint Organizing Committee (JOC) of the Global Atmospheric Research Program (GARP). Unfortunately the data network in the tropics is so sparse that the only studies done to date which describe even the bulk properties of cloud clusters have been limited to spectrum analysis such as Yanai (1970), Wallace (1969) and others have done, and statistical compositing techniques like those of Williams (1970). The proposed GATE (experiment) has assigned a major priority to the solution of this problem through the use of a finer resolution data network. Since one is able to attack the problem only through indirect statistical means using the conventional data network or only for short periods of time with special networks, one must ask if observations of the type possible with a geostationary satellite can be used to help answer some of the questions which have been posed. The geostationary satellites[2] which will be available in 1974, the planned date of the experiment, have a greater capability than the presently available ones of the ATS (satellite) series. Nevertheless, we can use data collected from ATS as a test of the capability of this type of observation.

---

[1]The latest in this series is the "Plan for U. S. Participation in the GARP Atlantic Tropical Experiment (1971)."

[2]The SMS satellite which is scheduled for launching in 1972 will have improved resolution, infrared day-night capability, and infrared cloud top temperature measurements for cloud height determination.

The ATS spin-scan cloud camera described by Suomi and Parent (1968) and Suomi and Vonder Haar (1969) produces a high resolution, geometrically precise photograph of a large portion of the tropical cloud field every twenty-five minutes. These photographs allow one to study various features of the cloud cluster and its ambient synoptic field over a tremendous range of time and space scales. Specifically, the following questions can be asked: 1) Can precise measurements of cloud displacements or trajectories be made from the pictures? 2) Can these cloud displacements give good estimates of the wind field at synoptic-scale resolution? 3) Can the divergence and vorticity of this satellite-derived wind field be measured to useful accuracy? The satellite gives precise information about the cloud cluster's location, horizontal extent, and change with time. If, in addition, the satellite can measure the expansion of the cirrus field as a measure of high level divergence (Sikdar, 1969), as well as give a description of the cloud cluster's internal structure by means of enhancement techniques as Martin and Suomi (1971) have shown, then we may have the tools necessary to answer some of the parameterization questions.

Now that we have mentioned some of the satellite data's potential in a general way, let us pose some of the more important questions which we may be able to answer in greater detail.

a) In terms of the description of the synoptic-scale field, can the satellite data be used to describe the following:

   (i) the types of disturbances and their climatology?
   (ii) the low-level wind field in the vicinity of cloud clusters?

b) Can the satellite data be used to measure the following cloud cluster bulk properties:

   (i) low-level divergence and vorticity?
   (ii) high-level divergence?
   (iii) subcloud layer mass divergence?
   (iv) the variability of the above quantities?

c) In respect to the parameterization of the bulk effects of the cloud clusters in the synoptic-scale field, can the satellite data be used to predict the future distribution of cloud clusters on the basis of analysis of the synoptic-scale field?

The purpose of this paper is to show which of these questions the satellite data is able to answer and which it cannot. In this respect we fall short of what is needed, i.e., the ability to parameterize the small scale motions of the tropics. However, we are able to show that observations from geostationary satellites can be a powerful tool to help reach that goal. After

describing the techniques which have been developed to obtain these meteorological quantities, we will illustrate the capability with a limited number of examples selected from the data set, a part of which is included in the appendices.

2. TECHNIQUES

2.1 Can Precise Measurements of Cloud Trajectories be Made?

The ATS spin-scan cloud camera produces a high resolution geometrically precise photograph of a large portion of the earth's cloud field every twenty-five minutes. The problem is to utilize as fully as possible these high resolution, high precision properties to obtain a sufficiently accurate measurement of cloud displacements or trajectories for useful meteorological quantities.

The problem of measuring trajectories can be broken down into the three steps shown in figure 1: 1) the navigation of points on the picture, i.e., points in the image plane, to corresponding locations on the earth's surface; 2) the alignment or superposition of pictures in sequence such that landmarks match; 3) the identification and measurement of differences in cloud position between pictures. The navigation problem fundamentally involves relating the x, y-coordinate system of the picture to the spherical coordinate system of the earth and includes effects of the satellite position. These navigation procedures are described in appendix A.

The alignment and difference measurements can be handled through a number of basically different techniques:

1. A false stereo technique which involves viewing a picture pair with a stereoscope. Cloud displacements appear as differences in height, in a quantitative manner.

2. The computer and mechanical correlation techniques in which a computer or a mechanical device is used to make measurements or the differences in cloud position between images.

3. The "blink" and movie techniques in which a picture time sequence is displayed rapidly on a worksheet and from which the operator can make direct displacement measurements.

Of the techniques listed above, the only one available to the writer was the movie technique which was expanded into the form described below.

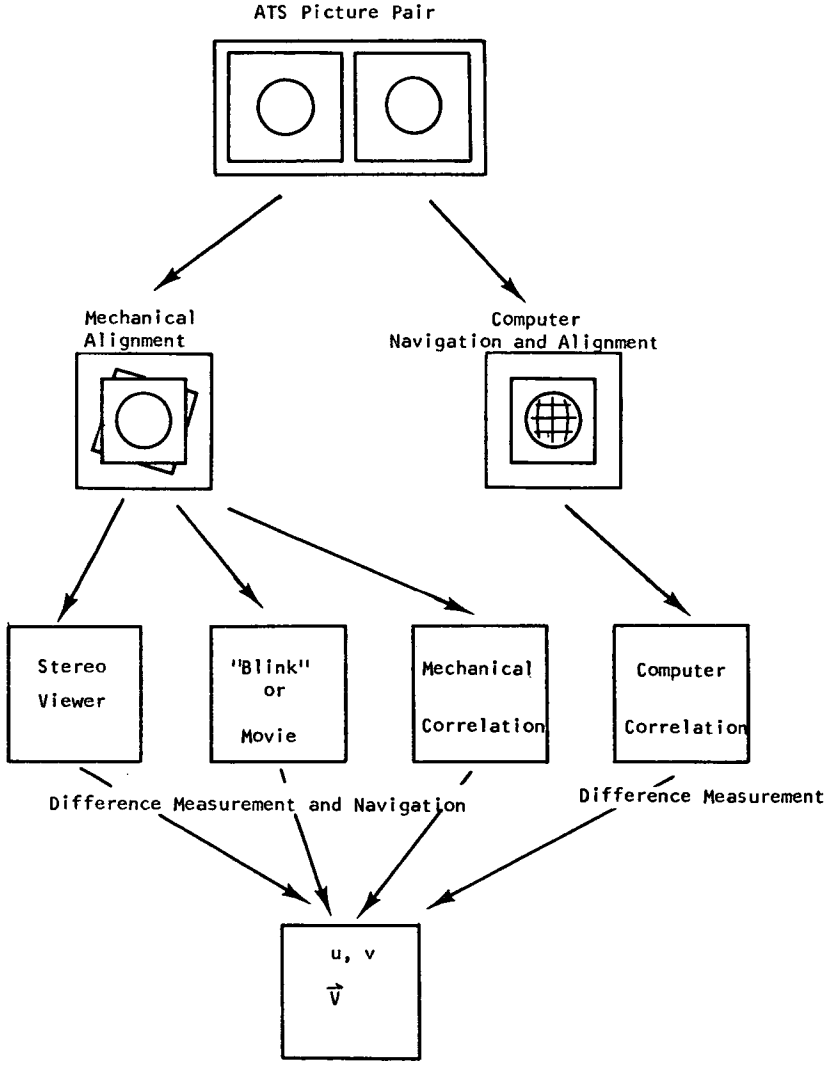

Figure 1. Techniques for cloud trajectory measurement.

2.1.1—Close-up Time Lapse Movie Technique. Movie loops can be made by aligning a sequence of ATS pictures according to their landmarks and photographing them to form a movie. However, with the 16 mm movie equipment available the resolution was too low and the registration of the movie frames in the camera and during projection was not good enough for accurate work. The solution to this problem was to make a close-up movie which viewed a small enough area that the 16 mm film resolution was adequate and which at the same time reduced the registration error to an insignificant level.

The next task was to navigate the cloud elements in the close-up movies. Even after the basic navigation problem was solved for measurements made on a full earth disk, the navigation of the close-up movie required additional work because there are not usually enough landmarks for use as a zero motion reference in a close-up picture. The equivalent was accomplished by making a measurement of the x and y coordinates of four widely spaced reference clouds or landmarks in the close-up picture and then measuring the same four reference marks in the previously navigated full earth picture. A step-by-step description of the technique and the equations used to transform close-up coordinates into full earth coordinates are given in appendix A.

2.1.2—Error Analysis. In order to ascertain the magnitude of the errors in the cloud trajectory measurements, an error analysis was carried out. The details of the analysis are given in appendix A. Both the random and systematic errors were estimated. The random error in the cloud motion was found to have a standard deviation of .5 m/s in speed and 2.5 degrees in direction. The random error estimate was based on measurement repeatability. The systematic error near primary landmarks was close to zero for most examples, and was seldom greater than 1 m/s. Even near secondary landmarks, those some distances from the primary landmark, the systematic error was seldom greater than 1.5 m/s. The systematic error estimate was based on measurements of apparent motion of landmarks. These error limits compare favorably with the GARP requirements for wind speed accuracy of 2.5 m/s which are based on the accuracy necessary for numerical models.

2.1.3—Comparison with Cloud Trajectories Measured by Other Techniques. In order to verify the credibility of the cloud trajectory measurements, comparisons were made with other techniques such as the University of Wisconsin Space Science and Engineering Center (SSEC) computer, correlation technique and the NOAA movie-loop technique. The details of these comparisons are given in appendix B. The comparisons with the correlation technique gives differences of less than 1.2 m/s and 7° for 68% of the data for the July 26, 1969 case and less than 2 m/s and 13° for 68% of the data for July 26 and 27 cases. The comparison with the NOAA movie-loop technique gives 68% of the speed differences to be less than 1.7 m/s and 68% of the direction

differences less than 16°. The agreement is very good considering the fact it was not possible to insure that the clouds used for intercomparison were, in fact, identical clouds.

2.2 Do the Cloud Trajectory Measurements Give Accurate Estimates of the Low-level Wind Field at Synoptic-scale Resolution?

Cloud displacements or trajectories, no matter how well we are able to measure them, are not a typical state parameter of the atmosphere. Clouds themselves are tracers and we use their motion to depict the wind field. It is possible to argue that clouds do not move with the wind, and one could illustrate this point by using orographic clouds as an extreme example. Few, however, will dispute that most clouds—especially small ones—do drift with the wind. Clearly the clouds we shall use have been selected to represent the group that drift with the wind.

The only way to answer this question completely would be through a ground truth experiment which would make sufficiently accurate independent measurements of both cloud trajectories and wind speed. Since this ground truth experiment has never been done, comparisons with rawin soundings will have to suffice.

2.2.1—Comparison with Rawinsonde Estimates of Wind Velocity. The level of best fit for the low cloud trajectories compared with 120 rawin soundings was 950 mb as shown in figures 2 and 3. Sixty-eight percent of the speed differences were less than 2.5 m/s and 68% of the direction differences were less than 30% for that level. Figure 4 shows the comparison for July 27, 1969 as an example of typical differences for the Caribbean region. More data on this comparison appears in appendix B. There is a lack of exact time and space matches and there are other sources of difference in this comparison which do not reflect on the validity of the cloud trajectories as wind estimates. For this reason the previous random and systematic error estimates of the measuring technique are considered to be more valid estimates of the actual error in the cloud trajectory measurements.

2.2.2—Cloud Trajectories as Wind Estimates. The two most convincing arguments for use of cloud trajectories as wind estimates are: 1) the consistency exhibited by the low level cloud trajectory fields (illustrated in figures 5 and 35 through 52 in appendix E); and 2) the agreement with the 950 mb winds discussed above. However, it might still be asked: How can cloud height be stimated? From climatology we know that convective cloud bases in the tropics are consistently located near 950 mb, which probably accounts for the best fit frequency maximum at that level. The low clouds used in this study were usually fairly large convective cloud ensembles of

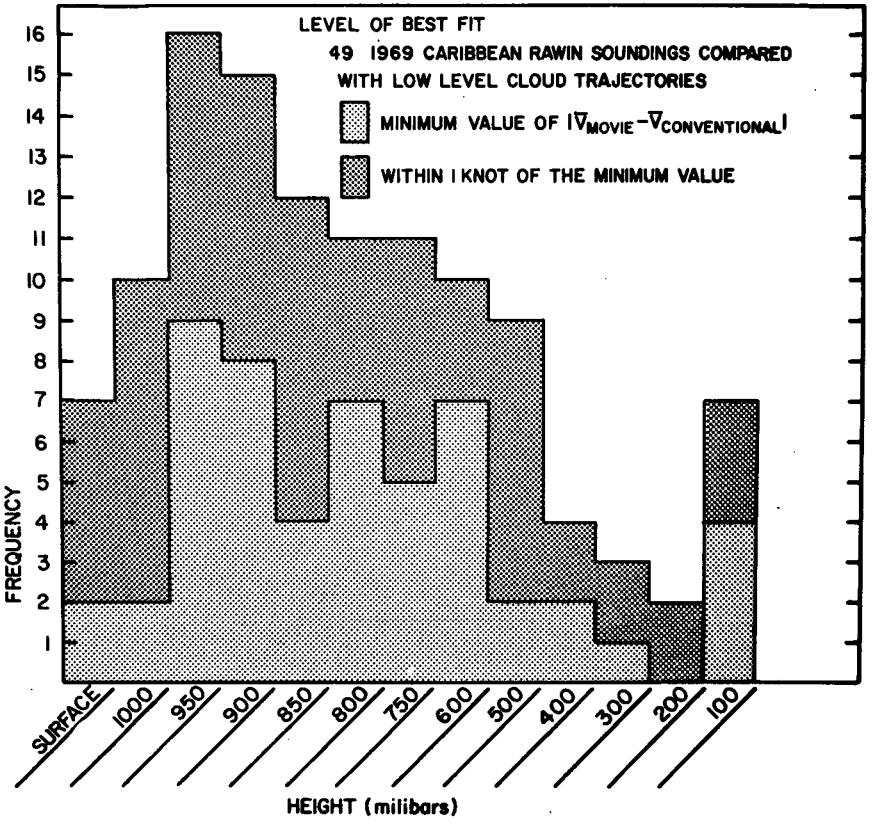

Figure 2. Level of best fit (49 Caribbean rawin soundings compared with low-level cloud trajectories).

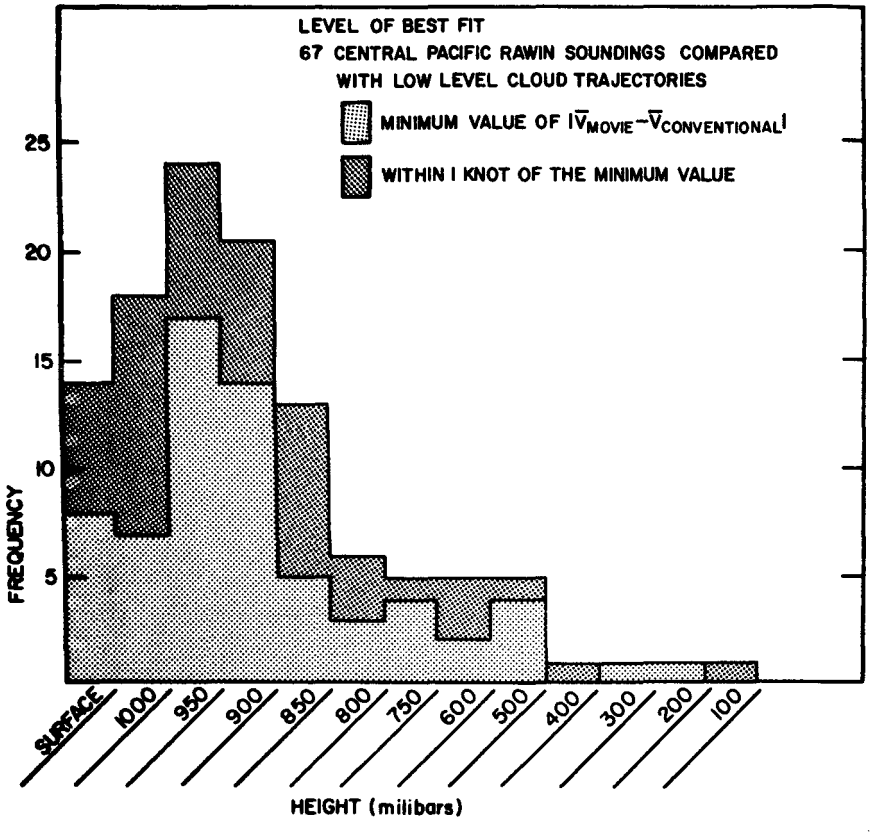

Figure 3. Level of best fit (67 central Pacific rawin soundings compared with low-level cloud trajectories).

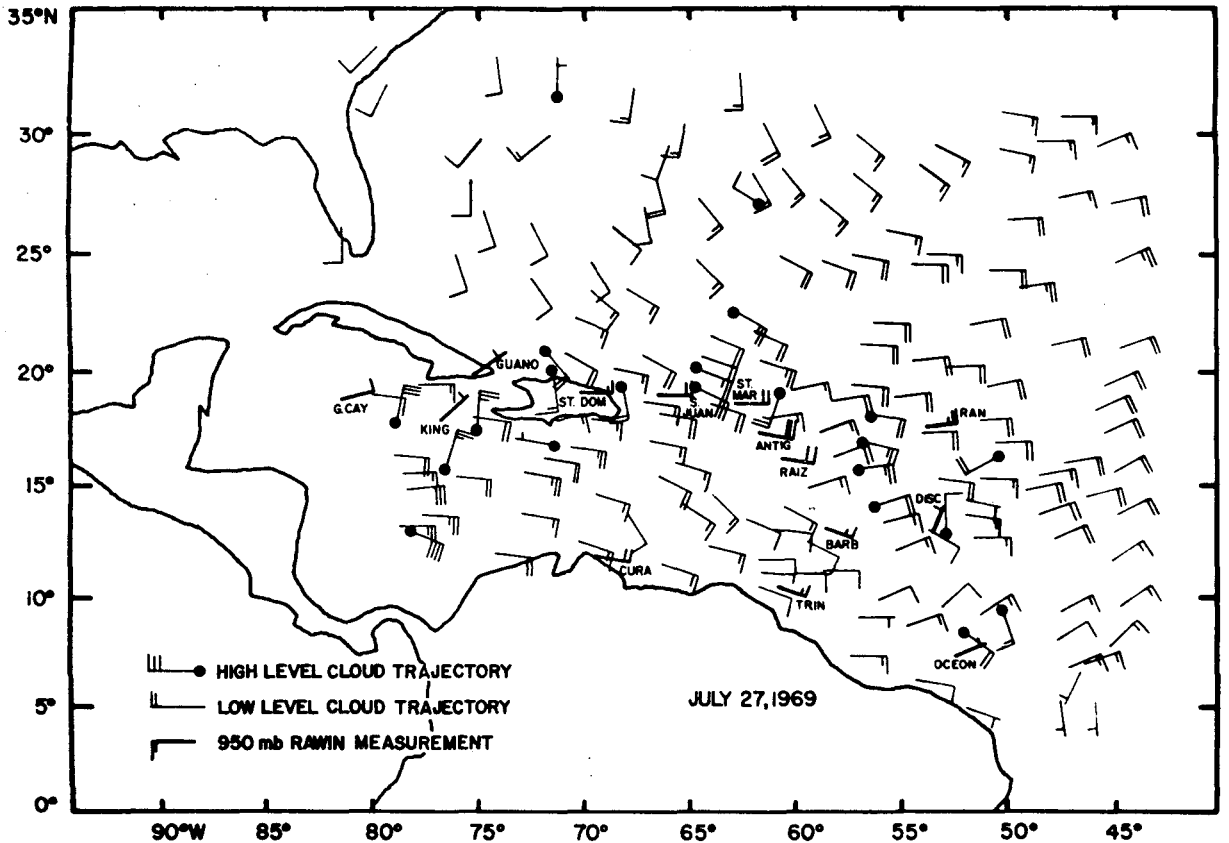

Figure 4. Cloud trajectories compared with July 27, 1969 rawinsonde winds.

approximately 8 km to 80 km in diameter. Clouds of this diameter would usually have considerable vertical extent. This proposition is supported by the level of best fit data for the Caribbean (figure 2) which indicates some matches with winds up to as high as 600 mb.[3] Examination of moisture profiles for July 26–28 Caribbean data indicates high humidity up to 650 mb in many cases. So if we assume that the clouds do have considerable vertical extent, we can assume that the cloud trajectory will represent the mean velocity for that layer. This is true because even if there is substantial shear, the convective cloud will tend to average the motion of the layer as seen by the satellite (see diagram).

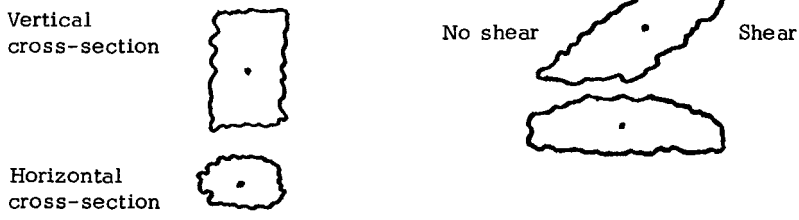

In summary we can say that the low cloud trajectories are good estimators of the wind at 950 mb, but it can also be argued that the trajectories are representative of a layer from 950 mb to the inversion level at 750 mb and in some cases even higher.

2. 2. 3— Spatial Density. The spatial density of low clouds was sufficient so that at least three low cloud trajectories could be measured for almost all 5° × 5° boxes over the Caribbean and the Central Pacific Ocean, and in the majority of them many more were available. Thus it is clear that low clouds can be measured at considerably better than synoptic scale resolution. In fact, in most areas we have observations of sufficient spatial density to satisfy the two-degree horizontal grid mesh spacing considered necessary for global numerical models. High clouds were not as abundant and were not evenly distributed. Occasionally there were enough cirrus outflow pieces to measure high level divergence; however, in most cases the cirrus shield expansion was the only means of obtaining a measure of the high level wind field.

---

[3] The Pacific data (figure 3) has a cutoff at about 850 mb which is caused at least in part because one-third of the soundings did not go above 850 mb.

2.3 Can the Divergence and Vorticity of the Satellite Derived Wind Field be Measured Accurately?

2.3.1—Polygon Technique for Measuring Divergence and Vorticity. An objective Lagrangian polygon technique was developed which gives divergence and vorticity measurements by following the relative motions of individual clouds as they drift along. The divergence measuring technique uses the area change of a polygon which has a cloud at each of its vertices while the vorticity measuring technique approximates the line integral $\oint \frac{\vec{V} \cdot \vec{ds}}{A}$ around the polygon. The technique is purely objective and does not depend on subjective streamline or isotach analysis. It can also be used directly on a vector field with nonuniform spacing.

A detailed description of the techniques and the system of equations used to compute the divergence and vorticity are given in appendix A.

2.3.2—Error Analysis. The analysis of systematic and random errors conducted for the cloud trajectories included a test of the accuracy of the divergence and vorticity measurements which was carried out by inserting the estimated cloud trajectory errors into the data set and evaluating the change in the output as explained in appendix A. The error analysis shows that the one sigma divergence and vorticity random error for the $5° \times 5°$ polygons is 4×10^{-6} sec^{-1}, for the $10° \times 10°$ polygons it is 1×10^{-6} sec^{-1}, and for the $15° \times 15°$ polygons it is 4×10^{-7} sec^{-1}. The systematic error in the divergence computation resulting from a misalignment error which would produce a 2 m/s speed error (larger than estimated for this data set) could be as large as 3×10^{-6} sec^{-1} and for vorticity, 1×10^{-6} sec^{-1} for the three scale sizes. Both values decrease in a linear manner as one approaches the subsatellite point. The magnitudes we must measure range from as high as 2×10^{-5} for the $5° \times 5°$ polygons to as high as 7×10^{-6} for the $15° \times 15°$ polygons. Therefore we are able to make measurements of at least the largest values expected for the $5° \times 5°$ polygons while for the $10° \times 10°$ and $15° \times 15°$ polygons we can describe a more complete field.

Scales smaller than $5° \times 5°$ were not used because the spatial density of the cloud trajectories was not sufficient in all areas. In addition the divergence and vorticity fields were found to have only fair continuity for the $5° \times 5°$ and smaller scales. However, we are able to describe the $10° \times 10°$ field well, which is the limit of good resolution for numerical models which have a grid mesh spacing even as small as two degrees.

3. RESULTS

In this section we intend to show, using selected examples, whether or not answers to the questions posed earlier can actually be obtained. Many additional examples were analyzed using the techniques described earlier and the full details of these analyses are given in appendices C and E. However, in order to avoid presenting the reader with a great mass of data, we will use selected samples from the large data set we analyzed.

3.1 Can the Satellite Field Data be Used to Describe the Synoptic-Scale Field?

The answer could include descriptive data such as types of disturbances, their distribution, lifetime, motion, etc. This type of study has already been carried out by Karst and Martin (1969), Kornfield et al. (1967), Kornfield and Hasler (1969), Frank (1970), Hayden (1971) and many others. Since these papers have already given a qualitative description of the synoptic-scale field, we will restrict this study to a quantitative description.

Synthetic data used in a numerical model of the atmosphere has inherently high precision to several decimal places. The wind field, for example, is specified precisely enough so the divergent component of the field can be obtained to high accuracy, limited only by the finite differencing scheme used. The key question here is whether or not we can obtain actual observations of comparable accuracy on a scale of resolution which will allow us to quantitatively describe features of the same scale size that the model can handle. We have shown earlier that we can make observations of sufficient accuracy and spatial resolution, while the following figures illustrate examples of these observations.

Figures 5–7 show the results of wind, divergence and vorticity field measurements for January 20, 1970. Figure 5 gives the high and low level cloud trajectory field superimposed on the close-up local noon ATS-I picture for January 20. The cloud trajectory speed is given by the arrow length to the nearest 5 knots. The central Pacific region is shown in figure 5 at about 40° latitude by 50° longitude. The large cloud cluster in the center is located to the southwest of Hawaii and northwest of Christmas Island at about 5°N, 165°W. The smaller arrows in figure 5 represent the low level cloud motion. The low level clouds selected were the smallest trade cumulus clouds visible in figure 5 which also had the three-hour lifetime necessary for accurate measurement. The low clouds which were used had dimensions of 8–80 km in diameter and formed a consistent velocity field. The low level trajectory field for January 20 shows obvious convergence near the cloud cluster, but no vortex is present and only a slight wave is in evidence to the north of the

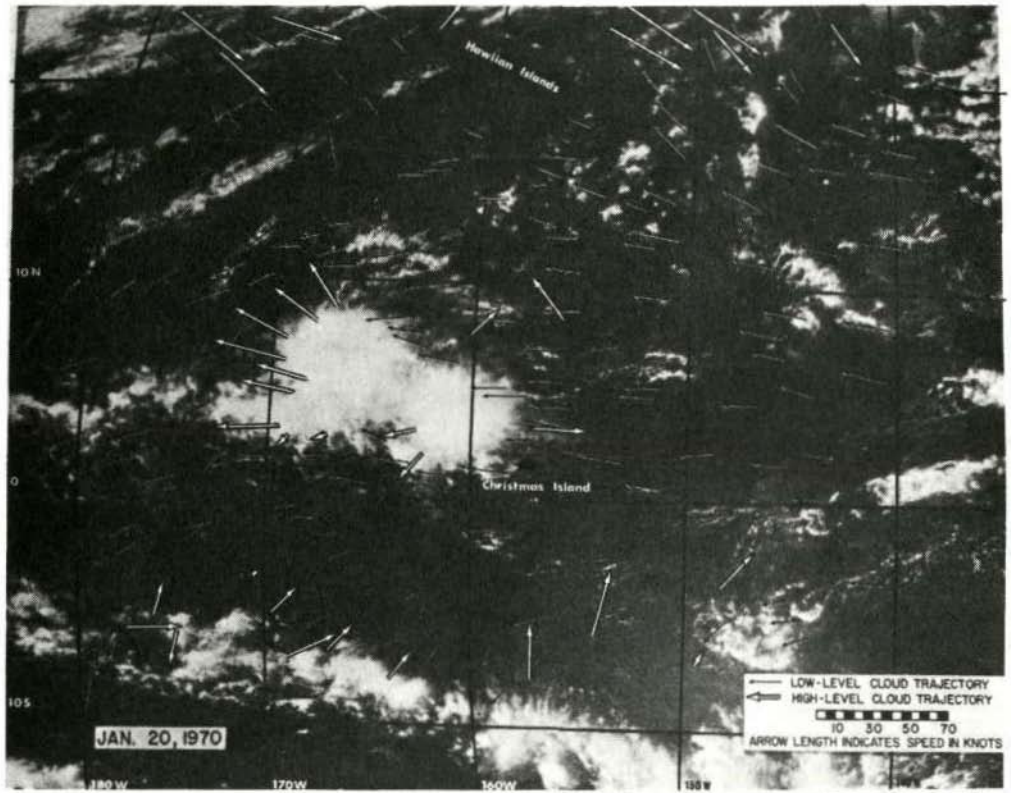

Reproduced from best available copy.

Figure 5. Cloud trajectory field superimposed on the central Pacific region of the ATS-I picture taken at approximately local noon, January 20, 1970. Low cloud trajectories are represented by the small black and white arrows. The cloud speed is given by the arrow length in knots according to the legend.

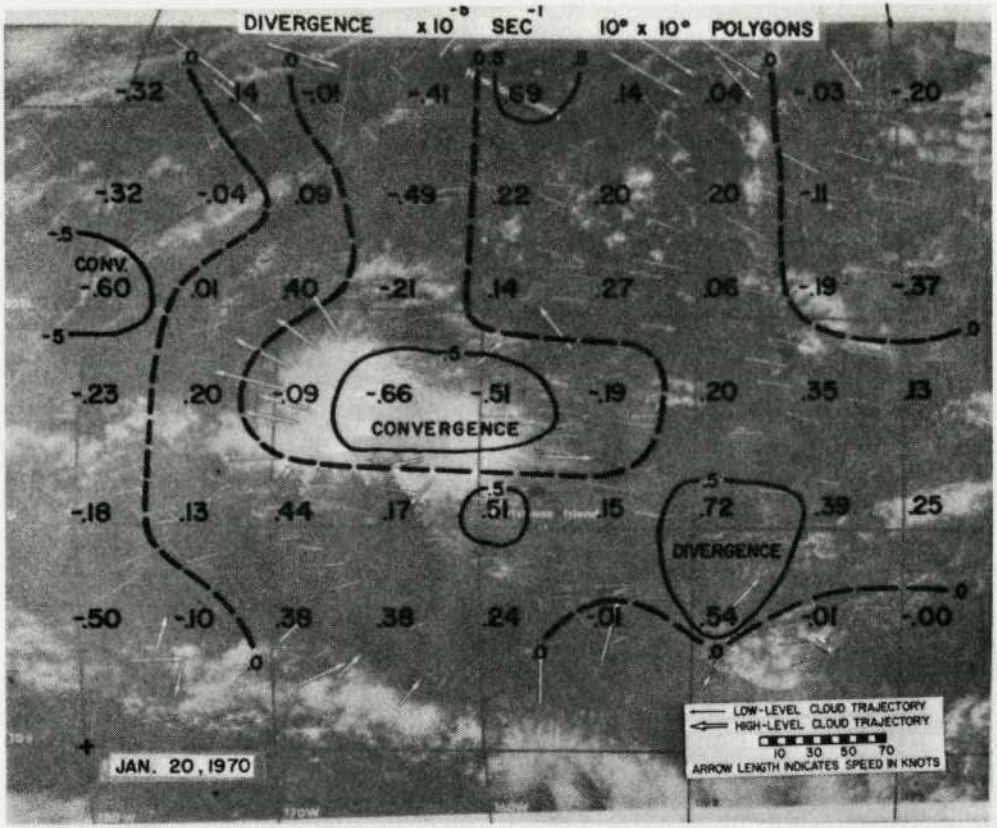

Reproduced from best available copy.

Figure 6. Horizontal divergence computed from the low cloud trajectory field superimposed on the ATS-I picture taken on January 20, 1970. Each value is obtained by computing $\Delta A/A\Delta t$ for a polygon about 10° in diameter which has approximately twelve vertices, i.e., cloud trajectories. Divergence is given in units of 10^{-5} sec^{-1}.

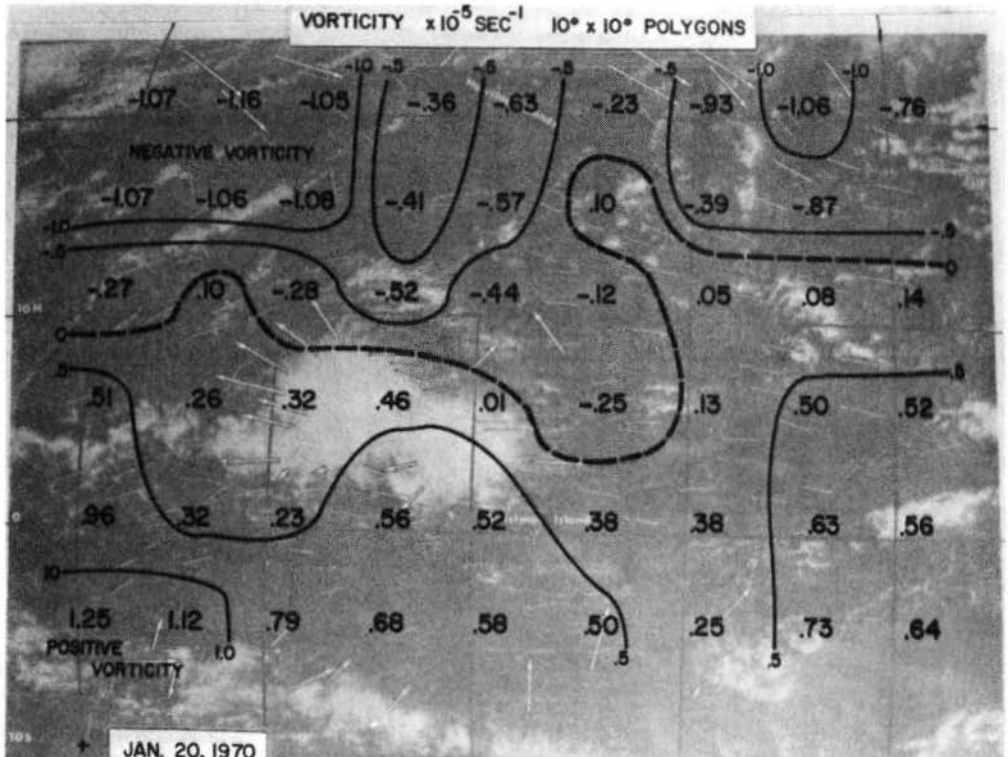

Figure 7. Horizontal component of relative vorticity computed from the low cloud trajectory field superimposed on the ATS-I picture from January 20, 1970. Each value is computed from an approximation of the expression $\oint \left(\frac{\vec{V} \cdot d\vec{s}}{A} \right)$ around a polygon about 10° in diameter which has approximately twelve vertices, i.e., cloud trajectories. Vorticity is given in units of 10^{-5}sec^{-1}.

cloud cluster. The larger arrows in figure 5 represent the high level cloud trajectories. The high clouds were identified primarily by their having significantly different speed or direction from the consistent low cloud velocity field. In some cases high clouds could also be recognized as thin cirrus pieces. In figure 5 the high level trajectories are typically in widely scattered groups, but cirrus pieces are abundant enough in the vicinity of the cloud cluster to describe the divergent field. However, on most of the remaining fourteen days of Pacific data and three days of Caribbean data shown in appendix E, the cirrus shield expansion was the only measure of the high level divergence.

Figures 6 and 7 show the divergence and vorticity fields for the 10° × 10° polygons superimposed on the ATS-I local noon close-up picture for January 20. Convergence maxima are plainly coincident with the cloud cluster and other relatively cloudy areas while clear areas tend to have divergence.

The relationship of convergence to cloudiness is not always so pronounced for the remaining seventeen days of convergence fields shown in appendix E. Figure 6 shows that the region of positive relative vorticity includes the cloud cluster region and extends southward, but there is no pronounced maximum in the vicinity of the cloud cluster.

Divergence and vorticity fields on the 5° × 5°, 10° × 10°, and 15° × 15° space scales for all eighteen days are contained in appendix E.

3.2 Can the Satellite Data be Used to Measure the Bulk Properties of the Cloud Cluster?

The U. S. plan for GATE (1971) makes the following statement concerning the present state of knowledge about the bulk properties of cloud clusters:[4]

> "...(c) BULK PROPERTIES OF CONVECTIVE ENSEMBLES. These have been studied independently by a number of investigators using compositing and spectrum-analysis techniques on radiosonde data from the western Pacific. Many of the following statistics represent averages of many systems obtained from these studies.
>
> Disturbed weather tends to occur near or slightly east of the low-level troughs in "cloud clusters" with dimensions on the order of

---

[4] i. e., convective ensembles.

2–10° of latitude on a side. Cloud clusters represent local maxima in cyclonic vorticity (about 10^{-5} sec^{-1}) and convergence (about 5×10^{-6} sec^{-1}) in the lower-tropospheric flow and anticyclonic vorticity (about 10^{-5} sec^{-1}) and divergence (1×10^{-5} to 2×10^{-5} sec^{-1}) at the 200-mb level. The low-level convergence of mass and moisture is spread through a rather deep layer of the lower troposphere, with only about 30 percent of the mass and about 50 percent of the moisture being supplied by the subcloud layer.

In the area average disturbed regions are cool in the lower troposphere, warm near the 300-mb level, and cool at the tropopause, relative to their surroundings. Temperature anomalies are on the order of 1–2°C at the surface and 0.5–1.0°C at the higher levels. Above the subcloud layer, relative humidities are 10–30 percent higher than in undisturbed regions but are still well below saturation. (Within the subcloud layer there is very little humidity difference between disturbed and undisturbed conditions.) Maximum rising motion occurs near the 300-mb level, where it reaches about 3 cm sec^{-1}. This is consistent with observed rainfall rates on the order of a few centimeters per day.

Most of the above statistics represent broad averages. It would be highly desirable to know how much variability there is from one cloud cluster to another and over the lifetime of an individual cluster. It will also be of prime importance to determine how much information the satellite can provide regarding the bulk properties of convective ensembles."

Let us see which of these properties have been measured in this study using satellite data alone and, in addition, let us see if we can find the relationships among the properties.

3.2.1—Low-Level Divergence and Vorticity of the Cloud Cluster. Special "cloud cluster polygons" were selected consisting of the set of low level cloud trajectories nearest to, and completely surrounding, the cloud cluster for measurement of the low level inflow and vorticity. The values obtained from these measurements for nineteen cloud clusters are shown in columns 1 and 2 of table 1. The average values for low-level divergence and vorticity were -7.2×10^{-6} sec^{-1} and 7.4×10^{-6} sec^{-1}. This compares very well with the values obtained by Williams (1970) which are stated in the GATE report.

Table 1. Bulk Cloud Cluster Properties

Date	ATS Satellite	Latitude Degrees (+ north)	Longitude Degrees (+ west)	Low level C. C. Polygon divergence $\times 10^{-5}$ sec^{-1} (1)	Low level C. C. Polygon vorticity $\times 10^{-5}$ sec^{-1} (2)	Planimeter measure Cirrus shield divergence $\times 10^{-5}$ sec^{-1} (3)	Polygon measure of cirrus shield divergence $\times 10^{-5}$ sec^{-1} (4)	High level C. C. Polygon divergence $\times 10^{-5}$ sec^{-1} (5)	K. T. Williams classification (6)	Area $\times 10^5$ km^2 (7)	Ratio (3/1) (8)	Zonal shear $(\frac{\Delta u}{\Delta y})$ 10^{-6} sec^{-1} (9)	Meridional shear $(\frac{\Delta v}{\Delta x})$ 10^{-6} sec^{-1} (10)
6/ 9/68	I	8	155	- .85	- .06	2.62			D. -D. (4)	10.2	3.1	1.2	3.7
7/26/69	III	15	59	-1.74	4.48	36.50	76.80		Cons. (3)	.2	21.0	8.0	23.7
7/26/69	III	12	62	-1.45	+ .63	9.30	17.30		Cons. (3)	.3	6.4	5.8	1.7
7/27/69	III	16	62	- .68	- .32	2.51	2.85		Dyng. (5)	.8	3.7	5.7	- 6.7
7/28/69	III	17	61	- .73	1.25	5.41	8.89		Cons. (3)	1.0	7.4	4.2	5.1
11/ 1/69	I	7	162	- .75	.47	3.67			D. -D. (4)	7.8	4.9	4.3	.17
12/15/69	I	5	-175	- .86	1.31	5.96			Dyng. (5)	6.7	6.9	4.2	.86
12/15/69	I	5	160	- .81	.37	2.96			Devl. (2)	5.6	3.6	7.7	3.9
12/16/69	I	5	170	- .62	.43	2.93		3.31	Dvng. (5)	14.4	4.7	3.0	1.2
12/17/69	I	5	160	- .54	1.65	7.15		4.88	D. -D. (4)	3.4	13.2	6.9	3.5
1/18/70	I	2	163	- .87	.47	5.47	4.79		D. -D. (4)	1.5	6.3	-3.4	3.1
1/18/70	I	3	172	- .25	.14	2.92	2.95		Dyng. (5)	1.5	11.7	1.7	.12
1/19/70	I	5	162	-1.03	.53	4.68		5.36	Devl. (2)	1.6	4.5	5.1	1.9
1/20/70	I	5	165	- .55	.44	3.72		4.77	Dyng. (5)	5.8	6.8	2.6	2.0
1/21/70	I												
3/27/70	I												
3/28/70	I	-12	135	- .34	.25	2.34		4.57	D. -D. (4)	4.9	6.9	2.3	-1.2
3/29/70	I												
5/ 5/70	I	3	167	- .64	- .08	7.34	5.74		Devl. (2)	2.5	9.0	2.6	-2.0
5/ 6/70	I	3	168	- .27	.18	2.40			Dyng. (5)	3.5	8.9	1.7	.06
5/ 6/70	I	- 8	160	- .65	.09	3.60	4.35		D. -D. (4)	5.9	6.7	- .26	- .46
5/ 7/70	I	-10	145	- .17	.16	.95	.97		D. -D. (4)	4.0	5.6	3.2	- .03

3.2.2—High-level Divergence Estimates from Measurements of the Cirrus Shield Expansion. Sikdar (1969) has shown that the expansion of the cirrus shield can be used to estimate the high level divergence if one makes an assumption about the thickness of the outflow layer. A planimeter was used to measure the change in area of the cirrus shield and the polygon technique was also applied. The planimeter divergence measurements appear in column 3 and the polygon divergence measurements appear in column 4 of table 1. The average value of the planimeter measurement of the cirrus shield divergence is 6×10^{-5} sec^{-1}. This value is somewhat higher than the Williams result used in the GATE report, but since his data is based on a statistical composite one would expect his outflow layer to be thicker and have a lower divergence value, which appears to be the case.

3.2.3—Subcloud Layer Mass Divergence. Estimates from a two-layer model, discussed below, give the mass convergence in the subcloud layer to be only 15% to 25% of the total. This estimate is also consistent with the magnitude given in the GATE report but tends to point toward a smaller value.

3.2.4—The Variability of the Above. One advantage of this type of analysis over the statistical compositing technique is that we can treat systems as separate cases. We have not only average values, but as requested in the final paragraph of the GATE statement above, an estimate of the variability of the data from the individual cases. The complete data set is presented in table 1. For the nineteen cloud clusters studied, the range of values for some variables was as follows:

1. Low level divergence: $-.2 \times 10^{-5}$ sec^{-1} to -1.7×10^{-5} sec^{-1}
2. Low level vorticity: $-.3 \times 10^{-5}$ sec^{-1} to 4.48×10^{-5} sec^{-1}
3. Planimeter measure of high level divergence: 1.0×10^{-5} sec^{-1} to 36.5×10^{-5} sec^{-1}.

It is clear that we have reasonable magnitudes for a number of cloud cluster bulk properties obtained from satellite data, which also means that we have answered (in part) the last GATE question above.

3.2.5—Relationships among the Bulk Properties. Probably the biggest advantage of the cast study approach we have used is the fact that the relationships among the bulk cloud cluster properties (listed in table 1) may be examined. The most dramatic correlation was found between low level convergence and the high level divergence[5] which is illustrated in figure 8.

---

[5] See appendix C for a description of some of the other relationships among the cloud cluster properties listed in table 1.

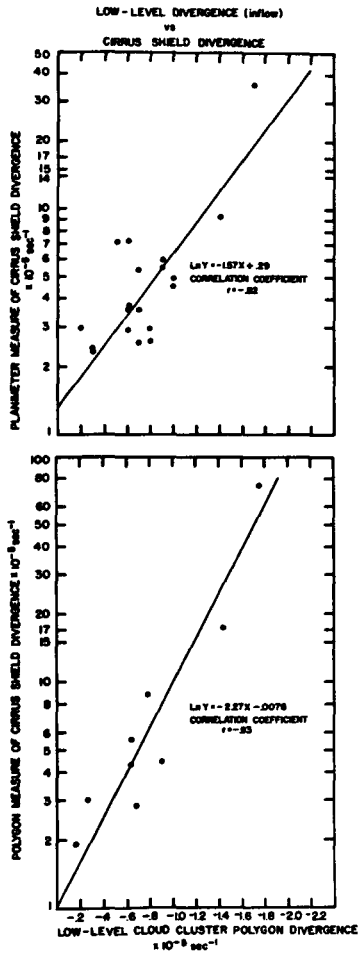

Figure 8. Low-level divergence (inflow) vs. cirrus shield divergence

When a least square logarithmic regression was applied, a correlation coefficient of .93 was obtained. This result suggests the use of mass continuity considerations to increase further the credibility of the bulk property observations. To do this exactly one would need a complete description of the wind field as a function of height. Offhand it might appear that the cloud photographs give only two levels of information—say, at 950 mb and at 200 mb. However, it may not be that limiting because the low level convective clouds represent a mean horizontal motion through a lower layer of some depth and the high level cirrus shield represents a mean motion through another depth. We do not have observations of the complete low level convergence profile and upper level divergence profile—we merely have samples of them. Nevertheless, it is possible to construct a two-level model of the mass flow balance if certain assumptions about the divergence profile are made.

According to Williams (1970), the low level convergence layer for 1257 Western North Pacific cloud clusters was very deep. The convergence was nearly constant from the surface to 450 mb as shown in figure 9. Byers and Braham (1949) also found a deep inflow layer which extended up to 500 mb for five Florida thunderstorms (see figure 9).[6] Furthermore, we have argued that the low cloud trajectories used in this study represent the motion of a fairly deep layer, say from 950 to 750 mb. Therefore we will assume that the average convergence value of 7×10^{-6} sec^{-1} obtained in this study is representative of the 950 mb–750 mb layer. Based on Williams' uniform divergence profile we could assign the convergence value of 7×10^{-6} sec^{-1} to a deeper layer extending from the surface to 450 mb. However, an examination of Level of Best Fit data (figure 2) and radiosonde moisture data indicates that cloud trajectories may be representative of a layer up to a maximum of 600 mb. Therefore let us restrict the model to inflow layers which range from the surface to a maximum of 600 mb. We will also assume that our value of 6×10^{-6} sec^{-1} for high level divergence can be assigned to a layer centered at 200 mb which is the location of the outflow layer of Williams' divergence profile (figure 9). Finally, we will assume a standard tropical temperature profile.

Based on the above assumptions we will propose the following versions of the cloud cluster model which is illustrated in figure 10:

1. If we assume uniform convergence from the surface to 600 mb, then mass flow is conserved if the cirrus outflow layer thickness, D_{COL}, is 1700 meters (m). This is thinner than the 3250-m thick layer which one obtains from Williams' data, but since his data is based on a statistical composite one would expect his outflow layer to be thicker and have a lower divergence value if there is any variation in the height of the outflow layer from case to case. We can also make an estimate of the subcloud layer mass convergence from the model. The thickness of the cloud layer, D_{CL}, is 3800 mb (950 mb to 600 mb). The thickness of the subcloud layer, D_{SCL}, is 500 m (surface

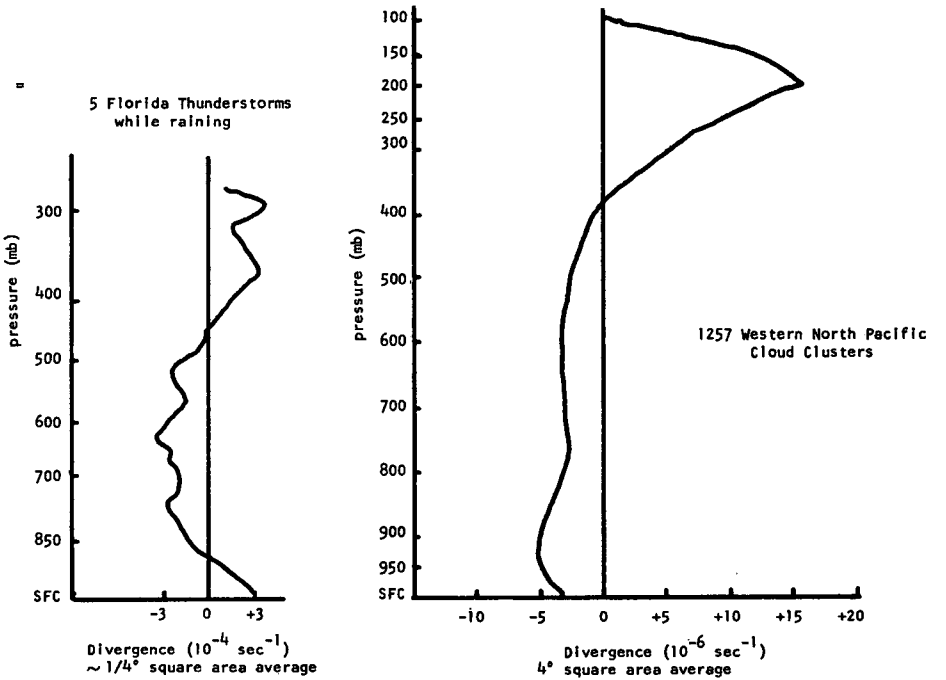

Figure 9. Divergence profiles from K. T. Williams (1970) and from Byers and Braham (1949).

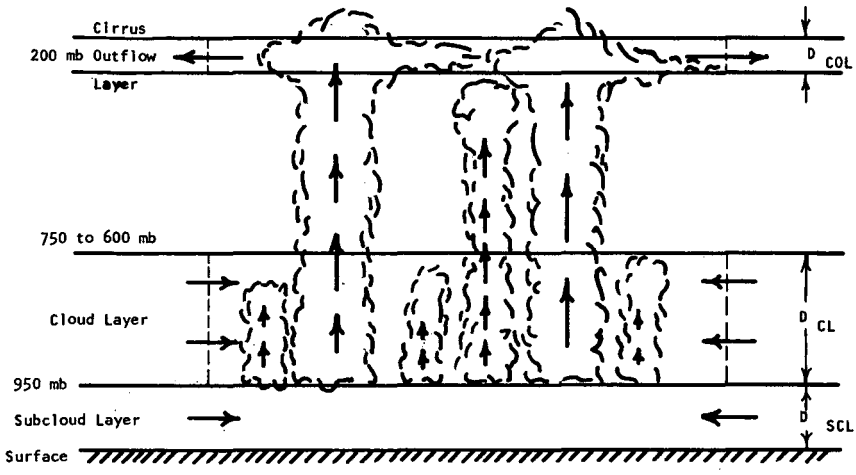

Figure 10. Two-level cloud cluster mass flow model.

to 950 mb). Therefore, with the assumption of uniform (area) convergence for both layers and allowing for density differences, the subcloud mass convergence would be about 15% of the total.

2. If we assume that the thickness of the cirrus outflow layer, D_{COL}, is 1000 m as suggested by Sikdar (1969) and others, then mass flow is conserved by an inflow layer extending from the surface to 750 mb. The subcloud layer mass convergence would be 25% of the total for this version.

We have found that by using the data from this study and some reasonable assumptions, we can make a reasonable model of a cloud cluster's mass flow balance. This result does in fact increase the credibility of the observations.

3.3 Can the Satellite Data be Used to Parameterize the Bulk Effects of the Cloud Cluster on the Synoptic-scale Field?

Parameterization concerns the interrelationship between the synoptic-scale fields discussed in 3.1 and the cloud cluster properties in 3.2. The interrelationships are much more complex and difficult to describe than the quantitative description of either the synoptic-scale fields or the bulk properties alone.

Despite the complexity of the interrelationships, an attempt was made to determine whether or not some aspects of the motion field could act as simple predictors of the generation and decay of cloud clusters. Some parameters which may control the formation of cloud clusters and statements of our ability to measure them from the satellite photographs are listed below.

	Measurement in the vicinity of cloud clusters	Measurement of the synoptic-scale field
1. Low level convergence	Yes	Yes
2. Low level positive vorticity	Yes	Yes
3. High level divergence	Yes	No
4. Vertical instability	No	No
5. Vertical wind shear	Grossly	No
6. Subcloud layer convergence	Indirectly	No
7. Subcloud layer humidity	No	No
8. Sea surface temperature	No	No

In this study, only the first three of these have been measured directly and only the first two have been described in terms of the synoptic-scale fields. An analysis of the nineteen cloud clusters of this study showed that the clusters were always located in regions of negative divergence and almost always in regions of positive relative vorticity. There seemed to be no unique relationship between divergence and vorticity maxima and the cloud cluster location on that day. However, we found that there was also negative divergence and positive vorticity 6° to the east on the previous day while on the following day (after dissipation) the correlation was much weaker. This was found to be true for almost all nineteen cloud clusters examined. It is likely that there are more complex relationships between the parameters listed in the table, but a detailed study of these multiple relationships was beyond the scope of this study.

4. CONCLUSION

We have developed a technique to measure cloud trajectories accurately from geostationary satellite pictures. These measurements allow a description of the synoptic-scale wind field over the data-poor regions of the tropics. It has been demonstrated that cloud trajectories are good estimators of the 950-mb winds. We have described the horizontal low level wind, divergence

and vorticity fields over almost all areas of the tropical oceans with the accuracy and spatial resolution considered necessary for global numerical models. The description of the high level winds was not as complete, but it has been shown that cirrus shield expansion can be used to estimate the high level divergence in disturbed regions. Mass continuity indicated by the high correlation of low level convergence to high level divergence greatly increases the credibility of these statements of accuracy. From this type of data an examination of large scale motions, subsynoptic-scale motions, and especially the interaction between them becomes possible.

Recently there has been considerable progress in the detection of large scale waves in the tropical atmosphere and in the theory of their behavior. In this study it was not possible to examine the spectrum of these motions using satellite data because of the difficulty of obtaining a long time series of continuous data. Future studies using more advanced "day-night" geostationary satellites should allow the observation of low level atmospheric waves over long continuous time periods, as a function of latitude and cloud cover.

The numerical model describes the atmospheric parameters at points on a grid mesh with a minimum feasible spacing of about 2°. However, it has been known for a long time that in the tropics the most important motion, i.e., cumulus "hot towers," occur on a scale much smaller than the grid mesh. For this reason it is essential to parameterize the subgrid scale parameters in terms of the parameters at the grid scale such as the rate and distribution of vertical transport of momentum, heat and moisture within the box. We have demonstrated in this paper that we can measure the convergence at the bottom and the divergence at the top of a cloud cluster contained by a box. With the aid of some additional measurements it should be possible to acquire the data needed to establish the required parameterization schemes.

In conclusion, it can be said that if we hope to achieve our goal of predicting the tropical atmosphere, the geostationary satellite pictures must rise from their role as a secondary data source to that of a primary observing system for a tropical experiment such as GATE.

APPENDIX A

Techniques

This appendix contains a description of the close-up time lapse movie technique and an error analysis, a description of the "polygon" technique for measuring divergence and vorticity, and an error analysis, and the mathematical basis of the techniques.

A. 1 A Close-up Time Lapse Movie Technique for Measuring Cloud Trajectories from Geostationary Satellite Pictures

A. 1. 1—Description. The steps involved in the close-up time lapse movie technique are illustrated in figure 11. The original negatives were aligned and punched on the University of Wisconsin SSEC precision "blink" alignment system. The blink system allows one to superposition two images by means of a partially transmitting 45° mirror and it illuminates each view alternately with variable frequency ranging from about 30 cycles per second to as slow as desired. Landmarks are viewed through magnifying optics and the position of one negative relative to the other is adjusted in x, y and θ until the apparent landmark motion is zero. Once the negative has been properly aligned, a set of registration holes are punched. When a sequence of nine negatives taken during the three hours of the day centered on local noon has been aligned and punched, they are placed successively on a registration jig and photographed. Bellows extensions or close-up lenses were used on an ordinary 16 mm camera to shoot film loops with reduced area coverage. The film loops were made with a sequence "endlessly" repeated, consisting of nine frames of the first and last negatives and three frames of the intermediate negatives.

These close-up movie loops were projected onto a work sheet and the locations of clouds and landmarks were plotted. First, four reference clouds or landmarks were measured on the close-up of the local noon picture, then the motion of cloud positions was measured from the close-up film loop.

In order to relate the geometry of the close-up picture to the earth's geometry, the same reference clouds or landmarks were measured on the full earth picture taken at local noon. In addition, one or more reference landmarks whose latitude and longitude were known and about 100 points on the earth's limb were also obtained. The plotted reference points and cloud trajectory plots were then measured using an x, y electronic digitizing table.

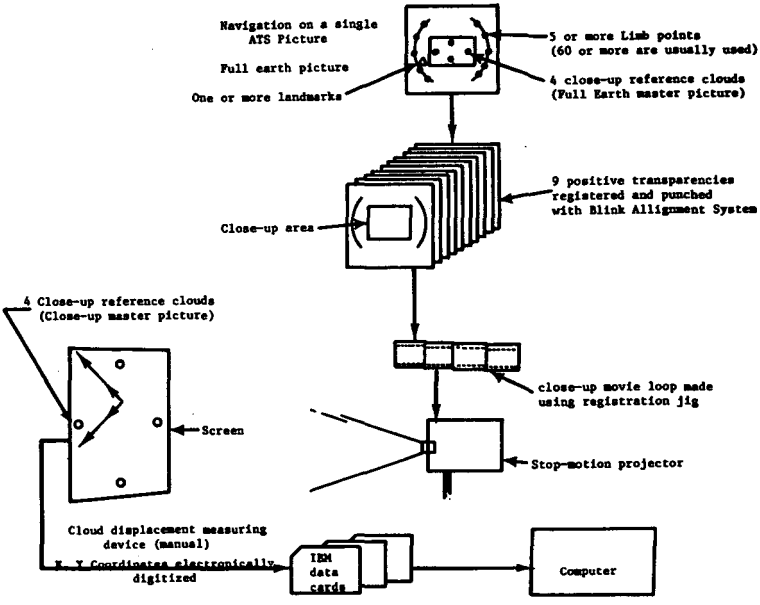

Figure 11. Close-up time lapse movie technique for measuring cloud trajectories from geostationary satellite pictures.

A. 1. 2—Computer Program. A computer program was written to take the raw data output of the electronic digitizing table and print out a complete description of the cloud trajectory field. The subroutines used to navigate the pictures and produce the descriptions of the cloud trajectory field included the following:

a) an ellipse-fitting subroutine which fits the limb points and allows the linear distortion to be removed (the mathematical basis for this nonlinear least square regression fit is presented in section A. 3. 2);

b) a subroutine to compute the distance on the earth's surface from x and y coordinates on the photo (see appendix D for a mathematical description);

c) a subroutine to navigate the pictures by spherical geometry (see A. 3. 3 for mathematical basis);

d) a subroutine to determine the direction of the cloud displacement vector (see A. 3. 4); and

e) an interpolation routine which allows one to navigate the close-up picture back to the full earth picture (see A. 3. 5).

Numerical values of the wind, divergence and vorticity fields printed out by this program are presented in appendix E.

A. 1. 3—Error Analysis. Both random and systematic errors in the cloud trajectory measurements are possible. The effects of random errors can be reduced if you have a large sample, but an unremovable systematic error is the most serious if absolute values are desired. The sources of random error were: human error in plotting the cloud trajectory from the film loop, electronic digitizing table measuring error, registration jig error, and camera and projector registration error. In order to estimate the random error a large number of cloud trajectory speeds were measured repeatedly from the film loops. The standard deviation (S_{speed}) of the speed was then calculated from these many samples. The expression, $S_{speed}/\sqrt{2}$, then represents the theoretical standard deviation of the error in the coordinates of the end points of the cloud trajectory vector. A random number generating function, RANNM(R), from the Univac 1108 library was used to generate a random error with a normal distribution. The error was then multiplied by $S_{speed}/\sqrt{2}$ and added to the x and y input coordinates of the data. The standard deviation of the vector speed and direction errors were estimated by subtracting the results of the program run with the error added from the results of the program run normally on the same data. The results of this test gave estimates of the standard deviation to be . 5 m/s in speed and 2. 5° in direction.

The sources of systematic error were: variations of the spacecraft motion from a true geosynchronous orbit; variations in the spin-scan rates of the camera; variations and errors in the reproduction of the pictures; and alignment error. The following methods were used to estimate systematic errors. In areas near landmarks, the error which results from any of the above sources will cause landmark motion. This motion was measured by the same method which cloud trajectories are measured and it can be subtracted out. In areas far away from landmarks only rough estimates can be made by interpolation from landmark motion. The results of this test gave the following estimates of the systematic errors: near primary landmarks the systematic error was often nearly zero and seldom greater than 1 m/s; near secondary landmarks the systematic error was seldom greater than 1. 5 m/s; near tertiary landmarks the systematic error ranged from near zero to as high as 10 m/s,

but in no case did the tertiary landmark fall inside the close-up area. The systematic errors varied both as a function of data set and as a function of distance from the primary landmark; however, the error varied in a relatively linear manner from one part of the picture to another. Since the error was variable and since in most cases it does not exceed 1.5 m/s within the close-up area, no attempt was made to remove it.

A.2 An Objective "Polygon" Technique for Measuring the Divergence and Vorticity of the Cloud Trajectory Field

A.2.1—Selection of a Technique to Measure Divergence. At the outset one would assume that divergence could be computed from either of the following approximations,

$$DIV_H = \frac{\Delta U}{\Delta X} + \frac{\Delta V}{\Delta Y} \quad \text{or} \quad DIV_H = \frac{\Delta A}{A\Delta t} \quad .$$

In the case of measurements made from pictures where an alignment rotation error exists, it can be shown that the expression $\frac{\Delta U}{\Delta X} + \frac{\Delta V}{\Delta Y}$ will contain an error due to the rotation, while the expression $\frac{\Delta A}{A\Delta t}$ will be independent of any alignment error. For this reason, the expression $\frac{\Delta A}{A\Delta t}$ was chosen for use in this paper. However, the above is true only for the case of a plane. In the case of geostationary satellite pictures of a near spherical earth, a misalignment of pictures results in a relative misnavigation of the picture. For typical alignment errors, a significant error results which increases systematically as you depart from the subsatellite point. The magnitude of this error is discussed in the error analysis section below.

A.2.2—"Polygon" Technique for Measuring Divergence and Vorticity. A ring of clouds (or velocity vectors) is selected which form a polygon which has an approximately circular shape and which is of the scale size desired. The area of the polygon is computed at times T_1 and T_2 and the change in area gives the divergence according to the system of equations derived in A.3.6. The technique is purely objective and does not depend on subjective streamline or isotach analysis. The technique can be used to calculate divergence directly from a vector field with nonuniform spacing. In the case of cloud clusters, a polygon may be selected using the nearest cloud trajectories, thereby giving the most accurate measurements of the divergence in the immediate vicinity of the cloud cluster.

The logical extension of the divergence measuring technique was to approximate the line integral $\oint \frac{\vec{V} \cdot \vec{ds}}{A}$ around the same polygon, thereby measuring the vorticity. The equations for this technique are presented in A. 3. 7. The technique therefore uses the identical data input as the convergence technique and makes the results directly comparable. The assumptions for the technique are nearly identical to those of the divergence technique. However, in this case the picture alignment error cannot be eliminated, and since any rotation error will be systematic over the entire picture, the measurement of vorticity in one part of the picture relative to another part should be independent of alignment error.

A. 2. 3—Data Selection and Description. The polygons were selected on three different horizontal space scales: boxes 5° of latitude by 5° of longitude (5° × 5° boxes); 10° × 10° boxes; and 15° × 15° boxes. The set of cloud trajectories (polygon) which described the smoothest curve and which correspond most closely to the particular box was chosen. The average number of cloud trajectories for the polygons of each space scale for the eighteen-day data set was as follows: 5° × 5° polygons—6; 10° × 10° polygons—12; and 15° × 15° polygons—18.

A. 2. 4—Tests of the Validity of the Techniques. The divergence and vorticity measuring techniques were compared with measurements made by conventional techniques. A uniformly spaced vector field was derived from satellite-determined cloud trajectories. The divergence and vorticity were then calculated using the equations

$$D_2V = \frac{\overline{\Delta U}}{\Delta X} + \frac{\overline{\Delta V}}{\Delta Y} \quad \text{and} \quad \zeta = \frac{\overline{\Delta V}}{\Delta X} - \frac{\overline{\Delta U}}{\Delta Y} \ .$$

The divergence and vorticity was then calculated for polygons consisting of the smallest squares made up by the uniform vector field. The correspondence between the two techniques was very good. The average difference between the two divergence techniques was 9. 5% with a standard deviation of 7. 7%. The average difference between the two vorticity techniques was 4. 2% with a standard deviation of 3. 8%.

A. 2. 5—Error Analysis. An analysis of the random and systematic errors of the divergence and vorticity techniques was carried out. The sources of random error are the same as those for the cloud trajectories and the method of estimating the random error was the same, i. e., a random error, normally distributed with mean zero and standard deviation, $S_{speed}/\sqrt{2}$, was added to each of the cloud trajectory end-point coordinates. The divergence and vorticity errors were then estimated by subtracting the results of the program run with the input errors from the results of the program run normally. The

standard deviation of the difference was then calculated. The standard deviation of the random error was estimated to be less than the following values:

$5° \times 5°$ polygons: $S_{divergence} = S_{vorticity} = \pm 3 \times 10^{-6}$ sec^{-1}

$10° \times 10°$ polygons: $S_{divergence} = S_{vorticity} = \pm 1 \times 10^{-6}$ sec^{-1}

$15° \times 15°$ polygons: $S_{divergence} = S_{vorticity} = \pm .4 \times 10^{-6}$ sec^{-1}

The sources of systematic errors are also the same as those for the cloud trajectories. The following method was used to estimate the systematic errors. The motion of the landmarks was measured as described in section A. 1. 3. Then an artificial alignment rotation and displacement error, corresponding to the maximum landmark motion, was introduced into the input coordinates. Finally, the divergence and vorticity values, resulting from the program run with the artificial alignment error, were subtracted from the values resulting when the program was run normally. Given an artificial alignment displacement error of $\Delta x = 16$ km, $\Delta y = 6$ km (this corresponds approximately to a speed error of 2 m/s), the output errors resulting in the close-up region were divergence, less than 3×10^{-6} sec^{-1}, decreasing in a linear manner toward the SSP; and vorticity, less than 1×10^{-6} sec^{-1}, decreasing in the same manner. Given an artificial alignment rotation error of 0. 1 radians (rotation about the SSP), the resulting output errors were as follows over the close-up region:

a) for the $5° \times 5°$ divergence polygons, the error was less than $.05 \times 10^{-6}$ sec^{-1} and decreasing toward the SSP;

b) for the $10° \times 10°$ divergence polygons, the error was less than $.2 \times 10^{-6}$ sec^{-1} and decreasing toward the SSP;

c) for the $15° \times 15°$ divergence polygons, the error was less than $.25 \times 10^{-6}$ sec^{-1} and decreasing toward the SSP; and

d) all vorticity polygons had a relatively constant error of 1.7×10^{-5} sec^{-1} .

In the limit where the polygon is a triangle, the technique is identical with the technique described by Bellamy (1949) which assumes linear variation of velocity. If five or more clouds are used and the polygon is nearly circular, the technique may give unbiased results for second order variations in velocity. In fact, it may approach the accuracy of the more sophisticated models derived by Schmidt and Johnson (1971).

A. 3 Mathematical Basis of the Techniques

Most of the equations and mathematical operations used in the cloud trajectory measuring techniques and the divergence and vorticity measuring techniques described in A. 1 and A. 2 are contained in this section. Some derivations are also included.

A. 3. 1—Some Basic Equations. Refer to Hasler et al. (1969), which is included as appendix D, for the following equations and derivations: the tangent plane approximation used in rectifying the pictures; the mathematical basis of the original distortion correction and superimposition procedure; and the equations for the rectification procedure.

A. 3. 2—Ellipse Fitting Technique. A nonlinear least-square regression was derived for a completely arbitrary (five-parameter) ellipse. This regression was used to determine the subsatellite point for the navigation of the pictures and to correct any linear distortion in the picture. Let

$$A'X_i^2 + B'Y_i^2 + C'X_iY_i + D'X_i + E'Y_i + F' = 0$$

be the most general equation for a planar ellipse, where $A', B', \ldots, F'$ are the coefficients and X_i, Y_i are the coordinates of the i^{th} point on the ellipse, then we can get:

$$AX_i^2 + BY_i^2 + CX_iY_i + DX_i + EY_i = 1 .$$

If we assume that the relationship between X and Y is not perfect, we can represent the error as ε_i for the i^{th} point so that

$$AX_i^2 + BY_i^2 + CX_iY_i + DX_i + EY_i - 1 + \varepsilon_i = 0 .$$

Let

$$AX_i^2 + BY_i^2 + CX_iY_i + DX_i + EY_i - 1 = W_i .$$

The least square estimators of A, B, ... E may be obtained by minimizing the quantity

$$Z = \Sigma (\varepsilon_i)^2 = \Sigma (W_i)^2$$

with respect to A, B, ... E (all sums are from $i = 1$ to $i = N$, where N is the number of data points). This can be done in the following manner: Let

$$\frac{\partial Z}{\partial A} = 2\Sigma X_i^2 W_i = 0$$

$$\frac{\partial Z}{\partial B} = 2\Sigma Y_i^2 W_i = 0$$

$$\frac{\partial Z}{\partial C} = 2\Sigma X_i Y_i W_i = 0$$

$$\frac{\partial Z}{\partial D} = 2\Sigma X_i W_i = 0$$

$$\frac{\partial Z}{\partial E} = 2\Sigma Y_i W_i = 0$$

where the values of A, B, ... E at the minimum are their estimators $\hat{A}$, $\hat{B}$, ... $\hat{E}$.

We now have five equations and five unknowns:

$$\hat{A}\Sigma X_i^4 + \hat{B}\Sigma X_i^2 Y_i^2 + \hat{C}\Sigma X_i^3 Y_i + \hat{D}\Sigma X_i^3 + \hat{E}\Sigma X_i^2 Y_i = \Sigma X_i^2$$

$$\hat{A}\Sigma X_i^2 Y_i^2 + \hat{B}\Sigma Y_i^4 + \hat{C}\Sigma X_i Y_i^3 + \hat{D}\Sigma X_i Y_i^2 + \hat{E}\Sigma Y_i^3 = \Sigma Y_i^2$$

$$\hat{A}\Sigma X_i Y_i^3 + \hat{B}\Sigma X_i Y_i^3 + \hat{C}\Sigma X_i^2 Y_i^2 + \hat{D}\Sigma X_i^2 Y_i + \hat{E}\Sigma X_i Y_i^2 = \Sigma X_i Y_i$$

$$\hat{A}\Sigma X_i^3 + \hat{B}\Sigma X_i Y_i^2 + \hat{C}\Sigma X_i^2 Y_i + \hat{D}\Sigma X_i^2 + \hat{E}\Sigma X_i Y_i = \Sigma X_i$$

$$\hat{A}\Sigma X_i^2 Y_i + \hat{B}\Sigma Y_i^3 + \hat{C}\Sigma X_i Y_i^2 + \hat{D}\Sigma X_i Y_i + \hat{E}Y_i^2 = \Sigma Y_i$$

which is $\bar{T} \cdot \bar{X} = \bar{V}$ in matrix notation, where

$$\bar{T} = \begin{vmatrix} \Sigma X_i^4 & \Sigma X_i^2 Y_i^2 & \Sigma X_i^3 Y_i & \Sigma X_i^3 & \Sigma X_i^2 Y_i \\ \Sigma X_i^2 Y_i^2 & \Sigma Y_i^4 & \Sigma X_i Y_i^3 & \Sigma X_i Y_i^2 & \Sigma Y_i^3 \\ \Sigma X_i^3 Y_i & \Sigma X_i Y_i^3 & \Sigma X_i^2 Y_i^2 & \Sigma X_i^2 Y_i & \Sigma X_i Y_i^2 \\ \Sigma X_i^3 & \Sigma X_i Y_i^2 & \Sigma X_i^2 Y_i & \Sigma X_i^2 & \Sigma X_i Y_i \\ \Sigma X_i^2 Y_i & \Sigma Y_i^3 & \Sigma X_i Y_i^2 & \Sigma X_i Y_i & \Sigma Y_i^2 \end{vmatrix} \qquad \bar{X} = \begin{vmatrix} \hat{A} \\ \hat{B} \\ \hat{C} \\ \hat{D} \\ \hat{E} \end{vmatrix}$$

$$\bar{V} = \begin{vmatrix} \Sigma X_i^2 \\ \Sigma Y_i^2 \\ \Sigma X_i Y_i \\ \Sigma X_i \\ \Sigma Y_i \end{vmatrix}$$

which may be solved for $\bar{X}$ by inverting the $\bar{T}$ matrix

$$\bar{X} = \bar{T}^{-1} \bar{V} .$$

This can be done easily by a computer library subroutine and gives the estimators

$$\hat{A}, \hat{B}, \hat{C}, \hat{D}, \hat{E} .$$

These are related to the coefficients used in appendix D by

$$T_1 = \frac{\hat{B}}{\hat{A}}, \quad T_2 = \frac{\hat{C}}{\hat{A}}, \quad T_3 = \frac{\hat{D}}{\hat{A}}, \quad T_4 = \frac{\hat{E}}{\hat{A}}, \quad T_5 = \frac{1}{\hat{A}} .$$

An estimate of the rotation, major and minor axes, and x and y coordinates of the center of the ellipse may be obtained from these coefficients as explained in appendix D.

A. 3. 3—Latitude-Longitude Equations (see figure 12). Given the following:

1) the X and Y coordinates (X_{ssp}, Y_{ssp}) of the subsatellite point on the picture as derived in section 2 above;

2) the latitude and longitude (α_{ssp}, γ_{ssp}) of the subsatellite point (part of orbital data supplied by NASA);

3) the X and Y coordinates (X_{lm}, Y_{lm}) of a landmark as measured directly from the picture;

4) the latitude and longitude (α_{lm}, γ_{lm}) of the landmark as determined from an atlas;

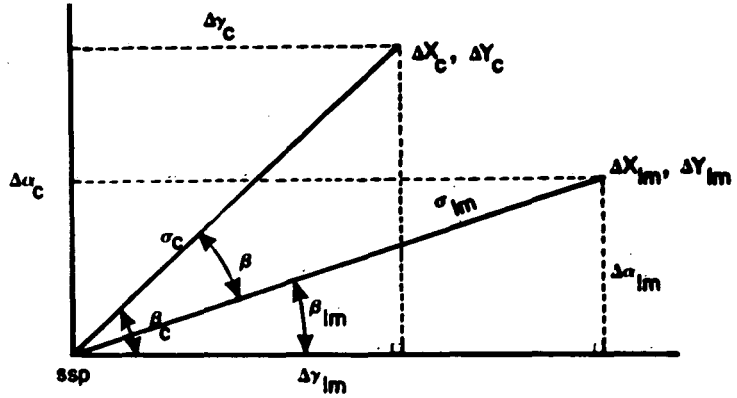

Figure 12. Spherical geometry used to determine the latitude and longitude of a point, given its x and y coordinates on the picture and other necessary constants.

---

5) the great circle distance between two points on the surface of the earth as a function of their X and Y coordinates on the picture as derived in the appendix D;

6) the X and Y coordinates (X_C, Y_C) of a point C on the picture as measured directly;

find the latitude and longitude $(\Delta\alpha_C, \Delta\gamma_C)$ of point C.

$$\Delta\alpha_{lm} = \alpha_{ssp} - \alpha_{lm}$$

$$\Delta\gamma_{lm} = \gamma_{ssp} - \gamma_{lm}$$

$$\Delta X_{lm} = X_{ssp} - X_{lm}$$

$$\Delta Y_{lm} = Y_{ssp} - Y_{lm}$$

$$\Delta X_C = X_{ssp} - X_C$$

$$\Delta Y_C = Y_{ssp} - Y_C$$

$$\left.\begin{aligned} \sigma_{lm} &= f(\Delta X_{lm}, \Delta Y_{lm}) \\ \sigma &= f(\Delta X_C, \Delta Y_C) \\ \beta &= f(\Delta X_{lm}, \Delta Y_{lm}, \Delta X_C, \Delta Y_C) \end{aligned}\right\} \text{ as derived in appendix D}$$

From the law of sines for a spherical triangle

$$\beta_{1m} = \arcsin\left(\frac{\sin\Delta\alpha_{1m}}{\sin\sigma_{1m}}\right)$$

$$\beta_c = \beta + \beta_{1m}$$

If $(X_{1m}Y_c - Y_{1m}X_c) < 0$, multiply β by -1. Then, again, from the law of sines

$$\Delta\alpha_c = \arcsin[\sin\beta_c \sin\sigma_c]$$

and from Napier's law for right spherical triangles

$$\Delta\gamma_c = \arcsin\tan\Delta\gamma_c[\tan(90^\circ - \beta_c)] .$$

A. 3. 4—Direction equations (see figure 13). Given the latitude and longitude of two points $(\alpha_1, \gamma_1, \alpha_2, \gamma_2)$ on the earth's surface less than 200 km apart, find the approximate direction $(\bar{\theta})$ of the great circle arc connecting them. The average X displacement is

$$\overline{\Delta X} = (\gamma_1 - \gamma_2)\cos\frac{(\alpha_1 + \alpha_2)}{2} .$$

The Y displacement is

$$\Delta Y = \alpha_2 - \alpha_1 .$$

Then the approximate direction is

$$\bar{\theta} = \arctan\frac{\Delta Y}{\overline{\Delta X}} .$$

If $\overline{\Delta X}$ and ΔY are divided by the time interval between pictures, we have the u and v components of the motion.

A. 3. 5—"Close-up" Transformation Equations. Given:

1) four reference points on a close-up picture (XR_i^{cu}, YR_i^{cu});

2) the same four reference points measured on a full earth picture (XR_i^{FE}, YR_i^{FE}),

3) an arbitrary point measured on the close-up picture (X_i^{cu}, Y_i^{cu});

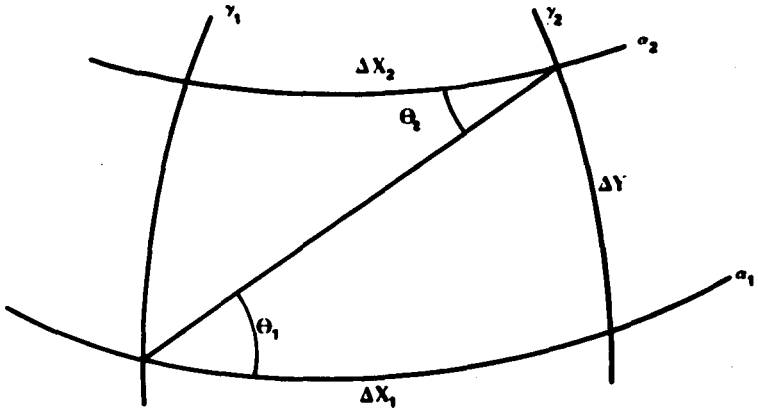

Figure 13. Geometry used to determine the approximate direction of a great circle arc connecting two points less than 200 km apart on the earth's surface.

---

find the necessary transformation equations to find the corresponding point on the full earth picture (X_1^{FE}, Y_1^{FE}).

The line connecting two reference points on the full-earth picture makes the angle θ_{FE} with the measuring table coordinate system where

$$\theta_{FE} = \arctan\left[\frac{XR_2^{FE} - XR_1^{FE}}{YR_2^{FE} - YR_1^{FE}}\right]$$

The corresponding angle on the close-up picture is

$$\theta_{cu} = \arctan\left[\frac{XR_2^{cu} - XR_1^{cu}}{YR_2^{cu} - YR_1^{cu}}\right]$$

therefore one picture must be rotated through an angle θ in order to bring it into alignment, where

$$\theta = \theta_{cu} - \theta_{FE}.$$

This can be accomplished by rotating each point on the close-up picture, including the four reference points, by using the following expressions:

$$X\theta_1^{cu} = X_1^{cu} \cos\theta + Y_1^{cu} \sin\theta$$

$$Y\theta_i^{cu} = -X_i^{cu} \sin\theta + Y_i^{cu} \cos\theta$$

$$XR\theta_i^{cu} = XR_i^{cu} \cos\theta + YR_i^{cu} \sin\theta$$

$$YR\theta_i^{cu} = -XR_i^{cu} \sin\theta + YR_i^{cu} \cos\theta .$$

The final step in the transformation is the sizing operation which is accomplished by the following interpolation equations:

$$X_i^{FE} = (X\theta_i^{cu} - XR\theta_3^{cu}) \frac{(XR_4^{FE} - XR_3^{FE})}{(XR\theta_4^{cu} - XR\theta_3^{cu})} + XR_3^{FE}$$

$$Y_i^{FE} = (Y\theta_i^{cu} - YR\theta_1^{cu}) \frac{(YR_2^{FE} - YR_1^{FE})}{(YR\theta_2^{cu} - YR\theta_1^{cu})} + YR_1^{FE}$$

A. 3. 6—Divergence Equations. Given the latitude and longitude of n clouds forming an irrgular n-sided polygon at times T_1 and T_2 (α_i^1, γ_i^1, α_i^2, γ_i^2) as shown in figure 14, find the divergence (horizontal).

Let divergence be defined as $D_2V = \frac{\Delta A_n}{A_n \Delta T}$, where A_n is the area of the polygon and ΔA_n is the change in area over the time interval $\Delta T = T_2 - T_1$. We can write an expression for the area of a polygon which is based on summing triangular-shaped subareas,

$$A_n = \sum_{i=1}^{n} \frac{Y_i(X_{i+1} - X_{i-1})}{2}$$

which is good for a rectangular coordinate system where X_i, Y_i are the coordinates of the vertices.

Now we can apply this expression to a spherical earth coordinate system. A good approximation for moderate sized areas can be made by multiplying the longitude differences between two points by the cosine of the average latitude of the two points.

Let the average latitude of clouds $i + 1$ and $i - 1$ at time T_1 be

$$\bar{\alpha}_i^1 = \frac{\alpha_{i+1}^1 + \alpha_{i-1}^1}{2}$$

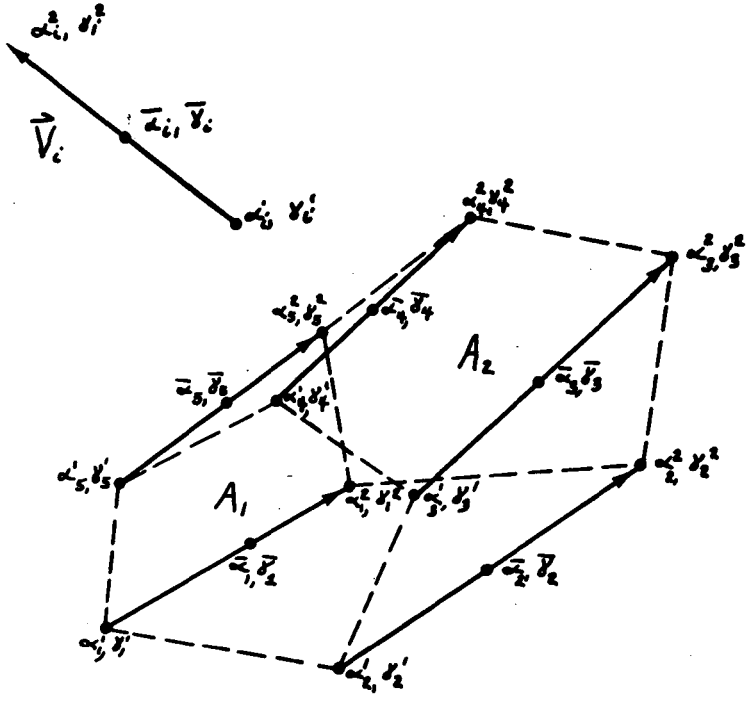

Figure 14. Above: Cloud displacement vector, $\vec{V}_i$, where the start point of the vector is at latitude and longitude (α_i^1, γ_i^1) of the cloud at time T_1. The end point is at latitude and longitude (α_i^2, γ_i^2) at time T_2. The mid-point of the vector is at average latitude and longitude α_i, γ_i.

Below: A five-sided polygon with area A_1 at time T_1 and area A_2 at time T_2.

and at time T_2

$$\bar{\alpha}_i^2 = \frac{\alpha_{i+1}^2 + \alpha_{i-1}^2}{2} .$$

Then the area of the polygon at time T_1 is

$$A_1 = \frac{\sum_{i=1}^{n} \alpha_i^1 (\gamma_{i+1}^1 - \gamma_{i-1}^1) \cos \bar{\alpha}_i^1}{2}$$

and at time T_2

$$A_2 = \frac{\sum_{i=1}^{n} \alpha_i^2 (\gamma_{i+1}^2 - \gamma_{i-1}^2) \cos \bar{\alpha}_i^2}{2} .$$

The divergence is then

$$D_2V = \frac{A_2 - A_1}{|A_1|(T_2 - T_1)} .$$

A. 3. 7—Vorticity Equations. Given the latitude and longitude of n clouds forming an irregular n-sided polygon at times T_1 and T_2 as shown in figure 15, find the vorticity (vertical component of relative vorticity).

Let vorticity be defined as $\zeta = \oint \frac{\vec{V} \cdot \vec{ds}}{A_n}$ where $\vec{V}$ is the horizontal wind vector at the location of elemental segment, $\vec{ds}$, which is on the line surrounding the area A_n. The symbol $\oint$ indicates the line integral taken around the area.

Now if we write this in finite difference form

$$\zeta = \sum_{i=1}^{n} \frac{|\vec{V}_i||\Delta\vec{S}_i| \cos \theta_i}{A_n} .$$

$|V_i|$ then represents the average speed of the wind blowing across the line segment $\Delta\vec{S}_i$ at the average angle θ_i. But since we know only $\vec{V}1_i$ and $\vec{V}2_i$, the wind vectors at each end of $\Delta\vec{S}_i$, and $\theta 1_i$ and $\theta 2_i$, the respective angles between the wind vectors, and $\Delta\vec{S}_i$, we must assume a linear variation of velocity between the ends of $\Delta\vec{S}_i$. In this case we can use the following expression:

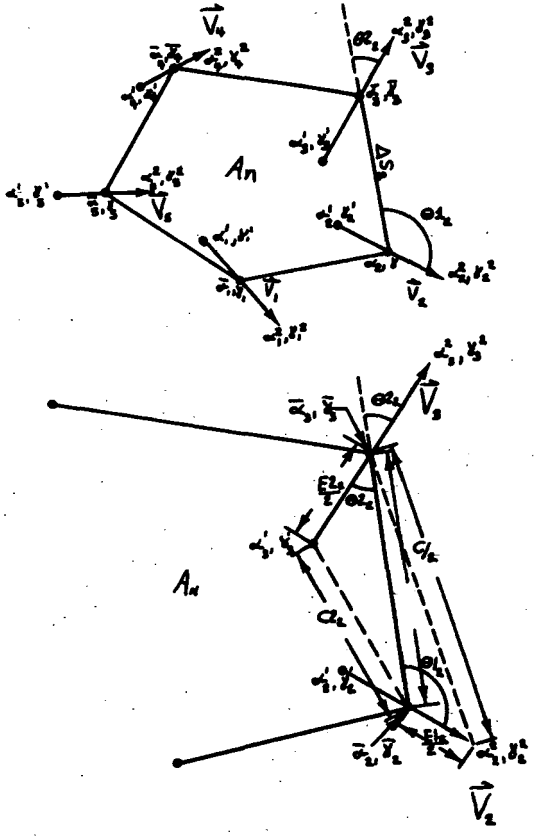

Figure 15. Above: A five-sided polygon described by the midpoints of the vectors with area A_n.

Below: Diagram of the geometry used in the vorticity measuring technique. The quantities A_i, $E1_i/2$, $E2_i/2$, $C1_i$, $C2_i$, $\theta 1_i$, $\theta 2_i$, are diagrammed for a specific case.

$$\zeta = \sum \frac{(|\vec{V}1_i| \cos \theta 1_i + |\vec{V}2_i| \cos \theta 2_i)|\Delta S_i|}{2A_n}$$

Let the latitude and longitude of the midpoint of the line connecting the cloud at time T_1 and time T_2 be

$$\alpha_i = \frac{\alpha_i^1 + \alpha_i^2}{2}$$

$$\gamma_i = \frac{\gamma_i^1 + \gamma_i^2}{2} .$$

Again, if we multiply the longitude differences between two points by the cosine of the average latitude of the two points, we have an approximate expression for a spherical coordinate system. We therefore define six average latitude functions:

$$\bar{\alpha}1_i = \frac{\bar{\alpha}_{i+1} + \bar{\alpha}_i}{2}$$

$$\bar{\alpha}2_i = \frac{\bar{\alpha}_{i+1} + \alpha_i^2}{2}$$

$$\bar{\alpha}3_i = \frac{\bar{\alpha}_i + \alpha_{i+1}^1}{2}$$

$$\bar{\alpha}4_i = \frac{\alpha_i^1 + \alpha_i^2}{2}$$

$$\bar{\alpha}5_i = \frac{\alpha_{i+1}^1 + \alpha_{i+1}^2}{2}$$

$$\bar{\alpha}6_i = \frac{\bar{\alpha}_{i+1} + \bar{\alpha}_{i+1}}{2}$$

and the following coefficients:

$$A_i = \sqrt{[(\bar{\gamma}_{i+1} - \bar{\gamma}_i) \cos \bar{\alpha}1_i]^2 + [\bar{\alpha}_{i+1} - \bar{\alpha}_i]^2}$$

$$C1_i = \sqrt{[(\bar{\gamma}_{i+1} - \gamma_i^2) \cos \bar{\alpha}2_i]^2 + [\bar{\alpha}_{i+1} - \alpha_i^2]^2}$$

$$C2_i = \sqrt{[(\bar{\gamma}_i - \gamma_{i+1}^2) \cos \bar{\alpha}3_i]^2 + [\bar{\alpha}_i^1 - \alpha_{i+1}]^2}$$

$$E1_i = \sqrt{[(\gamma_i^1 - \gamma_i^2)\cos \bar{\alpha}4_i]^2 + [\alpha_i^1 - \alpha_i^2]^2}$$

$$E2_i = \sqrt{[(\gamma_{i+1}^1 - \gamma_{i+1}^2)\cos \bar{\alpha}5_i]^2 + [\alpha_{i+1}^1 - \alpha_{i+1}^2]^2}$$

$$F_i = \bar{\alpha}_i(\bar{\gamma}_{i+1} - \bar{\gamma}_{i-1})\cos \bar{\alpha}6_i \ .$$

Then

$$V1_i = E1_i/\Delta T$$

$$V2_i = E2_i/\Delta T$$

$$\cos \theta 1_i = \frac{(E1_i/2)^2 + (A_i)^2 - (C1_i)^2}{A_i \cdot E1_i}$$

$$\cos \theta 2_i = \frac{(E2_i/2)^2 + (A_i)^2 - (C2_i)^2}{A_i \cdot E2_i}$$

$$\Delta s_i = A_i \ .$$

By summing we get the vorticity

$$\zeta = \sum_{i=1}^{n} \frac{(|V1_i| \cos \theta 1_i + |V2_i| \cos \theta 2_i)|\Delta S_i|/2}{\sum_{i=1}^{n} F_i/2}$$

where

$$A_n = \left| \sum_{i=1}^{n} F_i/2 \right| \ .$$

APPENDIX B

Comparison with Other Data

This appendix contains a comparison of the cloud trajectories measured in this study with The University of Wisconsin SSEC computer correlation technique for measuring cloud displacements, a comparison with the NOAA movie-loop technique for measuring cloud displacements, and a comparison with conventionally measured radiosonde winds.

B. 1 Comparison with Cloud Trajectories Measured by Other Techniques

B. 1. 1—Computer Correlation. A comparison was made with cloud displacements measured by a computer correlation technique which was recently developed by Smith and Phillips (1971) of the SSEC. The computer correlation technique, because of its ability to make very precise automated measurements, is the technique of the future. Figures 16 to 18 show the close-up movie loop and computer correlation cloud trajectories compared for July 26–28, 1969. Areas which contained two or more relatively consistent trajectories, as measured by both techniques, were selected. The average trajectories were calculated for each technique from the u and v components. These trajectories were then compared as to speed and direction, u component, v component, and absolute value of the vector difference. Table 2 shows the differences which were obtained from a total of thirty-three comparisons of 116 movie-loop trajectories with 116 computer correlation observations. The average difference is given for each day as well as the difference value which includes 68% of the comparisons.

The agreement for the July 26 case shown in table 2 is excellent, but the July 27 and 28 comparisons show fairly large systematic differences in the v component. Since these differences are systematic they may very well be caused by an alignment error unaccounted for in either system. If one subtracts out the systematic difference of $\Delta v = 5.6$ knots for July 26 and $\Delta v = 4.2$ knots for July 27, the average absolute value of the remaining Δv is 1.1 knots and 1.5 knots, respectively. This gives excellent agreement if one can find a rationale for subtracting out this systematic difference. However, since the differences found are within the error limits of the two systems combined, no adjustment has been made.

B. 1. 2—NOAA Movie-Loop Technique[1]. The close-up movie-loop cloud

[1]The NOAA technique as described by Hubert (1971).

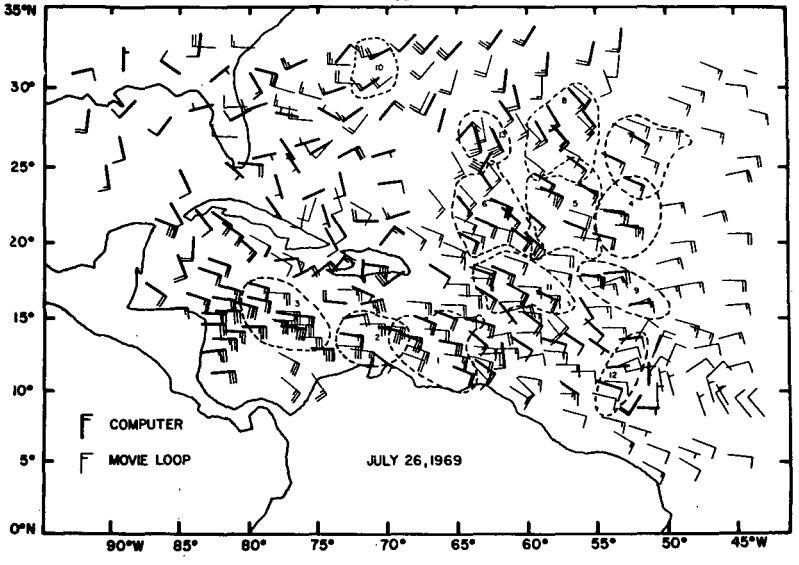

Figure 16. Close-up movie cloud trajectories compared with computer correlation cloud trajectories (July 26, 1969).

trajectories were compared with the forty-five NOAA movie-loop cloud trajectories for July 28 and 28, 1969. Figure 19 shows the July 28th comparison. A relatively consistent set of "CU" movie-loop cloud trajectories is selected which lie within 150 nm of a NOAA trajectory. The set is averaged and compared with the NOAA trajectory. The results of the comparison are shown in table 2.

For the July 26 and 28 combined we have 68% of the speed differences less than 3.4 knots, and 68% of the direction differences less than 15.7° . The results of the comparisons are not as good as the computer comparison for July 26, but are quite equivalent to the computer comparison for July 28.

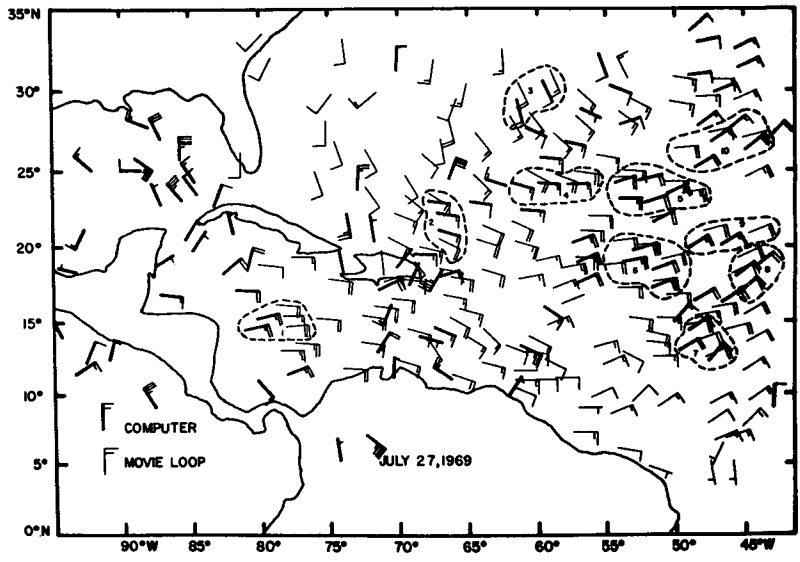

Figure 17. Close-up movie cloud trajectories compared with computer correlation cloud trajectories (July 27, 1969).

B. 2 Comparison with Conventionally Measured Winds

B. 2. 1—Ultimate Ground Truth Experiment. The ultimate ground truth experiment would measure two differences: the difference between the satellite-measured cloud trajectory and the actual trajectory, and the difference between the cloud trajectory and the wind. A possible method for measuring these differences would use an airplane to make high altitude aerial photographs of suitable clouds simultaneously with the satellite pictures. Precise height contouring and location measurements would be made from the aerial photographs. Other aircraft would simultaneously make precise measurements of the ambient wind field using doppler radar and also make photographic cloud base measurements.

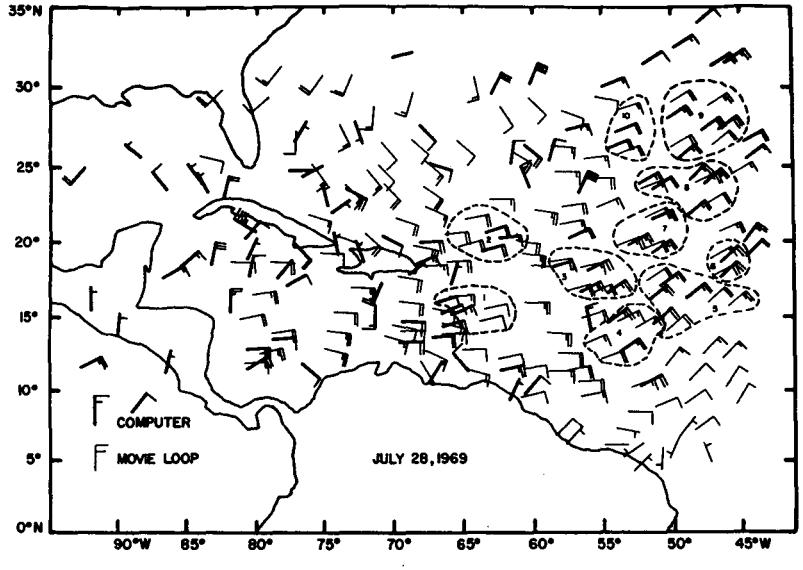

Figure 18. Close-up movie cloud trajectories compared with computer correlation cloud trajectories (July 28, 1969).

B. 2. 2—Comparison. Since the experiment described above has not yet been conducted, we are limited to comparing the cloud trajectories with conventional winds. This comparison will contain differences due to error in the cloud trajectory measurements, in the location of the cloud trajectory (primarily height error), and in the conventional wind measurements; and also due to the difference between the cloud trajectories and the ambient wind. Because of the first three errors any estimate of the latter by this method will be too large. However, improved technology and techniques such as high resolution pictures with infrared height information and more sophisticated computer programs should allow the reduction of the first three errors to an insignificant level in the future. The remaining difference between cloud trajectories and ambient wind, if significant, may be systematic and removable.

Table 2

Movie Loop vs. Computer Correlation

Date	Δu knots	Δu knots	$\lvert \vec{V}$ movie $- \vec{V}$ computer$\rvert$ knots		$\lvert \Delta$ speed $\rvert$ knots		$\lvert \Delta$ direction $\rvert$ degrees	
	Average	Average	Average	68%	Average	68%	Average	68%
July 26, 1969	- .1	1.0	2.7	2.4	1.9	2.3	4.9	6.8
July 27, 1969	- .8	5.6	5.9	6.4	2.6	2.8	14.0	15.1
July 28, 1969	2.0	4.2	4.7	6.5	3.7	5.3	7.6	11.1
Movie Loop vs. NOAA Movie Loop								
July 26, 1969	1.9	-3.6	6.0	7.6	2.6	2.9	19.8	21.7
July 28, 1969	.3	3.0	5.1	4.7	2.9	3.8	11.5	12.2
Combined	1.1	- .3	5.5	5.7	2.7	3.4	12.4	15.7

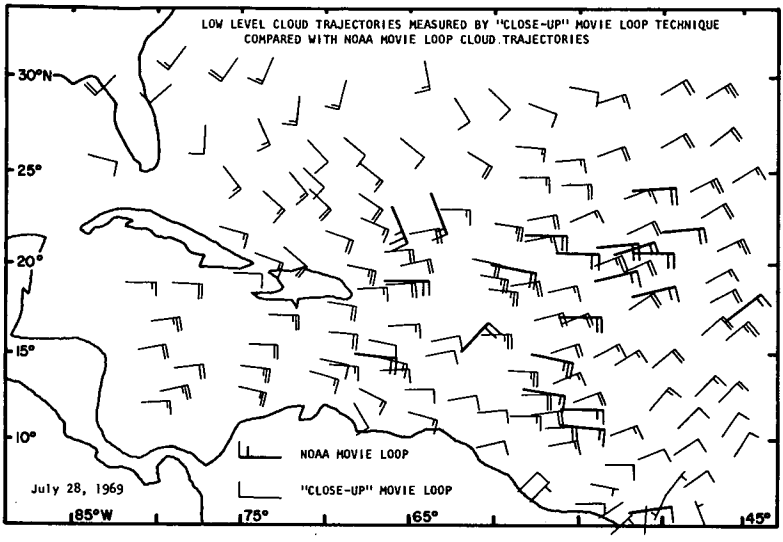

Figure 19. Low-level cloud trajectories measured by close-up movie technique compared with NOAA movie loop cloud trajectories.

Conventional wind observations were obtained from all sources available to the author. For example: The Northern Hemisphere Data Tabulation, Barbado Oceanographic and Meteorological Experiment (BOMEX) soundings, National Hurricane Center analyses, Pacific Fleet Weather Central analyses, New Zealand Meteorological Service data, as well as data from the National Climatic Center were used. Figure 4 shows as an example the conventionally measured 950 mb winds and the cloud trajectories plotted for the Caribbean on July 27, 1969.

To make the comparison, a relatively consistent set of cloud trajectories within 150 nm of a rawin sounding was averaged and compared with the sounding. The minimum magnitude of the vector difference between the average cloud velocity and sounding velocity was used to determine the level of best fit. Best fit frequency vs. altitude was plotted in the form of bar graphs. The vector speed and direction differences were calculated for the following levels: the best fit level, the most frequent best fit level (i.e., 950 mb), and the surface.

Figure 2 shows the frequency of best fit vs. altitude for low clouds in the Caribbean for the July 26-28, 1969 BOMEX dates. The maximum frequency of best fit is at 950 mb but the peak is quite broad. In fact, a number of cases have a best fit level as high as 600-500 mb. Figure 3 shows the frequency of best fit vs. altitude for low clouds in the central Pacific for the fifteen dates chosen. The maximum frequency of best fit is again at 950 mb with a much sharper peak. One reason for the sharper peak is that one-third of the Pacific soundings did not go above 850 mb.

In table 3, the data labeled "Best fit level" show that on the average one could find a level at which the sounding differed from the cloud trajectory by about 1 m/s and 14°. It is also revealed that the Caribbean and Pacific areas give nearly identical results in the comparisons. For the 950 mb level, 68% of the speed differences were less than about 2.5 m/s and the 68% of the direction differences were less than 30°. Systematic differences are small except for y during some Pacific days. Differences computed for the 900 mb level gave only slightly inferior results. Since a much greater number of surface winds were available, the comparison was made for this level also. The results, however, were considerably worse.

Comparisons made by Fujita et al. (1969) also give 950 mb as the best fit level, while Hubert and Whitney (1971) and Serebreny et al. (1969) arrive at 900 mb–850 mb from their comparisons. The comparison of NOAA cloud trajectories to the best fit level rawinsonde winds described by Hubert and Whitney gives an average vector difference of 9 knots. This comparison also gives 68% of the direction differences to be less than 40°. This is somewhat inferior to the comparison results from the close-up movie cloud trajectories which give an average vector difference of 7 knots and give 68% of the direction differences to be less than 30°. This result is expected since the NOAA trajectories were obtained under the pressure of an operational situation while more time was taken in obtaining the close-up movie trajectories.

Table 3

Cloud Trajectories Compared with Conventional Observations

	Δv knots	Δv knots	$\lvert\vec{V}$ movie $-\vec{V}$ conventional$\rvert$ knots		$\lvert\Delta$ speed$\rvert$ knots		$\lvert\Delta$ direction$\rvert$ degrees	
	Average	Average	Average	68%	Average	68%	Average	68%
			Best fit level					
BOMEX			3.7	4.3	2.4		13.7	
PACIFIC			4.1	4.8	2.5		13.6	
			950 mb level					
BOMEX	1.7	- .6	7.4	8.4	4.4	5.4	24	29
PACIFIC	.02	1.3	7.1	7.9	4.0	4.5	27	30
			Surface					
BOMEX and PACIFIC			9.6		5.2		34	

APPENDIX C

Analysis of Tropical Cloud Clusters

This appendix contains a description of some techniques for measuring low level convergence and vorticity, and high level divergence of cloud clusters, and the results obtained, as well as a number of other observations of cloud cluster properties.

C. 1 Cloud Cluster Low Level and High Level Divergence and Vorticity

C. 1. 1—Measuring Techniques and Observations. Polygons were constructed using low clouds which completely encircled large cloud clusters.[1] These polygons were used to measure the low level bulk divergence (inflow) and vorticity of the clusters. In some cases there were enough pieces of cirrus diverging from a cloud cluster that an outflow polygon at high levels could be selected also. However, since in most cases there were not enough cirrus pieces to describe the high level outflow, divergence calculations were made from measurements of the change in area of the cirrus shield. Unfortunately these area change measurements contain no vorticity information. For some of the cases the measurement was made using polygons consisting of many points along the edge of the expanding cirrus shield. However, since these polygon measurements were not made for all cloud clusters, a similar measurement using a planimeter to measure the area change was made over roughly the same time period for all clusters.

The divergence and vorticity measurements obtained from the low level polygons are shown in columns 1 and 2 of table 1. For the nineteen cloud clusters observed in this study, the average low level divergence and vorticity was -7×10^{-6} sec^{-1} and 7×10^{-6} sec^{-1}, respectively. The polygon divergence measurements made from high level cirrus pieces are shown in column 5 of table 1. For the five cloud clusters for which this measurement was possible, an average value of 5×10^{-5} sec^{-1} was obtained. The polygon measurements of cirrus shield expansion are given in column 4 of table 1. For the nine cloud clusters measured, the average value was 1×10^{-4} sec^{-1}.[2] The

---

[1] These polygons are different from those described in appendix A, in that they consist of the low clouds nearest the cloud cluster. The polygons described in appendix A are of uniform size and are selected at uniform intervals regardless of the presence of cloud clusters.

[2] This higher value is due to the fact that the two cloud clusters which had very high divergence are included in this sample, but not in the previous one.

planimeter high level divergence measurements appear in column 3 of table 1. The average value of the planimeter determinations for all nineteen cloud clusters was 6×10^{-5} sec^{-1} .

C. 1. 2—Relationships. Low level cloud cluster polygon divergence vs. polygon measurement of cirrus shield expansion were the two most highly correlated properties. Figure 8 illustrates the -. 93 logarithmic correlation of these two properties which are tabulated in column 1 and column 4 of table 1. The cirrus shield divergence was measured over exactly the same time interval and with the same measuring technique as the low level divergence which may account for the higher correlation than the planimeter results below.

Low level cloud cluster polygon divergence vs. planimeter measurement of cirrus shield expansion (1 vs. 3) had a slightly lower log correlation of -. 82 (see figure 8). This may be due to the fact that the planimeter measurements for these more complete data were not taken over exactly the same time interval as the low level divergence measurements. However, the results are still quite impressive considering the number of unknown variables which may contribute to the dispersion of the data.

One would expect a relatively high correlation between low level cloud cluster polygon divergence and low level polygon vorticity (table 1, column 1 vs. 2) especially since the measurement techniques correspond so closely. However, the correlation coefficient of -. 64 was not particularly large, as is illustrated in figure 20.

C. 2 Other Cloud Cluster Observations

C. 2. 1—Zonal vs. Meridional Shear Around Cloud Clusters. The low level trajectories previously selected for the cloud cluster polygons were divided into groups according to which side of the cloud cluster they were on. An average u component was computed for the zonal shear and an average v component for the meridional shear. For all cloud clusters the average zonal shear was 3.5×10^{-6} sec^{-1} (cyclonic) and the average meridional shear was 2.1×10^{-6} sec^{-1} knots (cyclonic). For northern hemisphere cloud clusters only, the zonal and meridional shear was 3.8×10^{-6} sec^{-1} and 2.7×10^{-6} sec^{-1}, respectively. For southern hemispheric cloud clusters only, the average zonal and meridional shear was 1.7×10^{-6} sec^{-1} and $-.56 \times 10^{-6}$ sec^{-1}, respectively. As shown in table 1, fifteen out of nineteen cloud clusters have greater zonal than meridional cyclonic shear.

C. 2. 2—"Enhanced" Core Photographs. If the signal from the ATS analogue tapes is electronically "enhanced," a picture which clearly shows small

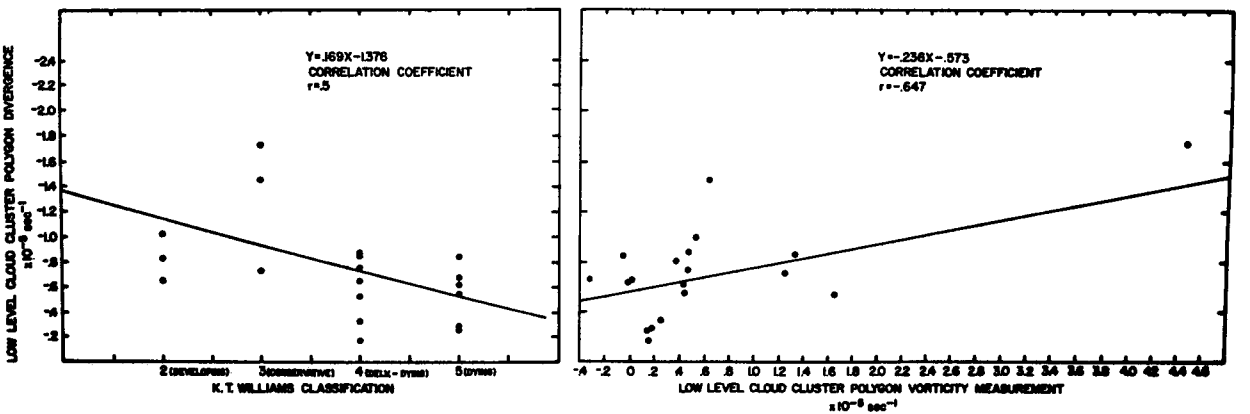

Figure 20. Low-level cloud cluster divergence vs. K. T. Williams' classification and low-level cloud cluster divergence vs. low-level vorticity.

differences in the bright clouds can be produced according to a technique discussed by Martin and Suomi (1971). Since clouds which are both high and deep will be brighter, it is thought that the bright spots which show up in the enhanced pictures represent active hot towers or deep convection. Figures 21 and 22 show enhanced pictures for July 26–28, 1969. All of the four cloud clusters studied have hot towers which can be seen in these figures. Unfortunately, there were no tapes available for any of the other dates which precluded any enhanced pictures for those days.

Reproduced from
best available copy.

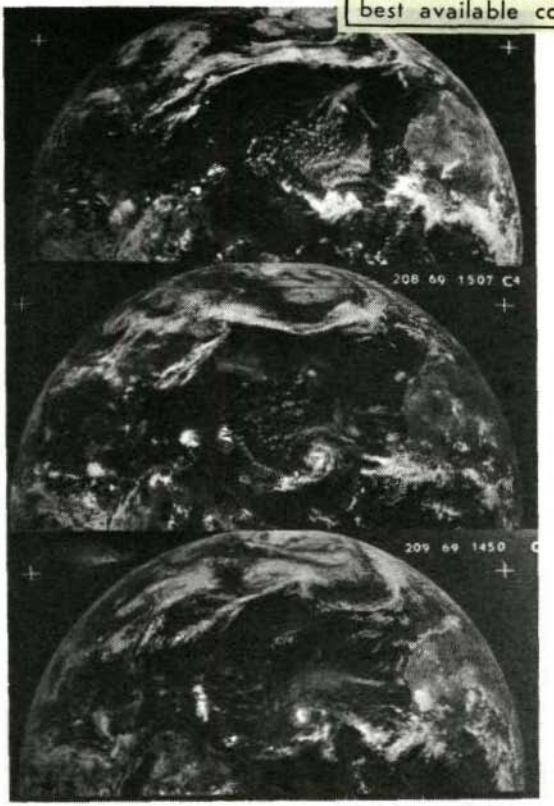

Figure 21. ATS-III pictures for local noon on July 26, July 27 and July 28, 1969, enhanced to emphasize the brightest clouds.

Figure 22. Close-up views of the Caribbean from the enhanced pictures of July 26–28, 1969, which are shown in figure 21.

(a) A small bright spot is apparent in the rather diffuse-looking upper cloud cluster. The movies for July 26 show an extremely rapidly expanding cirrus shield centered on the location of the bright spot. The lower cloud cluster appears somewhat brighter but with only very small bright spots. The lower cloud cluster expands rapidly, but not nearly as fast as the upper one.

(b) On the following day the upper cloud cluster from figure 22(a) appears to have moved to the west and has grown into the large cloud cluster on the left with the very large "hot spot" in the center. The cloud cluster on the right which has a number of bright spots has just formed.

(c) On the third day (July 28) the big cloud cluster on the left in figure 22(b) appears to have disappeared, while the new cloud cluster has become a large, vertically-oriented cloud cluster with many large bright spots.

Reproduced from
best available copy.

(a)

(b)

(c)

C. 2. 3—Low Level Convergence vs. K. T. Williams' Classifications. In order to see if the low level inflow was related to the state of development or decay, or the lifetime of the cloud cluster, the relationship between the low level cloud cluster polygon divergence and the K. T. Williams classification described below was investigated (see figure 20). Developing and conservative cloud clusters do seem to have slightly greater low level inflow than developing-dying and dying cloud clusters, but the correlation is not high. These properties are tabulated in columns 1 and 6 of table 1.

In a paper by K. T. Williams (1970), cloud clusters are classified as follows: a) prestorm cloud clusters were those cloud clusters which eventually develop into tropical storms or hurricanes; b) developing (Devl.) clusters were those cloud clusters which cannot be traced back to the previous day but which can be found on the following day; c) conservative (Cons.) clusters were those cloud clusters which can be traced to both the preceding and succeeding days; d) developing-dying (D.-D.) clusters were those cloud clusters which can't be traced to either the preceding or succeeding day; and 3) dying (Dyng.) clusters were those cloud clusters which can be traced to the preceding day but not the succeeding day. The Williams classification was made by observing a series of daily satellite pictures and judging the stage of development of the cloud clusters by the above criteria. If a cloud cluster of roughly the same size could not be found 4-6° to the east on the preceding and 4-6° to the west on the succeeding day by examining ESSA and ATS pictures, the cloud cluster was considered not to exist on those days.

C. 2. 4—Cloud Cluster Size vs. Divergence. The low level inflow as indicated by the low level cloud cluster polygon divergence seems to be relatively independent of cloud cluster size as shown in figure 23 (see also table 1, columns 1 and 7 for the original data).

The ratio of cirrus shield divergence (outflow) to low level divergence (inflow) seems to be slightly higher for small cloud clusters, but the correlation coefficient, -.43, is low as shown in figure 23. The measured values of ratio (outflow/inflow) and area are given in columns 8 and 7 of table 1.

C. 2. 5—The Scale Size of Low Level Divergence and Vorticity Fields vs. the Scale Size of Cloud Clusters. In the vicinity of large scale cloud clusters there is always a large scale low level convergence and positive relative vorticity. The small scale divergence and vorticity cannot be measured in this case by my technique because the clouds are hidden by the cirrus canopy. In the case of small scale cloud clusters there is not always convergence and positive relation vorticity on the 15° × 15° size scale, but there is always convergence and almost always positive vorticity at the same scale size as scale size of the cloud cluster.

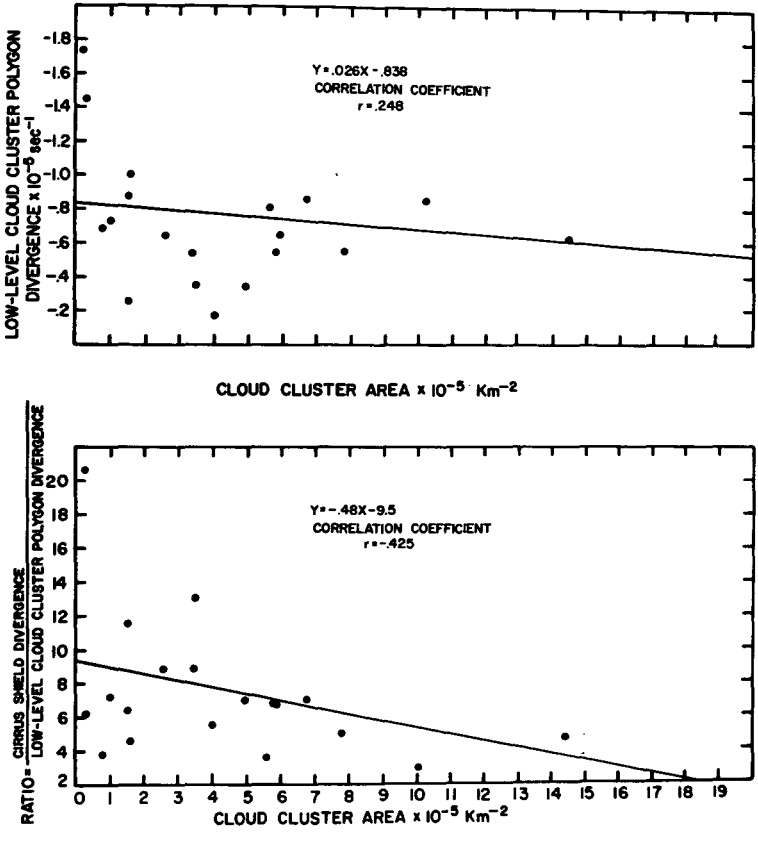

Figure 23. Cloud cluster area vs. low-level cloud cluster divergence and cloud cluster area vs. the ratio of cirrus shield divergence to low-level divergence.

APPENDIX D

A "Blink" Measuring Technique for Quantitative Measurement of Cloud Motion from ATS-I Spin Scan Camera Pictures

A. F. Hasler
J. Kornfield
L. Jensen
Department of Meteorology
The University of Wisconsin, Madison

Abstract:

A "blink" measuring technique for making quantitative geometric measurements of cloud displacements from a series of ATS-I pictures is explained. This technique requires two or more ATS-I pictures which are reasonably well superimposed by projectors on an electronic digitizing table. All geometric calculations, that is, distortion correction, superimposition and rectification, are done analytically through a computer program. The mathematical assumptions and operations involved are discussed in detail in the Appendix. A systematic testing program was devised to evaluate the technique first with an ideal grid and finally with real ATS-I pictures. Some possible applications of the technique include measurement of cloud trajectories (i.e., velocities), measurement of area change in clouds and cloud systems and measurement of location and orientation of cloud features. The best cloud displacement accuracy to date has been approximately 9 nautical miles which provides cloud speeds within approximately 3 knots for clouds that can be observed for 3 hours. Preliminary comparisons of cloud trajectories with standard wind observations are presented.

Description of the Technique

At first thought, an excellent method for making quantitative measurements of cloud motions would be to project a time-lapse movie [1] made from ATS Spin Scan Cloud Camera (SSCC) pictures onto an electronic measuring table

---

This appendix consists of a paper prepared for the NASA ATS Technical Data Report. The paper describes the original cloud motion measurements by the author and provides background material for the cloud motion measuring techniques used in the remainder of the thesis.

and to trace the motion of the clouds with a measuring head. Unfortunately, this method has the following limitations:

1. It is very difficult and time-consuming to superimpose the pictures accurately for the movie.

2. A registration error is introduced by the movie camera and the movie projector.

3. The resolution of presently available 16-mm film is inadequate to preserve the picture quality over the full earth disk.

4. It is difficult to correct for variable distortion and size changes from picture to picture.

A "blink" measuring system has been developed which, to a large extent, overcomes these problems. Two or three projectors are used to superimpose ATS SSCC pictures on an electronic measuring table (figure 24). The projectors allow adjustment of the picture in the film gates such that reasonably good superimposition of images on the table is achieved. Once the images are approximately superimposed, the film remains fixed. The projection lamps are easily controlled so that it is possible to blink rapidly from one picture to another giving a "movie" effect. The electronic measuring table is a 36-in. × 36-in. projection table with a measuring head on it. The head consists of a platin with inscribed cross-hairs, which is linked to a pair of rotary digital encoders. The encoders are interfaced directly to an on-line computer. This system enables one to record the x and y coordinates of any point on any picture.

The advantages of this system are as follows. It is in fact a 2- or 3-frame time-lapse movie with very high resolution because of the large 70-mm film size used. The fixed registration of the film allows the following mathematical operations: distortion correction, superimposition, rectification and all other geometric calculations to be performed on each picture individually in the computer.

Each image is located on the measuring table by determining the x and y coordinates of many points on the Earth's limb and the location of at least one landmark. The mathematical operations (discussed in detail in Part I of the Appendix) are then performed in the following manner:

1. Distortion Correction: An ellipse is fitted to the limb points by a least-squares technique and the parameters of the ellipse are computed. The Earth is then restored to a circle, correcting for any

Reproduced from
best available copy.

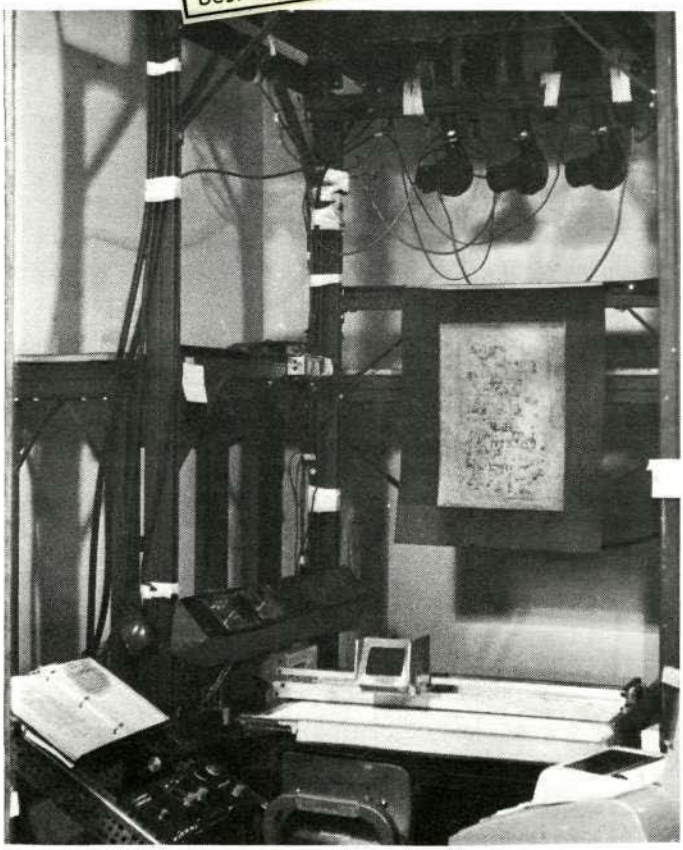

Figure 24. Projection System and Electronic Digitizing Table Used for Blink Measuring Technique. (Images from three overhead projectors are deflected onto the measuring table by a 45°-angle mirror. Projection lamp controls are on the operator's left. Operator positions measuring head by hand. The measuring head is linked to two rotary digital encoders which are interfaced through the teletype on the right to an on-line computer. X and Y coordinates of the measuring head are recorded when a foot switch is activated. The measuring system shown belongs to the High Energy Physics Group, Department of Physics, University of Wisconsin.)

linear distortion in the picture. The pictures are scaled using the apparent Earth radii for any size variability.

2. Superimposition: The center of each circle is transposed to the origin of the measuring table coordinate system and the pictures are rotated until the landmarks coincide.

3. Rectification: The picture is regarded as that made by a conventional camera so that a tangent plane approximation can be used. Distances between any two points on one or more pictures are calculated by spherical geometry.

Test Results

A systematic testing program was devised to evaluate the technique. The measuring system and the computer programs were tested first on an ideal grid[1] and finally on real ATS-I pictures.

1. The tangent plane approximation was evaluated theoretically.[2] The error introduced by using it was found to be less than 6 nm and was therefore neglected.

2. The distance-measuring calculations were carefully scrutinized for error and tested on the ideal grid by measuring distances on the measuring table. The average error in the distance between several pairs of points was only 3 nm, so the distance calculations were considered to be absolute and were used for all further evaluation.

3. The best possible accuracy with which landmarks can be located was tested by repeated measurements of the same landmark or cloud. The distance in nautical miles between successive measurements was used to give the relocation or repeatability error. For the highest quality ATS-I negatives,[3] the average error in relocating both clouds

---

[1] Computer-produced ATS-I grid supplied by NASA.

[2] A detailed evaluation of the tangent plane approximation is contained in Part I of the Appendix.

[3] Produced at The University of Wisconsin from an analog tape record of the ATS-I SSCC signal.

and landmarks was 3 nautical miles (nm), where 95 percent of the data points were within 6 nm. For the lower quality EIS negatives,[4] an average error of 6 nm was found with 95 percent of the data points within 11 nm. When the actual measurements were made, each cloud or landmark was measured three times and the average coordinates were taken to minimize the repeatability error.

4. Next, the accuracy with which two pictures can be superimposed by the technique was tested. This was done by carrying out the superimposition routine and then measuring the apparent displacement of stationary landmarks caused by errors in the superimposition. Location errors and any distortion errors which have been neglected are also included here so that the superimposition error gives a good estimate of the total error of the technique.

For the ideal grid, grid points near the subsatellite point were found to be superimposed with an average accuracy of 3 nm, which approaches the resolution limit (about 2 nm) of the ATS-I camera. For two different ATS-I pictures, the best superimposition achieved for points on Baja California and the Hawaiian Islands had an average error of 9 nm. These represent the best results achieved to date for real data. It has been found that clouds can often be traced for over 3 hours. If we use a total error of 9 nm, average cloud speeds over a 3-hour period can be determined within approximately 3 knots. According to a COSPAR [2] report, one of the global observation data requirements for prediction with diabatic numerical models is the knowledge of the horizontal wind within 4 to 6 knots. Therefore, if it can be established that cloud speeds can be accurately related to wind speeds, we are approaching the recommended accuracy.

Preliminary Comparison of Cloud Trajectories with Standard Wind Observations

The measuring procedure is thus: In the tropics, one selects the smallest persistent fair-weather cumulus clouds resolved by the ATS-I camera. Small cumulus clouds are used if possible because they most nearly resemble an ideal marker (i.e., a passive, infinitely small marker). Large clouds or cloud systems and large cloud decks are avoided if possible because they are more likely to affect the ambient wind field and are more likely to be propagated by wave phenomena than the smaller clouds. Distances are measured from cloud center to cloud center, as the operator determines by eye. For larger clouds whose centers cannot easily be determined, such as large convective cloud

---

[4] Negatives made by the EIS (Electronic Image Systems Corporation, Boston, Massachusetts) display system at the ground station as test pictures.

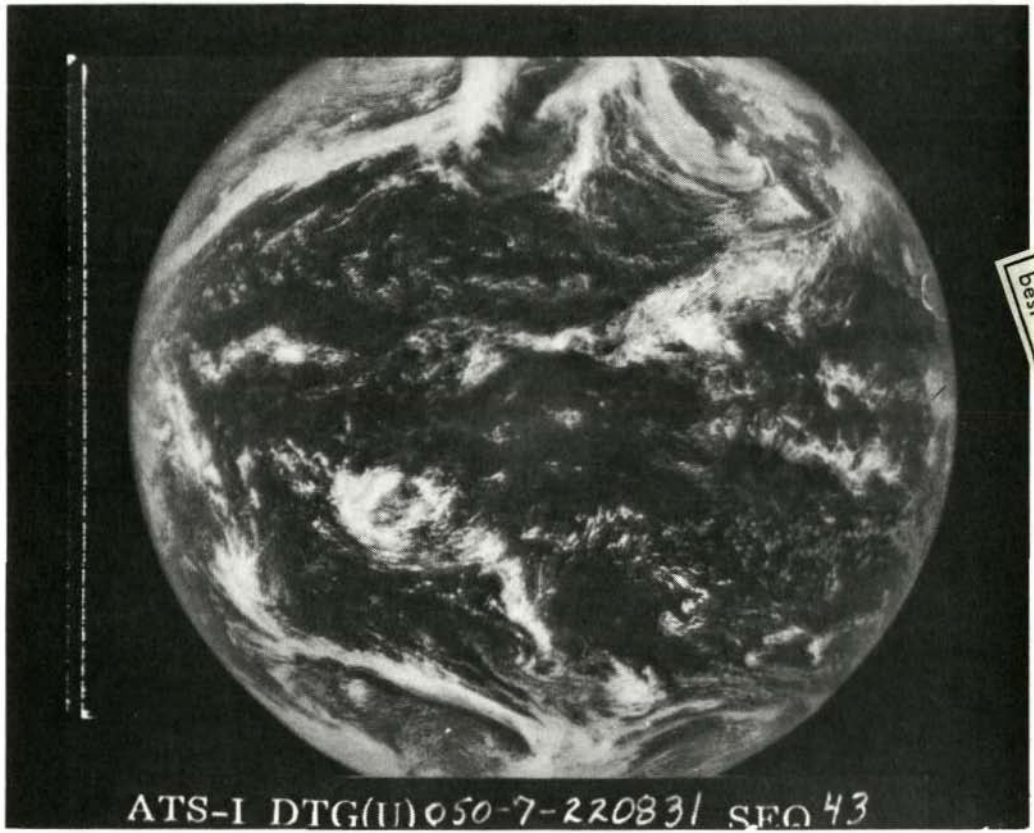

Reproduced from best available copy.

Figure 25. ATS-I SSCC Picture from 2208 (U) 19 February 1967. (Printed from a duplicate EIS negative.)

groups, bright spots or distinctive edge features are used. Cirrus clouds are less well defined and are therefore more difficult to locate accurately. However, since their velocities are usually higher, the error in location is still a small part of the distance traveled.

The first comparison of cloud trajectories with wind observations was done with data from 19 February 1967. The ATS-I SSCC pictures, taken at 2040 Universal Time (U), 2208 (U) and 2317 (U) on 19 February 1967, were selected. The ATS-I picture nearest local noon for the subsatellite point is 2208 (U). It is shown in figure 25. Trajectories of fair weather cumulus clouds, assumed to be low-level clouds, were compared with the surface wind observations from the U. S. Weather Bureau's Hawaiian analysis for 0000 (U) 20 February 1967. Trajectories of higher speed clouds, usually cirrus (assumed to be high-level clouds), were compared with the 200-250-300 millibar (mb) wind observations from rawinsondes and aircraft doppler radar, again from the Hawaiian analysis at 0000 (U) 20 February 1967. The comparison of these data is illustrated in figure 26. For this case, the average superimposition error was 9.3 nm and, since the period of observation was 3 hours, cloud speeds can be found within approximately 3 knots. Of 30 cumulus trajectories and 10 cirrus trajectories selected to cover the tropics as uniformly as possible, only four cases of cumulus trajectories and no cases of cirrus trajectories were found near enough (i.e., less than 200 nm) to be compared with the standard observations. This points up the difficulty of making this type of comparison. While a more complete selection of cumulus trajectories would have given a better comparison, there were virtually no upper air wind observations near enough to the cirrus clouds visible in this picture to make any comparisons. In the four cases of cumulus trajectories, the average speed difference between cloud and surface wind was 3 knots or 10 percent of the wind speed, while the average direction departure was 10°. Transequatorial cirrus flow from north to south at approximately 145° was measured at 32 knots, while a "cloud jet" over Baja California and Southwestern United States, flowing to the northeast, was measured at up to 52 knots. (See Figure 26.)

Two high-resolution negatives produced at The University of Wisconsin from analog tapes recorded at 2215 (U) on 21 June 1967 and at 0013 (U) on 22 June 1967 (see Figure 27) were used for a second comparison. These negatives are much better than the duplicate EIS negatives used for the 19 February case. In fact, they preserve nearly the full resolution of the ATS SSCC. An improved comparison procedure was used for this case. First, the locations of all surface and upper air wind observations were plotted on the measuring table. The actual wind data were omitted to prevent bias on the part of the operator. Cloud trajectories were selected which coincided as nearly as possible with the wind observation locations and times. When the cloud trajectories had been measured and plotted, the wind observations were then plotted and compared, as shown in Figure 28. In this case, the average superimposition error

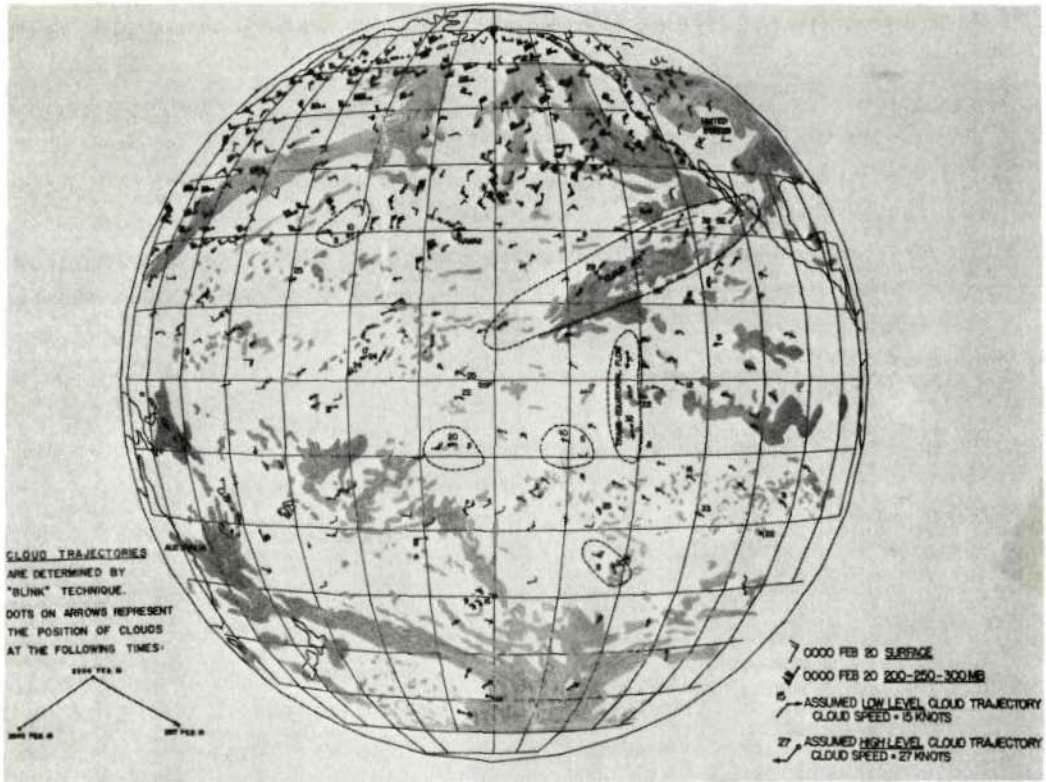

Figure 26. ATS-I Cloud Trajectories Compared with Surface and High-Level Winds. (19-20 February 1967 (U).)

Reproduced from best available copy.

Figure 27. ATS-I SSCC Picture from 2215 (U) 21 June 1967. (Printed from negatives made at the University of Wisconsin from ATS-I analog tape.)

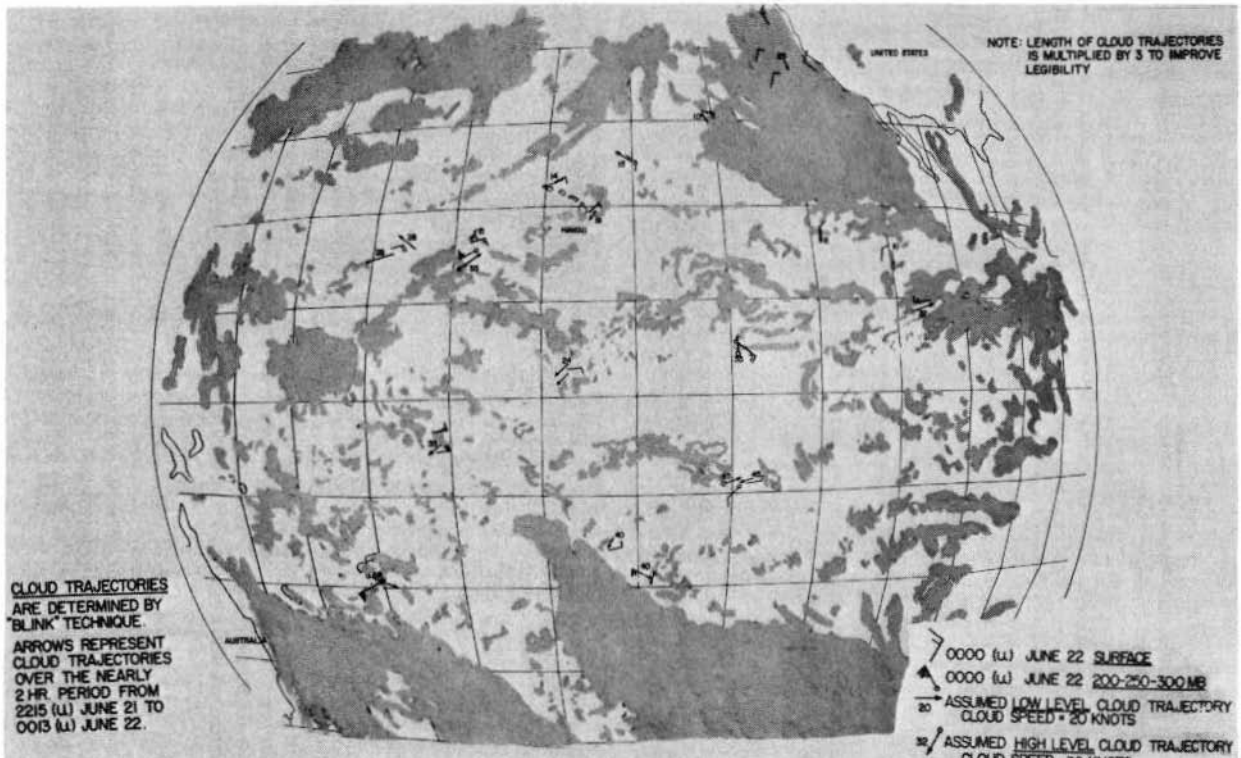

Figure 28. ATS-I Cloud Trajectories Compared with Surface and High-Level Winds. (21-22 June 1967 (U).)

was 18 nm and, since the period of observation was only 2 hours (negatives were not available for a longer period), cloud speeds can be found to within about 9 knots. For 12 cases of tropical cumulus trajectories compared with surface wind observations, the difference between surface wind speed and cloud speed was an average of 8 knots or 38 percent of the cloud speed, while the departure in direction averaged 15°. For four cases of cirrus trajectories compared with the 200-250-300 mb winds, the speed departure averaged 20 knots or 46 percent of the cloud speed, while the direction departure averaged 30°. These are only limited preliminary results and, while some of the departure may of course be attributed to actual differences between cloud and wind speed, because of relatively large differences in location and unknown differences in height of the compared data, there is fairly good agreement.

Conclusion

A practical technique for making quantitative measurements of cloud displacement from ATS-I pictures has been explained. Two ATS-I pictures were superimposed by two projectors on an electronic digitizing table. Distortion correction, superimposition and rectification were done analytically through a computer program. An estimate of the accuracy of the best results to date gave cloud speeds to within approximately 3 knots. A preliminary comparison of cloud trajectories with standard wind observations has been presented. Fairly good agreement was found in spite of relatively large differences in location of the compared data. Improved comparisons are planned in which cloud heights and complete wind profiles will be known.

APPENDIX

Tangent Plane Approximation

A box camera looking directly down on the subsatellite point would produce a circular image of the Earth. An ATS picture looks the same as one taken by an ordinary box camera; however, the Spin Scan Camera picture is a display of the intensities observed by its telescope as a function of the telescope's stepping and rotation angles. In order to find how much the two pictures actually differ, we first set up a coordinate system as follows.

Let the origin of the coordinate system be at the satellite as shown in Figure 29. The x-axis is directly along the line connecting the satellite's center and the Earth's center. The z-axis is parallel to the Earth's axis of rotation with the positive direction northward. The y-axis is perpendicular to both the x- and z-axes so as to form a right-handed coordinate system.

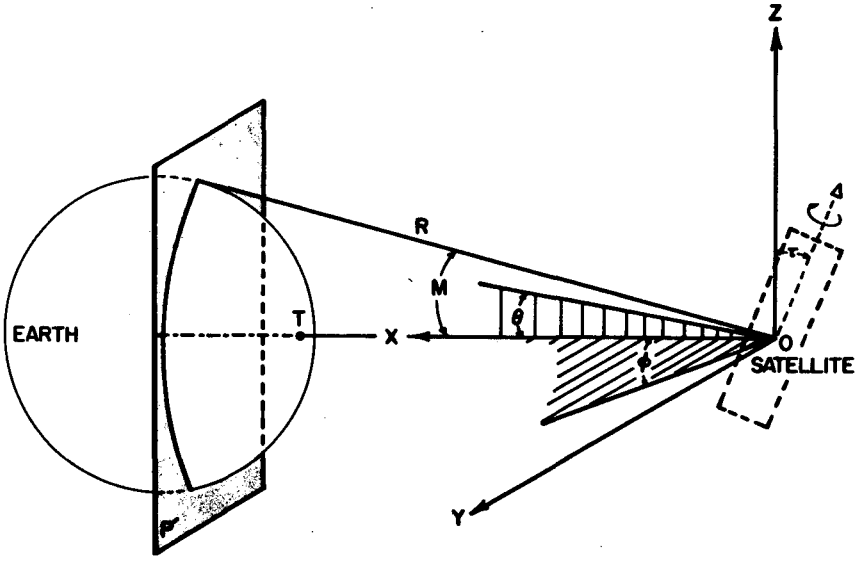

Figure 29. ATS SSCC Coordinate System. (The origin of the coordinate system, 0, is at the center of the satellite. The x-axis is directed along the line connecting the satellite's center and the Earth's center and passes through the subsatellite point T. The z-axis is parallel to the Earth's axis of rotation. The y-axis is mutually perpendicular to the x- and z-axes. θ is the stepping angle of the SSCC telescope, ϕ is the rotational angle of the satellite about its nominal spin axis z. τ is the deviation or tilt of the satellite spin axis with respect to z. If a line is constructed which passes through 0 and is tangent to the Earth's surface, R is the distance from 0 to the tangent point. The circle defined by all of these tangent points lies in the plane P'. M is the angle between the tangent line and the x-axis.)

Angular variations in the x-z plane are designated θ and measured from the x-axis. θ is the stepping angle of the ATS camera. In the x-y plane the angular variations are designaged by ϕ and are also measured from the x-axis. ϕ is the rotational angle of the satellite about its nominal spin axis z.

When viewed by an ordinary box camera, the Earth's disk would appear as a perfect circle formed by the rays tangent to the planet. To find the equation for the Earth's limb in spin scan picture coordinates we refer to Figure 29, in which the circle is formed by the tangents and lies in plane P'. Plane P' is described by the equation

$$x = \text{Constant} \tag{A-1}$$

If we express x in spherical coordinates, $x = R \cos\theta \cos\phi$. When R is fixed as the distance from the Earth's limbs to the satellite, one obtains the equation of the circle:

$$R \cos\theta \cos\phi = R \cos M \tag{A-2}$$

where 2M is the angle subtended by the Earth as seen from the satellite.

When the satellite's spin axis is tilted away from z by an angle, τ, we have merely a rotation about the y-axis so that equation (A-2) becomes

$$\cos\theta \cos\phi \cos\tau + \sin\phi \sin\tau = \cos M \tag{A-3}$$

Since the Earth's limb looks quite circular on an ATS picture, we approximate equation (A-3) as

$$(\theta - \tau)^2 + \theta^2 - M^2 = 0 \tag{A-4}$$

To test the approximation, values of θ, ϕ, τ and M were chosen that satisfied equation (A-3). The same values were used in equation (A-4). The amount by which equation (A-4) differed from zero was used to estimate the error in θ or ϕ. For a large tilt angle of $\tau = 2°$, the greatest error in θ and ϕ was less than 3×10^{-4} radians, or an error of about 6 nm at the limb of the Earth. Since τ is normally much less than 2° in the pictures used and the largest error occurs only in limited areas near the limb, the error is considered to be less than 6 nm and has been neglected.

Distortion Correction and Superimposition

A step-by-step description of the distortion correction and superimposition process is given below and illustrated in Figure 30. A detailed discussion of each step follows the list.

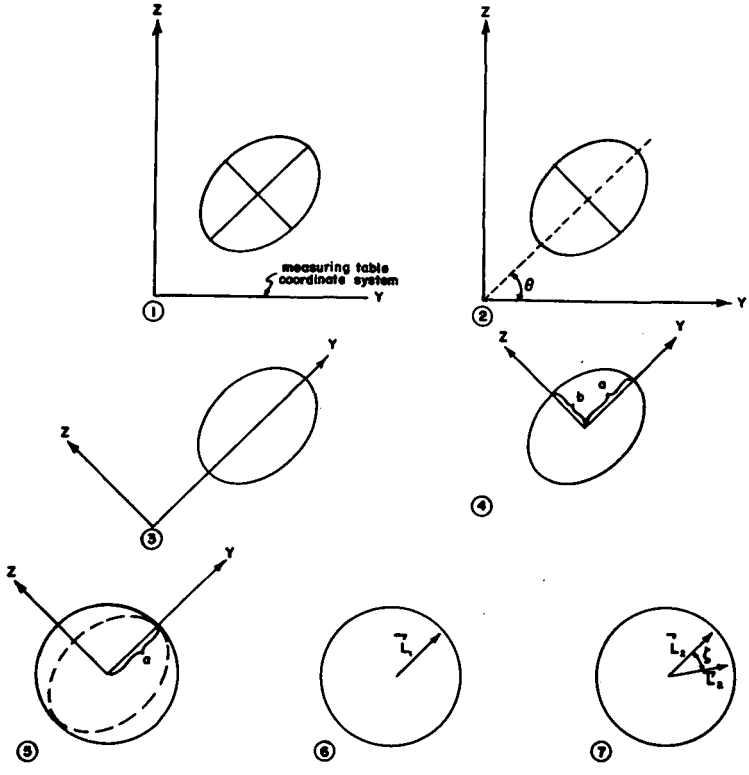

Figure 30. Step-by-step Process of Distortion Correction and Superimposition of ATS-I SSCC Pictures. (1. The elliptically distorted Earth arbitrarily positioned on the MTCS. 2. Determination of the angle between the major axis of the ellipse and the x-axis of the MTCS. 3. Rotation of the MTCS so that the x-axis is parallel to the major axis of the ellipse. 4. Translation of the origin of the MTCS to the center of the ellipse. τ. Transformation of the ellipse into a circle of radius a. 6. Rotation of one picture relative to another such that the vectors to a landmark, $\vec{L}_1$ and $\vec{L}_2$, are superimposed.

1. Fit an ellipse to the limb of the Earth (Figure 30, Part 1).

2. Determine the angle between the major axis of the ellipse and the x-axis of the measuring table coordinate system (MTCS) (Figure 30, Part 2).

3. Rotate the MTCS through this angle so that the x-axis is parallel to the major axis of the ellipse (Figure 30, Part 3).

4. Determine the semi-major and semi-minor axes of the ellipse.

5. Translate the origin of the MTCS to the center of the ellipse (Figure 30, Part 4).

6. Transform the ellipse into a circle (Figure 30, Part 5).

Each of the pictures is processed separately as above. Then a final step with both pictures produces the final superimposed image.

7. Rotate one picture relative to another so that vectors to a landmark $\vec{L}_1$ and $\vec{L}_2$ are superimposed (Figure 30, Part 6).

Each of these steps will now be taken up in more detail. The major distortion correction involves transforming the distorted Earth into a circle. The elliptical distortion is introduced when the SSCC scan lines are not reproduced with the proper line spacing or when linear stretching of the photographic material occurs. To determine the shape of the ellipse a least-squares fit to the limb of the Earth is made using the general equation for a conic section:

$$z^2 + T_1 yz + T_2 y^2 + T_3 z + T_4 y + T_5 = 0 \qquad \text{(A-5)}$$

where $T_1 \ldots T_5$ are fitted coefficients and y, z are the measuring table coordinates.

A rotation of the MTCS gives the elliptical equation

$$z^2 + (\frac{S}{P})z + (\frac{Q}{P})y^2 + (\frac{T}{P})y + (\frac{T_5}{P}) = 0 \qquad \text{(A-6)}$$

where

$$P = \cos^2\theta + T_1 \cos\theta \sin\theta + T_2 \sin^2\theta$$

$$Q = \sin^2\theta - T_1 \cos\theta \sin\theta + T_2 \cos^2\theta$$

$$S = T_3 \cos\theta + T_4 \sin\theta$$

$$T = -T_3 \sin\theta + T_4 \cos\theta$$

The angle θ is the smallest angle obtained from

$$\tan 2\theta = \frac{T_1}{1 - T_2} \tag{A-7}$$

Finding equation (A-6) is equivalent to the rotation discussed in steps 2 and 3. This equation can be modified further by completing the square and rearranging terms:

$$\frac{(x - x_0)^2}{a^2} + \frac{(y - y_0)^2}{b^2} = 1 \tag{A-8}$$

where

$$x_0 = -\frac{S}{2P} \qquad a^2 = \left(\frac{S}{2P}\right)^2 + \frac{T^2}{4PQ} - \frac{T_5}{P}$$

$$y_0 = -\frac{T}{2Q} \qquad b^2 = a^2 \frac{P}{Q}$$

The semi-major and semi-minor axes are a and b respectively. The center of the ellipse is at (x_0, y_0). Translation of the origin is accomplished by subtracting x_0 from every measured x and subtracting y_0 from every y. Transformation of the ellipse into a circle is accomplished by multiplying the translated y coordinate by the ratio a/b. The variation of the Earth's radius from its mean value is approximately 6 nm, so we can regard the Earth to be a circle. The circle then has radius a. Every time a distance is measured on the picture, it is divided by a. This normalizes every circle so that they are equivalent.

The final rotation is accomplished using vectors $\vec{L}_1$ and $\vec{L}_2$ on pictures 1 and 2, respectively. $\vec{L}$ is a vector from the origin to a particular landmark. The angle, ζ, between $\vec{L}_1$ and $\vec{L}_2$ is given by the dot product

$$\vec{L}_1 \cdot \vec{L}_2 = |\vec{L}_1||\vec{L}_2| \cos\zeta \tag{A-9}$$

One picture is then rotated with respect to another through the angle ζ. The procedure by which this is accomplished is discussed in the next section.

The process of superimposition is complete once the above is carried out. Displacements of clouds between the two pictures may now be computed since the two pictures can be regarded as one picture.

Rectification

The last problem is one of rectification or one of relating geometric distances on the photograph to actual distances on the Earth's surface. For the case of finding cloud trajectories the cloud displacement D is desired.

On a spherical Earth, the subsatellite point (SSP) and the positions of two clouds can be used to locate a spherical triangle. If we know two arcs, σ_1 and σ_2, and one angle, β, the third arc, ξ (or $D = R\xi$, where R is the Earth radius and D the displacement), can be found. See Figure 31. This situation is analogous to looking down upon the North Pole, where β is the longitude separation between two arcs of the triangle and each σ is 90° minus the latitude. D is the great circle distance between two clouds (or, in the case of one cloud, the displacement). Let us find the angles σ_1 and σ_2 first.

Using the same coordinate system as in Figure 29, position of a plane P perpendicular to x at the SSP. The arc length for σ_1 projects onto P as a straight line ℓ_1, with endpoints (H, 0, 0) and (H, y_1, z_1). H is the height of the satellite above the Earth's surface. See Figure 32.

The line r_1, from the origin through (H, y_1, z_1), intersects the Earth as shown in Figure 33. Figure 33 is just a cross-section from Figure 32.

The equation of the circle with center at E is:

$$[x - (R + H)]^2 + \rho^2 = R^2 \qquad H \leq x \leq 2R + H \qquad \text{(A-10)}$$

The line r_1 has equation

$$\rho = x \tan \alpha \qquad \text{(A-11)}$$

where

$$\cos \alpha = \cos \theta \cos \phi \qquad \text{(A-12)}$$

Substituting (A-11) into (A-10) and solving for x allows us to find σ_1 from

$$\tan \sigma = \frac{x \tan \alpha}{(R+H) - x} \qquad \text{(A-13)}$$

The process is repeated for σ_2. Thus, we have two sides of the triangle.

To find the remaining angle, β, we define the vector $\vec{\ell_1}$ as the vector of length ℓ_1 from the SSP (H, 0, 0) to (H, y_1, z_1). Vector $\vec{\ell_2}$ is similarly defined. Thus, by the dot product of two vectors

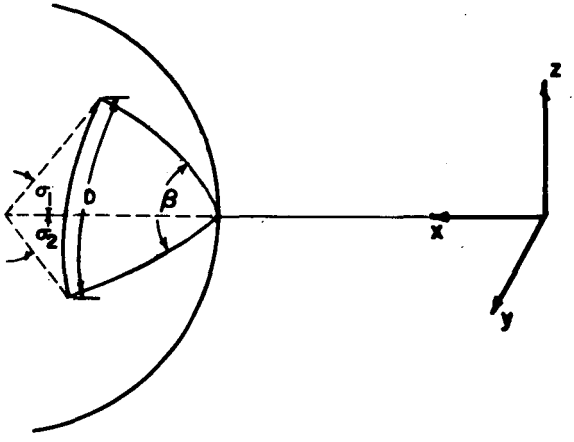

Figure 31. Spherical Triangle Used to Calculate a Displacement, D, on the Surface of the Earth Which is Part of the Rectification Process for ATS SSCC Pictures. (If we know two arcs, σ_1 and σ_2, and one angle, β, the third side, ξ (or $D = R\xi$, where R is the Earth radius and D is the displacement), can be found.)

$$\beta = \cos^{-1}\left(\frac{\vec{\ell}_1 \cdot \vec{\ell}_2}{|\vec{\ell}_1||\vec{\ell}_2|}\right) \tag{A-14}$$

The final side of our triangle follows directly from the spherical trigonometric relation

$$\cos \xi = \cos \sigma_1 \cos \sigma_2 + \sin \sigma_1 \sin \sigma_2 \cos \beta \tag{A-15}$$

whence the displacement, D, is

$$D = R\xi \tag{A-16}$$

where R = Earth's radius.

Note: The last step of superimposition (rotation through the angle ζ as defined in equation (A-9)) is accomplished by subtracting ζ from β each time β is calculated.

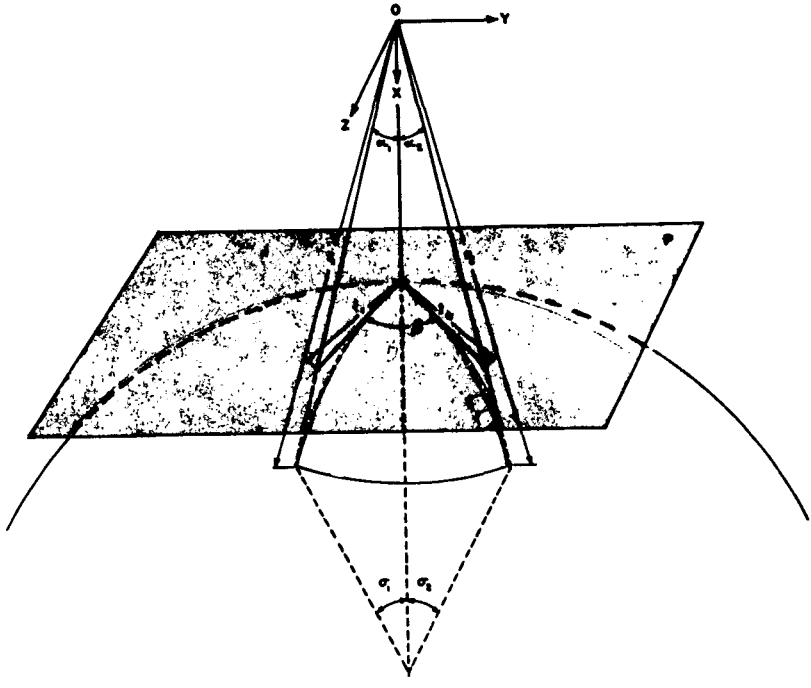

Figure 32. Geometrical Relationships Used to Rectify ATS SSCC Pictures. (r_1 = distance from origin to surface of Earth; α_1 = angle between r_1 and the x-axis; P = plane tangent to the Earth at the subsatellite point; σ_1 = great circle angle (see Figure 31); ℓ_1 = projection of arc length corresponding to σ_1 onto plane P; β = angle between ℓ_1 and ℓ_2, also angle between great circle segments $R\sigma_1$ and $R\sigma_2$, where R is the radius of the Earth. See Figure 31.)

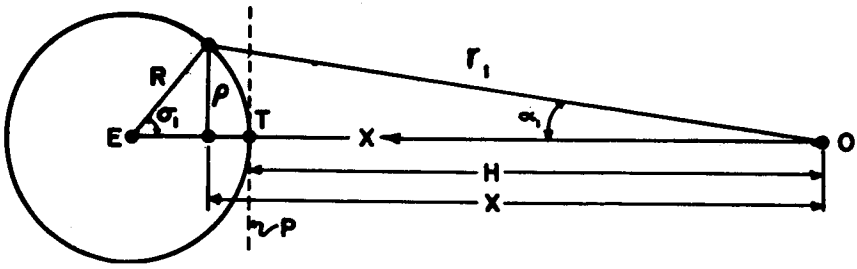

Figure 33. Cross-Section of Figure 32. (H = height of the satellite above Earth; ρ = half chord length; X = distance from origin to the intersection of ρ with the x-axis; R = radius of the Earth; E = center of the Earth; T = subsatellite point; P = plane tangent to Earth at subsatellite point.)

References

1. Hasler, A. F., and Kornfield, J.: Display and Analysis of ATS-I Spin Scan Camera Pictures Through Time-Lapse Movie Techniques. Weather in Motion, University of Wisconsin Press, in press.

2. COSPAR Working Group IV: Status Report on the Application of Space Technology to the World Weather Watch. Committee on Space Research, Paris, June 1967.

APPENDIX E

Data

The quantitative description of the wind, divergence, and vorticity fields for the 18 days studied can be obtained on writing to the author or to the Publications Office, Space Science and Engineering Center, 1225 W. Dayton St., Madison, Wisconsin 53715. The illustrations are, however, included in this appendix. The three sections of the data are basically:

Cloud Trajectory Fields

Figure 34 shows the full earth ATS-I picture from June 9, 1968 with the close-up area for that day outlined. The close-up area selected for June 9 is given in figure 35 with the high level and low level cloud trajectory field superimposed. The cloud trajectory vector speed is given by the arrow length to the nearest 5 knots. The remaining close-ups for fourteen days of Pacific data and three days of Caribbean data are given in figures 36–52.

Cloud Trajectory Tables

These tables (not shown) give a numberical description of the cloud trajectory fields shown in figures 36–52. For each day the low clouds are given first as labeled, followed by the high clouds and then some points used for navigation at the end.

Divergence and Vorticity Fields

Additional figures (not shown) give the low-level $5° \times 5°$, $10° \times 10°$, and $15° \times 15°$ polygon divergence and vorticity fields corresponding to the cloud trajectory fields shown in figures 35–52.

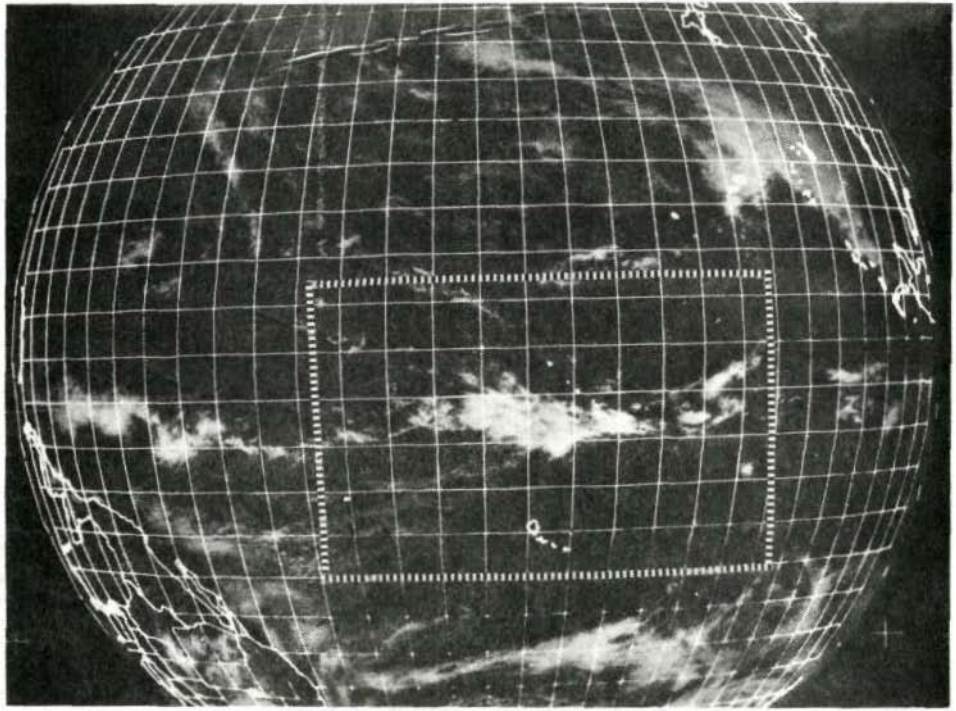

Reproduced from best available copy.

Figure 34. ATS-I spin-scan camera full earth picture taken at local noon June 9, 1968 with close-up area outlined.

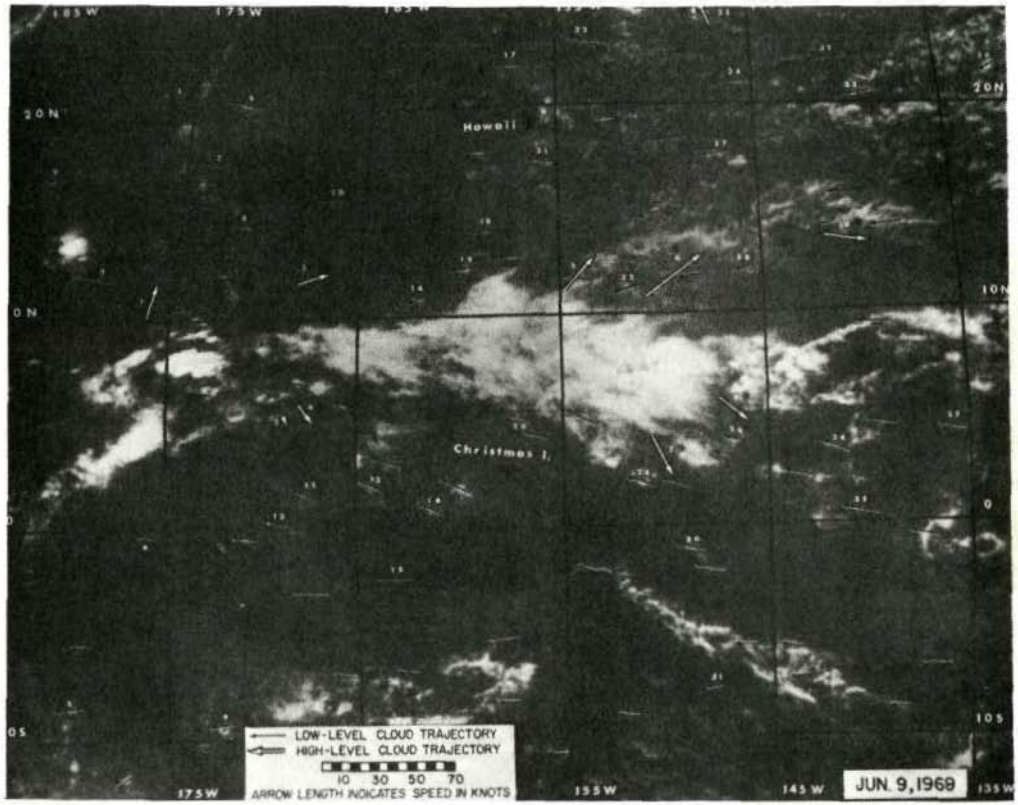

Figure 35. Cloud trajectory field superimposed on the close-up picture for June 9, 1968.

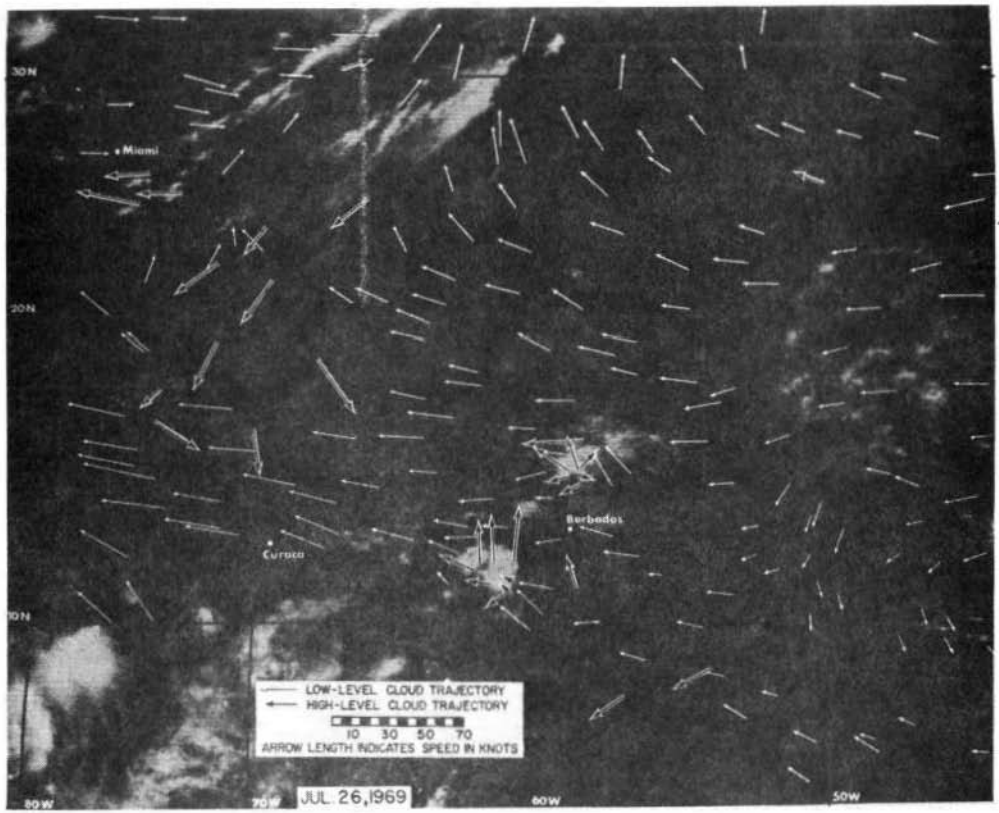

Figure 36. Cloud trajectory field for the Caribbean on July 26, 1969.

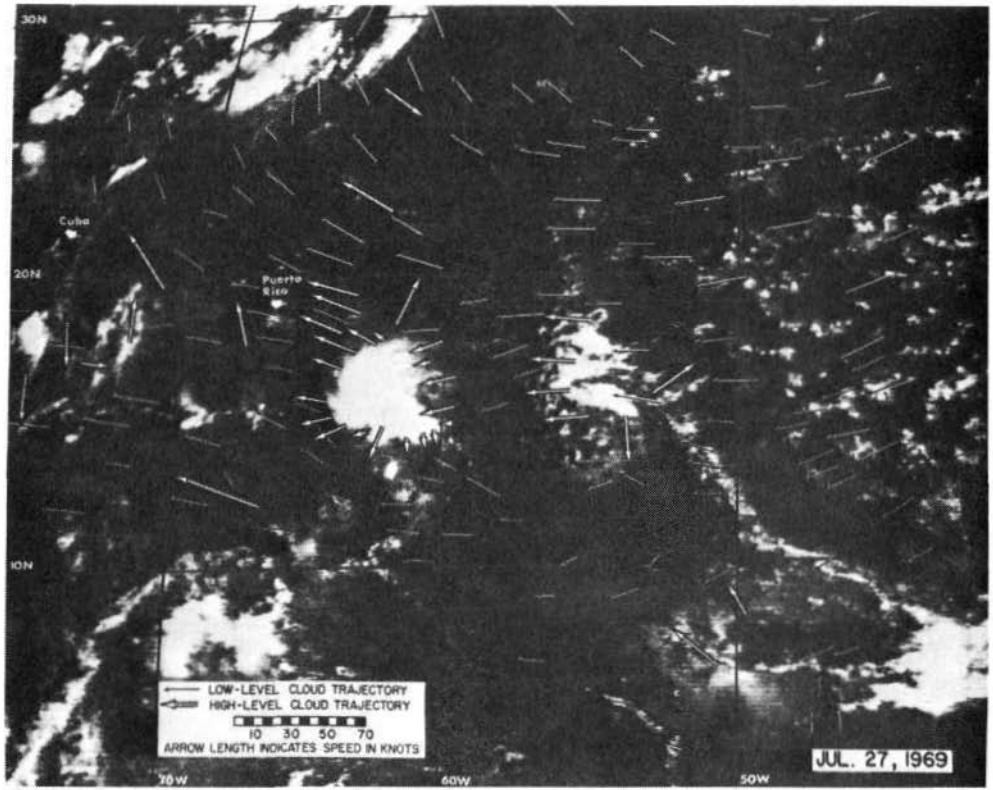

Figure 37. Cloud trajectory field for the Caribbean on July 27, 1969.

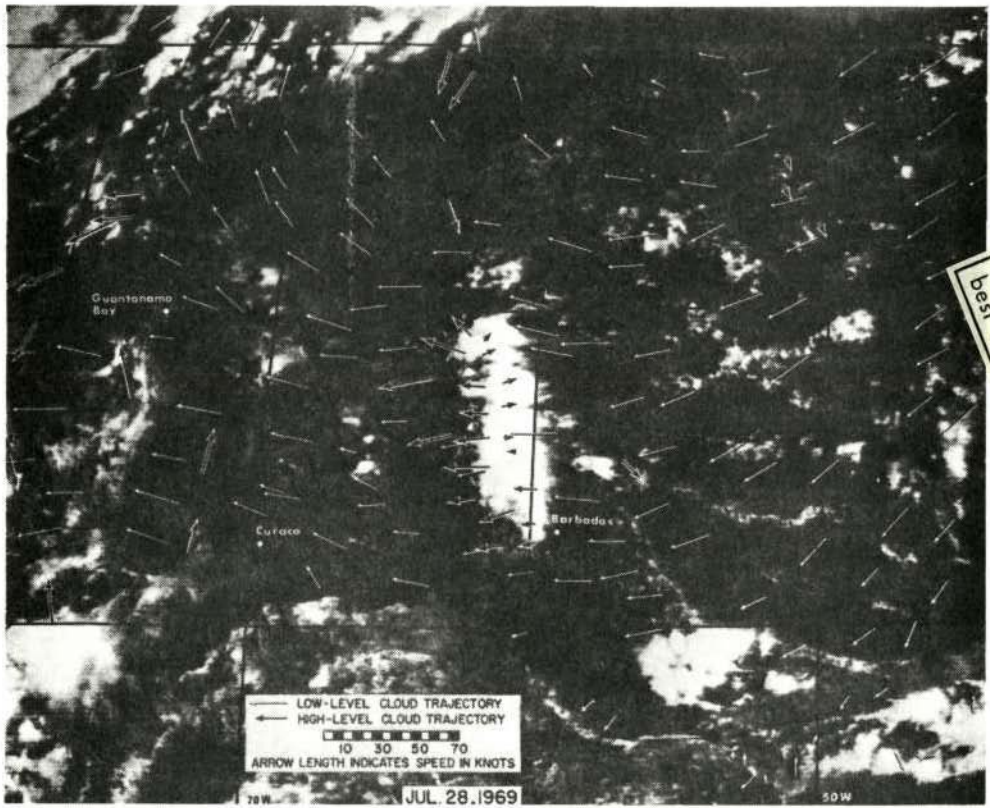

Reproduced from best available copy.

Figure 38. Cloud trajectory field for the Caribbean on July 28, 1969.

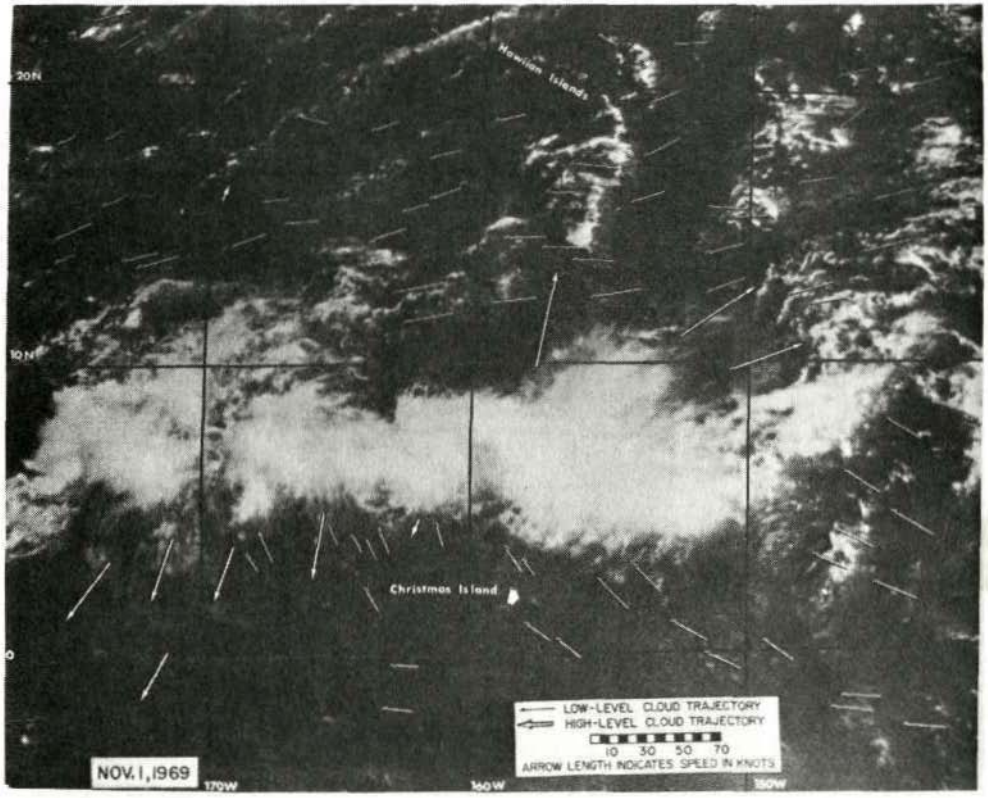

Figure 39. Cloud trajectory field for the central Pacific on November 1, 1969.

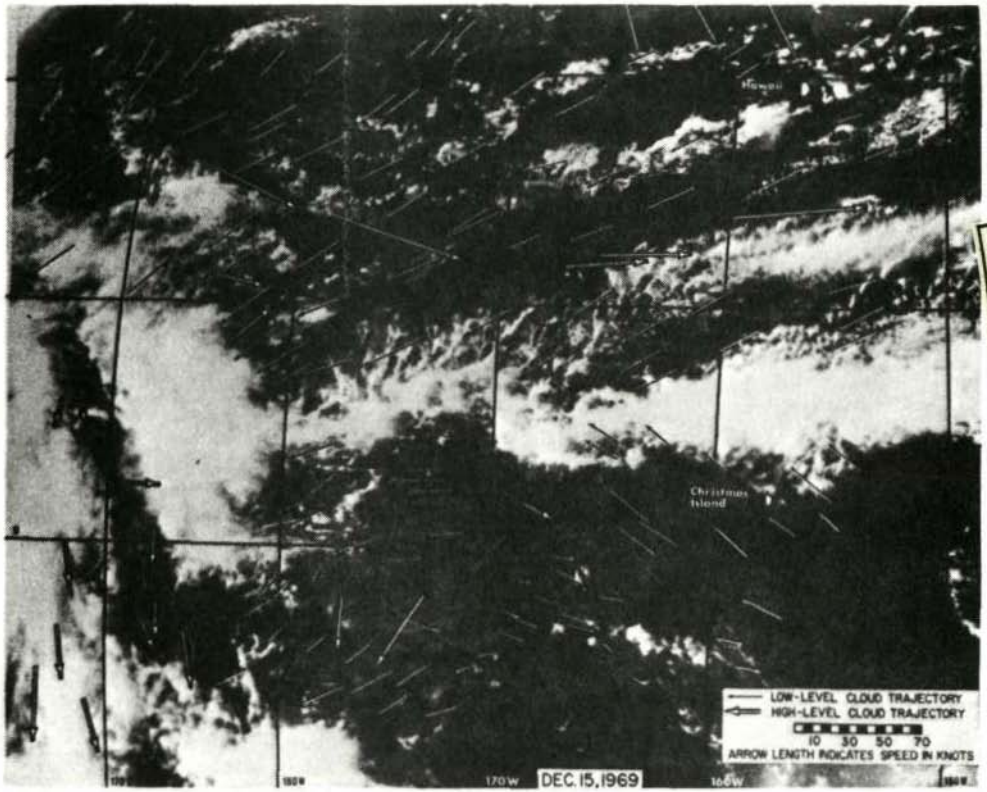

Reproduced from best available copy.

Figure 40. Cloud trajectory field for the east-central Pacific on December 15, 1969.

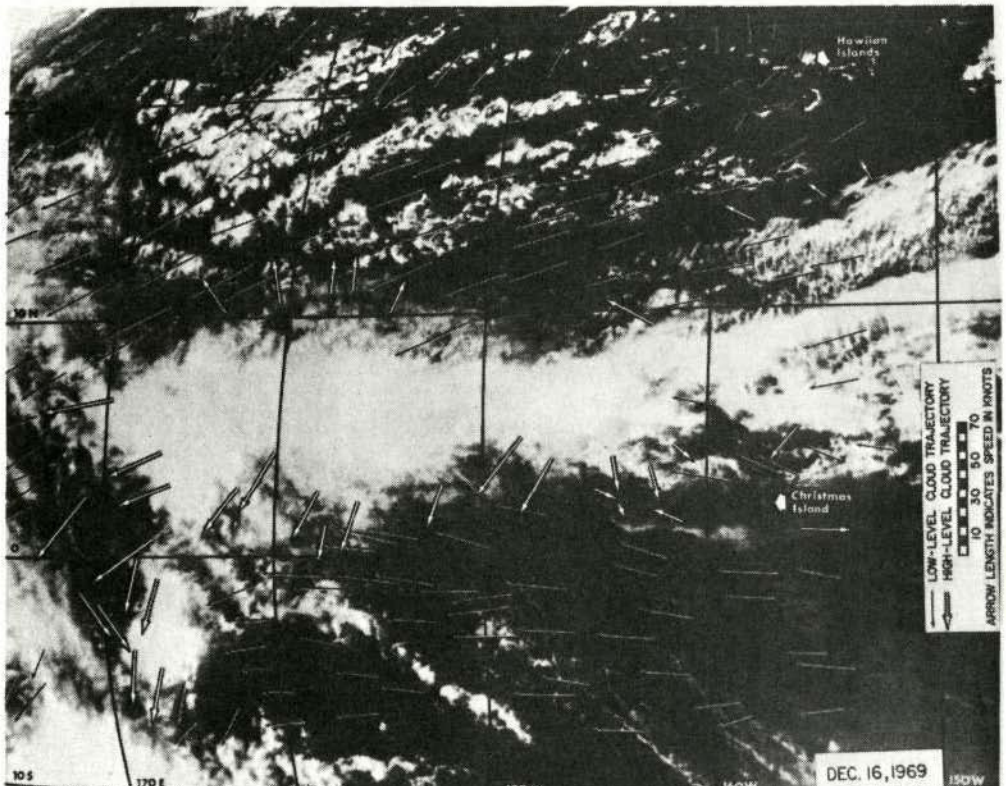

Figure 41. Cloud trajectory field for the east-central Pacific on December 16, 1969.

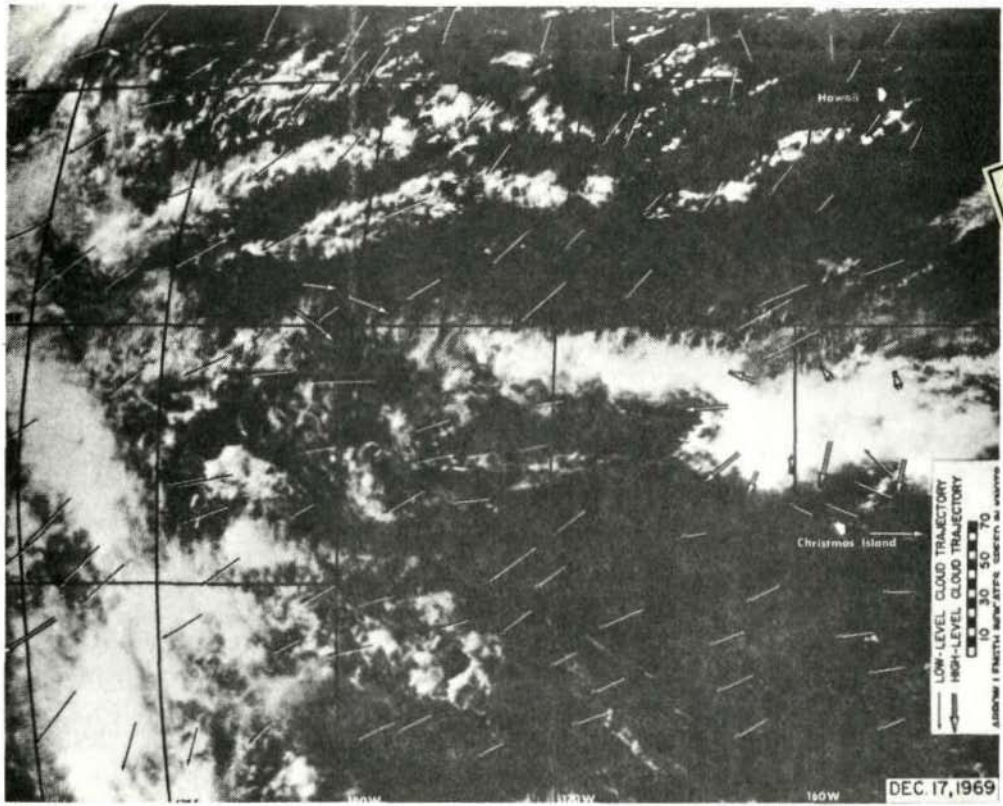

Reproduced from best available copy.

Figure 42. Cloud trajectory field for the east-central Pacific on December 17, 1969.

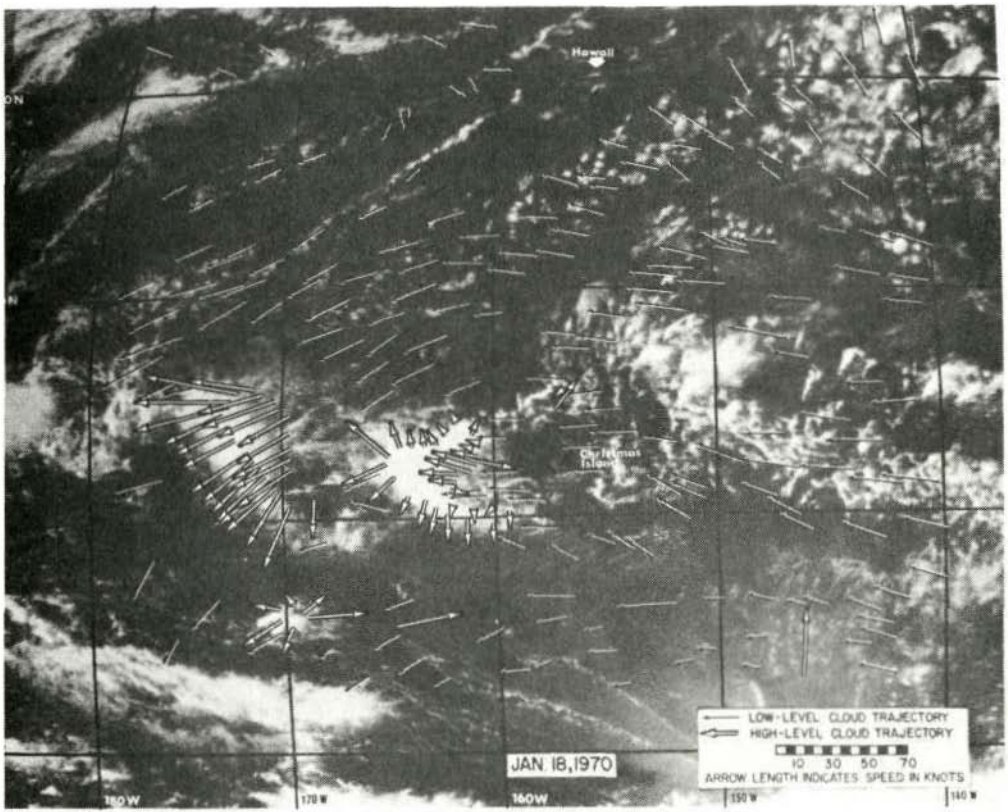

Figure 43. Cloud trajectory field for the central Pacific on January 18, 1970.

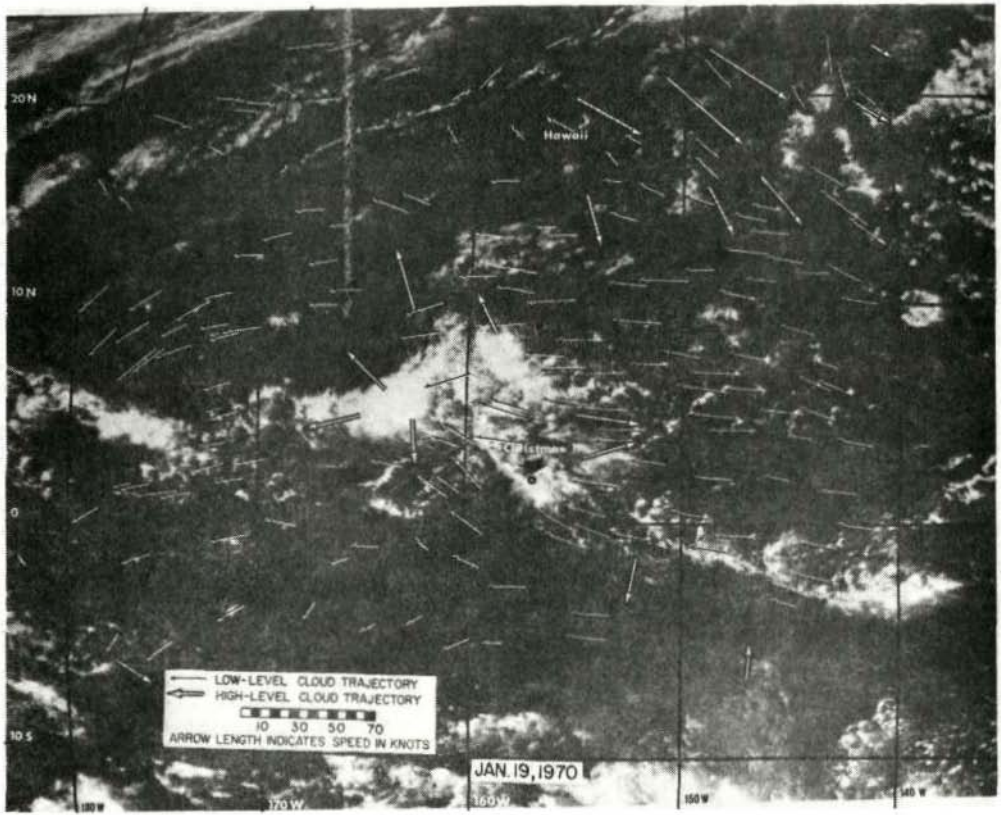

Reproduced from best available copy.

Figure 44. Cloud trajectory field for the central Pacific on January 19, 1970.

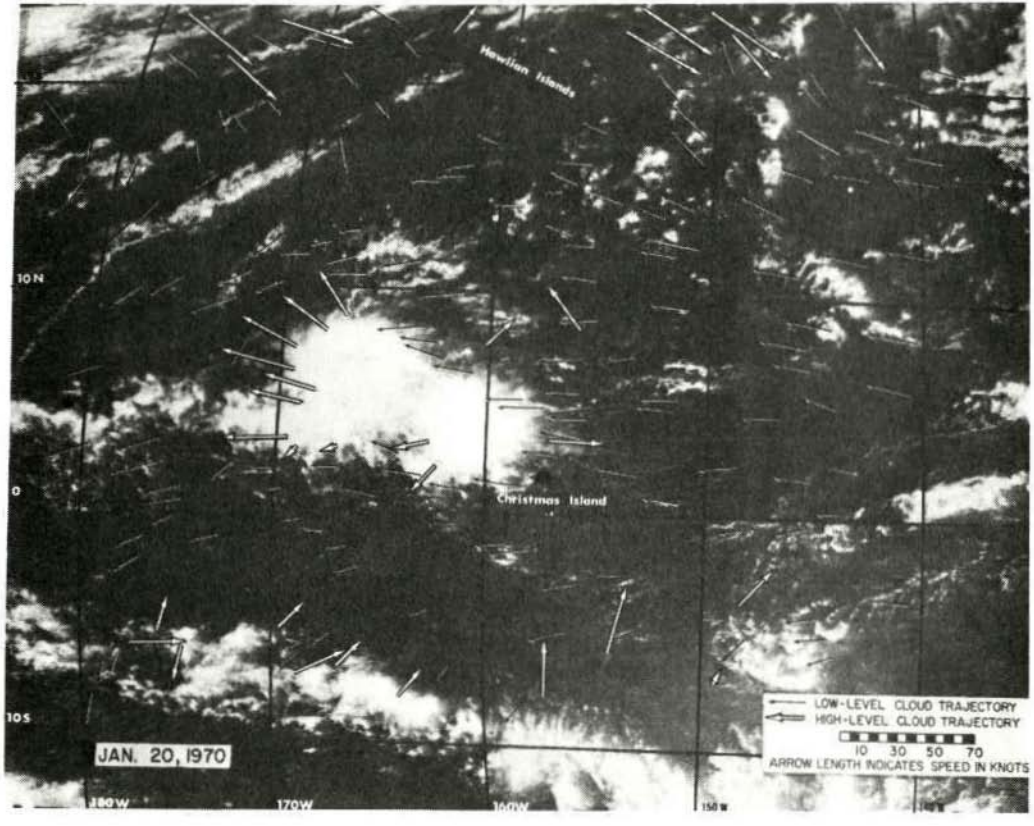

Figure 45. Cloud trajectory field for the central Pacific on January 20, 1970.

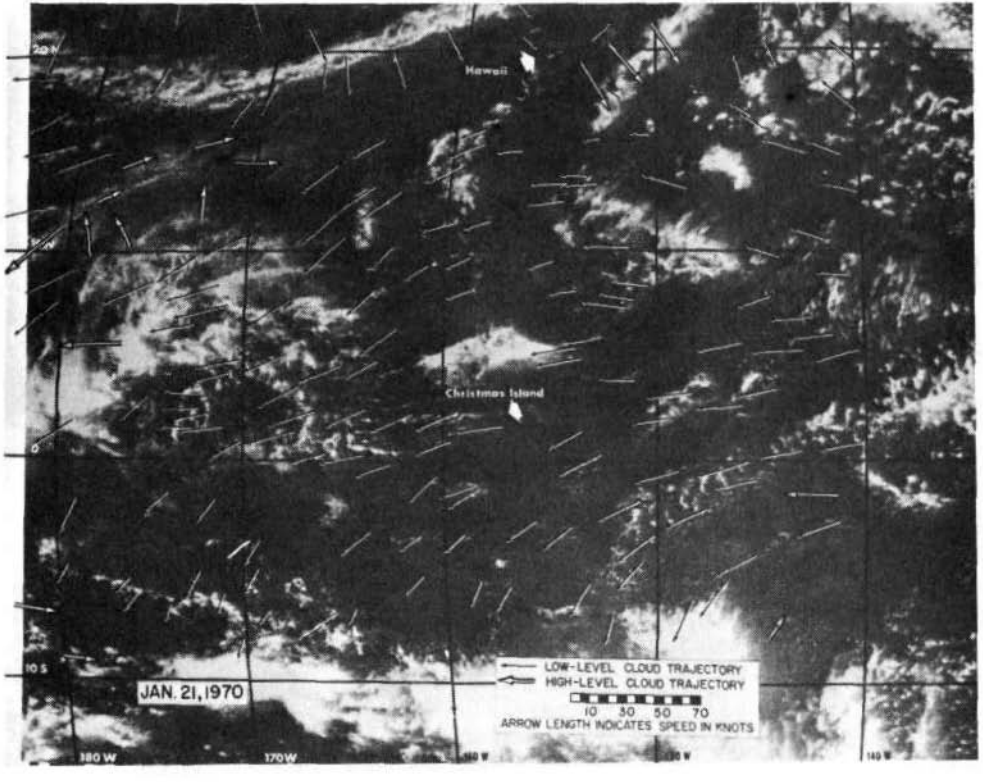

Figure 46. Cloud trajectory field for the central Pacific on January 21, 1970.

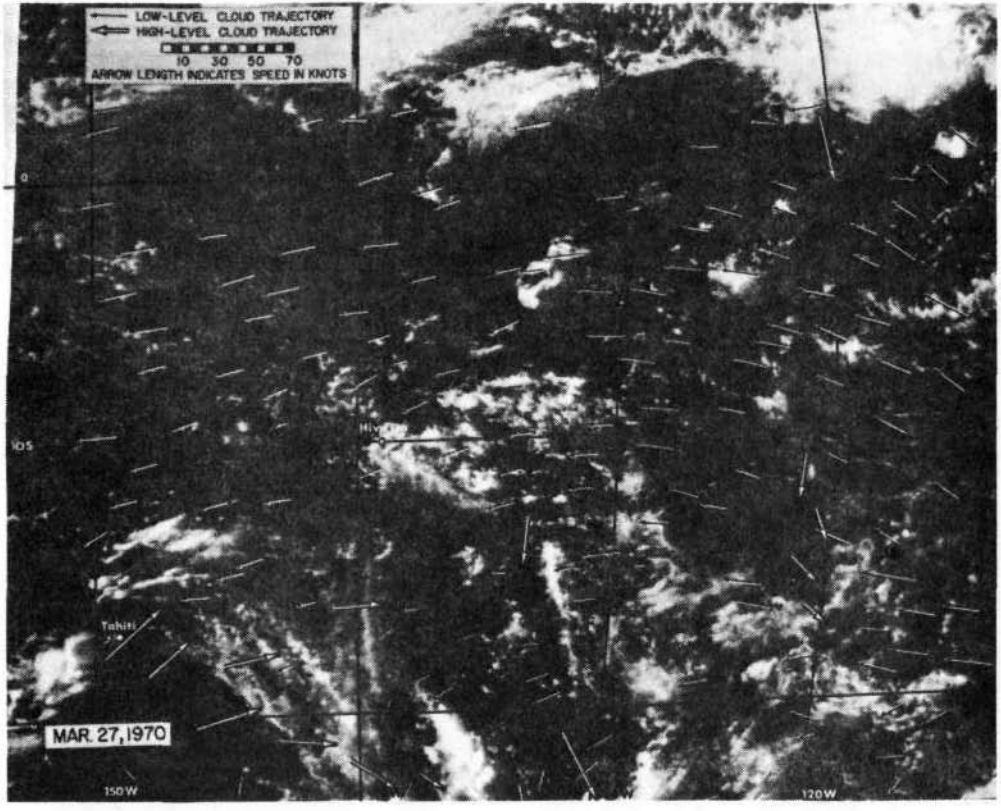

Figure 47. Cloud trajectory field for the south central Pacific on March 27, 1970.

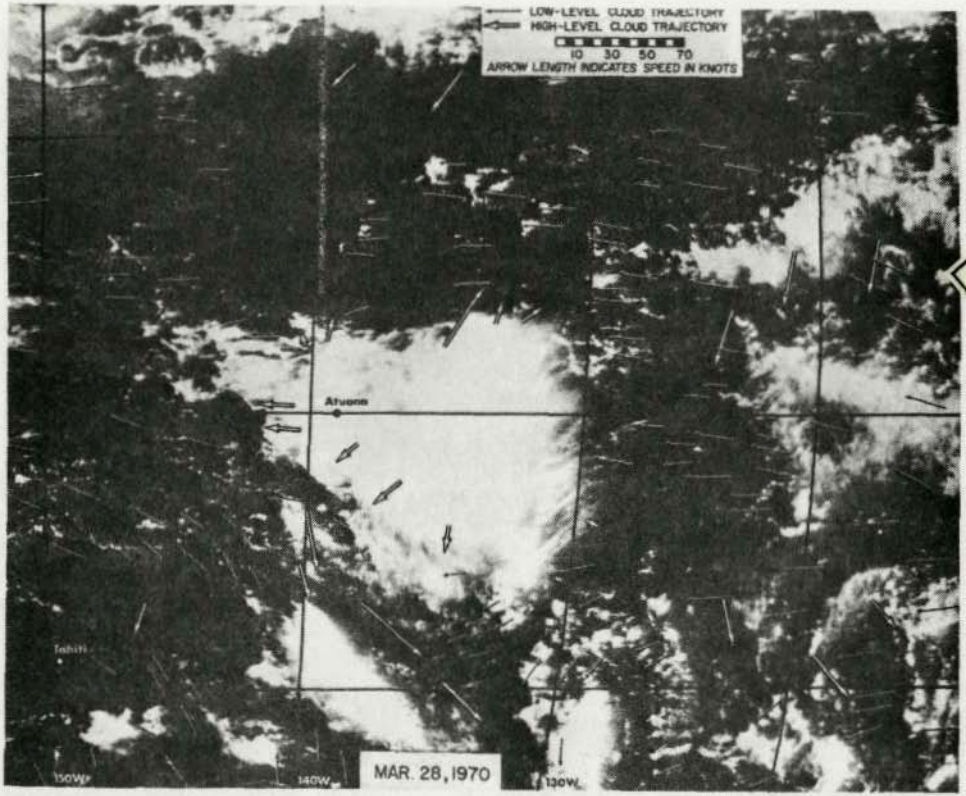

Reproduced from best available copy.

Figure 48. Cloud trajectory field for the south central Pacific on March 28, 1970.

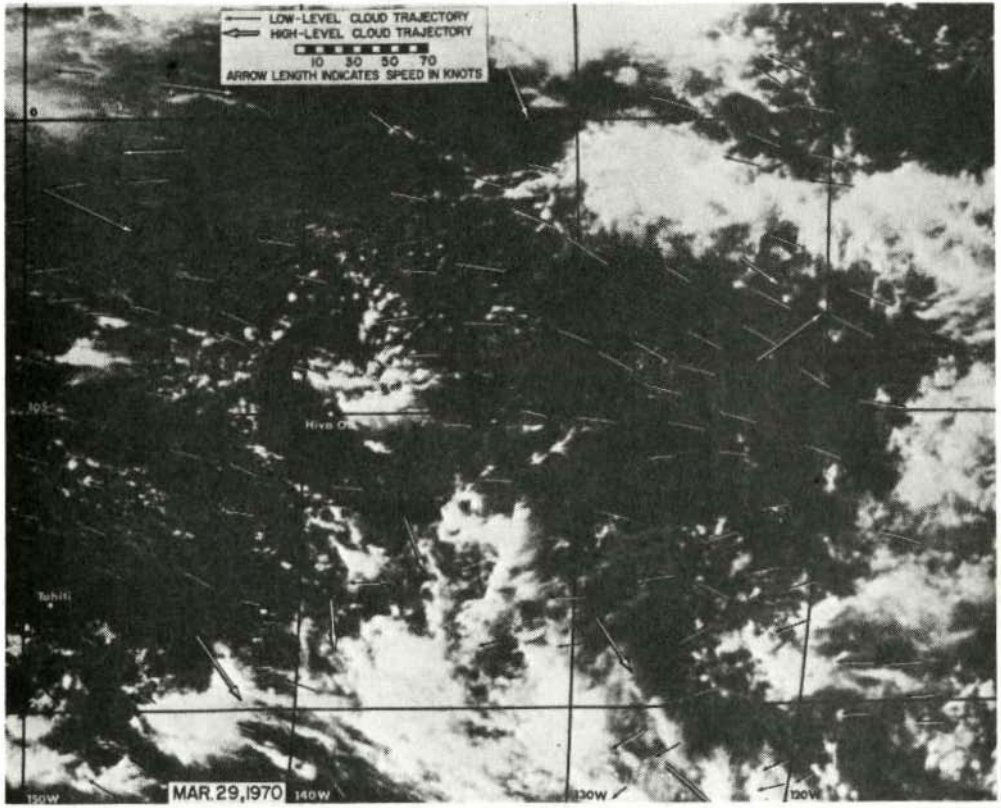

Figure 49. Cloud trajectory field for the south central Pacific on March 29, 1970.

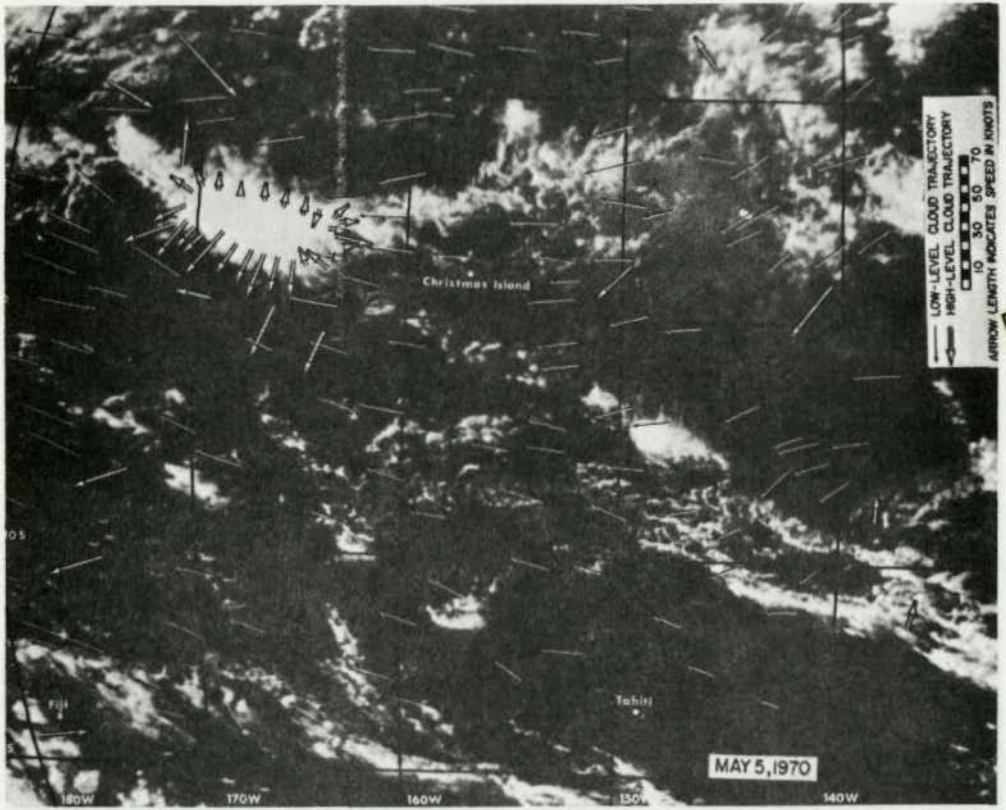

Reproduced from best available copy.

Figure 50. Cloud trajectory field for the central Pacific on May 5, 1970.

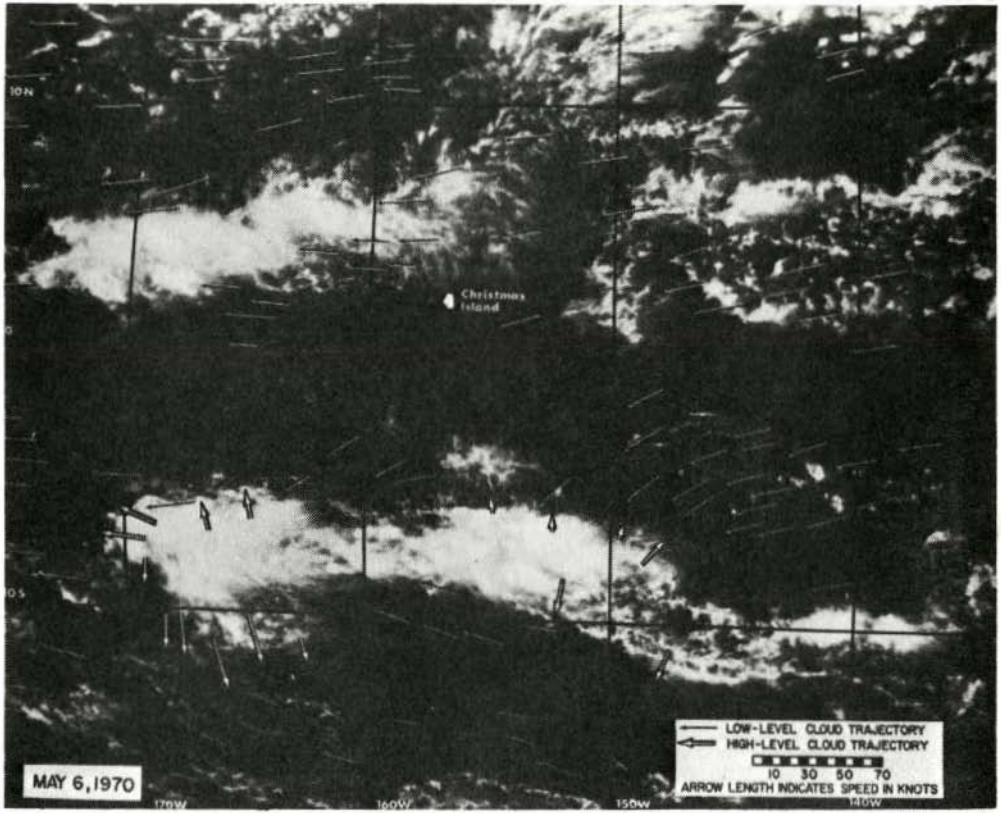

Figure 51. Cloud trajectory field for the central Pacific on May 6, 1970.

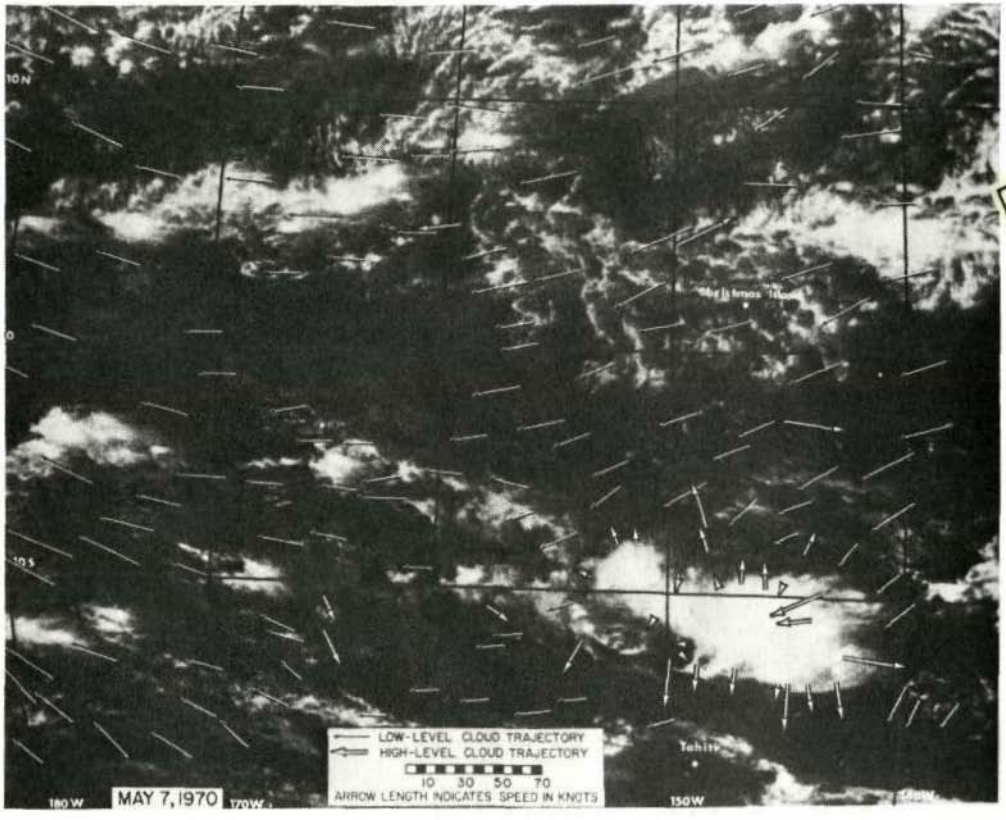

Reproduced from best available copy.

Figure 52. Cloud trajectory field for the central Pacific on May 7, 1970.

ACKNOWLEDGMENTS

I wish to express my thanks to Professor Verner E. Suomi for his insight with respect to many of the basic ideas of this thesis and for his patience with me while I finished. I wish also to thank Professor David Houghton and Dr. D. N. Sikdar for their suggestions and help with the final text.

I greatly appreciate the help of Jack Kornfield and Larry Jensen with the original navigation work and to Jack for his help with many problems along the way. My thanks also go to Tom Vonder Haar, Eric Smith and the many others who were instrumental in producing this paper.

REFERENCES

Bellamy, J. C., 1949: "Objective Calculations of Divergence, Vertical Velocity and Vorticity." Bull. Amer. Meteor. Soc., 30, 45-49.

Byers, H. R., and R. R. Braham, 1949: The Thunderstorm. U. S. Dept. of Commerce, Washington, D. C., 287 pp.

Frank, N. L., 1970: "Atlantic Tropical Systems of 1969." Mon. Wea. Rev., 98, 307-314.

Fujita, T. T., K. Watanabe and T. Izawa, 1969: "Formation and Structure of Equatorial Anticyclones Caused by Large-Scale Cross-Equatorial Flows Derived by ATS-I Photographs." J. Appl. Meteor., 8, 649-667.

Hayden, C. M., 1971: "An Objective Analysis of Cloud Cluster Dimensions and Spacing in the Tropical North Pacific." Mon. Wea. Rev., 99, 67-78.

Hubert, L. F., and L. F. Whitney, Jr., 1971: "Wind Estimation from Geostationary Satellite Pictures." Mon. Wea. Rev., 99, 665-672.

Karst, O., and D. W. Martin, 1969: "A Census of Cloud Systems over the Tropical Pacific." Studies in Atmospheric Energies based on Aerospace Probings, Annual Rept., 1968, SSEC, University of Wisconsin, 75 pp.

Kornfield, J., and A. F. Hasler, 1969: "A Photographic Summary of the Earth's Cloud Cover for the Year 1967." J. Appl. Meteor., 8, 687-700.

_____, _____, K. H. Hanson and V. E. Suomi, 1967: "Photographic Cloud Climatology from ESSA III and V Computer-Produced Mosaics." Bull. Amer. Meteor. Soc., 48, 878-883.

Martin, David W., and V. E. Suomi, 1971: "A Satellite Study of Cloud Clusters over the Tropical North Atlantic Ocean." Final Rept. on Tropical Cloud Organization Studies, Task Order No. 3 to STAG Contract E-127-69-(N), SSEC, University of Wisconsin, 80 pp.

Schmidt, P., and D. Johnson, 1971: "Vertical Profiles of Polynomial Filtered Winds, Divergence and Vertical Motion." Mon. Wea. Rev., (accepted for publication, 1971).

Serebreny, S. M., R. G. Hadfield, R. M. Trudean and E. J. Wiegman, 1969: "Comparison of Cloud Motion Vectors and Rawinsonde Data." Final Rept., SRI Project 7257, Stanford Research Institute, Menlo Park, California, 62 pp.

Sikdar, D. N., 1969: "Convective Heat Transport over the Tropical Mid-Pacific as Estimated from a Geosynchronous Satellite Altitude." Ph. D. thesis, Dept. of Meteorology, University of Wisconsin, 130 pp.

Smith, A. E., and D. R. Phillips, 1971: "Automatic Cloud Tracking Using Precisely Aligned Digital ATS Pictures." Paper presented at: The Two-Dimensional Digital Signal Processing Conference, University of Missouri, Oct. 6-8, 1971, 50 pp.

Suomi, V. E., and R. J. Parent, 1968: "A Color View of Planet Earth." Bull. Amer. Meteor. Soc., 49, 74-75.

_____, and T. H. Vonder Haar, 1969: "Geosynchronous Meteorological Satellites." J. Spacecraft and Rockets, 6, 342-350.

U. S. Committee for the Global Atmospheric Research Program, 1971: "Plan for U. S. Participation in the GARP Atlantic Tropical Experiment." National Academy of Sciences, Washington, D. C., 25 pp.

Wallace, J. M., and C. P. Chang, 1969: "Spectrum Analysis of Large-Scale Wave Disturbances in the Tropical Lower Troposphere." J. Atmos. Sci., 26, 1010-1025.

Williams, K. T., 1970: "A Statistical Analysis of Satellite-Observed Trade Wind Cloud Clusters in the Western North Pacific." Atmos. Sci. Paper No. 161, Dept. of Atmospheric Sciences, Colorado State University, 80 pp.

Yanai, M., and M. Murakami, 1970: "Spectrum Analysis of Symmetric and Antisymmetric Equatorial Waves." J. Meteor. Soc. Japan, Vol. 48, 331-347.

COVER DESCRIPTION

Cover figure diagrams a cloud motion field derived from the ATS-III satellite digital data by the WINDCO system. The motion was found by measuring cloud displacement with respect to the line and element coordinates of two successive ATS digital pictures. This displacement is then transformed to a displacement on the surface of the earth by a process called ATS Navigation. Cloud motions were measured where a cloud target has been designated by an operator. The displacements were then measured by a computer by a cross-correlation method.